

High-resolution Numerical Schemes for Compressible Flows and Compressible Two-phase Flows

**A thesis submitted in partial fulfillment
of the requirement for the degree of Doctor of Philosophy**

Qijie Li



**School of Engineering
Cardiff University**

July 2019

*To my girlfriend
for her love and encouragement.*

*To my parents and sister
for their support.*

Abstract

Several high-resolution numerical schemes based on the Constrained Interpolation Profile Conservative Semi-Lagrangian (CIP-CSL), Essentially Non-Oscillatory (ENO), Weighted ENO (WENO), Boundary Variation Diminishing (BVD), and Tangent of Hyperbola for INterface Capturing (THINC) schemes have been proposed for compressible flows and compressible two-phase flows.

In the first part of the thesis, three high-resolution CIP-CSL schemes are proposed. (i) A fully conservative and less oscillatory multi-moment scheme (CIP-CSL3-ENO) is proposed based on two CIP-CSL3 schemes and the ENO scheme. An ENO indicator is designed to intentionally select non-smooth stencil but can efficiently minimise numerical oscillations. (ii) Motivated by the observation that combining two different types of reconstruction functions can effectively reduce numerical diffusion and oscillations, a better-suited scheme CIP-CSL-ENO5 is proposed based on hybrid-type CIP-CSL reconstruction functions and a newly designed ENO indicator. (iii) To further reduce the numerical diffusion in vicinity of discontinuities, the BVD and THINC schemes are implemented in the CIP-CSL framework. The resulting scheme accurately capture both smooth and discontinuous solutions simultaneously by selecting an appropriate reconstruction function.

In the second part of the thesis, the TWENO (Target WENO) scheme is proposed to improve the accuracy of the fifth-order WENO scheme. Unlike conventional WENO schemes, the TWENO scheme is designed to restore the highest possible order inter-

polation when three sub-stencils or two adjacent sub-stencils are smooth. To further minimise the numerical diffusion across discontinuities, the TWENO scheme is implemented with the THINC scheme and the Total Boundary Variation Diminishing (TBVD) algorithm. The resulting scheme TBVD-TWENO-THINC is also applied to solve the five-equation model for compressible two-phase flows.

Verified through a wide range of benchmark tests, the proposed numerical schemes are able to obtain accurate and high-resolution numerical solutions for compressible flows and compressible two-phase flows.

Acknowledgements

I am very grateful to those who supported and helped me for this Ph.D. project during the past three and a half years. Firstly, I would like to express my gratitude to my supervisor, Dr Kensuke Yokoi, for his invaluable help, his technical expertise, his enthusiasm, his great sense of humor and his constant encouragements. I also extend my sincere gratitude to my second supervisor, Dr Hanxing Zhu, for his instructive advice, useful suggestions, and constant supports. I am deeply grateful of his help.

I will express my gratitude to all my colleagues of the laboratory for the pleasant working atmosphere. Particularly, I am thankful to Syazana Omar for the great discussion with her. We have learned a lot together. I also thank Dr Atheel Shuker Jameel and Dr Mohammed Al-Mosallam for our discussions on the programming, math, physics, and OpenFOAM. The great support received from Cardiff University is also gratefully acknowledged. In addition, I gratefully appreciate the financial support of Chinese Government Scholarships and Cardiff University.

I would like to express my special thanks to Prof Feng Xiao (Tokyo Institute of Technology) for welcoming me in Japan and for our very enlightening and interesting discussions. His integrity research attitude, profound knowledge, and kindness personality have a great influence on me. I would also like to show my special thanks to Dr Xi Deng for his welcoming, great help and support during my visit. The great discussion with him always very useful and enlightening.

I want to show my special gratitude and thanks to my family, along with the family

that made me who I am. They are always there for me. My parents and my old sister are very concerned about my life and care about my health. I have received more than I can imagine from them. Moreover, thank my lovely nephew keep on cheering for me (born in the period of my Ph.D.).

My final thanks go to my girlfriend from the deep of my heart. Thank for her deep love, painstaking care, instructive advice, constant encouragement and support. I am always getting enough motivations from her to push myself forward, to keep healthy, and to be a better man. Thank my love and my family again for their constant supports.

Finally, I would like to express my gratitude to my friends and those who ever helped me.

Contents

Abstract	iii
Acknowledgements	v
Contents	vii
List of Publications	xiii
List of Figures	xiv
List of Tables	xxii
List of Acronyms	xxiv
Nomenclature	xxviii
1 Introduction	1
1.1 Background	1
1.2 Purpose of the research	3
1.3 Outline of the thesis	3

2	Literature review	6
2.1	Governing equations	6
2.2	Numerical methods for Euler equations	7
2.3	Godunov-type high-resolution shock capturing methods	9
2.3.1	High-order reconstruction schemes	10
2.3.2	WENO-JS scheme	12
2.3.3	WENO-Z scheme	13
2.3.4	Numerical difficulties for WENO schemes	14
2.4	CIP-CSL schemes	15
2.4.1	CIP-CSL2 scheme	15
2.4.2	CIP-CSL3 schemes (CSL3CW and CSL3H)	18
2.4.3	CIP-CSLR scheme	20
2.4.4	CIP-CSL-WENO4 scheme	20
2.4.5	CIP-CSL schemes for the Euler conservation law	22
2.4.6	Numerical difficulties for CIP-CSL schemes	25
2.5	Boundary variation diminishing reconstruction	26
2.5.1	THINC	27
2.5.2	BVD selection criteria	28
2.6	Numerical methods for moving interface in two-phase flows	30
2.7	Numerical difficulties for compressible two-phase flows with moving interface	32
2.8	Summary and the way forward	32

3	Fourth-order essentially non-oscillatory CIP-CSL3 scheme	35
3.1	Numerical method	36
3.1.1	CIP-CSL3D scheme	36
3.1.2	CIP-CSL3U scheme	38
3.1.3	Fourier analysis of the CIP-CSL3D and CIP-CSL3U schemes	39
3.1.4	CIP-CSL3-ENO scheme	44
3.1.5	Implementation of boundary conditions	45
3.2	Numerical results	45
3.2.1	Sine wave propagation	45
3.2.2	Square wave propagation	47
3.2.3	Complex wave propagation	50
3.2.4	Extrema of the various smoothness problem	54
3.2.5	Burgers' equation	56
3.2.6	Sod's problem	58
3.2.7	Lax's problem	59
3.2.8	Shock-turbulence interaction	62
3.3	Summary	64
4	Fifth-order essentially non-oscillatory hybrid CIP-CSL scheme	65
4.1	Numerical method	66
4.1.1	CIP-CSL4Q scheme	66
4.1.2	CIP-CSL-ENO5 scheme	67

4.2	Numerical results	72
4.2.1	Sine wave propagation	72
4.2.2	Complex wave propagation	74
4.2.3	Lax’s problem	78
4.2.4	Shock turbulence problem	79
4.2.5	Two blast waves interaction problem	81
4.2.6	2D lid-driven cavity flow problem	82
4.3	Summary	83
5	Implementation of Boundary Variation Diminishing (BVD) algorithm in the CIP-CSL scheme	84
5.1	Numerical method	85
5.1.1	CIP-CSLT scheme	85
5.1.2	CIP-CSLT-WENO4-BVD scheme	86
5.2	Analysis of the computational efficiency for CIP-CSL schemes	87
5.3	Numerical results	88
5.3.1	Sine wave propagation	88
5.3.2	Complex wave propagation problem	89
5.3.3	Lax’s problem	91
5.3.4	Two blast waves interaction problem	93
5.3.5	2D circular explosion problem	93
5.4	Summary	96

6	Implementation of Total Boundary Variation Diminishing (TBVD) algorithm with the TWENO and THINC schemes	97
6.1	Numerical method	98
6.1.1	Target WENO (TWENO) scheme	98
6.1.2	THINC with adaptive β^T	101
6.1.3	TBVD-TWENO-THINC scheme	102
6.1.4	Time evolution method	104
6.2	Analysis of the computational efficiency for TBVD-TWENO-THINC	104
6.3	Numerical results	105
6.3.1	1D advection equation	105
6.3.2	1D Euler equations	111
6.3.3	2D square profile propagation in diagonal direction test	114
6.3.4	2D Zelasak's test	116
6.3.5	2D double-Mach reflection problem	117
6.4	Summary	122
7	Numerical simulation of compressible two-phase flows	123
7.1	Computational model	124
7.2	Numerical method	125
7.3	Numerical results	128
7.3.1	Passive advection of a square liquid column	128
7.3.2	Two-material impact problem	129
7.3.3	2D shock-bubble interaction problem	130

7.4	Summary	137
8	Summary and future work	138
8.1	Summary	138
8.2	Future work	141
A	Fourier analysis of the CIP-CSL3U and CIP-CSL3D schemes	142
A.1	Mathematical formulations of Fourier analysis of the CIP-CSL3U and CIP-CSL3D schemes	142
B	Roe’s Riemann solver for Euler equations	145
	Bibliography	152

List of Publications

The work introduced in this thesis is based on the following publications.

- Q.J. Li and K. Yokoi. A fifth-order weighted essentially non-oscillatory (WENO) shock capturing scheme for compressible flow. The 10th Gregynog Conference, Cardiff University, UK, June 26-28, 2018. [Best presentation]
- Q.J. Li, S. Omar, X. Deng, and K. Yokoi. Constrained Interpolation Profile Conservative Semi-Lagrangian Scheme Based on Third-Order Polynomial Functions and Essentially Non-Oscillatory (CIP-CSL3-ENO) Scheme. *Communications in Computational Physics*, Volume 22(3):765-788, 2017.
- Q.J. Li and K. Yokoi. Numerical simulations of multiphase flows using the CIP-CSL3-ENO scheme. The 3rd International Conference on Numerical Methods in Multiphase Flows, Tokyo, Japan, June 26-29, 2017.
- Q.J. Li and K. Yokoi. A fourth-order essentially non-oscillatory CIP-CSL scheme, UK Fluid conference 2016, Imperial College, London, UK, 2016.
- Q.J. Li and K. Yokoi. An efficient implementation of the CIP-CSL scheme. Toyo University-Cardiff University Workshop, Cardiff University, UK, February 2016.

List of Figures

2.1	Sketch of the fifth-order WENO-JS reconstruction. The candidate stencils include three sub-stencils S_0, S_1 and S_2	12
2.2	Schematic figures of the CIP-CSL2 scheme. The moments which are indicated by grey colour are used as constraints to construct interpolation function $\Phi_i^{CSL2}(x)$. The wave propagation speed $u_{i-1/2} < 0$ is assumed	15
2.3	Schematic figures of the CIP-CSL3 scheme. The moments which are indicated by grey colour are used as constraints to construct interpolation function $\Phi_i^{CSL3}(x)$. The wave propagation speed $u_{i-1/2} < 0$ is assumed	18
2.4	Reconstruction stencils for the weighted essentially non-oscillatory limiter	21
2.5	The simulation of the advection of a square wave by the CSL2 scheme on a 100-cell mesh	26
2.6	Illustration of one possible situation corresponding to $ \Phi_i^{THINC}(x_{i+1/2}) - \Phi_{i+1}^{WENO}(x_{i+1/2}) $ when calculating boundary variation at $x_{i+1/2}$	29
2.7	Illustration of one possible situation corresponding to $ \Phi_{i-1}^{WENO}(x_{i-1/2}) - \Phi_i^{THINC}(x_{i-1/2}) $ when calculating boundary variation at $x_{i-1/2}$	29

3.1	Schematic figures of the CIP-CSL3D scheme. $u_{i-1/2} < 0$ is assumed. The moments which are indicated by grey colour are used as constraints to construct interpolation function $\Phi_i^{CSL3D}(x)$	36
3.2	Schematic figures of the CIP-CSL3U scheme. $u_{i-1/2} < 0$ is assumed. The moments which are indicated by grey colour are used as constraints to construct interpolation function $\Phi_i^{CSL3U}(x)$	38
3.3	Spatial derivatives of the CIP-CSL3D and CIP-CSL3U schemes at a cell boundary $x_{i-1/2}$. The results of imaginary parts of (a) first derivatives, (b) second derivatives, (c) third derivatives	41
3.4	Spatial derivatives of the CIP-CSL3D and CIP-CSL3U schemes at a cell boundary $x_{i+1/2}$. The results of imaginary parts of (a) first derivatives, (b) second derivatives, (c) third derivatives	42
3.5	Spatial derivatives of the CIP-CSL3D and CIP-CSL3U schemes at the cell centre x_i . The results of imaginary parts of (a) first derivatives, (b) second derivatives, (c) third derivatives	43
3.6	Numerical results of square wave propagation test at t=16 (8,000 time steps). N=200 and CFL=0.2 are used. (a) CIP-CSL3D, (b) CIP-CSL3U, (c) CIP-CSL3-ENO	48
3.7	Numerical results of square wave propagation test at t=16 (2,000 time steps). N=200 and CFL=0.8 are used. (a) CIP-CSL3D, (b) CIP-CSL3U, (c) CIP-CSL3-ENO	49
3.8	Numerical results of complex wave propagation test at t=16 (4,000 time steps, 8 period). CFL=0.4 and N=200 are used. (a) CIP-CSL2, (b) CIP-CSL3CW, (c) CIP-CSL3H, (d) CIP-CSL3D, (e) CIP-CSL3U, (f) CIP-CSL3-ENO	51

3.9	Numerical results of complex wave propagation test at $t=160$ (40,000 time steps, 80 period). CFL=0.4 and $N=200$ are used. (a) CIP-CSL2, (b) CIP-CSL3CW, (c) CIP-CSL3H, (d) CIP-CSL3D, (e) CIP-CSL3U, (f) CIP-CSL3-ENO	52
3.10	Numerical results of capturing extrema of various smoothness test at $t=8$. $N=100$ and CFL=0.4 are used. (a) CIP-CSL2, (b) CIP-CSL3CW, (c) CIP-CSL3H, (d) CIP-CSL3D, (e) CIP-CSL3U, (f) CIP-CSL3-ENO	55
3.11	Numerical results of Burgers' equation at $t=1$. $N=200$ and CFL=0.2 are used. (a) CIP-CSL2, (b) CIP-CSL3CW, (c) CIP-CSL3H, (d) CIP-CSL3D, (e) CIP-CSL3U, (f) CIP-CSL3-ENO	57
3.12	Initial condition of shock tube problem	58
3.13	Numerical results of Sod's shock tube problem at $t = 0.2$ ($N=200$ and CFL=0.2). (a) CIP-CSL2, (b) CIP-CSL3CW, (c) CIP-CSL3H, (d) CIP-CSL3D, (e) CIP-CSL3U, (f) CIP-CSL3-ENO	60
3.14	Numerical results of Lax's shock tube problem at $t=0.12$ ($N=200$ and CFL=0.2). (a) CIP-CSL2, (b) CIP-CSL3CW, (c) CIP-CSL3H, (d) CIP-CSL3D, (e) CIP-CSL3U, (f) CIP-CSL3-ENO	61
3.15	Numerical results of shock-turbulence interaction problem at $t=1.8$ (CFL=0.2 and $N=400$). (a) CIP-CSL2, (b) CIP-CSL3CW, (c) CIP-CSL3H, (d) CIP-CSL3D, (e) CIP-CSL3U, (f) CIP-CSL3-ENO	63
4.1	Schematic figure of the CIP-CSL4Q scheme. $u_{i-1/2} < 0$ is assumed. The moments which are indicated by grey colour are used as constraints to construct the interpolation function $\Phi_i^{CSL4Q}(x)$	66
4.2	Sketch of the reconstruction stencils of the CIP-CSL-ENO5 scheme.	68

4.3	Reconstruction stencils for the CIP-CSL-ENO5 scheme. The entire reconstruction stencil is continuous, CSL4Q is used as the reconstruction scheme	70
4.4	Reconstruction stencils for the CIP-CSL-ENO5 scheme. The discontinuity exists in the region of downwind-side between x_{i-1} and $x_{i-1/2}$, CSL3U is used as the reconstruction scheme	71
4.5	Reconstruction stencils for the CIP-CSL-ENO5 scheme. The discontinuity exists in the region of upwind-side between $x_{i+1/2}$ and x_{i+1} , CSL3D is used as the reconstruction scheme	71
4.6	Reconstruction stencils for the CIP-CSL-ENO5 scheme. The discontinuity may appear in the region between $x_{i-1/2}$ and $x_{i+1/2}$, CSLR is used as the reconstruction scheme	72
4.7	Numerical results of complex wave propagation test at time $t=2$ (1 period). $N=200$ and $CFL=0.4$ are used. (a) CIP-CSLR, (b) CIP-CSL4Q, (c) CIP-CSL3-ENO, (d) CIP-CSL-ENO5	74
4.8	Numerical results of complex wave propagation test at time $t=100$ (50 periods). $N=200$ and $CFL=0.4$ are used. (a) CIP-CSLR, (b) CIP-CSL4Q, (c) CIP-CSL3-ENO, (d) CIP-CSL-ENO5	75
4.9	A comparison of numerical results by the WENO-Roe5 scheme [1] and the CIP-CSL-ENO5 scheme in complex wave propagation test at $t=8$ (4 periods: 2,000 time steps). $N=200$ and $CFL=0.4$ are used	77
4.10	A comparison of numerical results by the multi-moment WENO scheme, the MCV-WENO scheme, and the CIP-CSL-ENO5 scheme in complex wave propagation test at $t=2$ (1 period: 500 time steps). $N=200$ and $CFL=0.4$ are used	77

4.11	Numerical results of Lax's shock tube problem at $t=0.12$. $N=200$ and $CFL=0.2$ are used. (a) CIP-CSLR, (b) CIP-CSL4Q, (c) CIP-CSL3-ENO, (d) CIP-CSL-ENO5	78
4.12	Numerical results of shock-turbulence interaction problem at time $t=0.18$. $N=400$ and $CFL=0.2$ are used. (a) CIP-CSLR, (b) CIP-CSL4Q, (c) CIP-CSL3-ENO, (d) CIP-CSL-ENO5	79
4.13	Zoomed-in view of Fig. 4.12	80
4.14	Numerical results of two interacting blast waves problem at $t=0.038$. $N=400$. CIP-CSLR (left) and CIP-CSL-ENO5 (right)	81
4.15	The horizontal velocity component u along the $x = 0.5$ axis and the vertical velocity component v along the $y = 0.5$ axis. Displayed are the results of the CIP-CSL-ENO5 scheme on 100×100 meshes with the Reynolds number being 1000 (top) and 3200 (bottom) respectively	82
5.1	Numerical results of complex wave propagation test at time $t=2$ (1 period). $N=200$ and $CFL=0.4$ are used. (a) CIP-CSL3-ENO, (b) CIP-CSL-ENO5, (c) CIP-CSL-WENO4, (d) CIP-CSLT-WENO4-BVD	90
5.2	Numerical results of Lax's shock tube problem at $t=0.16$ and $N=100$. (a) CIP-CSL3-ENO, (b) CIP-CSL-ENO5, (c) CIP-CSL-WENO4, (d) CIP-CSLT-WENO4-BVD	92
5.3	Numerical results of two interacting blast waves problem at $t=0.038$ and $N=400$. (a) CIP-CSL-ENO5, (b) CIP-CSL-WENO4, (c) CIP-CSLT-WENO4-BVD	93
5.4	2D circular explosion results of the CIP-CSLT-WENO4-BVD scheme at $t=0.25$. The density profile, side view (top) and the density profile along the cross-section of $x = y$ with 200×200 meshes (bottom left) and 400×400 meshes (bottom right)	95

6.1	Sketch of the TWENO scheme with three sub-stencils S_0 , S_1 , and S_2 .	98
6.2	Discontinuity exists in sub-stencil S_1 , while adjacent sub-stencils S_0 and S_2 are smooth	99
6.3	Discontinuity exists in sub-stencil S_2 , while adjacent sub-stencils S_0 and S_1 are smooth	100
6.4	The relationship between the parameter β^T and the mesh number in the jump transition zone. [2]	101
6.5	Illustration of one possible situation corresponding to $ \Phi_{i-1}^{TWENO,L}(x_{i-1/2}) - \Phi_i^{THINC,R}(x_{i-1/2}) + \Phi_{i+1}^{TWENO,R}(x_{i+1/2}) - \Phi_i^{THINC,L}(x_{i+1/2}) $ when calculating TBV_i^{THINC}	103
6.6	Numerical results of square wave propagation test at $t=2$. $N=200$ and $CFL=0.4$ are used. (a) WENO-Z, (b) TWENO, (c) BVD-WENOZ-THINC, (d) TBVD-TWENO-THINC	107
6.7	Numerical results of complex wave propagation test at $t=2$. $N=200$ and $CFL=0.4$ are used. (a) WENO-Z, (b) TWENO, (c) BVD-WENOZ-THINC, (d) TBVD-TWENO-THINC	109
6.8	Numerical results of capturing the extrema of the various smoothness test at $t=2$. $N=100$ and $CFL=0.4$ are used. (a) WENO-Z, (b) TWENO, (c) BVD-WENOZ-THINC, (d) TBVD-TWENO-THINC	110
6.9	Numerical results for Sod's shock tube problem at $t = 0.2$ with density output ($CFL=0.2$ and $N=100$). (a) WENO-Z, (b) BVD-WENOZ-THINC, (c) TBVD-TWENO-THINC	112
6.10	Numerical results of Lax's shock tube problem at $t=0.16$ ($CFL=0.2$ and $N=100$). (a) WENO-Z, (b) BVD-WENOZ-THINC, (c) TBVD-TWENO-THINC	112

6.11	Numerical results of shock-turbulence interaction problem at time $t=0.18$ (CFL=0.2 and $N=200$). (a) WENO-Z, (b) BVD-WENOZ-THINC, (c) TBVD-TWENO-THINC	113
6.12	Numerical results of two interacting blast waves problem at $t=0.038$ and $N=400$. (a) WENO-Z, (b) BVD-WENOZ-THINC, (c) TBVD-TWENO-THINC	114
6.13	Numerical results of 2D square wave propagation test at $t=2$ from top views. (a) Initial profile, (b) WENO-Z, (c) BVD-WENOZ-THINC, (d) TBVD-TWENO-THINC	115
6.14	2D Zelask test. (a) Initial profile, (b) WENO-Z, (c) BVD-WENOZ-THINC, (d) TBVD-TWENO-THINC	116
6.15	Sketch of double-Mach reflection problem [3].	118
6.16	Experiment results of double-Mach reflection problem performed by L.G. Smith [4]	118
6.17	Zoomed-in view of double-Mach reflection test with a qualitative comparison: density contours by (a) WENO-Z, (b) BVD-WENOZ-THINC, (c) TBVD-TWENO-THINC, (d) WENO-CU6, (e) TENO8 and (f) TENO8-opt at $t = 0.2$, with a 512×128 mesh. This figure is drawn with density contours between 1.887 and 20.9	120
6.18	Zoomed-in view of double-Mach reflection test with a qualitative comparison: density contours by (a) WENO-Z, (b) BVD-WENOZ-THINC, (c) TBVD-TWENO-THINC, (d) WENO-CU6, (e) TENO8 and (f) TENO8-opt at $t = 0.2$, with a 1024×256 mesh. This figure is drawn with density contours between 1.887 and 20.9	121

7.1	Numerical results of a passive advection of a square liquid column. $N=200$, $t = 10$ ms. Left: volume fraction (α_1), right: mass fraction ($\alpha_1\rho_1$)	129
7.2	Numerical results of the two-material impact test. $N=200$, $t = 85\mu s$. left: volume fraction (α_1), right: mass fraction ($\alpha_1\rho_1$)	130
7.3	A schematic of the computational domain	131
7.4	Results for a planar Mach 1.22 shock wave in air interacting with a circular R22 gas bubble at $t = 55 \mu s$. (a) experiment, (b) VOF, (c) VOF with interface-sharpening, and (d) TBVD-TWENO-THINC	132
7.5	Same as Fig. 7.4, but at $t = 115 \mu s$	133
7.6	Same as Fig. 7.4, but at $t = 135 \mu s$	133
7.7	Same as Fig. 7.4, but at $t = 187 \mu s$	134
7.8	Same as Fig. 7.4, but at $t = 247 \mu s$	134
7.9	Same as Fig. 7.4, but at $t = 342 \mu s$	135
7.10	Same as Fig. 7.4, but at $t = 417 \mu s$	135

List of Tables

3.1	L_1 and L_∞ errors in sine wave propagation at $t=1$	46
3.2	L_1 and L_∞ errors in complex wave propagation test of the CIP-CSL2, CIP-CSL3CW, CIP-CSL3H, CIP-CSL3D, CIP-CSL3U, and CIP-CSL3-ENO schemes at $t=16$ (4000 time steps, 8 periods) and $t=160$ (40,000 time steps, 80 periods). $N=200$ and $CFL=0.4$ are used	53
3.3	Errors in capturing extrema of various smoothness test of the CIP-CSL2, CIP-CSL3CW, CIP-CSL3H, CIP-CSL3D, CIP-CSL3U, and CIP-CSL3-ENO schemes. $t=8$ (4 periods), $N=100$ and $CFL=0.4$	56
3.4	L_1 and L_∞ errors in Burgers' equation at $t=0.25$	58
4.1	L_1 and L_∞ errors in sine wave propagation at $t=1$	73
4.2	L_1 and L_∞ errors in complex wave propagation test at $t=2$ (1 period) and at $t=100$ (50 periods). $N=200$ and $CFL=0.4$ are used	76
5.1	Computational efficiency for solving square wave propagation problem by using CIP-CSL schemes. $t=2$ and $CFL=0.4$	87
5.2	L_1 and L_∞ errors in sine wave propagation at $t=1$	89
5.3	Numerical errors in complex wave propagation test at $t=2$ (1 period). $N=200$ and $CFL=0.4$ are used	91

6.1	Computational efficiency for solving square wave propagation problem by using WENO-JS, WENO-Z, TWENO, BVD-WENOZ-THINC, and TBVD-TWENO-THINC. $t=2$ and $CFL=0.4$	105
6.2	Errors and convergence rates for sine wave propagation test, at $t=2$. . .	106
6.3	Errors in capturing square wave advection test at $t=2$. $N=200$ and $CFL=0.4$ are used	108
6.4	Errors in capturing complex wave propagation test at $t=2$. $N=200$ and $CFL=0.4$ are used	109
6.5	Numerical errors in capturing extrema of the various smoothness test at $t=2$. $N=100$ and $CFL=0.4$ are used	111
6.6	Errors in capturing 2D square wave propagation test, mesh: $100*100$	116
6.7	Errors in capturing 2D Zelasak test, mesh: $200*200$	117
6.8	Errors and convergence rates for Zelesak test problem by TBVD-TWENO-THINC	117
7.1	Material quantities for liquid ($k=1$) and gas ($k=2$) in the stiffened gas equation of state	129
7.2	Material quantities for copper ($k=1$) and explosive ($k=2$) in Cochran-Chan equation of state	130
7.3	The initial state quantities of 2D shock-bubble interaction problem. Inside the gas bubble ($k=1$), pre-shock regions outside the bubble ($k=2$), and post-shock regions outside the bubble ($k=3$)	132

List of Acronyms

BEM Boundary Element Method

BV Boundary Variation

BVD Boundary Variation Diminishing

BVD-WENOZ-THINC BVD with WENO-Z and THINC reconstructions

CFD Computational Fluid Dynamics

CFL Courant-Friedrich-Lewy

CIP Constrained Interpolation Profile

CSL Conservative Semi-Lagrangian

CIP-CSL Constrained Interpolation Profile Conservative Semi-Lagrangian

CIP-CSL2 CIP-CSL scheme with a second-order polynomial function

CIP-CSL3 CIP-CSL scheme with a third-order polynomial

CIP-CSL3CW CIP-CSL3 scheme with Collela and Woodward's approximation

CIP-CSL3H CIP-CSL3 scheme with Hymann's approximation

CIP-CSL3U variant of the CIP-CSL3 scheme with constraints in upwind cells

CIP-CSL3D variant of the CIP-CSL3 scheme with constraints in downwind cells

CIP-CSLR CIP-CSL scheme with a Rational function

CIP-CSLT CIP-CSL scheme with a Tangent hyperbolic function

CIP-CSL-WENO4 CIP-CSL scheme with a fourth-order WENO limiter

CIP-CSL3-ENO CIP-CSL3 scheme with ENO

CIP-CSL4Q CIP-CSL scheme with a fourth-order Quartic polynomial function

CIP-CSL-ENO5 fifth-order CIP-CSL scheme with ENO

CIP-CSLT-WENO4-BVD BVD with CIP-CSLT and CIP-CSL-WENO4

CLSVOF Coupled Level-Set Volume of Fluid method

DOF Degree of Freedom

ENO Essentially Non-Oscillatory

FDM Finite Difference Method

FEM Finite Element Method

FVM Finite Volume Method

EOS Equations-of-State

HLL Harten, Lax, Van Leer Riemann solver

HLLC Contact HLL Riemann solver

HWENO Hermite-type WENO

IVP Initial Value Problem

IC Initial Condition

LS Level Set

MAC Marker-and-Cell

MCV Multi-moment Constrained finite Volume

MUSCL Monotonic Upwind Scheme for Conservation Laws

MCV-WENO MCV with a WENO limiter

NS Navier-Stokes

ODE Ordinary Differential Equation

PDE Partial Differential Equation

RK Runge-Kutta

SEM Spectral Element Method

SSP Strong Stability-Preserving

SSPRK Strong Stability-Preserving Runge-Kutta

DG Discontinuous Galerkin

TVD Total Variation Diminishing

TENO Targeted Essentially Non-oscillatory

TENO8 8th order TENO

THINC Tangent of Hyperbola for INterface Capturing

TBV Total Boundary Variation

TBVD Total Boundary Variation Diminishing

TBVD-TWENO-THINC TBVD with TWENO and THINC reconstructions

TWENO Target WENO

Volume of Fluid VOF

VSIAM3 Volume/Surface Integrated Average-based Multi-moment

WENO Weighted Essentially Non-Oscillatory

WENO-JS WENO with Jiang and Shu's smoothness indicator

WENO-CU Central-Upwind Weighted Essentially Non-Oscillatory

Nomenclature

$\alpha_i^{\hat{j}}$	nonlinear parameters of WENO, $\hat{j} = 0, 1, 2$
α_i^R	coefficients of a rational function
$\bar{\phi}_i$	cell average value for scalar conservation law
$\bar{\mathbf{U}}_i$	cell average values for Euler equations
β^{CSLT}	prescribed parameter of the tangent hyperbolic function for CIP-CSL
β^T	prescribed parameter of the tangent hyperbolic function for THINC
β_x^T	β^T component in the x-direction
β_y^T	β^T component in the y-direction
$\beta_i^{\hat{j}}$	smoothness indicator of WENO, $\hat{j} = 0, 1, 2$
β_i^R	coefficients of a rational function
Δx	mesh increment
ϵ	a small value to prevent division by zero
γ^{CSLT}	control parameter of the tangent hyperbolic function for CIP-CSL
γ^T	control parameter of the tangent hyperbolic function for THINC
$\Gamma_k(\rho_k)$	Grüneisen coefficient

- $\hat{\phi}_i$ interpolated value at the cell center
- λ_k characteristic speed, $k = 1, 2, 3$
- Λ the diagonal matrix of eigenvalues
- A** Jacobian matrix
- F** numerical flux for Euler equations
- L** the matrices of left eigenvectors
- R** the matrices of right eigenvectors
- $\mathbf{U}(x, t)$ solution function of Euler equations
- $\mathbf{U}_{i+1/2}^L$ left-side values of solution function $\mathbf{U}(x, t)$ for cell boundaries $x_{i+1/2}$
- $\mathbf{U}_{i+1/2}^R$ right-side values of solution function $\mathbf{U}(x, t)$ for cell boundaries $x_{i+1/2}$
- W** primitive variables of the linearised Euler equation
- \mathcal{C}_k characteristic curve, $k = 1, 2, 3$
- $\omega_i^{\hat{j}}$ nonlinear weight of WENO, $\hat{j} = 0, 1, 2$
- ϕ'_i first gradient at the cell center
- $\Phi_i(x)$ reconstruction function
- $\Phi'_i(x)$ derivative of the reconstruction function
- $\phi_{i+1/2}$ scalar values for cell boundaries $x_{i+1/2}$
- $\phi_{i-1/2}$ scalar values for cell boundaries $x_{i-1/2}$
- ρ density
- $\tau_{\hat{j}}$ global smoothness indicator of WENO, $\hat{j} = 0, 1, 2$

\mathbf{m}	momentum vector with three components denoted by m_x, m_y, m_z
\mathbf{u}	velocity vector with three components denoted by u, v, w
ρ	correlation coefficient
a	characteristic speed in a hyperbolic equation
c	sound speed
C_i	coefficients of a polynomial
$d_i^{\hat{j}}$	linear parameters of WENO, $\hat{j} = 0, 1, 2$
E	total energy
$E_{Dispersion}$	dispersion error
$E_{Dissipation}$	dissipation error
E_{Total}	total error
f	numerical flux for scalar conservation law
$F_{i+1/2}$	numerical flux at cell boundaries $x_{i+1/2}$ for Euler equations
$f_{i+1/2}$	numerical flux at cell boundaries $x_{i+1/2}$ for scalar conservation law
$F_{i-1/2}$	numerical flux at cell boundaries $x_{i-1/2}$ for Euler equations
$f_{i-1/2}$	numerical flux at cell boundaries $x_{i-1/2}$ for scalar conservation law
P	control parameter of WENO smoothness indicator
p	pressure
$r_{i+1/2}$	ratios of successive gradients for cell boundaries $x_{i+1/2}$
$r_{i-1/2}$	ratios of successive gradients for cell boundaries $x_{i-1/2}$

t time

$X(\mathcal{C}_k)$ point solutions on each characteristic curve, $k = 1, 2, 3$

x, y, z component of three dimensional local coordinate

Introduction

1.1 Background

Compressible flow is a kind of fluid where the compressibility effect cannot be ignored and may even dominate the flow phenomena. For compressible flow, Mach number is significantly bigger than zero and the flow velocity approaches or larger than the local speed of sound. Most of the real-case compressible flow problems involve complex flow structures including shock waves and vortices, such as those found in aerodynamics regarding the design of high-speed vehicles [5], gas turbines [6, 7, 8, 9, 10], reciprocating engines [11, 12], combustion engines [13], jet engines [14]. When compressible flow problems contain a mixing region of two materials with a moving interface, the material interface of compressible two-phase flows make the physics more complicate. For example, shock/interface interactions are thought to be crucial to the instability and evolution of material interfaces that separate different fluids. Compressible two-phase flows are widely found in a wide spectrum of phenomena, e.g. cavitation [15, 16, 17, 18]. Driven by the great demand of these engineering applications, it is essentially important to study and understand the physics of compressible fluid dynamics.

To study compressible flows and compressible two-phase flows, traditionally, either theoretical or experimental approaches are used. Theoretical analysis can promote a deep understanding of the mechanisms for the study of compressible flows. However,

theoretical approaches are quite limited only for a few simple fundamental cases in one dimension and cannot be applied to general multi-dimensional engineering problems. Moreover, it is impossible to mathematically analyse the problems associated with compressible, including both supersonic and subsonic flows due to the change in the mathematical behaviour of governing equations [19]. As a consequence of the challenge to theoretical analysis, a large number of experimental studies have been conducted to study compressible flow problems. However, for some practical applications with both high Mach number and high temperature in a trans-atmospheric vehicle, it is difficult to conduct the measurements. In addition, the material interfaces of compressible multi-phase fluids greatly complicate the physics and it is formidably difficult to carry out experimental measurements near interfaces where the length and time scales are small [20].

Due to the above reasons, computational fluid dynamics (CFD) [19, 21, 22, 23, 24, 25] is needed as a practical tool for the analysis of compressible flows in engineering and science. CFD is growing with the advancement of computer technology over the past decades. Nowadays, CFD is widely used in the study of compressible flow and has become an indispensable tool in engineering applications. The development of high-fidelity and high-accuracy numerical methods for compressible flows is one of the most active research areas in CFD. In past decades, tremendous efforts have been made and a great number of numerical methods have been developed to discretise the governing equations (i.e. Navier-Stokes or Euler equations) for the simulation of compressible fluid problems.

To resolve the vast range of spatial and temporal length-scales in compressible flow problems, high-order and high-resolution numerical schemes gain more and more attentions [26, 27]. Some typical high-resolution numerical schemes include the Essentially Non-Oscillatory (ENO) [28], Weighted Essentially Non-Oscillatory (WENO) [29, 1, 30, 31, 32, 33], and Constrained Interpolation Profile Conservative Semi-Lagrangian (CIP-CSL) [34, 35, 36, 37] schemes. It should be noted that traditional low-order

schemes e.g. the first-order Godunov scheme [38] is able to resolve the discontinuities monotonically, while the vortical structures and acoustic waves are also smeared by the large numerical dissipation. To achieve the same accuracy, high-resolution methods consume lower computational costs than low-order schemes [39]. Meanwhile, high-resolution schemes are more efficient in solving physical problems with small-scale and complex compressible flow structures [19]. Thus, the development of high-order, high-resolution numerical schemes for compressible flows has become one of the trends in current CFD research.

1.2 Purpose of the research

In this thesis, we aim to develop high-fidelity and high-resolution numerical schemes, which can more accurately capture both smooth and discontinuous solutions compared to existing (WENO and CIP-CSL) schemes, and which can be used for compressible flows and compressible two-phase flows.

1.3 Outline of the thesis

The remainder of thesis is organised as follows.

Chapter 2 primarily reviews the governing equations and the relevant literature with regard to current studies of numerical methods for computational fluid dynamics. Details of representative high-order reconstruction schemes including the conventional Weighted Essentially Non-Oscillatory (WENO) schemes and the Constrained Interpolation Profile Conservative Semi-Lagrangian (CIP-CSL) schemes are given. The unresolved problems of WENO and CIP-CSL schemes are highlighted and summarised at the end of this chapter.

In chapter 3, we propose the fourth-order CIP-CSL3-ENO scheme based on two CIP-

CSL3 schemes and the Essentially Non-Oscillatory (ENO) [28] scheme. The CIP-CSL3-ENO scheme is validated through various benchmark problems.

In chapter 4, we present a fifth-order CIP-CSL-ENO5 scheme to eliminate numerical oscillations and reduce numerical errors based on the CIP-CSL3-ENO scheme. The CIP-CSL-ENO5 scheme selects the most appropriate reconstruction candidate by using the proposed smoothness indicator which can detect the smoothness and the potential discontinuity of the reconstruction stencils. The numerical results of several widely-used benchmark tests are presented to verify the CIP-CSL-ENO5 scheme.

In chapter 5, we extend the Boundary Variation Diminishing (BVD) algorithm to the CIP-CSL framework. Firstly, we propose the CIP-CSLT (CIP-CSL with a tangent hyperbolic function) scheme as one candidate for discontinuity solutions. Secondly, a fourth-order CIP-CSL-WENO4 [37] (CIP-CSL with a WENO limiter) scheme is introduced as another candidate for smooth solutions. Based on the CIP-CSLT and CIP-CSL-WENO4 schemes, we propose the CIP-CSLT-WENO4-BVD scheme by using a modified version of the BVD algorithm. The CIP-CSLT-WENO4-BVD scheme is verified through various numerical benchmark tests in comparison with other high-order CIP-CSL schemes.

In chapter 6, firstly, we propose the TWENO (target WENO) scheme based on the fifth-order WENO scheme [32]. A target weighting strategy is designed for TWENO to restore the highest possible order interpolation when three target adjacent sub-stencils or two target adjacent sub-stencils are smooth. Secondly, the TBVD-TWENO-THINC scheme is proposed based on the newly proposed TWENO and Tangent of Hyperbola for INterface Capturing (THINC) [40, 2] schemes. The TBVD-TWENO-THINC scheme can effectively reduce numerical errors by implementing the Total Boundary Variation Diminishing (TBVD) [41] algorithm. Various numerical benchmark tests are conducted to validate the TBVD-TWENO-THINC scheme.

In chapter 7, the TBVD-TWENO-THINC scheme is applied to compressible two-phase flow problems. The five-equation model [42] is illustrated and solved. Towards

the end, the numerical results of benchmark tests are presented to demonstrate the solution quality of the present scheme compared to the analytical solutions and the experiment results.

Chapter 8 summarises the current study and provides suggestions for future research.

Literature review

In this chapter, the development of compressible fluid solvers is reviewed with emphasis on the spatial discretisation methods and interface capturing techniques. High-order numerical schemes based on Godunov-type finite volume method including the Weighted Essentially Non-Oscillatory (WENO) schemes, the Boundary Variation Diminishing (BVD) algorithm, and the Constrained Interpolation Profile Conservative Semi-Lagrangian (CIP-CSL) schemes are highlighted and the methodology details of these methods are explained. From the review, it is expected to identify the unsolved problems of developing high-resolution schemes based on WENO and CIP-CSL schemes and numerical difficulties for compressible two-phase flows with moving interface. The chapter ends by summarising the current review and suggesting new ideas for the current study.

2.1 Governing equations

The features of compressible fluid dynamics can be mathematically described by governing equations (i.e. Navier-Stokes or Euler equations). For viscous compressible flow, the governing equations can be expressed by the Navier-Stokes equations as

$$\frac{\partial \rho}{\partial t} + \nabla \cdot \mathbf{m} = 0, \quad (2.1)$$

$$\frac{\partial \mathbf{m}}{\partial t} + \nabla \cdot (\mathbf{m} \otimes \mathbf{u} + p\delta) = \nabla \cdot \tau, \quad (2.2)$$

$$\frac{\partial E}{\partial t} + \nabla \cdot (\mathbf{u}E + \mathbf{u}p) = \nabla \cdot (\mathbf{u} \cdot \tau - \dot{q}), \quad (2.3)$$

where ρ is density, $\mathbf{u} = (u, v)$ is velocity, $\mathbf{m} = (\rho u, \rho v)$ is momentum, p is pressure and $E = \rho e + \frac{1}{2}\rho \mathbf{u} \cdot \mathbf{u}$ is total energy. To close the system of equations, the ideal-gas equations of state (EOS) $p = (\gamma - 1)\rho e$ is employed. γ is the ratio of the specific heats. The heat flux is computed by $\dot{q} = -k\nabla T$. For a Newtonian fluid, according to Stokes' hypothesis, the viscous stress tensor τ can be evaluated as

$$\tau = 2\mu\mathbf{S} - \frac{2}{3}\mu(\nabla \cdot \mathbf{u})\delta \quad (2.4)$$

where μ is the coefficient of dynamic viscosity and $\mathbf{S} = \frac{1}{2}(\nabla \mathbf{u} + (\nabla \mathbf{u})^T)$ is the strain rate tensor.

For inviscid compressible flow, the governing equations can be expressed by the Euler equations as

$$\frac{\partial \rho}{\partial t} + \nabla \cdot \mathbf{m} = 0, \quad (2.5)$$

$$\frac{\partial \mathbf{m}}{\partial t} + \nabla \cdot (\mathbf{m} \otimes \mathbf{u} + p\delta) = 0, \quad (2.6)$$

$$\frac{\partial E}{\partial t} + \nabla \cdot (\mathbf{u}E + \mathbf{u}p) = 0, \quad (2.7)$$

where ρ is density, $\mathbf{u} = (u, v, w)$ is velocity, $\mathbf{m} = (m_x, m_y, m_z)$ is momentum, p is pressure, and E is total energy. Euler equations are the system of nonlinear hyperbolic conservation laws [43, 44, 45, 46], which will be our major concern in this work.

2.2 Numerical methods for Euler equations

Various numerical methods have been proposed for solving the Euler equations of inviscid compressible flow. In spite of different variants, the most common methods are

designed based on the Finite Difference Method (FDM), the Finite Element Method (FEM), and the Finite Volume Method (FVM).

In the FDM [47, 48, 49], the computational domain is usually divided into a network of locally structured grid (i.e. the grids are equally). The points of intersection of these lines are called grid points or mesh points. At each grid point, the differential equation is approximated by replacing the partial derivatives by their corresponding difference approximations. Taylor series expansion, polynomial fitting, spline fitting, integral method, and control volume approach [25, 50, 51] can be used to obtain various type of finite difference approximations. The FDM is able to be applied to both structured and unstructured grids. In practice, the FDM is best suitable for structured grids to obtain higher order schemes. In FDMs, special care needs to be taken in order to guarantee the conservation property. Moreover, the restriction to simple geometries is a significant disadvantage for FDMs in the simulation of complex flows.

In the FEM, the computational domain is divided into a set of discrete volumes or finite number of subregions called elements that are generally unstructured and for each element the variational formulation is constructed for the given differential equations using simple functions for approximations. Then the individual elements are assembled and the algebraic systems of equations are formed by a piecewise application of the variational method. Compared to the FDM and the FVM, the distinguishing feature of the FEM is that the equations are multiplied by a weight function [52] before they are integrated over the entire domain. The concept is achieved by expressing the solution variables by a trial solution using a set of trial piecewise functions with constants which are chosen to give the best solution to the governing equations. An important advantage of the FEM is the ability to deal with arbitrary geometries. Moreover, the FEM is relatively easy to analyse mathematically and have optimality properties for certain types of equations. The main drawback for the FEM is that, for unstructured grids, the matrices of the linearized equations are not as well structured as those for regular grids making it more difficult to find efficient solution methods.

In the FVM, the integral form of the conservation equations is used to guarantee the conservative property. The solution domain is subdivided into a finite number of small control volumes instead of the computational grid points in finite difference method. The computational variables are represented at the control volume centres. One of the advantages of the FVM is that local and global conservation is built into the method. This conservativeness of the numerical method is of great significance from physical viewpoint and can be accomplished by expressing fluxes of the conserved quantity through the cell faces of neighbouring computational cells. The direct connection between the physical conservation concepts and the numerical strategy constitutes one of the desirable features of finite volume method. Writing a balance equation for a physical quantity within a control volume makes the FVM easier to grasp than other numerical strategies. The method also offers the flexibility of application to various mesh structures and geometries. The formulation of the method fits natural execution of boundary conditions, even where the boundaries and related boundary conditions are complicated. The FVM works proficiently with both structured and unstructured grids. FVMs [53, 50, 54, 55, 56, 57] have got the overwhelming popularity in the related fields due to its rigorous numerical conservation and the flexibility to complex flow structures. In this work, the study of high-resolution numerical schemes for compressible flow problems will be proposed on the basis of FVM approach.

2.3 Godunov-type high-resolution shock capturing methods

The development of high-resolution shock capturing schemes to solve Euler equations for compressible fluid dynamics can back to Godunov's scheme [38], which is a conservative FVM with piece-wise constant reconstruction. Considering 1D Euler equations

$$\mathbf{U}_t + \mathbf{F}(\mathbf{U})_x = 0, \quad (2.8)$$

where

$$\mathbf{U} = \begin{pmatrix} \rho \\ \rho v \\ E \end{pmatrix}, \quad \mathbf{F}(\mathbf{U}) = \begin{pmatrix} \rho v \\ \rho v^2 + p \\ v(E + p) \end{pmatrix}, \quad (2.9)$$

Using an FVM framework, the cell average value of the solution function $\mathbf{U}(x, t)$ are defined as

$$\bar{\mathbf{U}}_i = \frac{1}{\Delta x} \int_{x_{i-1/2}}^{x_{i+1/2}} \mathbf{U}(x, t) dx. \quad (2.10)$$

$\bar{\mathbf{U}}_i$ is updated by

$$\frac{d\bar{\mathbf{U}}_i}{dt} = -\frac{1}{\Delta x} (\mathbf{F}_{i+1/2} - \mathbf{F}_{i-1/2}), \quad (2.11)$$

where the numerical fluxes $\mathbf{F}_{i+1/2}$ and $\mathbf{F}_{i-1/2}$ at cell boundaries are computed by a Riemann solver. There are several types of Riemann solvers, including the exact Riemann solver [58, 59, 60], Roe's Riemann solver [61, 62, 63, 64], Harten, Lax, Van Leer (HLL) Riemann solver [65, 66, 67, 68, 69], and Contact HLL (HLLC) Riemann solver [70, 71, 72, 73, 74, 72, 75] and Osher's Riemann solver [76, 77]. In spite of different variants, the canonical form of the Riemann flux can be written as

$$\mathbf{F}_{i+1/2} = \mathbf{F}_{i+1/2}^{\text{Riemann}}(\mathbf{U}_{i+1/2}^L, \mathbf{U}_{i+1/2}^R) = \frac{1}{2} \left(f(\mathbf{U}_{i+1/2}^L) + f(\mathbf{U}_{i+1/2}^R) - |a|(\mathbf{U}_{i+1/2}^R - \mathbf{U}_{i+1/2}^L) \right), \quad (2.12)$$

where a is the characteristic speed in a hyperbolic equation [44, 45, 46]. $\mathbf{U}_{i+1/2}^L$ and $\mathbf{U}_{i+1/2}^R$ are the left- and right-side values for cell boundaries $x_{i+1/2}$, $i = 1, 2, \dots, N$. To obtain solutions of the Riemann solver, a core problem is how to reconstruct the left- and right-side values for cell boundaries, which can fundamentally influence the numerical solution. In the following sections, a review of the conventional high-order reconstruction schemes is given.

2.3.1 High-order reconstruction schemes

Essentially Non-oscillatory (ENO)[28] scheme is a representative high-order reconstruction scheme proposed by Harten et al. The ENO scheme is an essentially non-

oscillatory piecewise polynomial reconstruction, which is an extension of the Monotonic Upwind Scheme for Conservation Laws (MUSCL) [78] scheme to an arbitrary order of accuracy. Such a reconstruction algorithm implements an adaptive stencil with piecewise data. Thus, high-order accuracy wherever the region is smooth can be achieved and numerical oscillations at discontinuities can be avoided as well.

Following the ENO [28, 79, 80] idea, the WENO (weighted ENO) [29, 1, 30, 31, 32, 33, 81, 82, 83, 84, 85, 86, 87] scheme was developed. Instead of using only one of the candidates to build the reconstruction, the WENO scheme uses a combination of all candidate stencils. In 1994, Liu et al. [29] proposed the first version of WENO schemes to solve the one-dimensional conservation law. Subsequently, an efficient implementation of the WENO scheme was proposed by Jiang and Shu (WENO-JS) [1]. Although the WENO-JS scheme achieves high-order accuracy in the smooth region, it still has excessive numerical diffusion in vicinity of discontinuities. To reduce the numerical diffusion near discontinuities of the WENO-JS scheme, the WENO-Z [32] scheme was proposed. In the WENO-Z scheme, a high-order smoothness indicator is devised as a linear combination of the lower-order local smoothness indicators. New non-oscillatory weights are built to achieve optimal order near discontinuities. Numerical diffusion can be reduced by assigning large weights to non-smooth stencils. In order to achieve both high-order and nonlinear adaption, an adaptive central-upwind sixth-order WENO-CU scheme was proposed by Hu et al. [33]. Recently, a family of targeted ENO (TENNO) schemes [88, 89] was proposed to achieve low numerical dissipation by introducing a cutoff function to renormalize the optimal weights. The TENNO scheme eliminates a candidate stencil entirely when it contains a genuine discontinuity with a certain strength.

The WENO concept provides a general framework to develop high-resolution schemes to achieve the highest possible order of accuracy for the smooth region and to effectively eliminate numerical oscillation in vicinity of the discontinuity region. In the next subsections Sec. 2.3.2 and Sec. 2.3.3, we provide a methodology review of two fifth-

order WENO schemes, the WENO-JS and WENO-Z schemes.

2.3.2 WENO-JS scheme

For simplicity, we consider the one-dimensional hyperbolic conservation law

$$\frac{\partial \phi}{\partial t} + \frac{\partial(u\phi)}{\partial x} = 0, \quad (2.13)$$

where ϕ is the scalar and u is the velocity. The cell average value for the scalar ϕ is defined as

$$\bar{\phi}_i = \frac{1}{\Delta x} \int_{x_{i-1/2}}^{x_{i+1/2}} \phi(x, t) dx. \quad (2.14)$$

$\bar{\phi}_i$ is updated by

$$\frac{d\bar{\phi}_i}{dt} = -\frac{1}{\Delta x} (f_{i+1/2} - f_{i-1/2}). \quad (2.15)$$

The numerical flux $f_{i+1/2}$ is calculated by a Riemann solver [54] using the left-side value $\phi_{i+1/2}^L$ and the right-side value $\phi_{i+1/2}^R$ obtained from the reconstructions over left- and right-biased stencils.

$$f_{i+1/2} = f_{i+1/2}^{\text{Riemann}}(\phi_{i+1/2}^L, \phi_{i+1/2}^R), \quad (2.16)$$

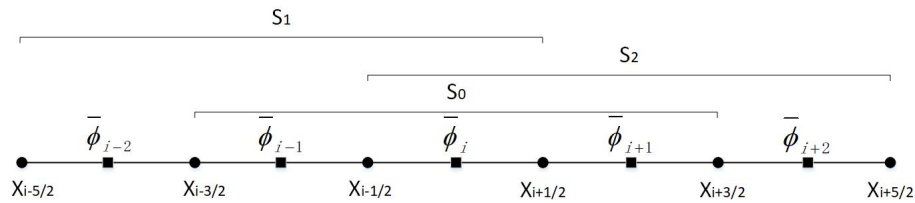


Figure 2.1: Sketch of the fifth-order WENO-JS reconstruction. The candidate stencils include three sub-stencils S_0 , S_1 and S_2 .

In the WENO-JS [1] scheme, three polynomials constructed over stencils S_0 , S_1 , and S_2 (shown in Fig. 2.1) are used to compute $\phi_{i+1/2}^L$ using the following formula,

$$\phi_{i+1/2}^L = \omega_i^0 \phi_{i+1/2}^0 + \omega_i^1 \phi_{i+1/2}^1 + \omega_i^2 \phi_{i+1/2}^2, \quad (2.17)$$

where $\phi_{i+1/2}^0, \phi_{i+1/2}^1, \phi_{i+1/2}^2$ are calculated by

$$\begin{aligned}\phi_{i+1/2}^0 &= -\frac{1}{6}\bar{\phi}_{i-1} + \frac{5}{6}\bar{\phi}_i + \frac{1}{3}\bar{\phi}_{i+1}, \\ \phi_{i+1/2}^1 &= \frac{1}{3}\bar{\phi}_{i-2} - \frac{7}{6}\bar{\phi}_{i-1} + \frac{11}{6}\bar{\phi}_i, \\ \phi_{i+1/2}^2 &= \frac{1}{3}\bar{\phi}_i + \frac{5}{6}\bar{\phi}_{i+1} - \frac{1}{6}\bar{\phi}_{i+2},\end{aligned}\tag{2.18}$$

and the nonlinear weights $\omega_i^{\hat{j}}$ are defined as

$$\omega_i^{\hat{j}} = \frac{\alpha_i^{\hat{j}}}{\alpha_i^0 + \alpha_i^1 + \alpha_i^2}, \alpha_i^{\hat{j}} = \frac{d_i^{\hat{j}}}{(\beta_i^{\hat{j}} + \epsilon)^P}, \hat{j} = 0, 1, 2.\tag{2.19}$$

In Eq. (2.19), the linear parameters $d_i^0 = 0.6$, $d_i^1 = 0.1$, and $d_i^2 = 0.3$ are the ideal weights since they generate the central upstream fifth-order scheme. $\epsilon = 10^{-12}$ is a small value to prevent division by zero. In general, $P = 1$ is used to accelerate the nonlinear adaptation towards the essentially non-oscillatory property and to control the excessive numerical diffusion in non-smooth regions. The smoothness indicator $\beta_i^{\hat{j}}$ [1] measure the smoothness of the \hat{j} th polynomial approximation $\phi_i^{\hat{j}}(x_i)$ at the stencil $S_{\hat{j}}$ and are defined by

$$\beta_i^{\hat{j}} = \sum_{l=1}^2 \Delta x^{2l-1} \int_{x_{i-1/2}}^{x_{i+1/2}} \left(\frac{d^l}{dx^l} \phi_i^{\hat{j}}(x) \right)^2 dx.\tag{2.20}$$

In FVM, based on cell-averaged values $\bar{\phi}_i$, the explicit form of the smoothness indicator $\beta_i^{\hat{j}}$ can be expressed as follows

$$\begin{aligned}\beta_i^0 &= \frac{13}{12}(\bar{\phi}_{i-1} - 2\bar{\phi}_i + \bar{\phi}_{i+1})^2 + \frac{1}{4}(\bar{\phi}_{i-1} - \bar{\phi}_{i+1})^2, \\ \beta_i^1 &= \frac{13}{12}(\bar{\phi}_{i-2} - 2\bar{\phi}_{i-1} + \bar{\phi}_i)^2 + \frac{1}{4}(\bar{\phi}_{i-2} - 4\bar{\phi}_{i-1} + 3\bar{\phi}_i)^2, \\ \beta_i^2 &= \frac{13}{12}(\bar{\phi}_i - 2\bar{\phi}_{i+1} + \bar{\phi}_{i+2})^2 + \frac{1}{4}(3\bar{\phi}_i - 4\bar{\phi}_{i+1} + \bar{\phi}_{i+2})^2.\end{aligned}\tag{2.21}$$

2.3.3 WENO-Z scheme

On the basis of the WENO-JS scheme, Borges et al. proposed the WENO-Z [32] scheme, which is an improved version of the classical fifth-order WENO scheme. In

the WENO-Z scheme, a new smoothness indicator is devised as

$$\tau_0 = |\beta_i^2 - \beta_i^1|. \quad (2.22)$$

Based on τ_0 , the unnormalized weights $\alpha_i^{\hat{j}}$ in Eq. (2.19) are redesigned as

$$\alpha_i^{\hat{j}} = d_i^{\hat{j}} \left(1 + \left(\frac{\tau_0}{\beta_i^{\hat{j}} + \epsilon} \right)^P \right), \quad (2.23)$$

where $d_i^{\hat{j}}$ and $\beta_i^{\hat{j}}$ are the same as those in the WENO-JS scheme.

2.3.4 Numerical difficulties for WENO schemes

For conventional high-order shock-capturing schemes e.g. WENO-JS [1] and WENO-Z [32], the excessive numerical diffusion across discontinuities is still a significant problem. Those numerical diffusion will smear the discontinuities in the numerical solutions. One of the reasons is that they tend to under-use all adjacent smooth sub-stencils thus fail to realise optimal interpolation. In conventional WENO schemes, nonlinear weights are one of the main sources of numerical dissipation. In the smooth region, the value of nonlinear weights should recover their optimal linear weights. In the discontinuous region, the weights for stencils containing discontinuities are assigned with small values. However, in this case, the weights for other smooth stencils are not guaranteed to recover their optimal ones.

Moreover, the conventional WENO scheme based on Finite Volume Method (FVM) approach assumes a jump at the cell boundary during the reconstruction procedure. The development of high-resolution WENO (FVM) scheme aims to minimise the reconstruction difference at cell interfaces for smooth solutions by using high-order polynomial reconstruction. However, when the solutions include discontinuities, the high-order polynomial cannot reduce the reconstruction difference with the increase in the polynomial order. In this case, it may not be suitable to reconstruct the discontinuous solutions by only using high-order polynomials.

2.4 CIP-CSL schemes

In the past decades, there is another trend to develop high-order, high-resolution FVMs by making use of the multi-moment concept such as Constrained Interpolation Profile Conservative Semi-Lagrangian (CIP-CSL) schemes [93, 94, 95, 34, 35, 36, 96, 97, 98], which uses cell average and boundary values as moments (variables) to solve conservation laws. CIP-CSL schemes have been applied to various types of fluid problems [99, 100, 101, 102, 103, 104] including inviscid compressible flows [101, 103], free-interface fluids [102] and interfacial flows such as droplet splashing [105, 106]. There are several variants of the CIP-CSL scheme, such as the CIP-CSL2 (CIP-CSL with a second-order polynomial function) [93], CIP-CSL3 (CIP-CSL with a third-order polynomial function) [94], and CIP-CSLR (CIP-CSL with a rational function) [95] schemes. The order of CIP-CSL schemes depends on the size of reconstruction stencil and the number of the constraints. In the following subsections, details of the CIP-CSL2, CIP-CSL3, and CIP-CSLR schemes are explained.

2.4.1 CIP-CSL2 scheme

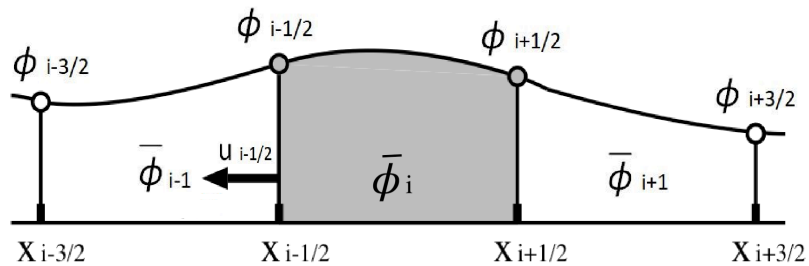


Figure 2.2: Schematic figures of the CIP-CSL2 scheme. The moments which are indicated by grey colour are used as constraints to construct interpolation function $\Phi_i^{CSL2}(x)$. The wave propagation speed $u_{i-1/2} < 0$ is assumed.

For simplicity, we consider the one-dimensional hyperbolic conservation law in Eq. (2.13). In the CIP-CSL2 scheme, three moments (i.e. a cell average $\bar{\phi}_i$ and two boundary values $\phi_{i-1/2}$ and $\phi_{i+1/2}$) within the upwind cell are used for the interpolation function as shown in Fig. 2.2. The CIP-CSL2 scheme is based on the following second-order polynomial interpolation function

$$\Phi_i^{CSL2}(x) = C_{2,i}^{CSL2}(x - x_{i-1/2})^2 + C_{1,i}^{CSL2}(x - x_{i-1/2}) + C_{0,i}^{CSL2}. \quad (2.24)$$

The interpolation function $\Phi_i^{CSL2}(x)$ is constructed using the following three constraints ($\phi_{i-1/2}$, $\bar{\phi}_i$, and $\phi_{i+1/2}$), which are indicated in Fig. 2.2,

$$\begin{cases} \phi_{i-1/2} = \Phi_i^{CSL2}(x_{i-1/2}), \\ \bar{\phi}_i = \frac{\int_{x_{i-1/2}}^{x_{i+1/2}} \Phi_i^{CSL2}(x) dx}{\Delta x}, \\ \phi_{i+1/2} = \Phi_i^{CSL2}(x_{i+1/2}). \end{cases} \quad (2.25)$$

Using the constraints in Eq. (2.25), these three coefficients ($C_{0,i}^{CSL2}$, $C_{1,i}^{CSL2}$, and $C_{2,i}^{CSL2}$) are obtained as follows

$$C_{0,i}^{CSL2} = \phi_{i-1/2}, \quad (2.26)$$

$$C_{1,i}^{CSL2} = \frac{1}{\Delta x} (6\bar{\phi}_i - 4\phi_{i-1/2} - 2\phi_{i+1/2}), \quad (2.27)$$

$$C_{2,i}^{CSL2} = \frac{1}{\Delta x^2} (-6\bar{\phi}_i + 3\phi_{i-1/2} + 3\phi_{i+1/2}). \quad (2.28)$$

By using the interpolation function $\Phi_i^{CSL2}(x)$, the cell average value $\bar{\phi}_i$ and the cell boundary value $\phi_{i-1/2}$ are updated by a third-order Total Variation Diminishing (TVD) Runge-Kutta formulation [107, 108].

In the third-order TVD Runge-Kutta formulation, we solve the following initial value problem:

$$\frac{\partial X}{\partial t} = -u(X, t), \quad (2.29)$$

$$X_0 = x_{i-1/2},$$

as follows,

$$X_1 = X_0 - u(X_0, t_0)\Delta t, \quad (2.30)$$

$$X_2 = \frac{3}{4}X_0 + \frac{1}{4}X_1 - \frac{1}{4}u(X_1, t_1)\Delta t, \quad (2.31)$$

$$X_3 = \frac{1}{3}X_0 + \frac{2}{3}X_2 - \frac{2}{3}u(X_2, t_2)\Delta t. \quad (2.32)$$

The temporary cell boundary value $\phi_{i-1/2}^{<k>}$ at each Runge-Kutta time step can be obtained as follows

$$\phi_{i-1/2}^{<k>} = \begin{cases} \Phi_{i-1}^{CSL2}(X_k) & \text{if } X_k - X_0 \leq 0, \\ \Phi_i^{CSL2}(X_k) & \text{if } X_k - X_0 > 0, \end{cases} \quad (2.33)$$

where k is the Runge-Kutta time step. The cell boundary value $\phi_{i-1/2}$ is updated by solving the conservation equation in differential form

$$\frac{\partial \phi}{\partial t} + u \frac{\partial \phi}{\partial x} = -\phi \frac{\partial u}{\partial x}, \quad (2.34)$$

and the solution is evolved as

$$\phi_{i-1/2}^{n+1} = \phi_{i-1/2}^{<3>} - \frac{\phi_{i-1/2}^{<0>} + \phi_{i-1/2}^{<1>} + 4\phi_{i-1/2}^{<2>}}{6} \frac{\partial u}{\partial x}(X_0)\Delta t. \quad (2.35)$$

The cell average value $\bar{\phi}_i$ is updated by a finite volume formulation as follows

$$\bar{\phi}_i^{n+1} = \bar{\phi}_i^n - \frac{F_{i+1/2} - F_{i-1/2}}{\Delta x}, \quad (2.36)$$

here

$$F_{i-1/2} = \frac{\phi_{i-1/2}^{<0>} + \phi_{i-1/2}^{<1>} + 4\phi_{i-1/2}^{<2>}}{6} u(X_0). \quad (2.37)$$

2.4.2 CIP-CSL3 schemes (CSL3CW and CSL3H)

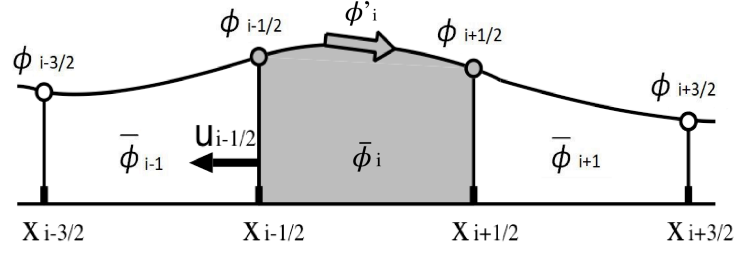


Figure 2.3: Schematic figures of the CIP-CSL3 scheme. The moments which are indicated by grey colour are used as constraints to construct interpolation function $\Phi_i^{CSL3}(x)$. The wave propagation speed $u_{i-1/2} < 0$ is assumed.

In the CIP-CSL3 scheme, a derivative at the cell centre (ϕ'_i) is used as an additional constraint as shown in Fig. 2.3. The derivative is a control parameter and mainly used as a limiter. The CIP-CSL3 scheme [94] is based on the following third-order polynomial interpolation function

$$\Phi_i^{CSL3}(x) = C_{3,i}^{CSL3}(x - x_{i-1/2})^3 + C_{2,i}^{CSL3}(x - x_{i-1/2})^2 + C_{1,i}^{CSL3}(x - x_{i-1/2}) + C_{0,i}^{CSL3}. \quad (2.38)$$

The interpolation function $\Phi_i^{CSL3}(x)$ is constructed using the following four constraints ($\phi_{i-1/2}$, $\bar{\phi}_i$, $\phi_{i+1/2}$, and ϕ'_i), which are indicated in Fig. 2.3.

$$\left\{ \begin{array}{l} \phi_{i-1/2} = \Phi_i^{CSL3}(x_{i-1/2}), \\ \bar{\phi}_i = \frac{\int_{x_{i-1/2}}^{x_{i+1/2}} \Phi_i^{CSL3}(x) dx}{\Delta x}, \\ \phi_{i+1/2} = \Phi_i^{CSL3}(x_{i+1/2}), \\ \phi'_i = \frac{d\Phi_i^{CSL3}(x_i)}{dx}. \end{array} \right. \quad (2.39)$$

Using the constraints in Eq. (2.39), these four coefficients ($C_{0,i}^{CSL3}$, $C_{1,i}^{CSL3}$, $C_{2,i}^{CSL3}$, and $C_{3,i}^{CSL3}$) are determined as

$$C_{0,i}^{CSL3} = \phi_{i-1/2}, \quad (2.40)$$

$$C_{1,i}^{CSL3} = \frac{1}{\Delta x} (-6\phi_{i-1/2} + 6\bar{\phi}_i - 2\phi'_i \Delta x), \quad (2.41)$$

$$C_{2,i}^{CSL3} = \frac{1}{\Delta x^2} (9\phi_{i-1/2} - 6\bar{\phi}_i - 3\phi_{i+1/2} + 6\phi'_i \Delta x), \quad (2.42)$$

$$C_{3,i}^{CSL3} = \frac{1}{\Delta x^3} (-4\phi_{i-1/2} + 4\phi_{i+1/2} - 4\phi'_i \Delta x). \quad (2.43)$$

There are several approximation formulas proposed to compute the derivative ϕ'_i , such as the CIP-CSL3H (CIP-CSL3 with the Hyman approximation) [109] and CIP-CSL3CW (CIP-CSL3 with the Collela and Woodward approximation) [110] schemes. In the CIP-CSL3H scheme, ϕ'_i is estimated as

$$\phi'_i = \frac{\hat{\phi}_{i+2} + 8\hat{\phi}_{i+1} - 8\hat{\phi}_{i-1} - \hat{\phi}_{i-2}}{12\Delta x}. \quad (2.44)$$

Although the CIP-CSL3H scheme has fourth-order accuracy for the smooth solution, it has spurious numerical oscillation in the presence of discontinuities [94].

In the CIP-CSL3CW scheme, ϕ'_i is estimated as

$$\phi'_i = \begin{cases} \frac{\min(|\hat{\phi}_{i+1} - \hat{\phi}_{i-1}|, 2|\hat{\phi}_{i+1} - \hat{\phi}_i|, 2|\hat{\phi}_i - \hat{\phi}_{i-1}|) \text{sgn}(\hat{\phi}_{i+1} - \hat{\phi}_{i-1})}{\Delta x} & \text{if } (\hat{\phi}_{i+1} - \hat{\phi}_i)(\hat{\phi}_i - \hat{\phi}_{i-1}) > 0 \\ 0 & \text{otherwise,} \end{cases} \quad (2.45)$$

where

$$\hat{\phi}_i = \frac{3}{2}\bar{\phi}_i - \frac{1}{4}(\phi_{i+1/2} + \phi_{i-1/2}). \quad (2.46)$$

The CIP-CSL3CW scheme has third-order-accurate in smooth regions; however, it tends to create excessive numerical diffusion in the area where the ϕ'_i changes sign [94].

2.4.3 CIP-CSLR scheme

The CIP-CSLR [95] scheme is based on the following piecewise rational interpolation function

$$\Phi_i^{CSLR}(x) = \frac{\alpha_i^R \beta_i^R (x - x_{i-1/2})^2 + 2\alpha_i^R (x - x_{i-1/2}) + \phi_{i-1/2}}{[1 + \beta_i^R (x - x_{i-1/2})]^2}. \quad (2.47)$$

The interpolation function $\Phi_i^{CSLR}(x)$ is constructed using the following three constraints

$$\begin{cases} \phi_{i-1/2} = \Phi_i^{CSLR}(x_{i-1/2}), \\ \bar{\phi}_i = \frac{\int_{x_{i-1/2}}^{x_{i+1/2}} \Phi_i^{CSLR}(x) dx}{\Delta x}, \\ \phi_{i+1/2} = \Phi_i^{CSLR}(x_{i+1/2}). \end{cases} \quad (2.48)$$

Using the constraints in Eq. (2.48), the coefficients (α_i^R and β_i^R) can be obtained as below

$$\alpha_i^R = \beta_i^R \bar{\phi}_i + (\bar{\phi}_i - \phi_{i-1/2}) / \Delta x, \quad (2.49)$$

$$\beta_i^R = \frac{1}{\Delta x} \left(\frac{|\phi_{i-1/2} - \bar{\phi}_i| + \epsilon}{|\bar{\phi}_i - \phi_{i+1/2}| + \epsilon} - 1 \right), \quad (2.50)$$

where $\epsilon = 10^{-12}$ is an infinitesimal number to avoid zero division.

2.4.4 CIP-CSL-WENO4 scheme

Recently, a WENO-limiter devised for the CIP-CSL scheme (CIP-CSL-WENO4) was proposed by Sun et al. [37]. The proposed WENO limiter is based on the idea of WENO scheme [1, 32] in Sec. 2.3.2 and Sec. 2.3.3. This scheme manifests the fourth-order accuracy and oscillation-suppressing property. The methodology of the CIP-CSL-WENO4 scheme is reviewed in this subsection.

The CIP-CSL-WENO4 scheme employs the same interpolation function as that in the CIP-CSL3 scheme Eq. (2.38). The difference between the CIP-CSL3 scheme and

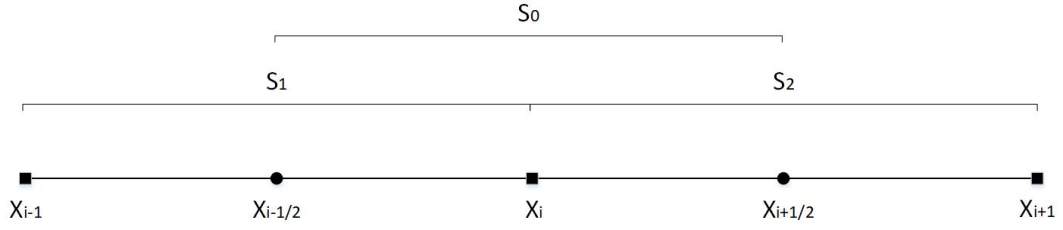


Figure 2.4: Reconstruction stencils for the weighted essentially non-oscillatory limiter.

the CIP-CSL-WENO4 scheme is how to reconstruct the derivative at the cell centre in the upwind cell (ϕ'_i). In the CIP-CSL-WENO4 scheme, a fourth-order WENO-limiter is designed to reconstruct the derivative ϕ'_i . The computation is built on the three sub-stencils S_0 , S_0 , S_0 , as shown in Fig. 2.4. For each stencil, we can construct a second-degree polynomial derivative $\phi'_i{}^{\hat{j}}$, $\hat{j} = 0, 1, 2$. The explicit form of $\phi'_i{}^{\hat{j}}$ are

$$\phi'_i{}^0 = \frac{\phi_{i+1/2} - \phi_{i-1/2}}{\Delta x}, \quad (2.51)$$

$$\phi'_i{}^1 = \frac{3\hat{\phi}_i + \hat{\phi}_{i-1} - 4\phi_{i-1/2}}{\Delta x}, \quad (2.52)$$

$$\phi'_i{}^2 = -\frac{3\hat{\phi}_i + \hat{\phi}_{i+1} - 4\phi_{i+1/2}}{\Delta x}. \quad (2.53)$$

In the CIP-CSL-WENO4 scheme, the derivative ϕ'_i is calculated by using a nonlinear combination of $\phi'_i{}^{\hat{j}}$ as

$$\phi'_i = \sum_{\hat{j}=0}^2 \omega_i^{\hat{j}} \phi'_i{}^{\hat{j}}. \quad (2.54)$$

In the literature, there are several variants proposed to compute the WENO nonlinear weights, such as WENO-JS scheme [1] in Sec. 2.3.2 and WENO-Z scheme [32] in Sec. 2.3.3. The classical WENO-JS has accuracy loss in the smooth area near the discontinuity. The WENO-Z scheme is able to improve the accuracy of the WENO-JS by using different nonlinear weights and smoothness measurements in the reconstruction. In addition, WENO-Z scheme shows a good balance between numerical accuracy and

algorithmic simplicity. Thus, the WENO-Z reconstruction formula is used to calculate the nonlinear weights $\omega_i^{\hat{j}}$ as follows

$$\omega_i^{\hat{j}} = \frac{\alpha_i^{\hat{j}}}{\alpha_i^0 + \alpha_i^1 + \alpha_i^2}, \quad \alpha_i^{\hat{j}} = \gamma_i^{\hat{j}} \left(1 + \left(\frac{\tau_0}{\beta_i^{\hat{j}} + \epsilon} \right)^P \right), \quad (2.55)$$

where the linear parameters are $\gamma_i^0 = \frac{2}{3}$, $\gamma_i^1 = \frac{1}{6}$, and $\gamma_i^2 = \frac{1}{6}$. $\epsilon = 10^{-12}$ is a small value to prevent division by zero. τ_0 is defined in Eq. (2.22). The value of P can be selected flexibly to optimise the numerical property of the scheme. $P = 1$ is suggested to control the excessive numerical diffusion in the non-smooth region. In the CIP-CSL-WENO4 scheme, the smoothness indicator is defined as

$$\beta_i^{\hat{j}} = \sum_{l=1}^2 \int_{x_{i-1/8}}^{x_{i+1/8}} \Delta x^{2l-1} \left(\frac{\partial^l \Phi_i^{\hat{j}}(x)}{\partial x^l} \right)^2 dx. \quad (2.56)$$

The smoothness indicator measures the smoothness of the reconstructed polynomials in the target cell. In the conventional WENO scheme, the upper and lower bound of integration is $x_{i-1/2}$ and $x_{i+1/2}$. In order to match the compact WENO reconstruction stencil of the CIP-CSL scheme, the upper and lower bound of integration in Eq. (2.56) are adjusted to $x_{i-1/8}$ and $x_{i+1/8}$ respectively.

The explicit form of $\beta_i^{\hat{j}}$ can be expressed as follows

$$\begin{cases} \beta_i^0 = \frac{193}{48} (\phi_{i-1/2} - 2\hat{\phi}_i + \phi_{i+1/2})^2 + \frac{1}{4} (\phi_{i+1/2} - \phi_{i-1/2})^2, \\ \beta_i^1 = \frac{193}{48} (\hat{\phi}_{i-1} - 2\phi_{i-1/2} + \hat{\phi}_i)^2 + \frac{1}{4} (\hat{\phi}_{i-1} - 4\phi_{i-1/2} + 3\hat{\phi}_i)^2, \\ \beta_i^2 = \frac{193}{48} (\hat{\phi}_i - 2\phi_{i+1/2} + \hat{\phi}_{i+1})^2 + \frac{1}{4} (3\hat{\phi}_i - 4\phi_{i+1/2} + \hat{\phi}_{i+1})^2. \end{cases} \quad (2.57)$$

2.4.5 CIP-CSL schemes for the Euler conservation law

The implementation of CIP-CSL schemes for the one-dimensional Euler conservation laws is described in [108]. Considering the 1D conservative form of Euler equations in Eq. (2.8), the linearised Euler equation about the primitive variables can be obtained as

$$\frac{\partial \mathbf{W}}{\partial t} + \mathbf{A} \frac{\partial \mathbf{W}}{\partial x} = 0, \quad (2.58)$$

by freezing the Jacobian matrix \mathbf{A} , where

$$\mathbf{W} = \begin{pmatrix} \rho \\ v \\ p \end{pmatrix}, \quad \mathbf{A} = \begin{bmatrix} v & \rho & 0 \\ 0 & v & 1/\rho \\ 0 & \rho c^2 & v \end{bmatrix}, \quad (2.59)$$

here the sound speed $c = \sqrt{\gamma p/\rho}$. Considering the hyperbolicity, the Jacobian matrix \mathbf{A} can be diagonalised by

$$\mathbf{A} = \mathbf{R}\Lambda\mathbf{L}, \quad (2.60)$$

where Λ is the diagonal matrix of eigenvalues, \mathbf{L} and \mathbf{R} are the matrices of left and right eigenvectors, respectively ($\mathbf{R} = \mathbf{L}^{-1}$). Eq. (2.58) can be recast into the characteristic form

$$\mathbf{L} \frac{\partial \mathbf{W}}{\partial t} + \Lambda \mathbf{L} \frac{\partial \mathbf{W}}{\partial x} = 0, \quad (2.61)$$

where

$$\Lambda = \begin{bmatrix} v & 0 & 0 \\ 0 & v+c & 0 \\ 0 & 0 & v-c \end{bmatrix}, \quad \mathbf{L} = \begin{bmatrix} 1 & 0 & -\frac{1}{c^2} \\ 0 & 1 & \frac{1}{\rho c} \\ 0 & 1 & -\frac{1}{\rho c} \end{bmatrix}. \quad (2.62)$$

For each characteristic direction $\frac{dx}{dt} = \lambda_k$, and the characteristic speeds $\lambda_1 = v$, $\lambda_2 = v+c$ and $\lambda_3 = v-c$ are the non-zero diagonal values of Λ . From Eq. (2.61), a decoupled system for the characteristic variables can be obtained as

$$d\rho - \frac{1}{c^2} dp = 0 \quad \text{along } \mathcal{C}_1 : \frac{dx}{dt} = \lambda_1 = v, \quad x(t=0) = X_0, \quad (2.63)$$

$$dv + \frac{1}{\rho c} dp = 0 \quad \text{along } \mathcal{C}_2 : \frac{dx}{dt} = \lambda_2 = v+c, \quad x(t=0) = X_0, \quad (2.64)$$

$$dv - \frac{1}{\rho c} dp = 0 \quad \text{along } \mathcal{C}_3 : \frac{dx}{dt} = \lambda_3 = v-c, \quad x(t=0) = X_0, \quad (2.65)$$

where \mathcal{C}_k , $k = 1, 2, 3$ represents each characteristic curve. Then, the primitive variables at $t = t^{n+1}$ can be found by the relations below,

$$\rho(X_0)^{n+1} - \rho(X(\mathcal{C}_1)) - \frac{1}{c^2} \{p(X_0)^{n+1} - p(X(\mathcal{C}_1))\} = 0, \quad (2.66)$$

$$v(X_0)^{n+1} - v(X(\mathcal{C}_2)) + \frac{1}{\rho c} \{p(X_0)^{n+1} - p(X(\mathcal{C}_2))\} = 0, \quad (2.67)$$

$$v(X_0)^{n+1} - v(X(\mathcal{C}_3)) - \frac{1}{\rho c} \{p(X_0)^{n+1} - p(X(\mathcal{C}_3))\} = 0, \quad (2.68)$$

where $X(\mathcal{C}_k)$, $k = 1, 2, 3$ indicates the point solutions on each characteristic curve.

The departure point of cell boundary $x = x_{i-1/2}$ is computed by solving the following trajectory equations along the characteristic curves

$$\begin{cases} \frac{dX}{dt} = -\lambda_k(X, t), \\ X(t=0) = X_0 = x_{i+\frac{1}{2}}, \end{cases} \quad k = 1, 2, 3. \quad (2.69)$$

We solve Eq. (2.69) by using the third-order TVD Runge-Kutta method, which reads

$$\begin{cases} X_1(\mathcal{C}_k) = X_0 - \lambda_k(X_0, t_0)\Delta t, \\ X_2(\mathcal{C}_k) = \frac{3}{4}X_0 + \frac{1}{4}X_1(\mathcal{C}_k) - \frac{1}{4}\lambda_k(X_0, t_1)\Delta t, \\ X_3(\mathcal{C}_k) = \frac{1}{3}X_0 + \frac{2}{3}X_2(\mathcal{C}_k) - \frac{2}{3}\lambda_k(X_0, t_2)\Delta t, \end{cases} \quad (2.70)$$

Consequently, by solving the linear system Eq. (2.66), Eq. (2.67), and Eq. (2.68) for primitive variables along characteristic curves, we have

$$\begin{aligned} p_{i+\frac{1}{2}}^{(l)} &= \frac{1}{2} \left(p(X_l(\mathcal{C}_2)) + p(X_l(\mathcal{C}_3)) + \rho_{i+\frac{1}{2}}^{(l-1)} c_{i+\frac{1}{2}}^{(l-1)} (v(X_l(\mathcal{C}_2)) - v(X_l(\mathcal{C}_3))) \right), \\ v_{i+\frac{1}{2}}^{(l)} &= \frac{1}{2} \left(v(X_l(\mathcal{C}_2)) + v(X_l(\mathcal{C}_3)) + \frac{1}{\rho_{i+\frac{1}{2}}^{(l-1)} c_{i+\frac{1}{2}}^{(l-1)}} (p(X_l(\mathcal{C}_2)) - p(X_l(\mathcal{C}_3))) \right), \\ \rho_{i+\frac{1}{2}}^{(l)} &= \rho(X_l(\mathcal{C}_1)) + \frac{1}{(c_{i+\frac{1}{2}}^{(l-1)})^2} \left(p_{i+\frac{1}{2}}^{(l)} - p(X_l(\mathcal{C}_3)) \right), \end{aligned} \quad (2.71)$$

where $\rho(x)$, $v(x)$, and $p(x)$ represent the interpolation functions for the primitive variables ρ , v , and p , respectively. Thus $\rho(X_l(\mathcal{C}_k))$, $v(X_l(\mathcal{C}_k))$, and $p(X_l(\mathcal{C}_k))$ denote the semi-Lagrangian solutions of the primitive variables along characteristic curve \mathcal{C}_k at the l -th Runge-Kutta substep ($l = 1, 2, 3$).

Subsequently, the primitive variables at cell boundary $x = x_{i-\frac{1}{2}}$ of step $n+1$ can be updated directly by

$$\begin{aligned} p_{i-\frac{1}{2}}^{n+1} &= p_{i-\frac{1}{2}}^{\langle 3 \rangle}, \\ v_{i-\frac{1}{2}}^{n+1} &= v_{i-\frac{1}{2}}^{\langle 3 \rangle}, \\ \rho_{i-\frac{1}{2}}^{n+1} &= \rho_{i-\frac{1}{2}}^{\langle 3 \rangle}. \end{aligned} \quad (2.72)$$

Analogous to the case of the scalar conservation law, the cell average value of the conservative variables $\bar{\phi}$ are simply updated using a finite volume formulation as

$$\bar{\phi}_i^{n+1} = \bar{\phi}_i^n - \frac{\Delta t}{\Delta x} (\mathbf{F}_{i+\frac{1}{2}} - \mathbf{F}_{i-\frac{1}{2}}), \quad (2.73)$$

where the numerical flux $\mathbf{F}_{i+\frac{1}{2}}$ can be computed by the numerical integration of the boundary values of the primitive variables at the substeps of the Runge-Kutta integration scheme, i.e.

$$\mathbf{F}_{i+\frac{1}{2}} = \frac{\mathbf{F}(\mathbf{W}_{i+\frac{1}{2}}^{\langle 0 \rangle}) + \mathbf{F}(\mathbf{W}_{i+\frac{1}{2}}^{\langle 1 \rangle}) + 4\mathbf{F}(\mathbf{W}_{i+\frac{1}{2}}^{\langle 2 \rangle})}{6}. \quad (2.74)$$

2.4.6 Numerical difficulties for CIP-CSL schemes

Despite the superiority of high-order multi-moments CIP-CSL schemes in resolving complex structures of smoothness, numerical oscillation associated with discontinuity turns out to be an important problem. When the flux profile includes the jump discontinuity, the large gradient will cause numerical oscillations cross discontinuities. Those numerical oscillation will cause unphysical values and can be disastrous in the computation of Euler equations since the density or pressure can be as low as almost zero [111]. The tiny oscillations may result in the negative value for physical quantity, which can blow up the numerical computation. How to reconstruct the discontinuities with high accuracy and less numerical oscillation is still a difficult challenge in the development of high-resolution CIP-CSL schemes.

To demonstrate the numerical oscillations, we compute the advection equation $\phi_t + \phi_x = 0$ with the square wave as an initial profile for one period by the CIP-CSL2

scheme. The numerical results along with the exact solution are depicted in Fig. 2.5. It can be observed that there are significant overshoots and undershoots near the jump discontinuities.

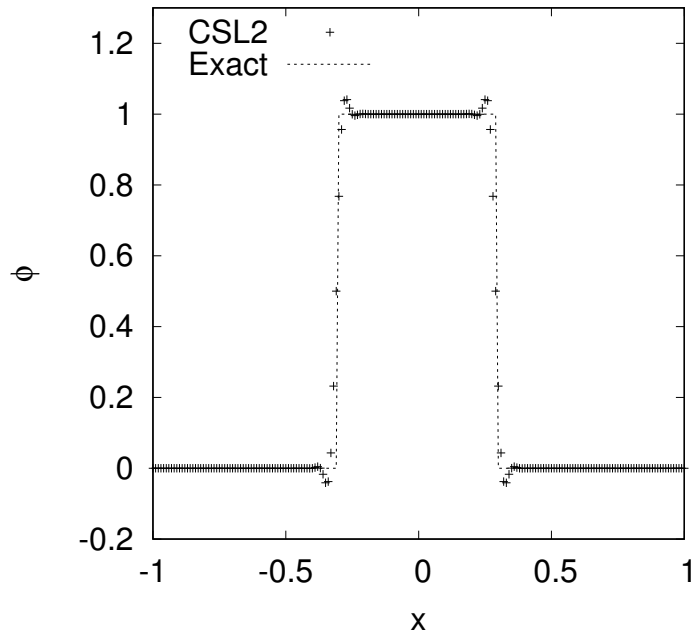


Figure 2.5: The simulation of the advection of a square wave by the CSL2 scheme on a 100-cell mesh.

2.5 Boundary variation diminishing reconstruction

The Boundary Variation Diminishing (BVD) [90, 41] algorithm was originally proposed to improve Godunov-type schemes. This reconstruction approach effectively reduces the numerical diffusion by minimising the variations at cell boundaries. In the BVD reconstruction algorithm, two candidate schemes are used to construct the interpolation functions. In order to enable the resulting scheme to accurately solve both smooth and discontinuous solutions, a high-order polynomial function (e.g. WENO-Z [32]) is used for the smooth solution and a sigmoid function (e.g. THINC [40, 2]) is used for the discontinuous solution. The details of the WENO-Z scheme have been

given in Sec. 2.3.3. The next subsections Sec. 2.5.1 and Sec. 2.5.2 provide a review of the alternative reconstruction candidate (THINC scheme) and the BVD selection criteria, respectively.

2.5.1 THINC

The Tangent of Hyperbola for Interface Capturing (THINC) [40, 2, 91, 92] scheme was devised to compute moving interfaces in multiphase flow simulations based on the piecewise hyperbolic tangent function. The piecewise hyperbolic tangent function of THINC can be defined as

$$\Phi_i^T(x) = \phi_{min} + \frac{\phi_{max}}{2} \left[1 + \gamma^T \tanh \left(\beta^T \left(\frac{x - x_{i-1/2}}{x_{i+1/2} - x_{i-1/2}} - \tilde{x} \right) \right) \right], \quad (2.75)$$

where $\phi_{min} = \min(\bar{\phi}_{i-1}, \bar{\phi}_{i+1})$, $\phi_{max} = \max(\bar{\phi}_{i-1}, \bar{\phi}_{i+1})$, $\gamma^T = 1$ for $\bar{\phi}_{i-1} < \bar{\phi}_{i+1}$ and $\gamma^T = -1$ for $\bar{\phi}_{i-1} > \bar{\phi}_{i+1}$. β^T is a parameter to control the jump thickness of the tangential hyperbolic function. In the original BVD algorithm, $\beta^T = 1.6$. \tilde{x} represents the location of the jump centre, which can be determined by the following constraint condition.

$$\frac{1}{\Delta x} \int_{x_{i-1/2}}^{x_{i+1/2}} \Phi_i^T(x) dx = \bar{\phi}_i, \quad (2.76)$$

as

$$\tilde{x}_i = \frac{1}{2\beta^T} \ln \left(\frac{\exp \beta^T - A_i}{A_i - \exp(-\beta^T)} \right), \quad (2.77)$$

here

$$A_i = \exp \left(\frac{\beta^T (2C_i - 1)}{\gamma^T} \right) \text{ and } C_i = \frac{\bar{\phi}_i - \phi_{min}}{\phi_{max} - \phi_{min}}. \quad (2.78)$$

The explicit formulation of the THINC scheme for the left-side value $\phi_{i+1/2}^L$ is

$$\phi_{i+1/2}^L = \Phi_i^T(x_{i+1/2}) = \phi_{min} + \frac{\phi_{max}}{2} \left(1 + \gamma^T \frac{\tanh(\beta^T) + A}{1 + A \tanh(\beta^T)} \right), \quad (2.79)$$

where $A = \frac{B/\cosh(\beta^T) - 1}{\tanh(\beta^T)}$, $B = \exp(\gamma^T \beta^T (2C - 1))$, $C = \frac{\bar{\phi}_i - \bar{\phi}_{min} + \epsilon}{\phi_{max} + \epsilon}$ and $\epsilon = 10^{-20}$.

BVD algorithm prefers the THINC reconstruction when a discontinuity is detected. In practice, a cell where a discontinuity may exist can be identified by the following conditions

$$\begin{aligned} \epsilon < C < 1 - \epsilon, \\ (\bar{\phi}_{i+1} - \bar{\phi}_i)(\bar{\phi}_i - \bar{\phi}_{i-1}) > 0. \end{aligned} \quad (2.80)$$

2.5.2 BVD selection criteria

In the BVD algorithm [90], an adaptive selection criterion was proposed to minimise the jump between the left- and right-side values at cell boundaries. We define $\Phi_i^{<WENO>}(x)$ and $\Phi_i^{<THINC>}(x)$ to represent the WENO and THINC reconstruction, respectively. The selection criteria of the BVD reconstruction can be described as follows.

Selection criteria:

1. Calculating the boundary variation (BV) at $x_{i+1/2}$ as

$$BV(\Phi)_{i+1/2} = |\Phi_i^{<p>}(x_{i+1/2}) - \Phi_{i+1}^{<q>}(x_{i+1/2})|, \quad (2.81)$$

where $\Phi_i^{<p>}(x_{i+1/2})$ and $\Phi_{i+1}^{<q>}(x_{i+1/2})$ with p and q being either *WENO* or *THINC*. Fig. 2.6 illustrates one possible situation of calculating the $BV(\Phi)_{i+1/2}$ for the target cell. Find the $\Phi_i^{<p>}(x_{i+1/2})$ and $\Phi_{i+1}^{<q>}(x_{i+1/2})$, so that the $BV(\Phi)_{i+1/2}$ is minimised.

2. Calculating the boundary variation (BV) at $x_{i-1/2}$ as

$$BV(\Phi)_{i-1/2} = |\Phi_{i-1}^{<p'>}(x_{i-1/2}) - \Phi_i^{<q'>}(x_{i-1/2})|, \quad (2.82)$$

where $\Phi_{i-1}^{<p'>}(x_{i-1/2})$ and $\Phi_i^{<q'>}(x_{i-1/2})$ with p' and q' being either *WENO* or *THINC*. Fig. 2.7 illustrates one possible situation of calculating $BV(\Phi)_{i-1/2}$ for the target cell. Find the $\Phi_{i-1}^{<p'>}(x_{i-1/2})$ and $\Phi_i^{<q'>}(x_{i-1/2})$, so that the $BV(\Phi)_{i-1/2}$ is minimised.

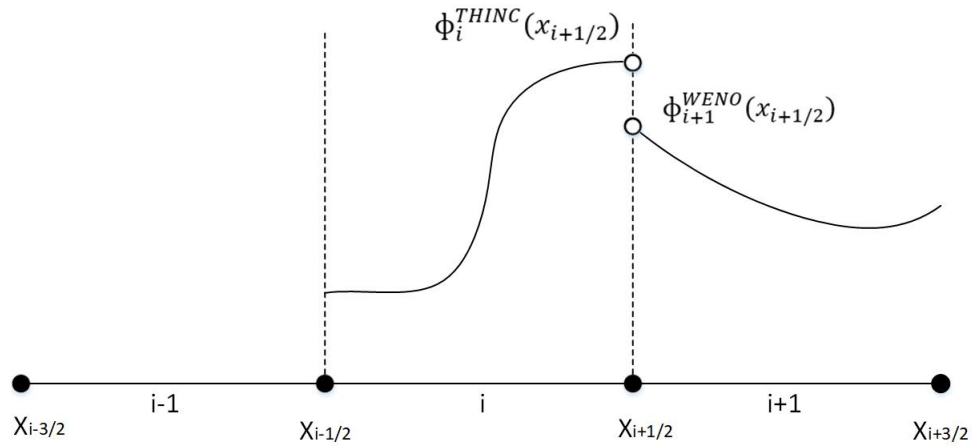


Figure 2.6: Illustration of one possible situation corresponding to $|\Phi_i^{THINC}(x_{i+1/2}) - \Phi_{i+1}^{WENO}(x_{i+1/2})|$ when calculating boundary variation at $x_{i+1/2}$.

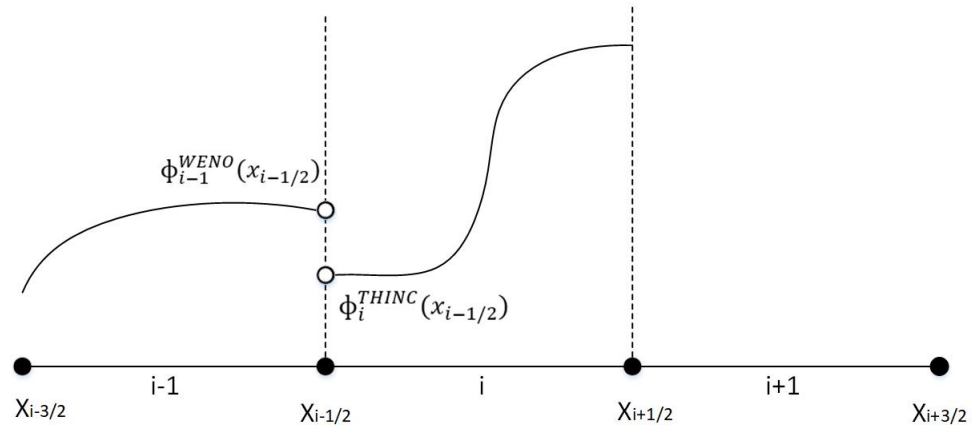


Figure 2.7: Illustration of one possible situation corresponding to $|\Phi_{i-1}^{WENO}(x_{i-1/2}) - \Phi_i^{THINC}(x_{i-1/2})|$ when calculating boundary variation at $x_{i-1/2}$.

3. Determine the reconstruction function as follows

$$\Phi_i^{<BVD>}(x) = \begin{cases} \Phi_i^{<WENO>}(x) & \text{if } \left(\Phi_i^{<p>}(x_{i+1/2}) - \Phi_{i+1}^{<q>}(x_{i+1/2}) \right) \left(\Phi_{i-1}^{<p'>}(x_{i-1/2}) - \Phi_i^{<q'>}(x_{i-1/2}) \right) < 0, \\ \Phi_i^{<THINC>}(x) & \text{otherwise.} \end{cases} \quad (2.83)$$

4. Compute the left-side value $\phi_{i+\frac{1}{2}}^L$ and the right-side value $\phi_{i-\frac{1}{2}}^R$ for each cell by

$$\phi_{i+\frac{1}{2}}^L = \Phi_i^{<BVD>}(x_{i+\frac{1}{2}}) \quad \text{and} \quad \phi_{i-\frac{1}{2}}^R = \Phi_i^{<BVD>}(x_{i-\frac{1}{2}}). \quad (2.84)$$

The BVD algorithm provides practical and effective selection criteria to construct high-resolution schemes for resolving smooth and discontinuous solutions simultaneously.

2.6 Numerical methods for moving interface in two-phase flows

The simulation of two-phase flows requires numerical technique to identify and compute moving interfaces. In the past decades, various of interface capturing techniques have been developed for two-phase flows. In general, there are two distinct categories, Lagrangian methods on moving mesh, Eulerian methods on fixed mesh [112, 113, 114, 115, 116].

In Lagrangian approach, the computational mesh moves with the fluids to track the interface motion. For example, in the Boundary Element Method (BEM) [117, 118], the mesh is advected with the fluid and calculations are performed on the deforming mesh. Despite the promising accuracy in tracking of the interface motion, the non-automatic handling of topological change and large deformations in the free surface make problems formidably difficult and requires extensive remeshing and substantial computational effort.

In Eulerian approach, the interface motion is tracked on a fixed grid to treat large interfacial deformations with relatively simple interface description. It is more straightforward to implement in multi-dimension and more applicable to simulate complex interfacial flows. The representative methods can be categorised into volume tracking methods and surface tracking methods.

In volume tracking methods, a volume fraction (or color function) is assigned to each of the grid cells and advected at each time step. The representative method is the Volume of Fluid (VOF) method [119]. The VOF method is able to deal with large topological deformations and changes without extra efforts. Moreover, it can be extended to multidimensional problems directly. On the other hand, the VOF may cause numerical diffusion errors and non-physical behaviour in the interface motion, because the interface representation is discrete.

In surface tracking methods, the surface is described by using a set of marker points or height function. Examples of surface tracking methods are the front tracking method [120], the Level Set (LS) method [121], and the Marker-and-Cell (MAC) method [122]. For front tracking method, it is difficult to be applied for topological changes problem such as breakup [123]. For Level-Set method, it suffers from poor mass conservation, with mass being spuriously created or destroyed, especially under significant topological changes. To address this issue, Sussman and Puckett proposed Coupled Level-Set Volume of Fluid method (CLSVOF) [124], which guarantee the mass conservation of the VOF method and maintain the sharp interface of the LS method. For the MAC method, it is difficult to maintain a sharp interface. Popinet and Zaleski [125] successfully improved the original MAC method with a well-defined surface by using cubic splines to interpolate surface marker particles. In order to improve the accuracy and robust in the simulation of two-phase flows undergoing arbitrary topology changes, Lind and Phillips combined the MAC method with Spectral Element Method (SEM) [126]. The governing equations are solved by using the SEM with high-order accuracy and the two phases are modelled using the MAC with minimal numerical diffusion and robustness. This scheme has been successfully applied to simulate bubble collapse in compressible fluids for both Newtonian fluids and viscoelastic fluids [126, 127].

2.7 Numerical difficulties for compressible two-phase flows with moving interface

For incompressible two-phase flows, the density and other physical properties are constant in each fluid; therefore, the Single-Equivalent-Fluid model [128, 42] can be directly implemented with an assumption that the physical fields change monotonically across the interface region. However, for compressible two-phase flows, the moving interface between two different fluids usually associate with strong discontinuities and phase changes. When implementing the one-fluid model to compressible two-phase flows with moving interface, there are two substantial difficulties. Firstly, density and energy are calculated separately in addition to the indication function, hence special formulations are required to reach a balanced state among all variables for the interface cell. Secondly, the numerical dissipation in high-resolution schemes designed for solving single phase compressible flow involving shock waves tends to smear out discontinuities, including the material interfaces.

2.8 Summary and the way forward

This chapter presents a review of the main approaches (FDM, FEM, and FVM) of spatial discretisation for Euler equations as well as the comparison of the advantages and drawbacks among these spatial discretisation methods. Moreover, this chapter reviews the methodologies of developing high-resolution spatial discretisation methods (particularly the CIP-CSL, WENO schemes, and the BVD algorithm) and interface capturing techniques. Based on this knowledge, we aim to propose several high-fidelity and high-resolution numerical schemes, which can more accurately capture both smooth and discontinuous solutions compared to existing (CIP-CSL and WENO) schemes using the following ideas.

1. By combining two CIP-CSL3 schemes using the idea of the ENO scheme, a less

oscillatory scheme will be proposed to efficiently minimise numerical oscillation in the vicinity of discontinuity and to sharply capture smooth solutions.

2. Motivated by the observation that combining two different types (one oscillatory and one diffusive) of reconstruction functions has a great potential to effectively reduce numerical diffusion and oscillations, a high-order hybrid CIP-CSL scheme will be designed based on polynomial functions, rational function, and ENO idea. The proposed scheme should be able to effectively minimise numerical oscillations and diffusion.
3. Based on the observation that diminishing the jump at the cell boundary can effectively reduce the numerical diffusion near discontinuities, we propose a novel CIP-CSL scheme by employing the modified version of the BVD algorithm. The proposed scheme is expected to further reduce the numerical errors and the numerical diffusion in the vicinity of discontinuities compared to other CIP-CSL schemes.
4. To improve the reconstruction strategy of the WENO scheme, a target WENO scheme will be designed to restore the highest possible order interpolation when three target sub-stencils or two target adjacent sub-stencils are smooth. The proposed scheme will be formulated under the original smoothness indicators of the conventional WENO scheme to reduce numerical diffusion near discontinuous regions.
5. To further minimise the numerical diffusion across discontinuities of the newly proposed target WENO scheme, a high-resolution scheme will be proposed based on the target WENO and THINC schemes. The reconstruction criterion will be designed by the modified version of the BVD algorithm. The proposed scheme is expected to capture both smooth and discontinuous solutions simultaneously with less numerical diffusion.
6. To reach a balanced state among all variables for the interface cell, the five-

equation model [42] is used as the partial differential equation (PDE) to simulate compressible two-phase flows. To reduce the numerical dissipation, which smears out discontinuities, including the material interfaces, the proposed high-resolution reconstruction scheme is used to minimize the total variations (jumps) of the reconstructed variables at cell boundaries, which in turn effectively eliminates the numerical dissipations in numerical solutions.

Fourth-order essentially non-oscillatory CIP-CSL3 scheme

In this chapter, firstly, we propose the CIP-CSL3U (U of CIP-CSL3U stands for Upwind) scheme on the basis of the CIP-CSL3D (D of CIP-CSL3D stands for Downwind) [35] scheme. In the CIP-CSL3D scheme, a moment in the downwind cell is used as a constraint instead of the derivative used in the CIP-CSL3 scheme. While in the CIP-CSL3U scheme, an additional moment in the upwind side is used as a constraint instead of a moment in the downwind cell of the CIP-CSL3D scheme.

Secondly, we present a less oscillatory CIP-CSL3-ENO scheme by combining the CIP-CSL3U and CIP-CSL3D schemes using the idea of the ENO scheme. In the CIP-CSL3-ENO scheme, an ENO indicator is proposed to design the selection criteria (either CIP-CSL3D or CIP-CSL3U). The CIP-CSL3-ENO scheme minimises numerical oscillations in CIP-CSL3D and CIP-CSL3U by taking advantage of the complementary nature of these two schemes. The CIP-CSL3-ENO scheme captures discontinuities and smooth solutions simultaneously with less numerical oscillations for solutions which include discontinuities.

3.1 Numerical method

In this section, firstly, two variants of CIP-CSL3 scheme (CIP-CSL3D and CIP-CSL3U) are explained. Subsequently, we present the CIP-CSL3-ENO scheme, which is based on the CIP-CSL3D and CIP-CSL3U schemes and the newly proposed ENO indicator.

3.1.1 CIP-CSL3D scheme

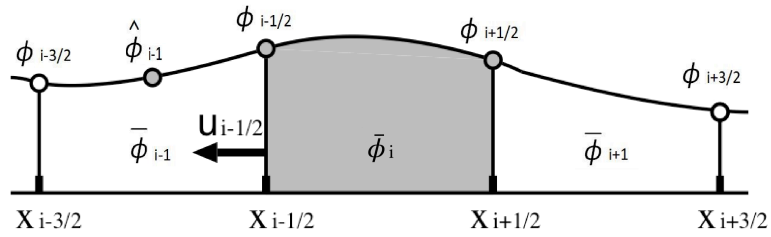


Figure 3.1: Schematic figures of the CIP-CSL3D scheme. $u_{i-1/2} < 0$ is assumed. The moments which are indicated by grey colour are used as constraints to construct interpolation function $\Phi_i^{CSL3D}(x)$.

The CIP-CSL3D scheme is a variant of the CIP-CSL3 scheme, which is based on a third-order polynomial interpolation function. For the case of $u_{i-1/2} < 0$, the interpolation function of the CIP-CSL3D scheme is

$$\Phi_i^{CSL3D}(x) = C_{3,i}^{CSL3D}(x-x_{i-1/2})^3 + C_{2,i}^{CSL3D}(x-x_{i-1/2})^2 + C_{1,i}^{CSL3D}(x-x_{i-1/2}) + C_{0,i}^{CSL3D}. \quad (3.1)$$

This interpolation function $\Phi_i^{CSL3D}(x)$ is constructed using the following four constraints (three constraints $\phi_{i-1/2}$, $\bar{\phi}_i$, $\phi_{i+1/2}$ in the upwind cell and a constraint $\hat{\phi}_{i-1}$ in

the downwind cell, as shown in Fig. 3.1.

$$\left\{ \begin{array}{l} \phi_{i-1/2} = \Phi_i^{CSL3D}(x_{i-1/2}), \\ \bar{\phi}_i = \frac{\int_{x_{i-1/2}}^{x_{i+1/2}} \Phi_i^{CSL3D}(x) dx}{\Delta x}, \\ \phi_{i+1/2} = \Phi_i^{CSL3D}(x_{i+1/2}), \\ \hat{\phi}_{i-1} = \Phi_i^{CSL3D}(x_{i-1}). \end{array} \right. \quad (3.2)$$

The coefficients are obtained as follows

$$C_{3,i}^{CSL3D} = \frac{1}{3\Delta x^3} (15\phi_{i-1/2} - 18\bar{\phi}_i + 7\phi_{i+1/2} - 4\hat{\phi}_{i-1}), \quad (3.3)$$

$$C_{2,i}^{CSL3D} = \frac{1}{2\Delta x^2} (9\phi_{i-1/2} - 6\bar{\phi}_i + \phi_{i+1/2} - 4\hat{\phi}_{i-1}), \quad (3.4)$$

$$C_{1,i}^{CSL3D} = -\frac{1}{6\Delta x} (9\phi_{i-1/2} - 18\bar{\phi}_i + 5\phi_{i+1/2} + 4\hat{\phi}_{i-1}), \quad (3.5)$$

$$C_{0,i}^{CSL3D} = \phi_{i-1/2}. \quad (3.6)$$

Analogously, for the case of $u_{i-1/2} \geq 0$, the cubic interpolation function is

$$\Phi_{i-1}^{CSL3D}(x) = C_{3,i-1}^{CSL3D}(x-x_{i-1/2})^3 + C_{2,i-1}^{CSL3D}(x-x_{i-1/2})^2 + C_{1,i-1}^{CSL3D}(x-x_{i-1/2}) + C_{0,i-1}^{CSL3D}. \quad (3.7)$$

The coefficients are

$$C_{3,i-1}^{CSL3D} = -\frac{1}{3\Delta x^3} (15\phi_{i-1/2} - 18\bar{\phi}_{i-1} + 7\phi_{i-3/2} - 4\hat{\phi}_i), \quad (3.8)$$

$$C_{2,i-1}^{CSL3D} = -\frac{1}{2\Delta x^2} (9\phi_{i-1/2} - 6\bar{\phi}_{i-1} + \phi_{i-3/2} - 4\hat{\phi}_i), \quad (3.9)$$

$$C_{1,i-1}^{CSL3D} = \frac{1}{6\Delta x} (9\phi_{i-1/2} - 18\bar{\phi}_{i-1} + 5\phi_{i-3/2} + 4\hat{\phi}_i), \quad (3.10)$$

$$C_{0,i-1}^{CSL3D} = \phi_{i-1/2}. \quad (3.11)$$

3.1.2 CIP-CSL3U scheme

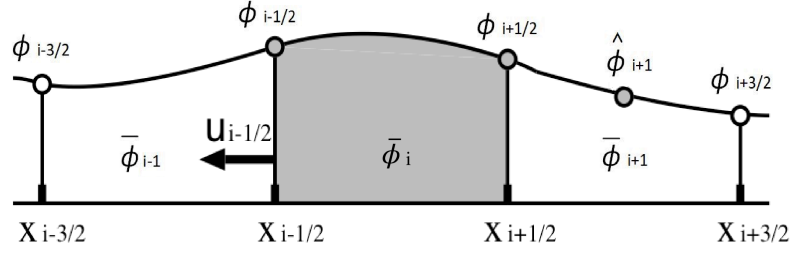


Figure 3.2: Schematic figures of the CIP-CSL3U scheme. $u_{i-1/2} < 0$ is assumed. The moments which are indicated by grey colour are used as constraints to construct interpolation function $\Phi_i^{CSL3U}(x)$.

On the basis of the CIP-CSL3D scheme, we proposed another variant of the CIP-CSL3 scheme called CIP-CSL3U, which uses an additional moment in the upwind side. For the case of $u_{i-1/2} < 0$, the interpolation function of the CIP-CSL3U scheme is

$$\Phi_i^{CSL3U}(x) = C_{3,i}^{CSL3U}(x-x_{i-1/2})^3 + C_{2,i}^{CSL3U}(x-x_{i-1/2})^2 + C_{1,i}^{CSL3U}(x-x_{i-1/2}) + C_{0,i}^{CSL3U}. \quad (3.12)$$

This interpolation function $\Phi_i^{CSL3U}(x)$ is constructed using the following four constraints ($\phi_{i-1/2}$, $\bar{\phi}_i$, $\phi_{i+1/2}$, and $\hat{\phi}_{i+1}$) in the upwind cell, as shown in Fig. 3.2.

$$\begin{cases} \phi_{i-1/2} = \Phi_i^{CSL3U}(x_{i-1/2}), \\ \bar{\phi}_i = \frac{\int_{x_{i-1/2}}^{x_{i+1/2}} \Phi_i^{CSL3U}(x) dx}{\Delta x}, \\ \phi_{i+1/2} = \Phi_i^{CSL3U}(x_{i+1/2}), \\ \hat{\phi}_{i+1} = \Phi_i^{CSL3U}(x_{i+1}). \end{cases} \quad (3.13)$$

The coefficients are obtained as follows

$$C_{3,i}^{CSL3U} = \frac{1}{3\Delta x^3}(-7\phi_{i-1/2} + 18\bar{\phi}_i - 15\phi_{i+1/2} + 4\hat{\phi}_{i+1}), \quad (3.14)$$

$$C_{2,i}^{CSL3U} = \frac{1}{2\Delta x^2}(13\phi_{i-1/2} - 30\bar{\phi}_i + 21\phi_{i+1/2} - 4\hat{\phi}_{i+1}), \quad (3.15)$$

$$C_{1,i}^{CSL3U} = \frac{1}{6\Delta x}(-31\phi_{i-1/2} + 54\bar{\phi}_i - 27\phi_{i+1/2} + 4\hat{\phi}_{i+1}), \quad (3.16)$$

$$C_{0,i}^{CSL3U} = \phi_{i-1/2}. \quad (3.17)$$

Analogously, for the case of $u_{i-1/2} \geq 0$, the cubic interpolation function is

$$\Phi_{i-1}^{CSL3U}(x) = C_{3,i-1}^{CSL3U}(x-x_{i-1/2})^3 + C_{2,i-1}^{CSL3U}(x-x_{i-1/2})^2 + C_{1,i-1}^{CSL3U}(x-x_{i-\frac{1}{2}}) + C_{0,i-1}^{CSL3U}. \quad (3.18)$$

The coefficients are

$$C_{3,i-1}^{CSL3U} = -\frac{1}{3\Delta x^3}(-7\phi_{i-1/2} + 18\bar{\phi}_{i-1} - 15\phi_{i-3/2} + 4\hat{\phi}_{i-2}), \quad (3.19)$$

$$C_{2,i-1}^{CSL3U} = \frac{1}{2\Delta x^2}(13\phi_{i-1/2} - 30\bar{\phi}_{i-1} + 21\phi_{i-3/2} - 4\hat{\phi}_{i-2}), \quad (3.20)$$

$$C_{1,i-1}^{CSL3U} = -\frac{1}{6\Delta x}(-31\phi_{i-1/2} + 54\bar{\phi}_{i-1} - 27\phi_{i-3/2} + 4\hat{\phi}_{i-2}), \quad (3.21)$$

$$C_{0,i-1}^{CSL3U} = \phi_{i-1/2}. \quad (3.22)$$

3.1.3 Fourier analysis of the CIP-CSL3D and CIP-CSL3U schemes

In this section, we conduct Fourier analysis [129] of the newly proposed CIP-CSL3U scheme and the CIP-CSL3D scheme. In this analysis, we consider the case of $u_{i-1/2} < 0$. Fourier analysis shows resolution of spatial derivatives in the wavenumber space. The spatial profile of $\Phi(x)$ is defined over the domain $[0, L]$ with a uniform grid spacing Δx , and is decomposed into the following Fourier series

$$\Phi(x) = \sum_k \Phi(k) e^{jwx/\Delta x}, \quad (3.23)$$

where $w = 2\pi k\Delta x/L$ is the scaled wavenumber, and $j = \sqrt{-1}$. At $x_{i-1/2}$, the point value is decomposed as

$$\Phi_{i-1/2} = \sum_k \Phi(k) e^{jwx_{i-1/2}/\Delta x}. \quad (3.24)$$

Using Eq.(3.24), the value at $x_{i-1/2+m}$ is decomposed as

$$\Phi_{i-1/2+m} = \Phi_{i-1/2} e^{jwm}. \quad (3.25)$$

The cell average $\bar{\Phi}_i$ is decomposed as

$$\bar{\Phi}_i = \frac{1}{\Delta x} \int_0^{\Delta x} \Phi(x_{i-1/2} + x) dx = \Phi_{i-1/2} \frac{e^{jw} - 1}{jw}. \quad (3.26)$$

Eq. (3.26) represents the relationship between the point value and the cell average. The accuracy of the CIP-CSL3U and CIP-CSL3D schemes at $x_{i-1/2}$ can be examined by using Eq. (3.25) and Eq. (3.26). Analogously, we conduct Fourier analysis at x_i and $x_{i+1/2}$. The mathematical formulations are given in Appendix A.1. Figs. 3.3, 3.4, and 3.5 depict the results of Fourier analysis of the CIP-CSL3U scheme with those of the CIP-CSL3D scheme at $x_{i-1/2}$, $x_{i+1/2}$ and x_i , respectively.

Fig. 3.3 shows that at $x_{i-1/2}$, CIP-CSL3D is consistently superior to CIP-CSL3U. This is because the additional moment of CIP-CSL3D ($\hat{\phi}_{i-1}$) is closer to $x_{i-1/2}$ than that of CIP-CSL3U ($\hat{\phi}_{i+1}$). Analogously, at $x_{i+1/2}$, CIP-CSL3U is superior to CIP-CSL3D, as shown in Fig. 3.4. The results at $x_{i-1/2}$ and $x_{i+1/2}$ are symmetrical due to the nature of discretizations. At the cell centre x_i , the results of CIP-CSL3U and CIP-CSL3D are identical, as shown in Fig. 3.5. This is because both schemes are symmetrical at x_i .

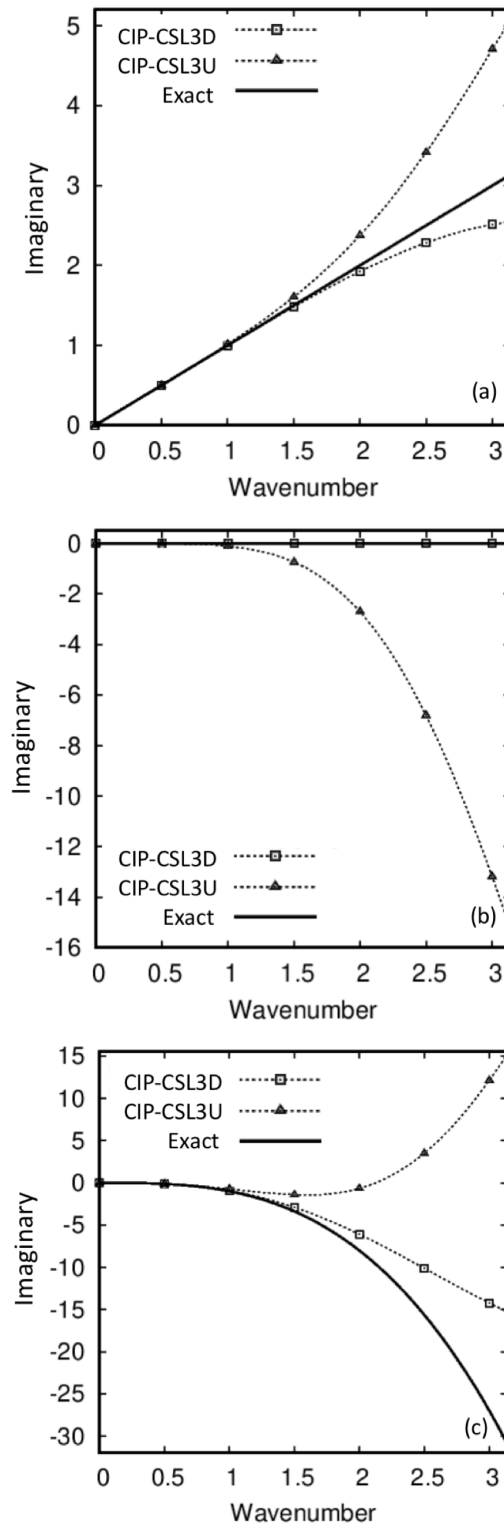


Figure 3.3: Spatial derivatives of the CIP-CSL3D and CIP-CSL3U schemes at a cell boundary $x_{i-1/2}$. The results of imaginary parts of (a) first derivatives, (b) second derivatives, (c) third derivatives.

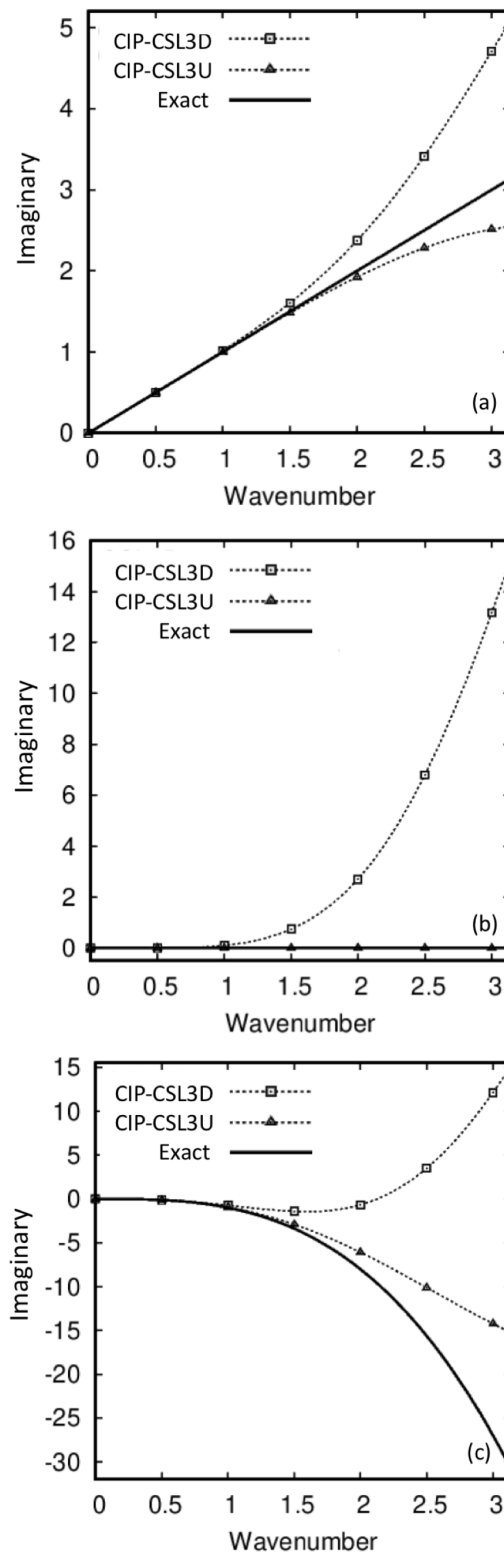


Figure 3.4: Spatial derivatives of the CIP-CSL3D and CIP-CSL3U schemes at a cell boundary $x_{i+1/2}$. The results of imaginary parts of (a) first derivatives, (b) second derivatives, (c) third derivatives.

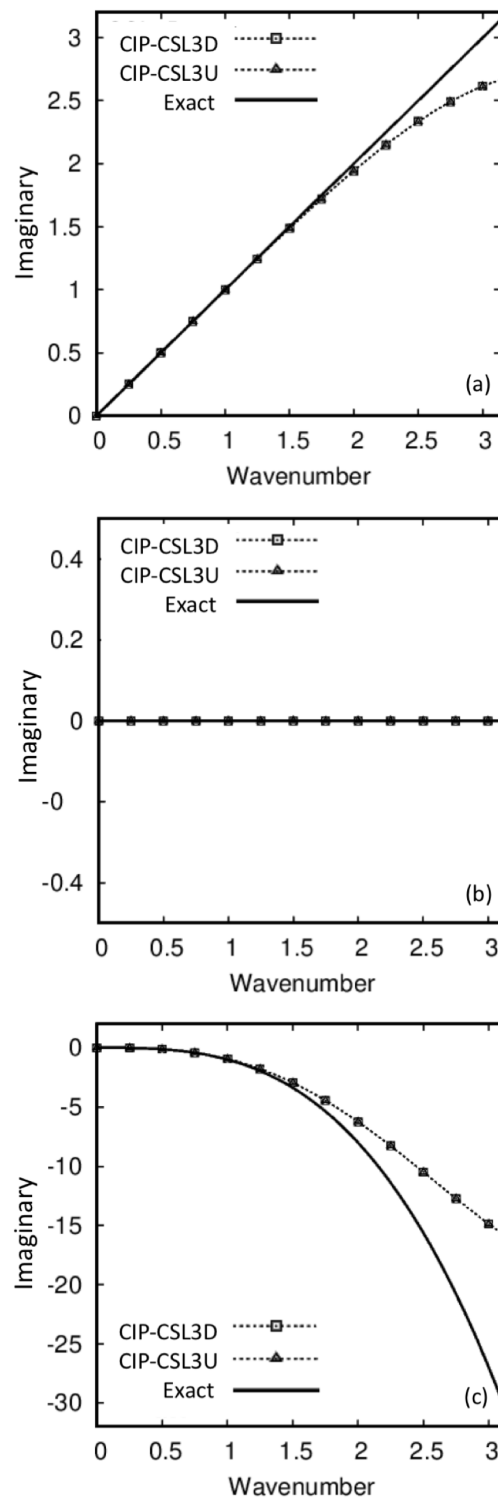


Figure 3.5: Spatial derivatives of the CIP-CSL3D and CIP-CSL3U schemes at the cell centre x_i . The results of imaginary parts of (a) first derivatives, (b) second derivatives, (c) third derivatives.

3.1.4 CIP-CSL3-ENO scheme

Based on the CIP-CSL3D and CIP-CSL3U schemes, we propose the CIP-CSL3-ENO scheme in this section. In the CIP-CSL3D and CIP-CSL3U schemes, three different types of moments (i.e. $\phi_{i-1/2}$, $\bar{\phi}_i$, and $\hat{\phi}_i$) are used. Although many possible selectors/indicators are tested, in this section, we propose a simple and efficient selector based on a type of ratios of successive gradients.

Considering the case as shown in Fig. 3.1 and Fig. 3.2 (i.e. $u_{i-1/2} < 0$), the smoothness indicator of the CIP-CSL3D and CIP-CSL3U stencils are designed by using ratios of successive gradients, $r_{i+1/2}$ and $r_{i-1/2}$, respectively. $r_{i+1/2}$ and $r_{i-1/2}$ are defined as

$$r_{i+1/2} = \text{sgn}\left(\frac{\hat{\phi}_i - \phi_{i+1/2}}{\phi_{i+1/2} - \hat{\phi}_{i+1}}\right) \max\left(\frac{|\hat{\phi}_i - \phi_{i+1/2}|}{|\phi_{i+1/2} - \hat{\phi}_{i+1}|}, \frac{|\phi_{i+1/2} - \hat{\phi}_{i+1}|}{|\hat{\phi}_i - \phi_{i+1/2}|}\right). \quad (3.27)$$

$$r_{i-1/2} = \text{sgn}\left(\frac{\hat{\phi}_i - \phi_{i-1/2}}{\phi_{i-1/2} - \hat{\phi}_{i-1}}\right) \max\left(\frac{|\hat{\phi}_i - \phi_{i-1/2}|}{|\phi_{i-1/2} - \hat{\phi}_{i-1}|}, \frac{|\phi_{i-1/2} - \hat{\phi}_{i-1}|}{|\hat{\phi}_i - \phi_{i-1/2}|}\right), \quad (3.28)$$

Using $r_{i+1/2}$ and $r_{i-1/2}$, we select a stencil by the following selection criteria.

Selection criteria:

1. If both $r_{i+1/2}$ and $r_{i-1/2}$ are negative, the larger one is selected.
2. If one of $r_{i+1/2}$ and $r_{i-1/2}$ is negative, the negative one is selected.
3. If both $r_{i+1/2}$ and $r_{i-1/2}$ are positive, the larger one is selected.

When $r_{i+1/2}$ (or $r_{i-1/2}$) is negative, it represents opposite slopes. It has been considered that such a stencil should be avoided. However, as shown in Sec. 3.2 (for instance, sharp edges around $x = -0.7$ and $x = 0.1$ in Fig. 3.8 (d) and (e), and Fig. 3.9 (d) and (e)), both CIP-CSL3D and CIP-CSL3U deal with pre-existing opposite slopes very well. Therefore, we considered that we do not have to avoid such stencils which have negative successive gradients and designed a selector which intentionally selects such a non-smooth stencil. We found this selection criteria after numerous numerical

experiments and this selector worked well in our numerical experiments, as shown in Sec. 3.2. For the case of $u_{i-1/2} \geq 0$, the smoothness indicator of the CIP-CSL3D and CIP-CSL3U schemes are designed by $r_{i-1/2}$ and $r_{i-3/2}$, respectively.

3.1.5 Implementation of boundary conditions

CFD problems are defined in terms of initial and boundary conditions. It is important to specify boundary conditions correctly. In constructing the grid arrangement, we set up additional nodes surrounding the physical boundaries. The calculations are performed at internal nodes only. Two notable features of the arrangement are (i) the physical boundaries coincide with the control volume boundaries and (ii) the node just outside the inlet of the domain are available to store the inlet conditions.

3.2 Numerical results

In this section, various benchmark tests are conducted to validate the proposed schemes.

3.2.1 Sine wave propagation

This sine wave propagation is used to check the convergence rate of the proposed schemes. The conservation Eq. (2.13) is solved with the initial condition $\phi(x, 0) = \sin(2\pi x)$. Periodic boundary conditions are used. $u(x) = 1$ and the domain is $[0, 1]$. Four different grid sizes ($N = 100, 200, 400$ and 800) are used with $\Delta x = 1/N$ and $\Delta t = 0.4\Delta x$. L_1 and L_∞ errors are defined as follows

$$L_1 = \frac{1}{N} \sum_{i=1}^N |\phi_i - \phi_{exact,i}|, \quad (3.29)$$

$$L_\infty = \max(|\phi_i - \phi_{exact,i}|). \quad (3.30)$$

Table 3.1: L_1 and L_∞ errors in sine wave propagation at $t=1$.

Method	N	L_1 error	L_1 order	L_∞ error	L_∞ order
CIP-CSL2	100	6.28×10^{-6}	-	9.86×10^{-6}	-
	200	7.85×10^{-7}	3.00	1.23×10^{-6}	3.00
	400	9.82×10^{-8}	3.00	1.54×10^{-7}	3.00
	800	1.23×10^{-8}	3.00	1.93×10^{-8}	3.00
CIP-CSL3CW	100	5.85×10^{-4}	-	5.04×10^{-3}	-
	200	1.18×10^{-4}	2.31	1.80×10^{-3}	1.49
	400	2.29×10^{-5}	2.36	6.27×10^{-4}	1.52
	800	4.57×10^{-6}	2.33	2.14×10^{-4}	1.55
CIP-CSL3H	100	8.33×10^{-8}	-	1.23×10^{-7}	-
	200	4.56×10^{-9}	4.19	6.94×10^{-9}	4.15
	400	2.72×10^{-10}	4.07	4.21×10^{-10}	4.04
	800	1.61×10^{-11}	4.02	2.61×10^{-11}	4.01
CIP-CSL3D	100	1.07×10^{-7}	-	1.68×10^{-7}	-
	200	6.68×10^{-9}	4.00	1.05×10^{-8}	4.00
	400	4.18×10^{-10}	4.00	6.56×10^{-10}	4.00
	800	2.61×10^{-11}	4.00	4.10×10^{-11}	4.00
CIP-CSL3U	100	9.13×10^{-8}	-	1.43×10^{-7}	-
	200	5.71×10^{-9}	4.00	8.97×10^{-9}	3.99
	400	3.57×10^{-10}	4.00	5.60×10^{-10}	4.00
	800	2.23×10^{-11}	4.00	3.50×10^{-11}	4.00
CIP-CSL3-ENO	100	2.26×10^{-7}	-	2.47×10^{-6}	-
	200	1.54×10^{-8}	3.88	2.89×10^{-7}	3.10
	400	1.01×10^{-9}	3.93	3.33×10^{-8}	3.13
	800	6.70×10^{-11}	3.91	3.80×10^{-9}	3.13

Table 3.1 presents the numerical results of the CIP-CSL2, CIP-CSL3CW, CIP-CSL3H, CIP-CSL3D, CIP-CSL3U, and CIP-CSL3-ENO schemes. It is observed that CIP-CSL3CW is less accurate than all others due to the slope limiter. CIP-CSL3H is the most accurate scheme in this test because CIP-CSL3H uses a wider stencil than other compared CIP-CSL schemes. CIP-CSL3-ENO approximately has fourth-order accuracy for L_1 and third-order accuracy for L_∞ . CIP-CSL2 has third-order accuracy and CIP-CSL3H, CIP-CSL3D and CIP-CSL3U have fourth-order accuracy.

3.2.2 Square wave propagation

In this section, the square wave propagation test is conducted to verify the proposed schemes of capturing discontinuity. In this test, $u(x) = 1$, the domain $[-1, 1]$, $N = 200$, $\Delta x = 2/N$, $t=16$, and periodic boundary conditions are used. The initial condition is given as

$$\phi(x, 0) = \begin{cases} 1 & \text{if } -0.3 \leq x < 0.3 \\ 0 & \text{otherwise.} \end{cases} \quad (3.31)$$

We tested different CFL numbers (CFL=0.2 and 0.8) due to the reason that CIP-CSL3D and CIP-CSL3U show different behaviours depending on the CFL number. Fig. 3.6 shows numerical results of the CIP-CSL2, CIP-CSL3CW, CIP-CSL3H, CIP-CSL3D, CIP-CSL3U, and CIP-CSL3-ENO schemes with CFL=0.2. It is observed that CIP-CSL3U has larger numerical oscillation than that of CIP-CSL3D when the CFL number is 0.2 (less than 0.5) as shown in Fig. 3.6 (b). This is because when $\text{CFL} < 0.5$, the departure point is closer to the additional moment of CIP-CSL3D (i.e. $\hat{\phi}_{i-1}$ in Fig. 3.1).

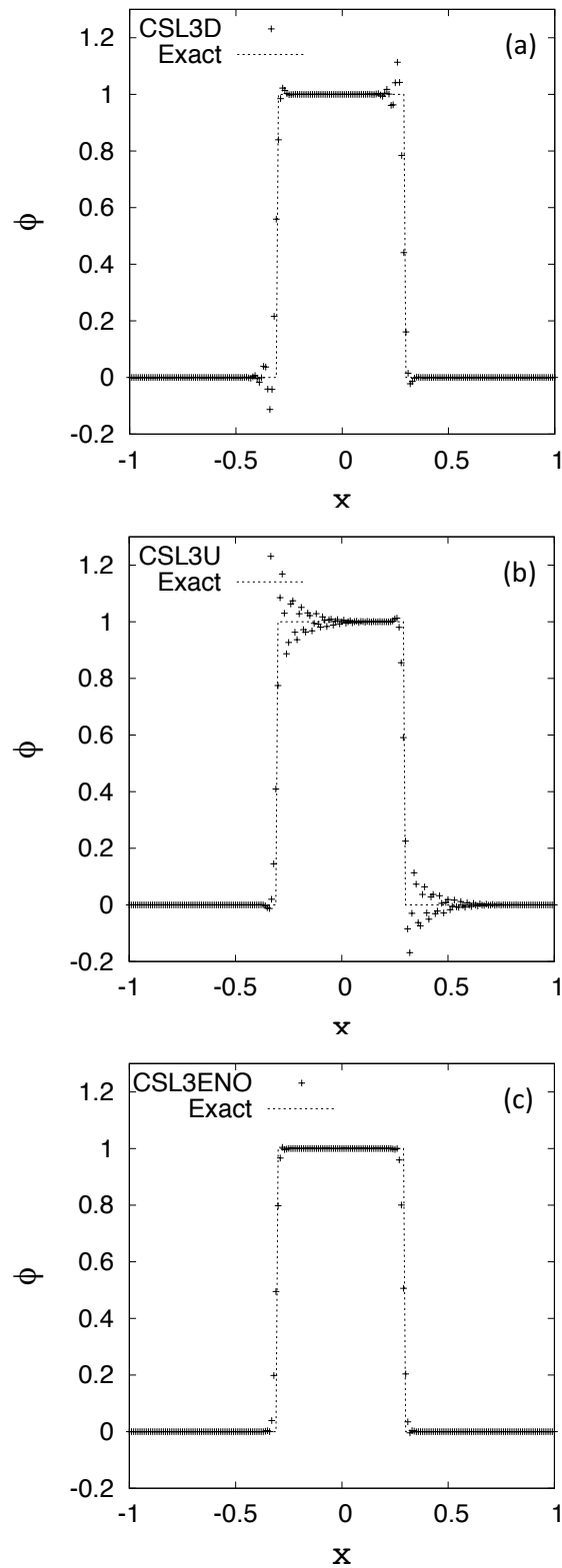


Figure 3.6: Numerical results of square wave propagation test at $t=16$ (8,000 time steps). $N=200$ and $CFL=0.2$ are used. (a) CIP-CSL3D, (b) CIP-CSL3U, (c) CIP-CSL3-ENO.

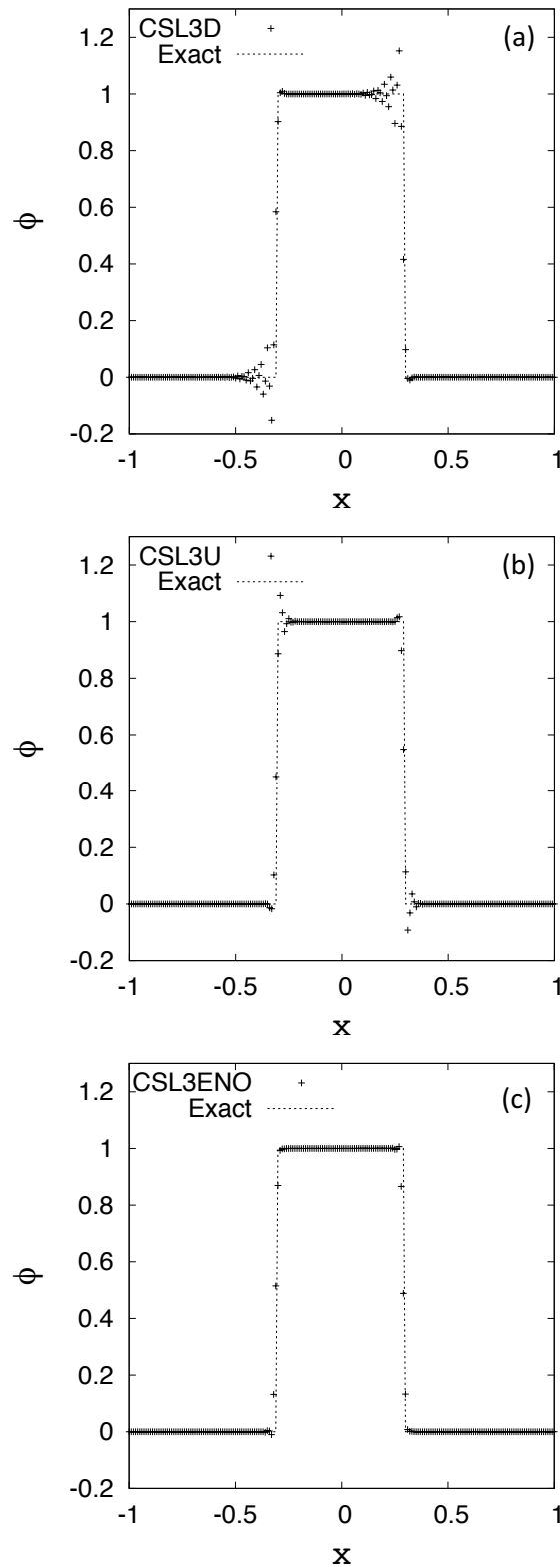


Figure 3.7: Numerical results of square wave propagation test at $t=16$ (2,000 time steps). $N=200$ and $CFL=0.8$ are used. (a) CIP-CSL3D, (b) CIP-CSL3U, (c) CIP-CSL3-ENO.

On the other hand, Fig. 3.7 shows numerical results of the CIP-CSL2, CIP-CSL3CW, CIP-CSL3H, CIP-CSL3D, CIP-CSL3U, and CIP-CSL3-ENO schemes with CFL=0.8. It is observed that CIP-CSL3D has larger numerical oscillation when the CFL number is 0.8 (larger than 0.5) as shown in Fig. 3.7 (a). This is due to the reason that when $\text{CFL} > 0.5$, the departure point is closer to the additional moment of CIP-CSL3U (i.e. $\hat{\phi}_{i+1}$ in Fig. 3.2). This trend is consistent with the results of Fourier analysis, as shown in Sec. 3.1.3. In addition, CIP-CSL3-ENO can deal with different CFL numbers, as shown in Fig. 3.6 (c) and Fig. 3.7 (c).

3.2.3 Complex wave propagation

In this test, the Jiang-Shu complex wave propagation problem [1] is conducted to validate the proposed CIP-CSL schemes of capturing complex profiles, including discontinuities. The domain $[-1, 1]$, $u(x) = 1$, $N = 200$, $\Delta x = 2/N$, $\text{CFL} = 0.4$, and periodic boundary conditions are used in this test. The initial condition is given as

$$\phi(x, 0) = \begin{cases} \frac{1}{6} (G(x, \beta, z - \delta) + G(x, \beta, z + \delta) + 4G(x, \beta, z)), & -0.8 \leq x \leq -0.6, \\ 1, & -0.4 \leq x \leq -0.2, \\ 1 - |10(x - 0.1)|, & 0.0 \leq x \leq 0.2, \\ \frac{1}{6} (F(x, \alpha, a - \delta) + F(x, \alpha, a + \delta) + 4F(x, \alpha, a)), & 0.4 \leq x \leq 0.6, \\ 0, & \text{otherwise,} \end{cases} \quad (3.32)$$

where

$$G(x, \beta, z) = e^{-\beta(x-z)^2}, \quad (3.33)$$

$$F(x, \alpha, a) = \sqrt{\max(1 - \alpha^2(x - a)^2, 0)}, \quad (3.34)$$

here $a = 0.5$, $z = -0.7$, $\delta = 0.005$, $\alpha = 10$ and $\beta = \log(2)/(36\delta^2)$.

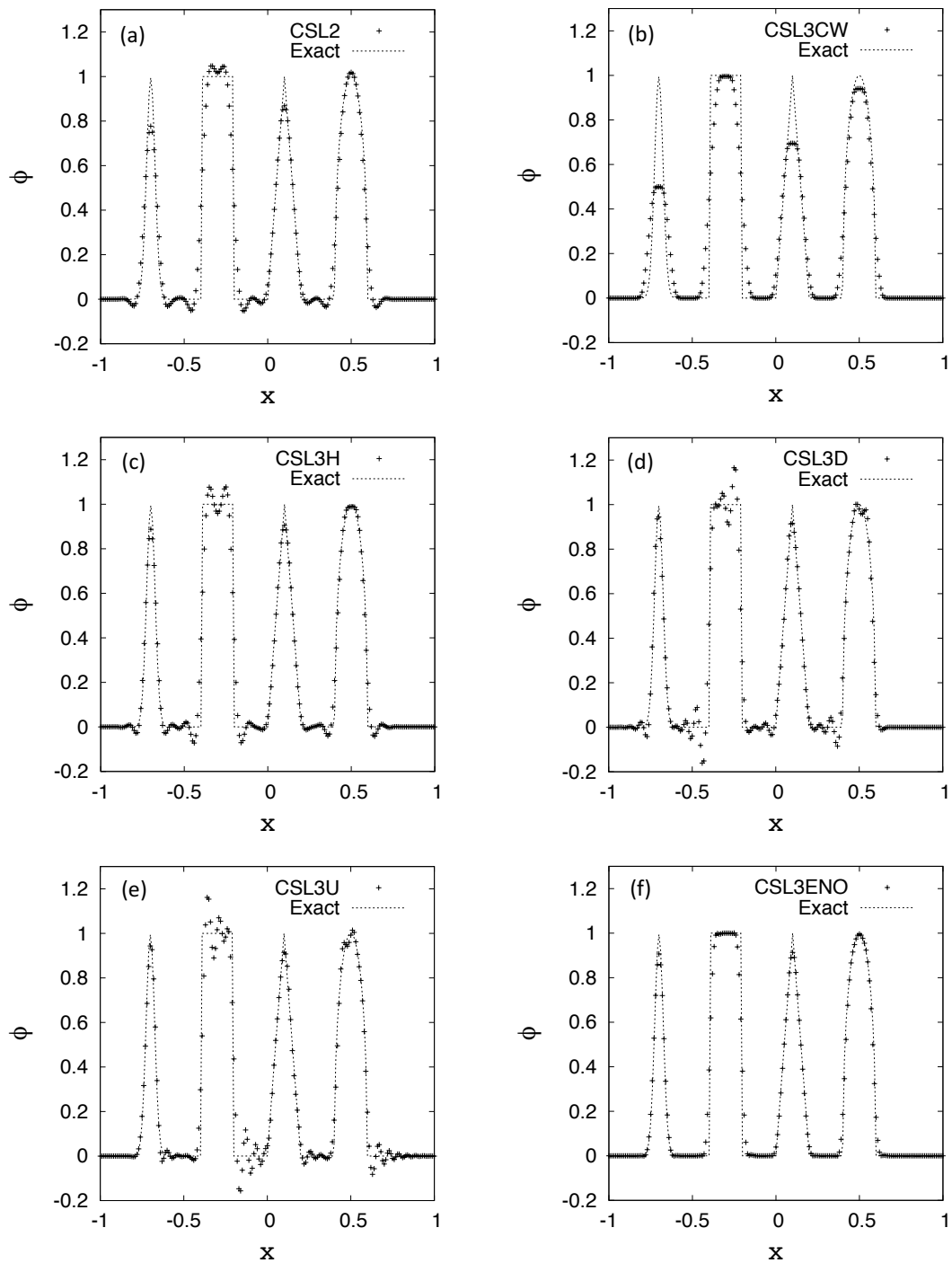


Figure 3.8: Numerical results of complex wave propagation test at $t=16$ (4,000 time steps, 8 period). CFL=0.4 and $N=200$ are used. (a) CIP-CSL2, (b) CIP-CSL3CW, (c) CIP-CSL3H, (d) CIP-CSL3D, (e) CIP-CSL3U, (f) CIP-CSL3-ENO.

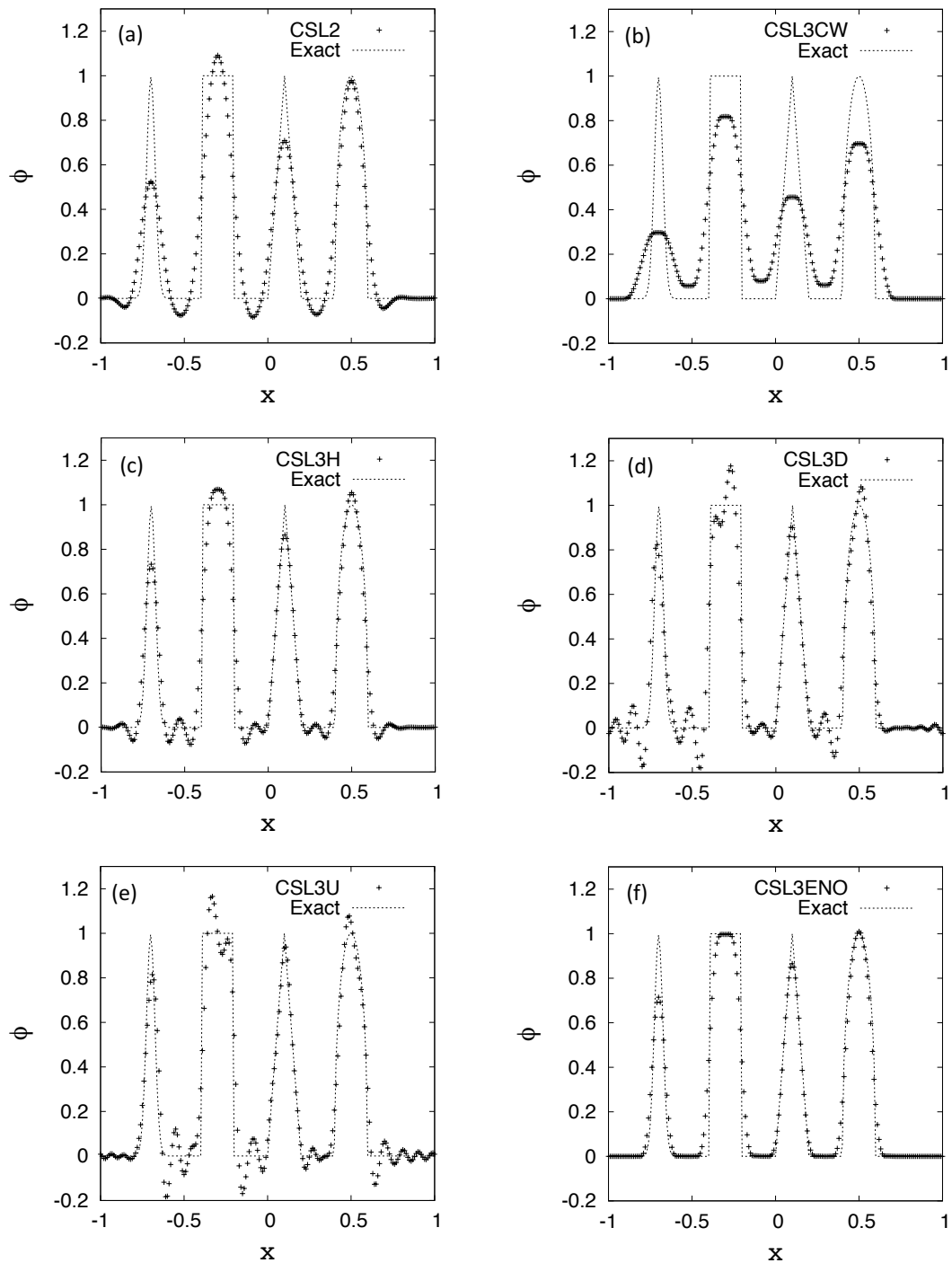


Figure 3.9: Numerical results of complex wave propagation test at $t=160$ (40,000 time steps, 80 period). $CFL=0.4$ and $N=200$ are used. (a) CIP-CSL2, (b) CIP-CSL3CW, (c) CIP-CSL3H, (d) CIP-CSL3D, (e) CIP-CSL3U, (f) CIP-CSL3-ENO.

Fig. 3.8 illustrates the results of the CIP-CSL2, CIP-CSL3CW, CIP-CSL3H, CIP-CSL3D, CIP-CSL3U, and CIP-CSL3-ENO schemes at $t=16$ (8 periods). It is observed that CIP-CSL2, CIP-CSL3H, CIP-CSL3D, and CIP-CSL3U are oscillatory around discontinuities. CIP-CSL3CW has no numerical oscillations, however, the results of CIP-CSL3CW are diffusive. CIP-CSL3D has larger numerical oscillations around discontinuities when discontinuities appear in the downwind side. The trend is opposite to CIP-CSL3U due to the nature of CIP-CSL3D and CIP-CSL3U (i.e. CIP-CSL3D and CIP-CSL3U use an additional moment in downwind and upwind sides, respectively). CIP-CSL3-ENO minimises numerical oscillations with minimum numerical diffusion.

Fig. 3.9 illustrates the results of the CIP-CSL2, CIP-CSL3CW, CIP-CSL3H, CIP-CSL3D, CIP-CSL3U, and CIP-CSL3-ENO schemes at $t=160$ (80 periods). The results show that CIP-CSL3-ENO still captures discontinuities and cusps well without numerical oscillation after 80 periods. However, CIP-CSL2, CIP-CSL3H, CIP-CSL3D and CIP-CSL3U have significant numerical oscillations, and CIP-CSL3CW has excessive numerical diffusion.

Table 3.2: L_1 and L_∞ errors in complex wave propagation test of the CIP-CSL2, CIP-CSL3CW, CIP-CSL3H, CIP-CSL3D, CIP-CSL3U, and CIP-CSL3-ENO schemes at $t=16$ (4000 time steps, 8 periods) and $t=160$ (40,000 time steps, 80 periods). $N=200$ and $CFL=0.4$ are used.

	4000 time steps		40,000 time steps	
	L_1 error	L_∞ error	L_1 error	L_∞ error
CIP-CSL2	4.32×10^{-2}	4.22×10^{-1}	9.28×10^{-2}	4.70×10^{-1}
CIP-CSL3CW	6.49×10^{-2}	4.94×10^{-1}	1.49×10^{-1}	6.97×10^{-1}
CIP-CSL3H	3.39×10^{-2}	3.97×10^{-1}	5.63×10^{-2}	4.35×10^{-1}
CIP-CSL3D	3.34×10^{-2}	4.60×10^{-1}	6.62×10^{-2}	5.50×10^{-1}
CIP-CSL3U	3.68×10^{-2}	4.66×10^{-1}	6.56×10^{-2}	5.45×10^{-1}
CIP-CSL3-ENO	2.30×10^{-2}	3.86×10^{-1}	4.43×10^{-2}	4.31×10^{-1}

Table 3.2 shows L_1 and L_∞ errors of the CIP-CSL2, CIP-CSL3CW, CIP-CSL3H, CIP-CSL3D, CIP-CSL3U, and CIP-CSL3-ENO schemes. The results show that CIP-CSL3-ENO is consistently superior to other CIP-CSL schemes in this test.

3.2.4 Extrema of the various smoothness problem

In this section, we verify the proposed scheme by conducting the extrema of the various smoothness test. The domain $[-1.5, 0.5]$, $u(x) = 1$, $N = 100$, CFL=0.4, $t=8$ (4 periods) and periodic boundary conditions are used. The initial condition is given as

$$\phi(x + 0.5, 0) = \begin{cases} -x \sin(1.5\pi x^2) & \text{if } -1 \leq x < -1/3 \\ |\sin(2\pi x)| & \text{if } |x| \leq 1/3 \\ 2x - 1 - \sin(3\pi x)/6 & \text{otherwise,} \end{cases} \quad (3.35)$$

Fig. 3.10 shows the numerical results of the CIP-CSL2, CIP-CSL3CW, CIP-CSL3H, CIP-CSL3D, CIP-CSL3U, and CIP-CSL3-ENO schemes. It is observed that CIP-CSL2, CIP-CSL3H, CIP-CSL3D, and CIP-CSL3U have numerical oscillations in vicinity of discontinuities. CIP-CSL3CW has excessive numerical diffusion not only around discontinuities but also smooth regions. CIP-CSL3ENO captures discontinuities and smooth profiles well without numerical oscillations. Table 3.3 presents L_1 and L_∞ errors of the CIP-CSL2, CIP-CSL3CW, CIP-CSL3H, CIP-CSL3D, CIP-CSL3U, and CIP-CSL3-ENO schemes. The results show that CIP-CSL3ENO has the least numerical errors.

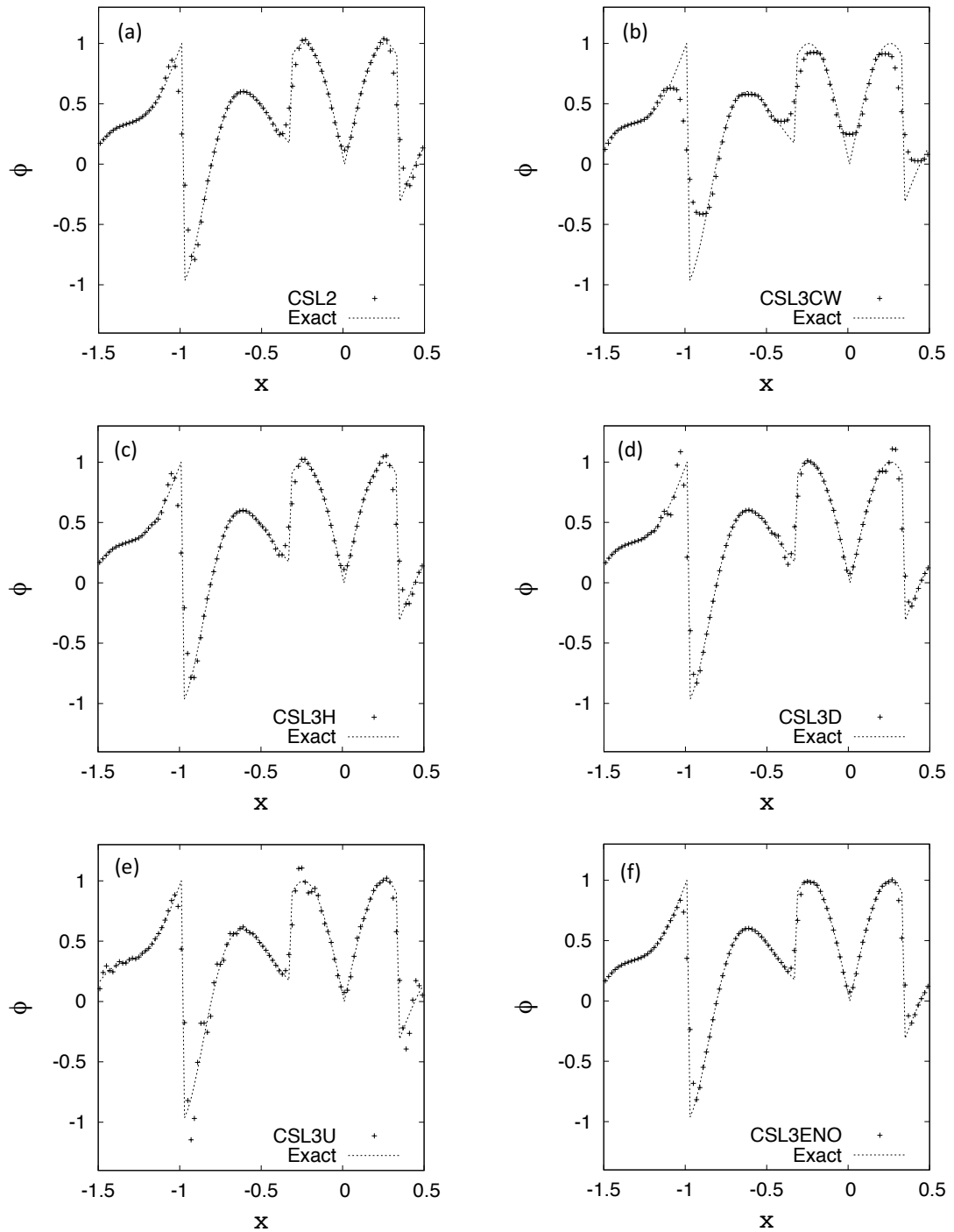


Figure 3.10: Numerical results of capturing extrema of various smoothness test at $t=8$. $N=100$ and $CFL=0.4$ are used. (a) CIP-CSL2, (b) CIP-CSL3CW, (c) CIP-CSL3H, (d) CIP-CSL3D, (e) CIP-CSL3U, (f) CIP-CSL3-ENO.

Table 3.3: Errors in capturing extrema of various smoothness test of the CIP-CSL2, CIP-CSL3CW, CIP-CSL3H, CIP-CSL3D, CIP-CSL3U, and CIP-CSL3-ENO schemes. $t=8$ (4 periods), $N=100$ and $CFL=0.4$.

	L_1 error	L_∞ error
CIP-CSL2	6.29×10^{-2}	7.85×10^{-1}
CIP-CSL3CW	1.12×10^{-1}	8.84×10^{-1}
CIP-CSL3H	6.00×10^{-2}	7.53×10^{-1}
CIP-CSL3D	5.73×10^{-2}	8.41×10^{-1}
CIP-CSL3U	6.34×10^{-2}	8.52×10^{-1}
CIP-CSL3-ENO	4.13×10^{-2}	7.24×10^{-1}

3.2.5 Burgers' equation

In this section, the proposed scheme is validated by solving the nonlinear inviscid Burgers' equation in its conservative formulation

$$\frac{\partial u}{\partial t} + \frac{\partial(u^2/2)}{\partial x} = 0, \quad (3.36)$$

In this test, the domain $[0, 1]$, $N = 200$, $CFL = 0.2$ and periodic boundary conditions are used. The initial condition $u(x, 0) = 0.5 + 0.4\cos(2\pi x)$. The reference solution is created by using CIP-CSL3CW with $N = 10,000$. Fig. 3.11 illustrates the results of the CIP-CSL2, CIP-CSL3CW, CIP-CSL3H, CIP-CSL3D, CIP-CSL3U, and CIP-CSL3-ENO schemes at $t=1$. It is observed that CIP-CSL2, CIP-CSL3H, CIP-CSL3D, and CIP-CSL3U have numerical oscillation around the discontinuities. Although both CIP-CSL3CW and CIP-CSL3-ENO have no numerical oscillation in vicinity of the discontinuities, CIP-CSL3CW is more diffusive than CIP-CSL3-ENO. Table 3.4 shows errors of the CIP-CSL3D, CIP-CSL3U, and CIP-CSL3-ENO schemes at $t=0.25$ (before the shock is fully formed). CIP-CSL3D, CIP-CSL3U, and CIP-CSL3-ENO have approximately fourth-order accuracy.

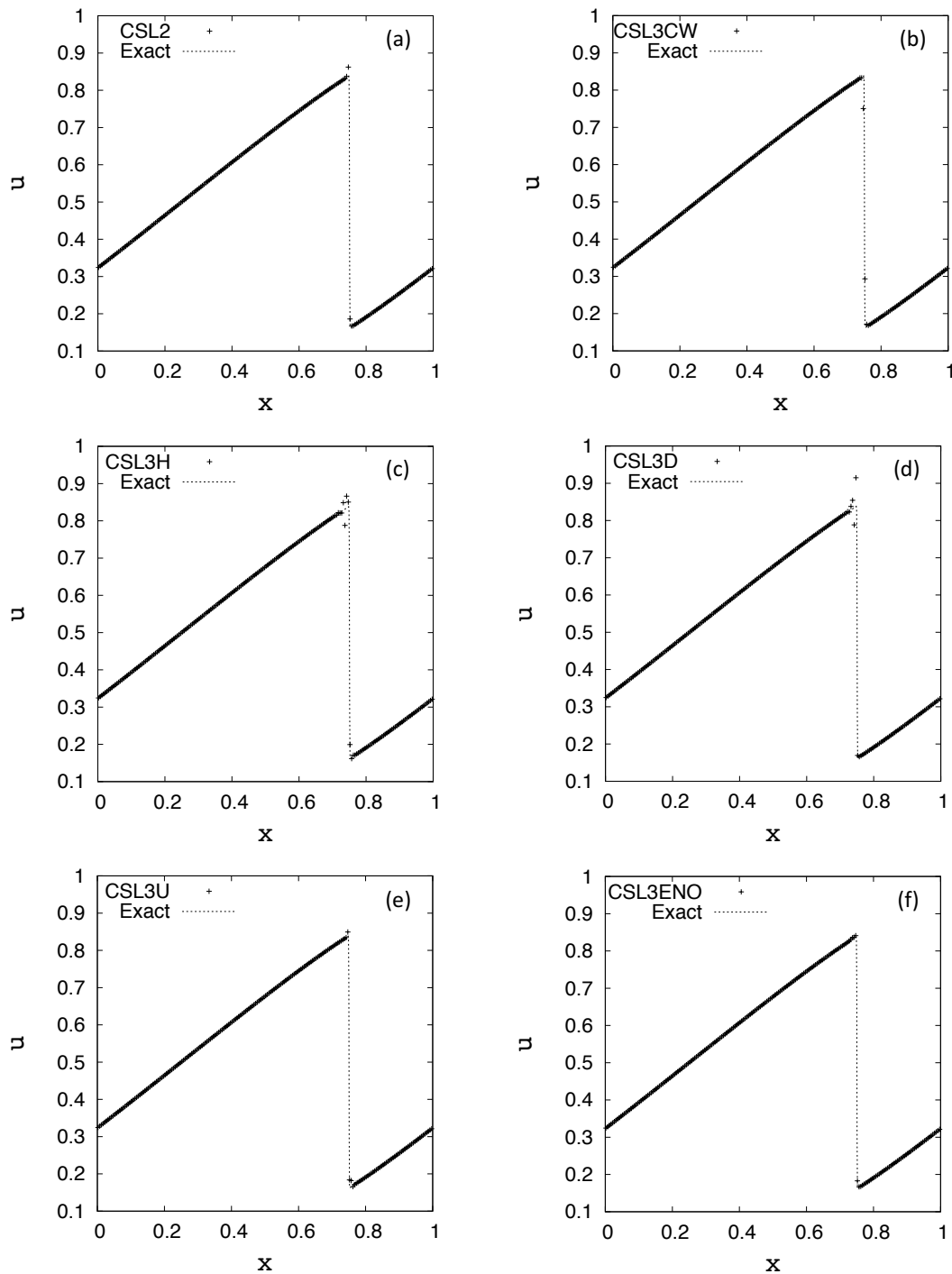


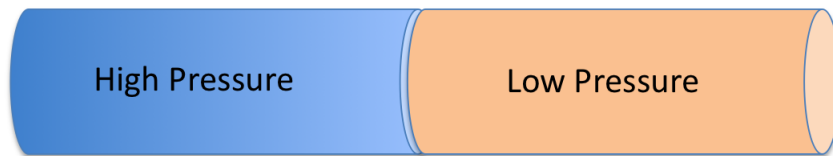
Figure 3.11: Numerical results of Burgers' equation at $t=1$. $N=200$ and $CFL=0.2$ are used. (a) CIP-CSL2, (b) CIP-CSL3CW, (c) CIP-CSL3H, (d) CIP-CSL3D, (e) CIP-CSL3U, (f) CIP-CSL3-ENO.

Table 3.4: L_1 and L_∞ errors in Burgers' equation at $t=0.25$.

Method	N	L_1 error	L_1 order	L_∞ error	L_∞ order
CIP-CSL3D	100	6.61×10^{-8}	-	3.97×10^{-7}	-
	200	4.52×10^{-9}	3.87	2.84×10^{-8}	3.81
	400	2.97×10^{-10}	3.93	2.00×10^{-9}	3.83
	800	2.32×10^{-11}	3.68	1.76×10^{-10}	3.51
CIP-CSL3U	100	3.88×10^{-8}	-	2.35×10^{-7}	-
	200	2.48×10^{-9}	3.97	1.50×10^{-8}	3.97
	400	1.59×10^{-10}	3.96	9.20×10^{-10}	4.03
	800	1.11×10^{-11}	3.84	5.74×10^{-11}	4.00
CIP-CSL3-ENO	100	5.16×10^{-8}	-	2.78×10^{-7}	-
	200	3.56×10^{-9}	3.86	2.01×10^{-8}	3.79
	400	2.32×10^{-10}	3.94	1.39×10^{-9}	3.85
	800	1.39×10^{-11}	4.06	8.08×10^{-11}	4.10

3.2.6 Sod's problem

In this section, we test the proposed schemes using Sod's problem [130], which is a one-dimensional shock tube with a thin diaphragm placed in the middle to separate a high-pressure region and a lower-pressure region as shown in Fig. 3.12.

**Figure 3.12:** Initial condition of shock tube problem

The initial condition is given as

$$\begin{aligned} \rho(x, 0) &= 1; & u(x, 0) &= 0; & p(x, 0) &= 1; & \text{if } x < 0.5 \\ \rho(x, 0) &= 0.125; & u(x, 0) &= 0; & p(x, 0) &= 0.1; & \text{otherwise,} \end{aligned} \quad (3.37)$$

where ρ is density and p is pressure. In this test, the domain $[0, 1]$, $N = 200$ and $\text{CFL} = 0.2$. Fig. 3.13 shows the numerical results of the CIP-CSL2, CIP-CSL3CW, CIP-CSL3H, CIP-CSL3D, CIP-CSL3U, and CIP-CSL3-ENO schemes at $t=0.2$. It is observed that CIP-CSL2, CIP-CSL3H, CIP-CSL3D, and CIP-CSL3U have numerical oscillations in the vicinity of the discontinuities. Although both CIP-CSL3CW and CIP-CSL3-ENO have no numerical oscillation around the discontinuities, CIP-CSL3CW is more diffusive than CIP-CSL3-ENO.

3.2.7 Lax's problem

In this section, the proposed schemes are validated using Lax's problem, which includes a discontinuity in the velocity initial condition. The initial condition is

$$\begin{aligned} \rho(x, 0) &= 0.445; & u(x, 0) &= 0.698; & p(x, 0) &= 3.528; & \text{if } x < 0 \\ \rho(x, 0) &= 0.5; & u(x, 0) &= 0; & p(x, 0) &= 0.571; & \text{otherwise,} \end{aligned} \quad (3.38)$$

In this test, the domain $[-0.5, 0.5]$, $N = 200$ and $\text{CFL} = 0.2$. Fig. 3.14 illustrates the numerical results of the CIP-CSL2, CIP-CSL3CW, CIP-CSL3H, CIP-CSL3D, CIP-CSL3U, and CIP-CSL3-ENO schemes at $t=0.12$. It is observed that CIP-CSL2, CIP-CSL3H, CIP-CSL3D, and CIP-CSL3U have significant numerical oscillations in the vicinity of the discontinuities. CIP-CSL3CW is diffusive, particularly near the contact discontinuity. CIP-CSL3-ENO captures the smooth solutions well along with a good solution around the contact discontinuity and the shock.

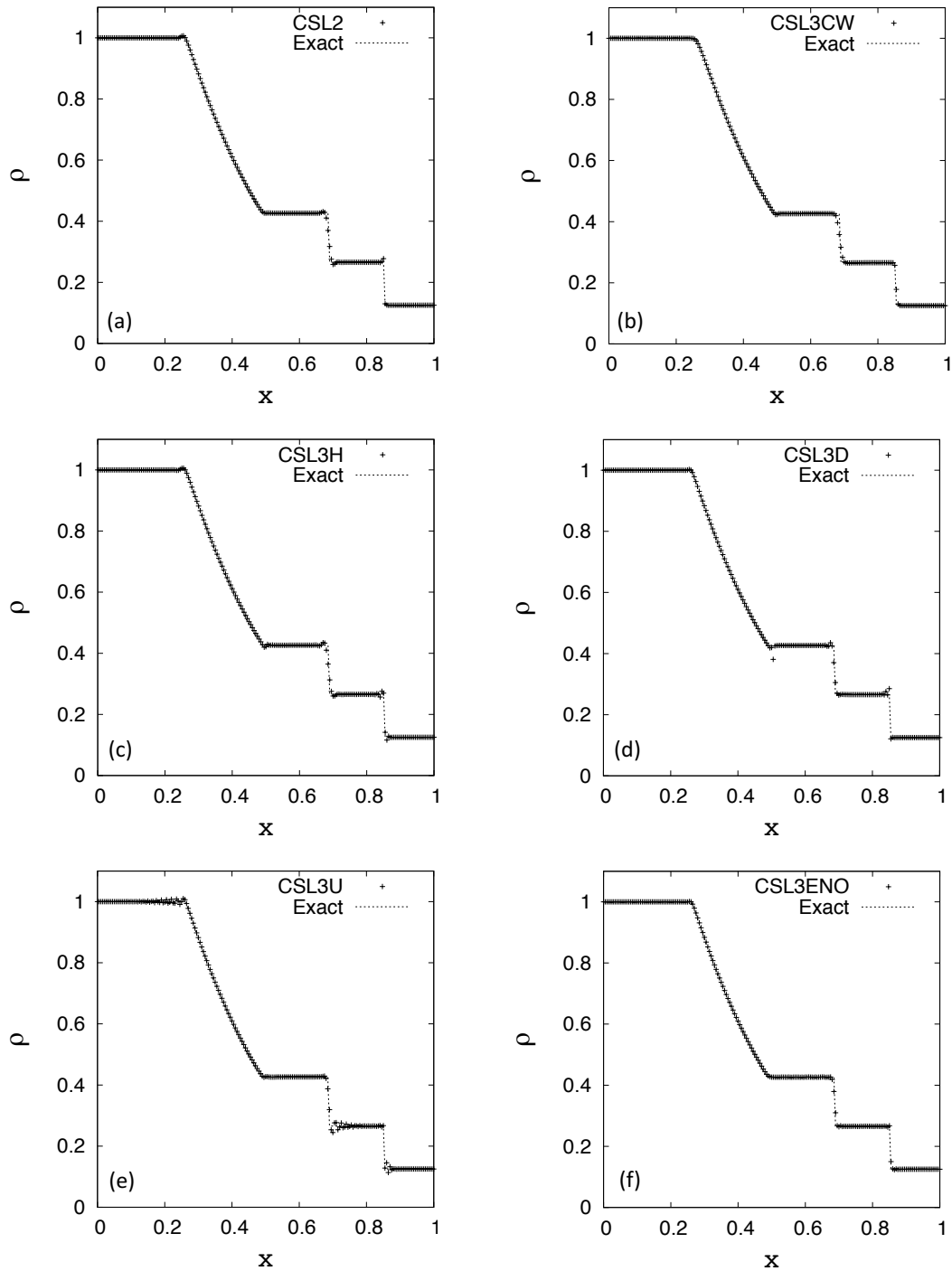


Figure 3.13: Numerical results of Sod's shock tube problem at $t = 0.2$ ($N=200$ and $CFL=0.2$). (a) CIP-CSL2, (b) CIP-CSL3CW, (c) CIP-CSL3H, (d) CIP-CSL3D, (e) CIP-CSL3U, (f) CIP-CSL3-ENO.

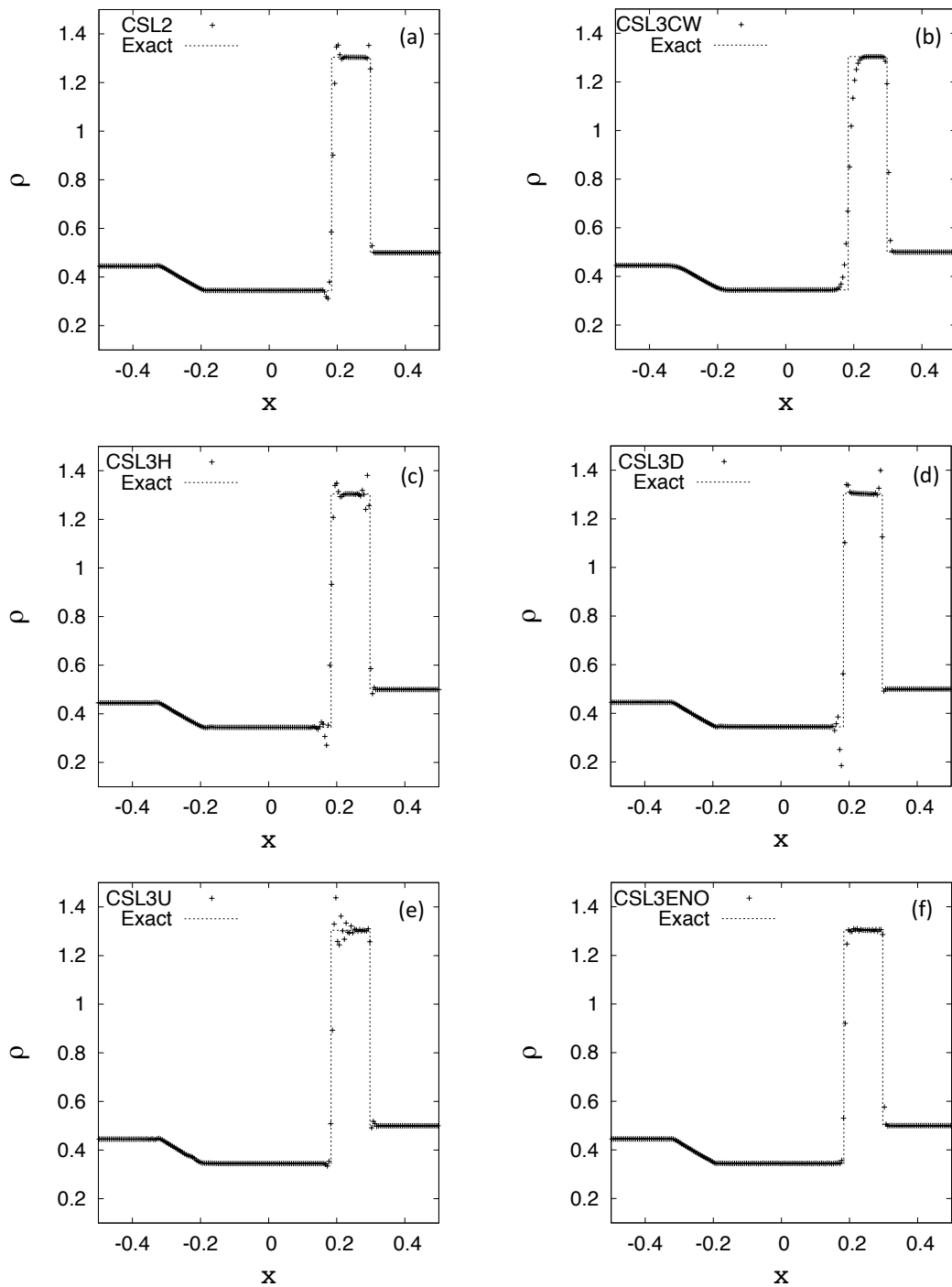


Figure 3.14: Numerical results of Lax's shock tube problem at $t=0.12$ ($N=200$ and $CFL=0.2$). (a) CIP-CSL2, (b) CIP-CSL3CW, (c) CIP-CSL3H, (d) CIP-CSL3D, (e) CIP-CSL3U, (f) CIP-CSL3-ENO.

3.2.8 Shock-turbulence interaction

We also test the proposed schemes through the shock-turbulence interaction problem [79]. Interactions between a shock wave and perturbations are simulated with the following initial condition:

$$\begin{aligned} \rho(x, 0) &= 3.857148; & u(x, 0) &= 2.629369; & p(x, 0) &= 10.333333; & 0 \leq x < 1 \\ \rho(x, 0) &= 1 + 0.2 \sin(5x - 5); & u(x, 0) &= 0; & p(x, 0) &= 1; & \text{otherwise.} \end{aligned} \quad (3.39)$$

$N = 400$ and $CFL = 0.2$ are used in this test. The reference solution is generated by using the CIP-CSL3CW scheme with $N = 10,000$. Fig. 4.12 shows the numerical results of the CIP-CSL2, CIP-CSL3CW, CIP-CSL3H, CIP-CSL3D, CIP-CSL3U, and CIP-CSL3-ENO schemes at $t=1.8$. Results show that CIP-CSL3ENO captures discontinuities as well as high- and low-frequency wave profiles well with less numerical oscillation and diffusion. CIP-CSL2, CIP-CSL3H, CIP-CSL3D, and CIP-CSL3U have numerical oscillations around the discontinuities and CIP-CSL3CW is diffusive at discontinuities and for the high-frequency wave.

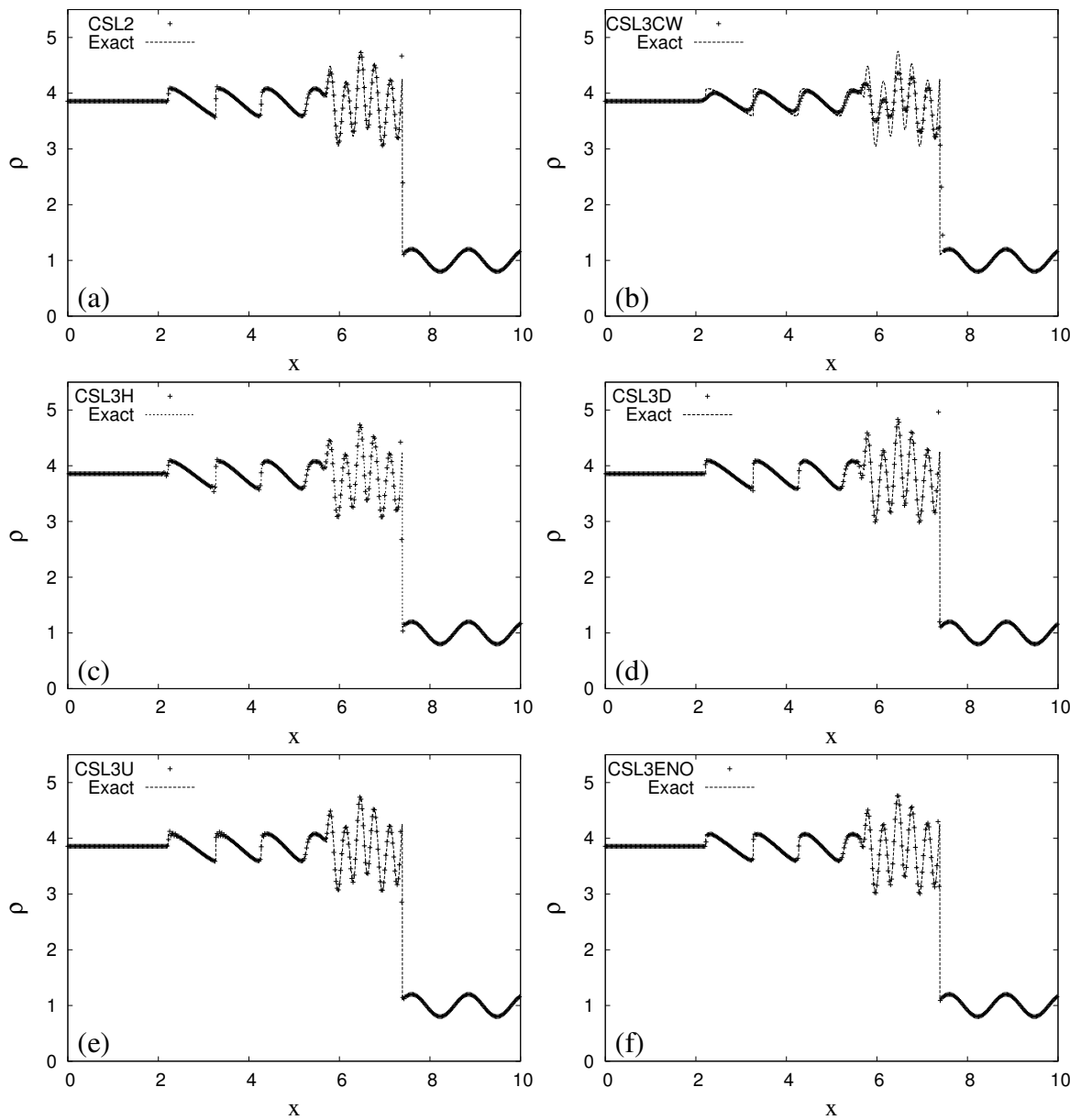


Figure 3.15: Numerical results of shock-turbulence interaction problem at $t=1.8$ (CFL=0.2 and $N=400$). (a) CIP-CSL2, (b) CIP-CSL3CW, (c) CIP-CSL3H, (d) CIP-CSL3D, (e) CIP-CSL3U, (f) CIP-CSL3-ENO.

3.3 Summary

In this chapter, the CIP-CSL3-ENO scheme was proposed based on two variants of the CIP-CSL3 scheme (CIP-CSL3D and CIP-CSL3U). An ENO indicator was designed for the CIP-CSL3ENO scheme based on the ratios of successive gradients which minimises numerical oscillations and diffusion simultaneously. Various numerical benchmark tests are studied, including linear and nonlinear scalar wave transport problems, and compressible flows problems. Results show that the CIP-CSL3-ENO scheme has approximately fourth-order accuracy for the sine wave propagation test and captures discontinuities and smooth solutions well in various test problems. The CIP-CSL3-ENO scheme minimises numerical oscillation and diffusion more efficiently than the CIP-CSL3D scheme and the CIP-CSL3U scheme individually.

Fifth-order essentially non-oscillatory hybrid CIP-CSL scheme

In chapter 3, a fourth-order CIP-CSL3-ENO scheme was proposed, and various numerical benchmark tests show the superiority of the CIP-CSL3-ENO scheme. However, when strong shocks exist, for example, two blast wave interaction problem, it was observed that the CIP-CSL3-ENO scheme cannot obtain the numerical solution. To address this problem, we propose the fifth-order CIP-CSL-ENO5 scheme in this chapter. Unlike the CIP-CSL3-ENO scheme, the CIP-CSL-ENO5 uses not only polynomial functions but also a monotone rational function, which can be used to suppress the potential oscillation for the discontinuity region. This is motivated by the observation that combining two different types (one oscillatory and one diffusive) of reconstruction functions has great potential to effectively reduce numerical diffusion and oscillations.

The CIP-CSL-ENO5 scheme is based on two cubic polynomial functions (CIP-CSL3D and CIP-CSL3U), a newly proposed quartic polynomial function (CIP-CSL4Q), and a rational function (CIP-CSLR). In the CIP-CSL-ENO5 scheme, an ENO indicator is designed based on the modified smoothness indicator in the WENO scheme. This ENO indicator can detect the smoothness and the potential discontinuity of the reconstruction stencil. The CIP-CSL-ENO5 scheme can accurately capture both smooth and discontinuous solutions simultaneously by selecting an appropriate reconstruction function.

4.1 Numerical method

Firstly, the newly proposed CIP-CSL4Q scheme is explained. Subsequently, we present the CIP-CSL-ENO5 scheme, which is based on the CIP-CSL3D (Sec. 3.1.1), CIP-CSL3U (Sec. 3.1.2), CIP-CSLR (Sec. 2.4.3), and CIP-CSL4Q schemes.

4.1.1 CIP-CSL4Q scheme

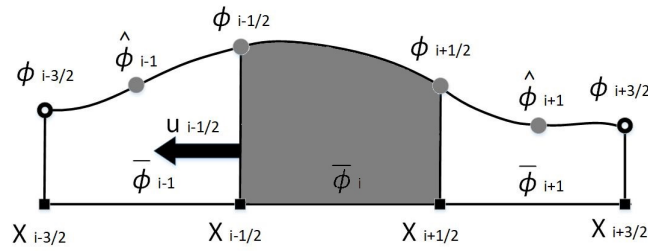


Figure 4.1: Schematic figure of the CIP-CSL4Q scheme. $u_{i-1/2} < 0$ is assumed. The moments which are indicated by grey colour are used as constraints to construct the interpolation function $\Phi_i^{CSL4Q}(x)$.

The CIP-CSL4Q scheme is based on the following fourth-order quartic polynomial interpolation function

$$\begin{aligned} \Phi_i^{CSL4Q}(x) = & C_{4,i}^{CSL4Q}(x - x_{i-1/2})^4 + C_{3,i}^{CSL4Q}(x - x_{i-1/2})^3 \\ & + C_{2,i}^{CSL4Q}(x - x_{i-1/2})^2 + C_{1,i}^{CSL4Q}(x - x_{i-1/2}) + C_{0,i}^{CSL4Q}. \end{aligned} \quad (4.1)$$

The interpolation function $\Phi_i^{CSL4Q}(x)$ is constructed using the following five constraints ($\phi_{i-1/2}$, $\bar{\phi}_i$, $\phi_{i+1/2}$, $\hat{\phi}_{i-1}$, and $\hat{\phi}_{i+1}$) which are indicated in Fig. 4.1

$$\left\{ \begin{array}{l} \phi_{i-1/2} = \Phi_i^{CSL4Q}(x_{i-1/2}), \\ \bar{\phi}_i = \frac{\int_{x_{i-1/2}}^{x_{i+1/2}} \Phi_i^{CSL4Q}(x) dx}{\Delta x}, \\ \phi_{i+1/2} = \Phi_i^{CSL4Q}(x_{i+1/2}), \\ \hat{\phi}_{i-1} = \Phi_i^{CSL4Q}(x_{i-1}), \\ \hat{\phi}_{i+1} = \Phi_i^{CSL4Q}(x_{i+1}). \end{array} \right. \quad (4.2)$$

By using the constraints in Eq. (4.2), the coefficients ($C_{0,i}^{CSLAQ}, C_{1,i}^{CSLAQ}, C_{2,i}^{CSLAQ}, C_{3,i}^{CSLAQ}$, and $C_{4,i}^{CSLAQ}$) in Eq. (4.1) are obtained as follows

$$C_{0,i}^{CSLAQ} = \phi_{i-1/2}, \quad (4.3)$$

$$C_{1,i}^{CSLAQ} = \frac{1}{42\Delta x}(-79\phi_{i-1/2} - 107\phi_{i+1/2} + 198\bar{\phi}_i - 20\hat{\phi}_{i-1} + 8\hat{\phi}_{i+1}), \quad (4.4)$$

$$C_{2,i}^{CSLAQ} = \frac{1}{7\Delta x^2}(-26\phi_{i-1/2} + 2\phi_{i+1/2} + 12\bar{\phi}_i + 13\hat{\phi}_{i-1} - \hat{\phi}_{i+1}), \quad (4.5)$$

$$C_{3,i}^{CSLAQ} = \frac{1}{21\Delta x^3}(193\phi_{i-1/2} + 137\phi_{i+1/2} - 270\bar{\phi}_i - 44\hat{\phi}_{i-1} - 16\hat{\phi}_{i+1}), \quad (4.6)$$

$$C_{4,i}^{CSLAQ} = \frac{5}{28\Delta x^4}(-22\phi_{i-1/2} - 22\phi_{i+1/2} + 36\bar{\phi}_i + 4\hat{\phi}_{i-1} + 4\hat{\phi}_{i+1}). \quad (4.7)$$

4.1.2 CIP-CSL-ENO5 scheme

Based on the CIP-CSL3D, CIP-CSL3U, CIP-CSLR, CIP-CSL4Q, we propose the CIP-CSL-ENO5 scheme. Reconstruction stencils of the CIP-CSL-ENO5 scheme can be explained using Fig. 4.2. The stencils $S_3^0, S_3^1, S_3^2, S_4^1, S_4^2$, and S_5 are defined as

$$\left\{ \begin{array}{l} S_3^0 = [x_{i-1/2}, x_i, x_{i+1/2}], \\ S_3^1 = [x_{i-1}, x_{i-1/2}, x_i], \\ S_3^2 = [x_i, x_{i+1/2}, x_{i+1}], \\ S_4^1 = [x_{i-1}, x_{i-1/2}, x_i, x_{i+1/2}], \\ S_4^2 = [x_{i-1/2}, x_i, x_{i+1/2}, x_{i+1}], \\ S_5 = [x_{i-1}, x_{i-1/2}, x_i, x_{i+1/2}, x_{i+1}]. \end{array} \right. \quad (4.8)$$

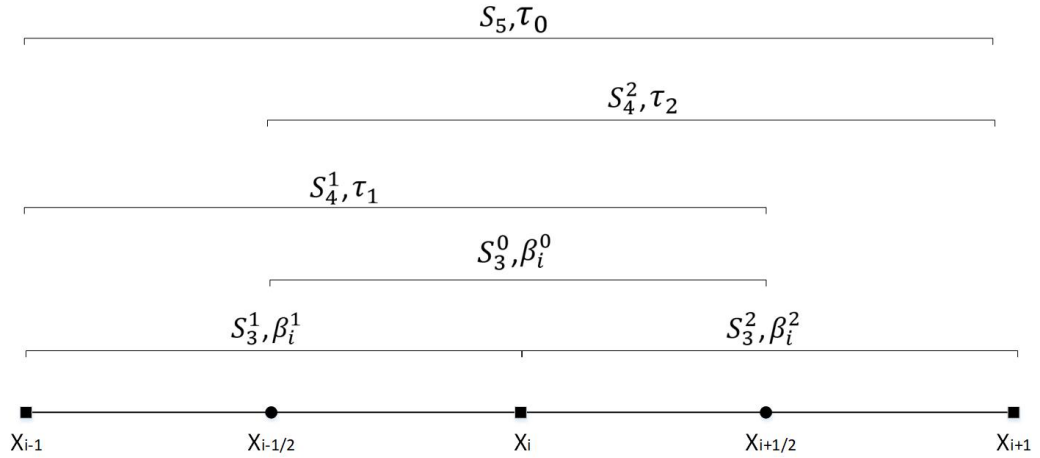


Figure 4.2: Sketch of the reconstruction stencils of the CIP-CSL-ENO5 scheme.

In the CIP-CSL-ENO5 scheme, the reconstruction selection criterion is proposed based on the smoothness indicators $\beta_i^{\hat{j}}$ ($\hat{j} = 0, 1, 2$) in Eq. (2.56) and τ_0 in Eq. (2.22). $\tau_0 = |\beta_i^2 - \beta_i^1|$ is indeed calculated using the stencil S_5 ($S_3^0 \cup S_3^1 \cup S_3^2$) (shown in Fig. 4.2). Firstly, we list the two relationships between τ_0 and $\beta_i^{\hat{j}}$ introduced by Borges et al. [32] as follows:

1. If the stencil S_5 does not contain discontinuities, then $\tau_0 \ll \beta_i^{\hat{j}}$ for $\hat{j} = 0, 1, 2$ [32]. This is because that on smooth parts of the solution, the smoothness indicators $\beta_i^{\hat{j}}$ are all small and about the same size. Therefore, $\tau_0 = |\beta_i^2 - \beta_i^1| \ll \beta_i^{\hat{j}}$.
2. If the solution is continuous at some stencils $S_3^{\hat{j}}$, but discontinuous in the stencil S_5 , then $\beta_i^{\hat{j}} \ll \tau_0$, for those \hat{j} where the solution is continuous [32]. For example, if the solution is continuous at the stencils S_3^0 and S_3^1 (β_i^0 and β_i^1 are small and about the same size), but discontinuous in the whole stencil S_5 , which means the discontinuity exists in the stencil S_3^2 (β_i^2 is relatively bigger than β_i^0 and β_i^1). Then $\beta_i^2 \gg \beta_i^0$ and $\beta_i^2 \gg \beta_i^1$. Therefore, $\tau_0 = |\beta_i^2 - \beta_i^1| \gg \beta_i^0$ and $\tau_0 = |\beta_i^2 - \beta_i^1| \gg \beta_i^1$.

Based on the above two listed relationships between τ_0 and $\beta_i^{\hat{j}}$, we design the indicators to check if the stencil S_5 contains discontinuities as follows:

- If the stencil S_5 does not contain discontinuities, the indicator is designed as

$$\tau_0 \leq \min(\beta_i^0, \beta_i^1, \beta_i^2). \quad (4.9)$$

This is due to the reason that if the stencil S_5 contains discontinuities, as mentioned above (the second relationship between τ_0 and $\beta_i^{\hat{j}}$), we have $\beta_i^{\hat{j}} \ll \tau_0$, for those \hat{j} where the solution is continuous. Thus $\tau_0 > \min(\beta_i^0, \beta_i^1, \beta_i^2)$, which is not consistent with $\tau_0 \leq \min(\beta_i^0, \beta_i^1, \beta_i^2)$. Therefore, when $\tau_0 \leq \min(\beta_i^0, \beta_i^1, \beta_i^2)$ is satisfied, the stencil S_5 does not contain discontinuities.

- If the stencil S_5 contains discontinuities, the indicator is designed as

$$\tau_0 > \min(\beta_i^0, \beta_i^1, \beta_i^2). \quad (4.10)$$

This is due to the reason that if S_5 does not contain discontinuities, as mentioned above (the first relationship between τ_0 and $\beta_i^{\hat{j}}$), we have $\tau_0 \ll \beta_i^{\hat{j}}$ for $\hat{j} = 0, 1, 2$. Thus $\tau_0 < \min(\beta_i^0, \beta_i^1, \beta_i^2)$, which is not consistent with $\tau_0 > \min(\beta_i^0, \beta_i^1, \beta_i^2)$. Therefore, when $\tau_0 > \min(\beta_i^0, \beta_i^1, \beta_i^2)$ is satisfied, the stencil S_5 contains discontinuities.

Based on $\tau_0 = |\beta_i^2 - \beta_i^1|$, we define τ_1 and τ_2 [131] as

$$\begin{cases} \tau_1 = |\beta_i^0 - \beta_i^1|, \\ \tau_2 = |\beta_i^0 - \beta_i^2|. \end{cases} \quad (4.11)$$

τ_1 and τ_2 are calculated using the stencils $S_4^1 (S_3^0 \cup S_3^1)$ and $S_4^2 (S_3^0 \cup S_3^2)$, respectively (shown in Fig. 4.2). Analogously, we can design the indicators to check if the stencils S_4^1 and S_4^2 contain discontinuities by using τ_1 , τ_2 , and $\beta_i^{\hat{j}}$ as follows:

- If the stencil S_4^1 does not contain discontinuities, the indicator is designed as

$$\tau_1 \leq \min(\beta_i^0, \beta_i^1). \quad (4.12)$$

- If the stencil S_4^1 contains discontinuities, the indicator is designed as

$$\tau_1 > \min(\beta_i^0, \beta_i^1). \quad (4.13)$$

- If the stencil S_4^2 does not contain discontinuities, the indicator is designed as

$$\tau_2 \leq \min(\beta_i^0, \beta_i^2). \quad (4.14)$$

- If the stencil S_4^2 contains discontinuities, the indicator is designed as

$$\tau_2 > \min(\beta_i^0, \beta_i^2). \quad (4.15)$$

Based on the indicators Eqs. (4.9), (4.12), (4.13), (4.14), and (4.15), the selection criteria of the CIP-CSL-ENO5 scheme are devised as follows:

Selection criteria:

- Case 1. If the entire reconstruction stencil S_5 does not contain discontinuities, the CSL4Q reconstruction is selected as shown in Fig. 4.3. In this case, Eq. (4.9) is used to indicate the stencil S_5 does not contain discontinuities.

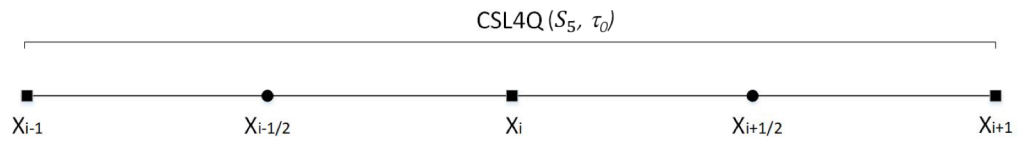


Figure 4.3: Reconstruction stencils for the CIP-CSL-ENO5 scheme. The entire reconstruction stencil is continuous, CSL4Q is used as the reconstruction scheme.

- Case 2. If the discontinuity exists in the region of downwind-side between x_{i-1} and $x_{i-1/2}$ as shown in Fig. 4.4, the CSL3U reconstruction is selected to eliminate the numerical oscillation.

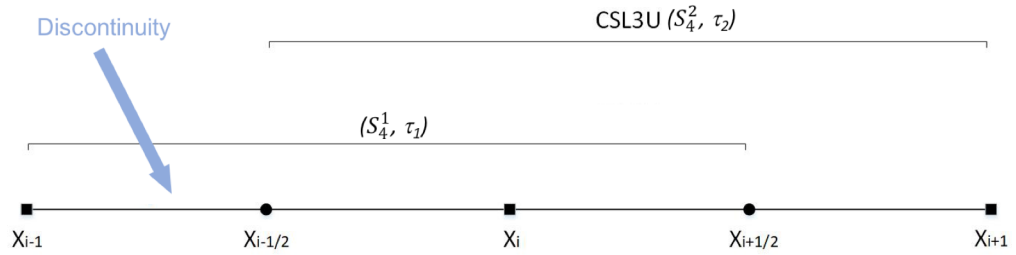


Figure 4.4: Reconstruction stencils for the CIP-CSL-ENO5 scheme. The discontinuity exists in the region of downwind-side between x_{i-1} and $x_{i-1/2}$, CSL3U is used as the reconstruction scheme.

In this case, the solution is continuous on stencil S_4^2 , but discontinuous on stencil S_4^1 . The indicator is designed by using Eq. (4.13) and Eq. (4.14).

- Case 3. Analogously, if the discontinuity appears in the upwind-side region between $x_{i+1/2}$ and x_{i+1} as shown in Fig. 4.5, the CSL3D reconstruction is selected to eliminate the numerical oscillation. In this case, the solution is continuous on stencil S_4^1 , but discontinuous on stencil S_4^2 . The indicator is designed by using Eq. (4.12) and Eq. (4.15).

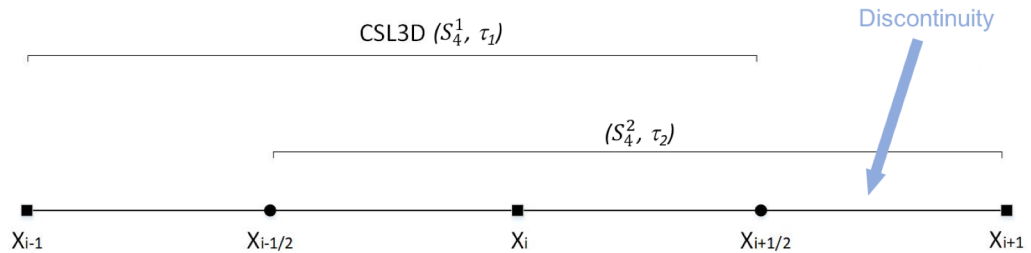


Figure 4.5: Reconstruction stencils for the CIP-CSL-ENO5 scheme. The discontinuity exists in the region of upwind-side between $x_{i+1/2}$ and x_{i+1} , CSL3D is used as the reconstruction scheme.

- Case 4. In addition, the discontinuity may appear in the region between $x_{i-1/2}$ and $x_{i+1/2}$ as shown in Fig. 4.6. In this case, we select the monotone and non-oscillatory CSLR scheme, which can suppress the potential numerical oscillation

for the discontinuity region.

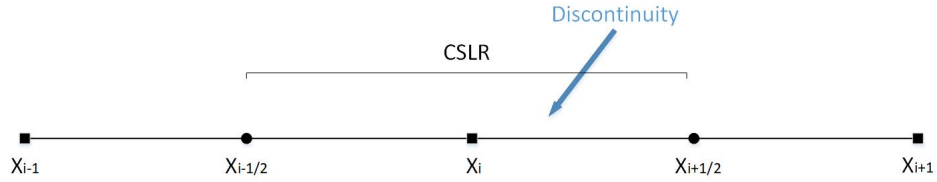


Figure 4.6: Reconstruction stencils for the CIP-CSL-ENO5 scheme. The discontinuity may appear in the region between $x_{i-1/2}$ and $x_{i+1/2}$, CSLR is used as the reconstruction scheme.

The reconstruction criterion of the CIP-CSL-ENO5 scheme can be summarised as follows

$$\Phi_i^{CSL-ENO5}(x) = \begin{cases} \Phi_i^{CSL4Q}(x), & \tau_0 \leq \min(\beta_i^0, \beta_i^1, \beta_i^2), \\ \Phi_i^{CSL3D}(x), & \tau_1 > \min(\beta_i^0, \beta_i^1) \text{ and } \tau_2 \leq \min(\beta_i^0, \beta_i^2), \\ \Phi_i^{CSL3U}(x), & \tau_1 \leq \min(\beta_i^0, \beta_i^1) \text{ and } \tau_2 > \min(\beta_i^0, \beta_i^2), \\ \Phi_i^{CSLR}(x). & \text{otherwise} \end{cases} \quad (4.16)$$

By using the interpolation function $\Phi_i^{CSL-ENO5}(x)$, the cell average $\bar{\phi}_i$ and boundary value $\phi_{i-1/2}$ are updated by a third-order TVD Runge-Kutta formulation [46] as explained in Sec. 2.4.1.

4.2 Numerical results

We validate the proposed methods through various benchmark tests and compare the results with those of the CIP-CSLR and CIP-CSL3-ENO schemes.

4.2.1 Sine wave propagation

In this test, we solve the conservation equation Eq.(2.13) with the same initial conditions, as described in Sec.3.2.1. The computation domain is $[0, 1]$, $u(x) = 1$ and the

periodic boundary conditions are used. Four different grid sizes ($N = 20, 40, 80, 160,$ and 320) are used with $\Delta t = 0.1\Delta x$ and $\Delta x = 1/N$.

Table 4.1: L_1 and L_∞ errors in sine wave propagation at $t=1$.

Method	N	L_1 error	L_1 order	L_∞ error	L_∞ order
CIP-CSLR	20	1.53×10^{-2}	-	4.11×10^{-2}	-
	40	3.63×10^{-3}	2.08	1.68×10^{-2}	1.30
	80	8.80×10^{-4}	2.04	6.58×10^{-3}	1.35
	160	1.94×10^{-4}	2.18	2.51×10^{-3}	1.39
	320	4.35×10^{-5}	2.16	9.41×10^{-4}	1.42
CIP-CSL4Q	20	6.08×10^{-6}	-	9.55×10^{-6}	-
	40	1.93×10^{-7}	4.98	3.04×10^{-7}	4.97
	80	6.08×10^{-9}	4.99	9.54×10^{-9}	4.98
	160	1.90×10^{-10}	5.00	2.99×10^{-10}	5.00
	320	5.95×10^{-12}	5.00	9.34×10^{-12}	5.00
CIP-CSL-ENO5	20	6.08×10^{-6}	-	9.55×10^{-6}	-
	40	1.93×10^{-7}	4.98	3.04×10^{-7}	4.97
	80	6.08×10^{-9}	4.99	9.54×10^{-9}	4.98
	160	1.90×10^{-10}	5.00	2.99×10^{-10}	5.00
	320	5.95×10^{-12}	5.00	9.34×10^{-12}	5.00

Table 4.1 presents the numerical results of the CIP-CSLR, CIP-CSL4Q and CIP-CSL-ENO5 schemes. It is evident that CIP-CSLR has about second-order accuracy for L_1 and less than second-order accuracy for L_∞ . Both CIP-CSL4Q and CIP-CSL-ENO5 have fifth-order accuracy for L_1 and L_∞ , respectively. This indicates that the CIP-CSL-ENO5 scheme automatically selects the highest possible polynomial interpolation for the smooth solution.

4.2.2 Complex wave propagation

In this test, the Jiang-Shu complex wave propagation problem [1] is investigated. The initial conditions are the same as those in Sec. 3.2.3.

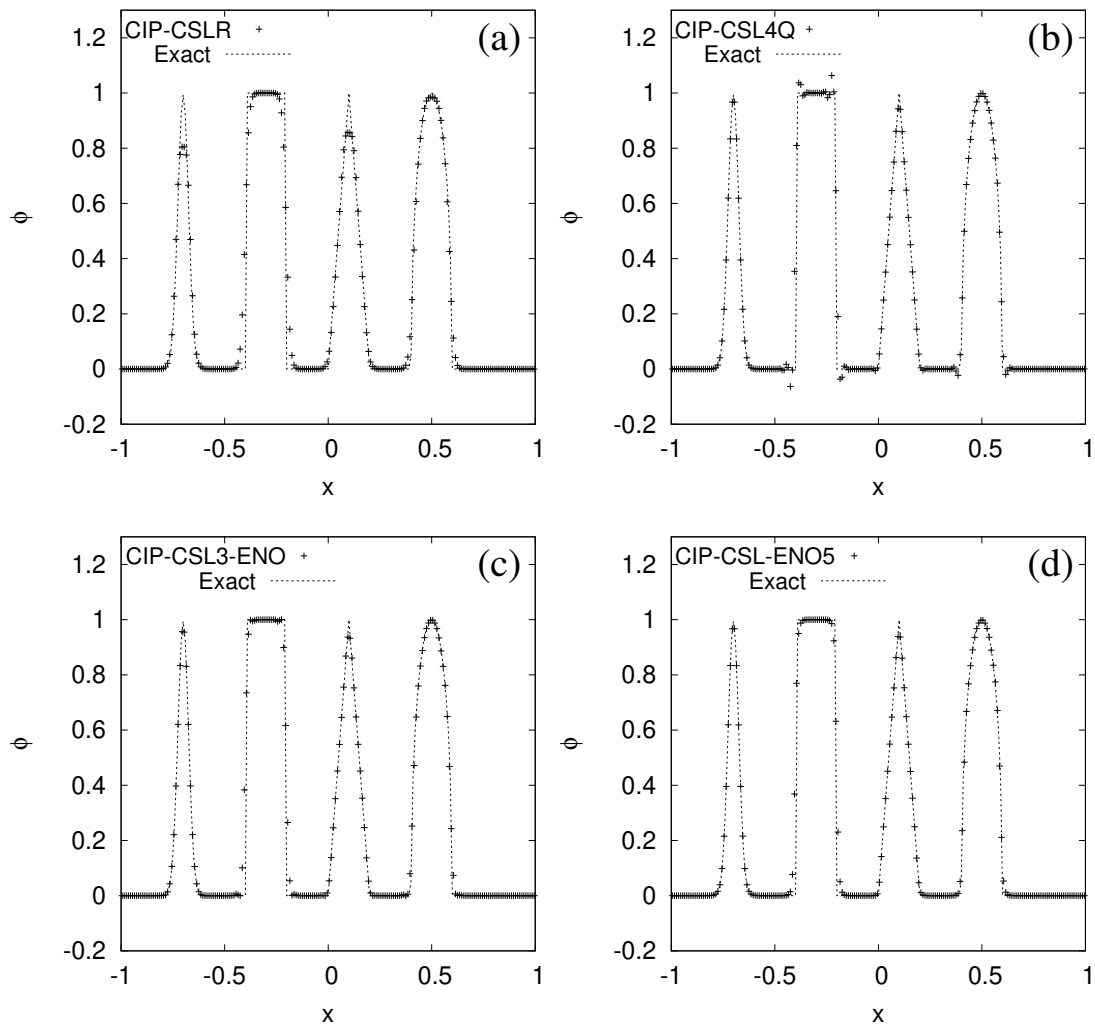


Figure 4.7: Numerical results of complex wave propagation test at time $t=2$ (1 period). $N=200$ and $CFL=0.4$ are used. (a) CIP-CSLR, (b) CIP-CSL4Q, (c) CIP-CSL3-ENO, (d) CIP-CSL-ENO5.

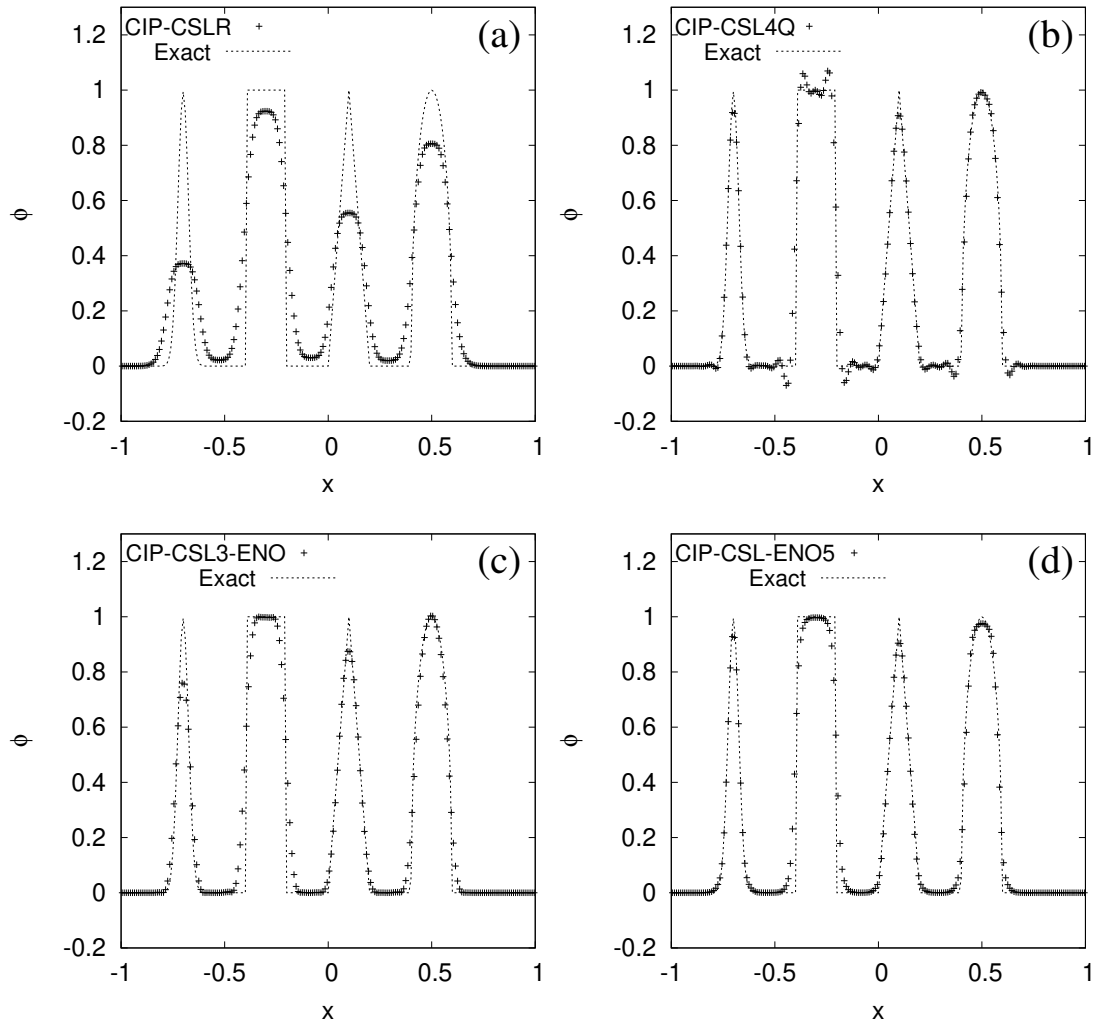


Figure 4.8: Numerical results of complex wave propagation test at time $t=100$ (50 periods). $N=200$ and $CFL=0.4$ are used. (a) CIP-CSLR, (b) CIP-CSL4Q, (c) CIP-CSL3-ENO, (d) CIP-CSL-ENO5.

Fig. 4.7 illustrates the results of the CIP-CSLR, CIP-CSL4Q, CIP-CSL3-ENO, and CIP-CSL-ENO5 schemes at time $t=2$ (1 period). It is observed that CIP-CSL4Q captures smooth profiles well; however, it has significant oscillations around the discontinuities. Although CIP-CSLR has no numerical oscillation around discontinuities, it is diffusive in both smooth profiles and discontinuities. Both CIP-CSL3-ENO and CIP-CSL-ENO5 accurately capture smooth profiles and discontinuities simultaneously

with minimised numerical oscillations and diffusion. Fig. 4.8 illustrates the results the CIP-CSLR, CIP-CSL4Q, CIP-CSL3-ENO, and CIP-CSL-ENO5 schemes at time $t=100$ (50 periods). It is observed that CIP-CSLR has obvious numerical diffusion, while CIP-CSL4Q has significant numerical oscillations. Both CIP-CSL3-ENO and CIP-CSL-ENO5 capture the complex waves well. CIP-CSL3-ENO obtains sharper solutions around $x = 0.5$ and CIP-CSL-ENO5 captures sharper solutions for the cusps around $x = -0.7$ and $x = 0.1$. Table 4.2 shows L_1 and L_∞ errors the CIP-CSLR, CIP-CSL4Q, CIP-CSL3-ENO, and CIP-CSL-ENO5 schemes at time $t=2$ and $t=100$, respectively. The results indicate that CIP-CSL-ENO5 is superior to CIP-CSLR and CIP-CSL3-ENO. Although CIP-CSL4Q has the least numerical errors, it has significant numerical oscillation.

Table 4.2: L_1 and L_∞ errors in complex wave propagation test at $t=2$ (1 period) and at $t=100$ (50 periods). $N=200$ and $CFL=0.4$ are used.

	t=2		t=100	
	L_1 error	L_∞ error	L_1 error	L_∞ error
CIP-CSLR	2.24×10^{-2}	3.33×10^{-1}	1.03×10^{-1}	5.97×10^{-1}
CIP-CSL4Q	7.55×10^{-3}	1.93×10^{-1}	2.25×10^{-2}	3.29×10^{-1}
CIP-CSL3-ENO	9.39×10^{-3}	2.65×10^{-1}	3.56×10^{-2}	3.97×10^{-1}
CIP-CSL-ENO5	8.44×10^{-3}	2.31×10^{-1}	2.45×10^{-2}	3.51×10^{-1}

In addition, we compare numerical results by the CIP-CSL-ENO5 scheme with numerical results by a standard WENO scheme (WENO-Roe5) [1], the fifth-order multi-moment WENO scheme [132], and the MCV-WENO scheme [133]. Fig. 4.9 illustrates a comparison of numerical results by the WENO-Roe5 and CIP-CSL-ENO5 schemes in complex wave propagation test at $t=8$. The CIP-CSL-ENO5 scheme is less diffusive than the WENO-Roe5 scheme. Fig. 4.10 shows a comparison of numerical results by the multi-moment WENO scheme [132], the MCV-WENO scheme [133], and the

CIP-CSL-ENO5 scheme, in the complex wave propagation test at $t=2$. The result reveals that the CIP-CSL-ENO5 scheme is less diffusive than the multi-moment WENO scheme and the MCV-WENO scheme.

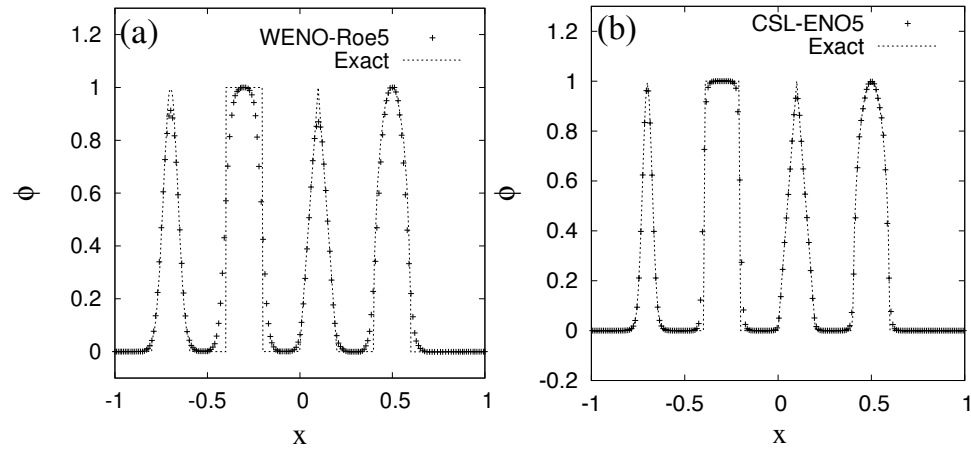


Figure 4.9: A comparison of numerical results by the WENO-Roe5 scheme [1] and the CIP-CSL-ENO5 scheme in complex wave propagation test at $t=8$ (4 periods: 2,000 time steps). $N=200$ and $CFL=0.4$ are used.

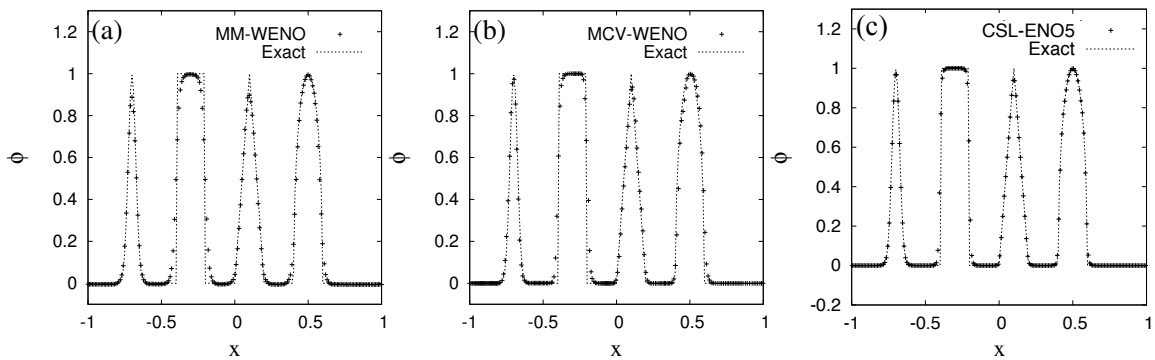


Figure 4.10: A comparison of numerical results by the multi-moment WENO scheme, the MCV-WENO scheme, and the CIP-CSL-ENO5 scheme in complex wave propagation test at $t=2$ (1 period: 500 time steps). $N=200$ and $CFL=0.4$ are used.

4.2.3 Lax's problem

In this section, the numerical test of Lax's problem with strong shock and contact discontinuity is conducted. The initial condition is

$$\begin{aligned} \rho(x, 0) &= 0.445; & u(x, 0) &= 0.698; & p(x, 0) &= 3.528; & \text{if } x < 0.5 \\ \rho(x, 0) &= 0.5; & u(x, 0) &= 0; & p(x, 0) &= 0.571; & \text{otherwise,} \end{aligned} \quad (4.17)$$

In this test, the domain $[0, 1.0]$, $N = 200$ and $\text{CFL} = 0.2$. Fig. 4.11 illustrates the numerical result of the CIP-CSLR, CIP-CSL4Q, CIP-CSL3-ENO, and CIP-CSL-ENO5 schemes at time $t=0.12$.

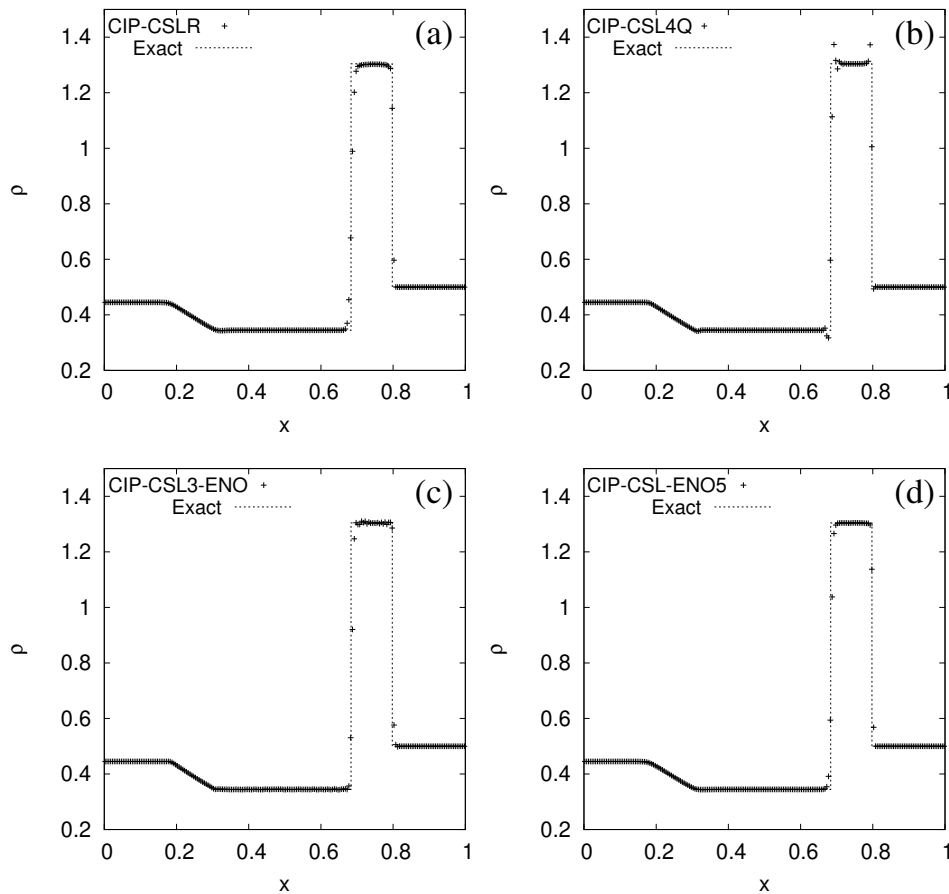


Figure 4.11: Numerical results of Lax's shock tube problem at $t=0.12$. $N=200$ and $\text{CFL}=0.2$ are used. (a) CIP-CSLR, (b) CIP-CSL4Q, (c) CIP-CSL3-ENO, (d) CIP-CSL-ENO5.

It is observed that CIP-CSL4Q has numerical oscillations and CIP-CSLR is diffusive at discontinuities (particularly the contact discontinuity). Both CIP-CSL3-ENO and CIP-CSL-ENO5 minimise numerical oscillations and numerical diffusion in vicinity of discontinuities.

4.2.4 Shock turbulence problem

In this section, the numerical test of a shock-turbulence problem [79] is conducted.

The initial condition is

$$\begin{aligned} \rho(x, 0) &= 3.857148; & u(x, 0) &= 2.629369; & p(x, 0) &= 10.333333; & 0 \leq x < 0.1 \\ \rho(x, 0) &= 1 + 0.2 \sin(5x - 5); & u(x, 0) &= 0; & p(x, 0) &= 1; & \text{otherwise.} \end{aligned} \quad (4.18)$$

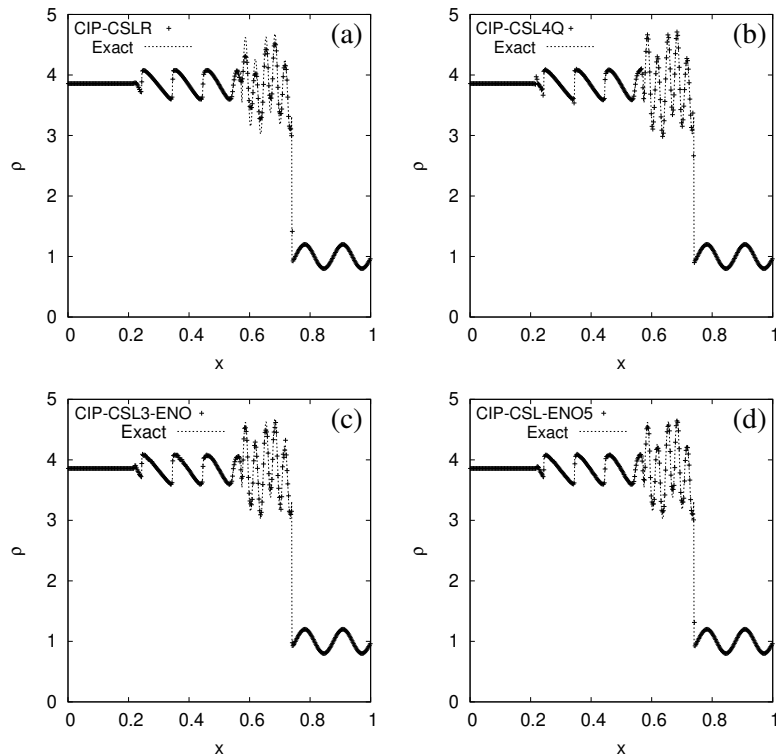


Figure 4.12: Numerical results of shock-turbulence interaction problem at time $t=0.18$. $N=400$ and $CFL=0.2$ are used. (a) CIP-CSLR, (b) CIP-CSL4Q, (c) CIP-CSL3-ENO, (d) CIP-CSL-ENO5.

In this test, $N = 400$ and $CFL = 0.2$. Fig. 4.12 shows the numerical results of the CIP-CSLR, CIP-CSL4Q, CIP-CSL3-ENO, and CIP-CSL-ENO5 schemes at $t=0.18$. Fig. 4.13 shows the zoomed-in view of Fig. 4.12. It is evident that CIP-CSL4Q has numerical oscillations around the discontinuities, and CIP-CSLR is diffusive for capturing discontinuities and high-frequency waves. CIP-CSL3-ENO captures discontinuities and low-frequency wave profiles well. However, CIP-CSL3-ENO has small numerical oscillation for high-frequency wave profiles as shown in Fig. 4.13. CIP-CSL-ENO5 captures discontinuities, high-frequency and low-frequency wave profiles well without numerical oscillations.

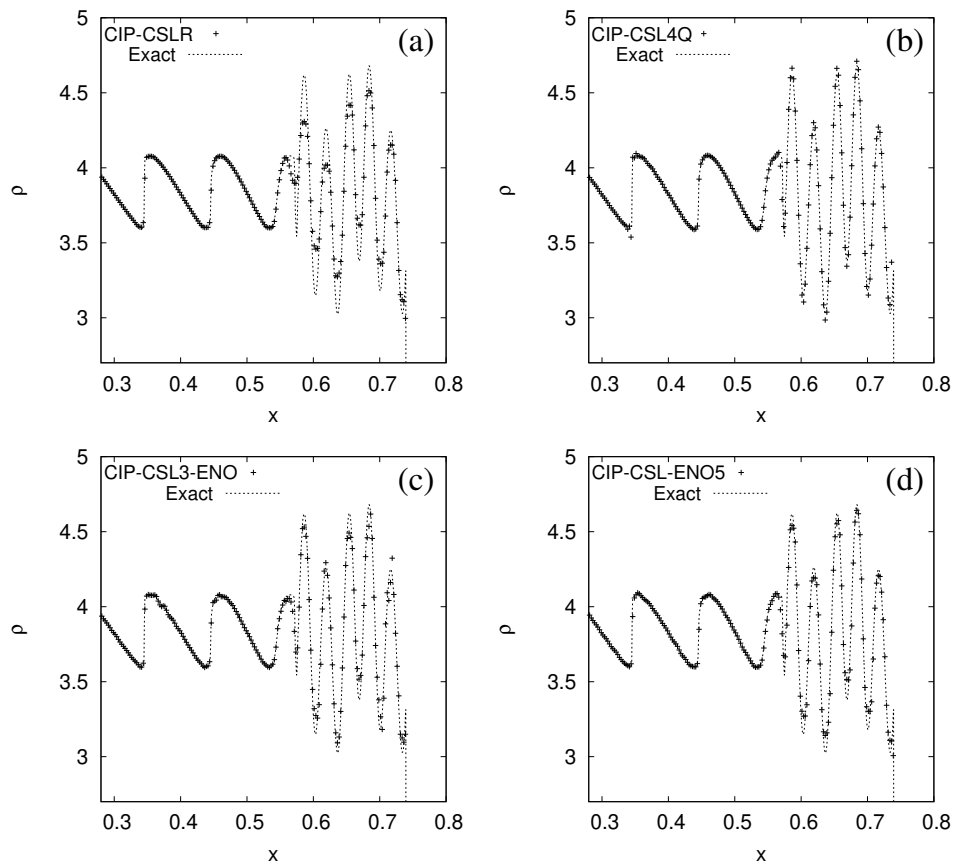


Figure 4.13: Zoomed-in view of Fig. 4.12

4.2.5 Two blast waves interaction problem

In this section, the CIP-CSL-ENO5 scheme is validated through a simulation of two interacting blast waves [134] with the following initial condition

$$(\rho_0, u_0, p_0) = \begin{cases} (1, 0, 1000) & \text{for } 0 \leq x < 0.1 \\ (1, 0, 0.01) & \text{for } 0.1 \leq x \leq 0.9 \\ (1, 0, 100) & \text{otherwise,} \end{cases} \quad (4.19)$$

The numerical mesh size $N = 400$, $CFL = 0.2$ and the reflecting boundary condition is used. In this test, two blast waves are formed by the initial jumps. Expansion fans, contact discontinuities, and strong shocks are generated and interacted with each other. Due to the violent interactions of shocks, the existence of numerical oscillation will cause the breakup of the simulation. CIP-CSL4Q and CIP-CSL3-ENO could not obtain the solution. The numerical results of CIP-CSLR and CIP-CSL-ENO5 at time $t = 0.038$ are shown in Fig. 4.14.

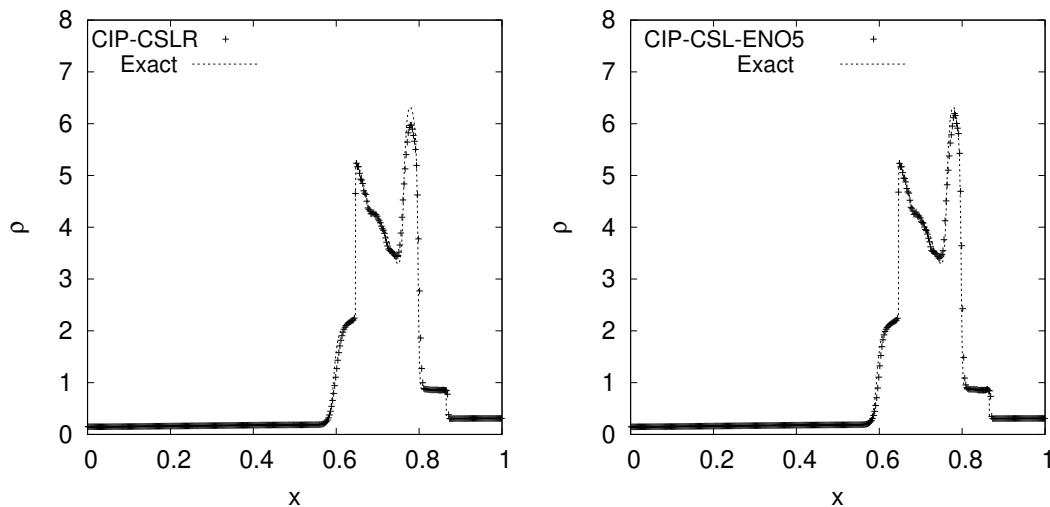


Figure 4.14: Numerical results of two interacting blast waves problem at $t=0.038$. $N=400$. CIP-CSLR (left) and CIP-CSL-ENO5 (right).

It is observed that both CIP-CSLR and CIP-CSL-ENO5 capture the contact discontinuity and shock without numerical oscillations, however, CIP-CSL-ENO5 performs better than CIP-CSLR around $x = 0.78$.

4.2.6 2D lid-driven cavity flow problem

In this section, we conduct a widely used benchmark test, which is called 2D lid-driven cavity flow test. In this tests, numerical simulations with Reynolds numbers 1000 and 3200 respectively are conducted on a Cartesian grids (100×100). The computation domain is $[0, 1][0, 1]$ with a driving velocity of the upper lid $u = 1$.

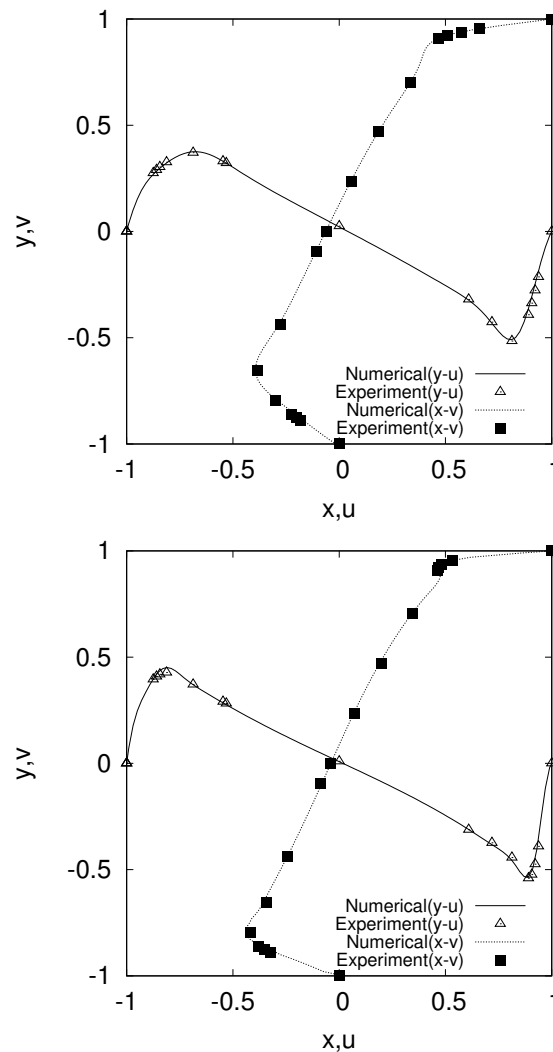


Figure 4.15: The horizontal velocity component u along the $x = 0.5$ axis and the vertical velocity component v along the $y = 0.5$ axis. Displayed are the results of the CIP-CSL-ENO5 scheme on 100×100 meshes with the Reynolds number being 1000 (top) and 3200 (bottom) respectively.

We compare the results between the numerical simulation and the experiment conducted by Ghia [138]. The results of horizontal velocity component u along the $x = 0.5$ axis and the vertical velocity component v along the $y = 0.5$ axis with two different Reynolds numbers are shown in Fig. 4.15. It is evident that the velocity components are accurately simulated by using the CIP-CSL-ENO5 scheme.

4.3 Summary

In this chapter, the CIP-CSL-ENO5 scheme was proposed based on the CIP-CSL3D, CIP-CSL3U, CIP-CSLR, and CIP-CSL4Q schemes. An ENO indicator was designed for the CIP-CSL-ENO5 scheme by using the total variations of the derivative. In the CIP-CSL-ENO5 scheme, the reconstruction criterion is designed by selecting either high-order polynomial functions or rational function on the basis of the smoothness of the reconstruction stencils. The CIP-CSL-ENO5 scheme has fifth-order accuracy for the sine wave propagation test and captures both discontinuities and smooth solutions well in various test problems. The CIP-CSL-ENO5 scheme is less diffusive than WENO-Roe5 scheme, multi-moment WENO scheme, and MCV-WENO scheme. Compared to the CIP-CSLR and CIP-CSL3-ENO schemes, the CIP-CSL-ENO5 scheme has smaller numerical errors in various test problems. In addition, it was observed that the CIP-CSL3-ENO scheme cannot resolve the numerical solution for the two blast waves interaction test. The CIP-CSL-ENO5 scheme addressed this issue. Moreover, the CIP-CSL-ENO5 scheme is robust for solving 2D lid-driven cavity flow problem and is able to accurately simulate the velocity components.

Implementation of Boundary Variation Diminishing (BVD) algorithm in the CIP-CSL scheme

To further minimise the numerical diffusion across discontinuities of the CIP-CSL scheme, in this chapter, we implement the Boundary Variation Diminishing (BVD) [90] algorithm in the CIP-CSL scheme. The proposed high-resolution scheme (CIP-CSLT-WENO4-BVD) is designed based on the CIP-CSLT (CIP-CSL scheme with the tangent hyperbolic function) and CIP-CSL-WENO4 schemes, as well as the modified version of the BVD algorithm.

In the CIP-CSLT-WENO4-BVD scheme, the CIP-CSL-WENO4 scheme is used as one reconstruction candidate, which maintains the fourth-order accuracy and oscillation-suppressing property for both scalar and Euler conservation laws. Details of the CIP-CSL-WENO4 scheme have been explained in Sec. 2.4.4. In addition, we propose another reconstruction candidate CIP-CSLT based on the CIP-CSL scheme and the THINC [40] scheme, which is able to represent the jump-like discontinuity sharply without numerical oscillations. The proposed CIP-CSLT-WENO4-BVD scheme is able to effectively reduce numerical errors and the numerical diffusion in vicinity of discontinuities.

5.1 Numerical method

For simplicity, we consider a one-dimensional conservation law to explain the numerical method. Herein, we recast the one-dimensional conservation law as follows

$$\frac{\partial \phi}{\partial t} + \frac{\partial(u\phi)}{\partial x} = 0, \quad (5.1)$$

where ϕ is the scalar and u is the velocity.

5.1.1 CIP-CSLT scheme

The CIP-CSLT scheme is based on the piece-wise tangent hyperbolic function [40], which can be expressed as

$$\Phi_i^{CSLT}(x) = \phi_{min} + \frac{\phi_{max} - \phi_{min}}{2} \left[1 + \gamma^{CSLT} \tanh\left(\beta^{CSLT} \left(\frac{x - x_{i-1/2}}{\Delta x} - \tilde{x}_i\right)\right) \right], \quad (5.2)$$

where $\phi_{min} = \min(\bar{\phi}_{i-1}, \bar{\phi}_{i+1})$, $\phi_{max} = \max(\bar{\phi}_{i-1}, \bar{\phi}_{i+1})$. $\gamma^{CSLT} = 1$ for $\bar{\phi}_{i-1} < \bar{\phi}_{i+1}$ and $\gamma^{CSLT} = -1$ for $\bar{\phi}_{i-1} > \bar{\phi}_{i+1}$. β^{CSLT} is a prescribed parameter to control the slope and the thickness of the jump. Based on our numerical experiments, when β^{CSLT} is from 1.4 to 2.4, we can obtain acceptable numerical results. Given β^{CSLT} and γ^{CSLT} , the only unknown parameter left is the jump centre \tilde{x}_i , which can be determined by the following constraint condition.

$$\frac{1}{\Delta x} \int_{x_{i-1/2}}^{x_{i+1/2}} \Phi_i^{CSLT}(x) dx = \bar{\phi}_i, \quad (5.3)$$

as

$$\tilde{x}_i = \frac{1}{2\beta^{CSLT}} \ln\left(\frac{\exp\beta^{CSLT} - A_i}{A_i - \exp(-\beta^{CSLT})}\right), \quad (5.4)$$

here

$$A_i = \exp\left(\frac{\beta^{CSLT}(2C_i - 1)}{\gamma^{CSLT}}\right) \text{ and } C_i = \frac{\bar{\phi}_i - \phi_{min}}{\phi_{max} - \phi_{min}}. \quad (5.5)$$

After obtaining the reconstructed function from Eq.(5.2), the cell average value $\bar{\phi}_i$ and the boundary value $\phi_{i-1/2}$ can be updated by a third-order TVD Runge-Kutta formulation [107, 108] in Sec. 2.4.1.

5.1.2 CIP-CSLT-WENO4-BVD scheme

Based on the CIP-CSLT and CIP-CSL-WENO4 [136] schemes, we propose the CIP-CSLT-WENO4-BVD scheme in this section. For the smooth region, as explained in Sec. 4.1.2, $\tau_0 \leq \min(\beta_0, \beta_1, \beta_2)$ is used in the CIP-CSL-ENO5 scheme to indicate the smooth condition. Analogously, in the CIP-CSLT-WENO4-BVD scheme, we use $\tau_0 \leq \min(\beta_0, \beta_1, \beta_2)$ to indicate the smooth condition. In this case, the fourth-order CIP-CSL-WENO4 reconstruction scheme is selected.

In non-smooth region, the reconstruction stencil may contain a genuine discontinuity with a certain strength. To reduce the numerical diffusion near the discontinuous region, we implement the Boundary Variation Diminishing (BVD) [90] algorithm in the CIP-CSL framework. Details of the BVD algorithm is given in Sec. 2.5.2. Firstly, we modify the definition of boundary variation (BV) at $x_{i-1/2}$ and $x_{i+1/2}$ as

$$BV_{x_{i-1/2}} = |\Phi'_{i-1}(x_{i-1/2}) - \Phi'_i(x_{i-1/2})|. \quad (5.6)$$

$$BV_{x_{i+1/2}} = |\Phi'_{i+1}(x_{i+1/2}) - \Phi'_i(x_{i+1/2})|. \quad (5.7)$$

where, $\Phi'_i(x)$ represents the derivative of the reconstruction function $\Phi_i(x)$. Based on Eqs. (5.6) and (5.7), we define the total boundary variation of the derivative as

$$TBV = BV_{x_{i-1/2}} + BV_{x_{i+1/2}}. \quad (5.8)$$

Here, we use TBV^{CSLT} and $TBV^{CSL-WENO4}$ to represent the TBV of CSL-WENO4 and CSLT, respectively. TBV^{CSLT} and $TBV^{CSL-WENO4}$ are calculated by using Eq. (5.8). If $TBV^{CSLT} \leq TBV^{CSL-WENO4}$, the CIP-CSLT reconstruction is selected. Otherwise, the high-order reconstruction scheme CIP-CSL-WENO4 is selected.

The reconstruction criterion of the CIP-CSLT-WENO4-BVD scheme can be expressed

as follows

$$\Phi_i(x) = \begin{cases} \Phi_i^{CSL-WENO4}(x) & \text{if } \tau_0 \leq \min(\beta_0, \beta_1, \beta_2), \\ \Phi_i^{CSLT}(x) & \text{else if } TBV^{CSLT} \leq TBV^{CSL-WENO4}, \\ \Phi_i^{CSL-WENO4}(x) & \text{else .} \end{cases} \quad (5.9)$$

5.2 Analysis of the computational efficiency for CIP-CSL schemes

In this section, we measure the computational efficiency of CIP-CSL schemes by calculating the computational time of the advection of a square wave after one period. The initial conditions are the same as those in Sec. 3.2.2. $t=2$ and $CFL=0.4$.

Table 5.1: Computational efficiency for solving square wave propagation problem by using CIP-CSL schemes. $t=2$ and $CFL=0.4$.

Method	L_1 error	Mesh number	CPU time
CIP-CSL3-ENO	1.0×10^{-3}	3100	628.5s
CIP-CSL-ENO5	1.0×10^{-3}	2350	396.7s
CIP-CSL-WENO4	1.0×10^{-3}	2300	208.8s
CIP-CSLT-WENO4-BVD	1.0×10^{-3}	1730	112.2s

In this quantitative measurement, table 5.1 presents the mesh number and CPU time for different CIP-CSL schemes to obtain a given level of accuracy (L_1 error = 1.0×10^{-3}). It is observed that both CIP-CSL-ENO5 and CIP-CSL-WENO4 use less mesh numbers and CPU time than CIP-CSL3-ENO. CIP-CSL-WENO4 costs less CPU time than CIP-CSL-ENO5. Moreover, we can see that CIP-CSLT-WENO4-BVD uses the least mesh number and CPU time among all the compared CIP-CSL schemes.

5.3 Numerical results

We validate the proposed methods through various benchmark problems and compare the results with those of the CIP-CSL3-ENO, CIP-CSL-ENO5, and CIP-CSL-WENO4 schemes. Several types of numerical errors are calculated. The definitions of L_1 error and L_∞ error have been provided in Eqs. (6.17) and (3.30). The total error [137] is defined as

$$E_{Total} = \frac{1}{N} \sum_{i=0}^{\infty} (\phi_i - \phi_i^e)^2, \quad (5.10)$$

where ϕ_i^e is the exact solution and ϕ_i is the numerical solution of the cell i , and N is the mesh number. The total error includes two parts: the dissipation error and the dispersion error. It can be expressed as

$$E_{Total} = E_{Dissipation} + E_{Dispersion}. \quad (5.11)$$

The dissipation error and the dispersion error can be calculated by

$$E_{Dissipation} = (\sigma(\phi_i) - \sigma(\phi_i^e))^2 + (\bar{\phi}_i - \bar{\phi}_i^e)^2, \quad (5.12)$$

$$E_{Dispersion} = 2(1 - \rho)\sigma(\bar{\phi}_i)\sigma(\phi_i^e), \quad (5.13)$$

where $\sigma(\phi_i)$ is the standard deviation of numerical solution ϕ_i , and $\sigma(\phi_i^e)$ is the standard deviation of analytical solution ϕ_i^e . Further, $\bar{\phi}_i$, $\bar{\phi}_i^e$ are the mean values of ϕ_i and ϕ_i^e , respectively. ρ is the correlation coefficient of ϕ_i and ϕ_i^e , and it is defined as

$$\rho = \frac{cov(\phi_i, \phi_i^e)}{\sigma(\phi_i)\sigma(\phi_i^e)}, \quad (5.14)$$

where $cov(\phi_i, \phi_i^e)$ is the covariance of ϕ_i and ϕ_i^e .

5.3.1 Sine wave propagation

In this section, we solve the conservation equation Eq.(5.1) with the same initial condition as described in Sec. 3.2.1 to calculate L_1 errors and L_∞ errors and convergence

rates of the CIP-CSL-WENO4 and CIP-CSLT-WENO4-BVD schemes. The computation domain is $[0, 1]$, $u(x) = 1$ and periodic boundary conditions are used. Moreover, five different grid sizes ($N = 20, 40, 80, 160,$ and 320) are used.

Table 5.2: L_1 and L_∞ errors in sine wave propagation at $t=1$.

Method	N	L_1 error	L_1 order	L_∞ error	L_∞ order
CIP-CSL-WENO4	20	4.39×10^{-6}	-	6.65×10^{-6}	-
	40	2.74×10^{-7}	4.00	4.29×10^{-7}	3.95
	80	1.72×10^{-8}	4.00	2.69×10^{-8}	3.99
	160	1.07×10^{-9}	4.00	1.69×10^{-9}	4.00
	320	6.73×10^{-11}	4.00	1.06×10^{-10}	4.00
CIP-CSLT-WENO4-BVD	20	4.39×10^{-6}	-	6.65×10^{-6}	-
	40	2.74×10^{-7}	4.00	4.29×10^{-7}	3.95
	80	1.72×10^{-8}	4.00	2.69×10^{-8}	3.99
	160	1.07×10^{-9}	4.00	1.69×10^{-9}	4.00
	320	6.73×10^{-11}	4.00	1.06×10^{-10}	4.00

Table 5.2 presents the L_1 errors and L_∞ errors and convergence rates of the CIP-CSL-WENO4 and CIP-CSLT-WENO4-BVD schemes. It is evident that both CIP-CSL-WENO4 and CIP-CSLT-WENO4-BVD have fourth-order accuracy for L_1 and L_∞ . This indicates that the implementation of the BVD algorithm automatically selects the highest possible polynomial interpolation for a smooth profile.

5.3.2 Complex wave propagation problem

In this test, the Jiang-Shu complex wave propagation problem [1] is conducted. The initial conditions are the same as those in Sec. 3.2.3. Fig. 5.1 illustrates the results

of the CIP-CSL3-ENO, CIP-CSL-ENO5, CIP-CSLWENO4, and CIP-CSLT-WENO4-BVD schemes at time $t=2$ (1 period).

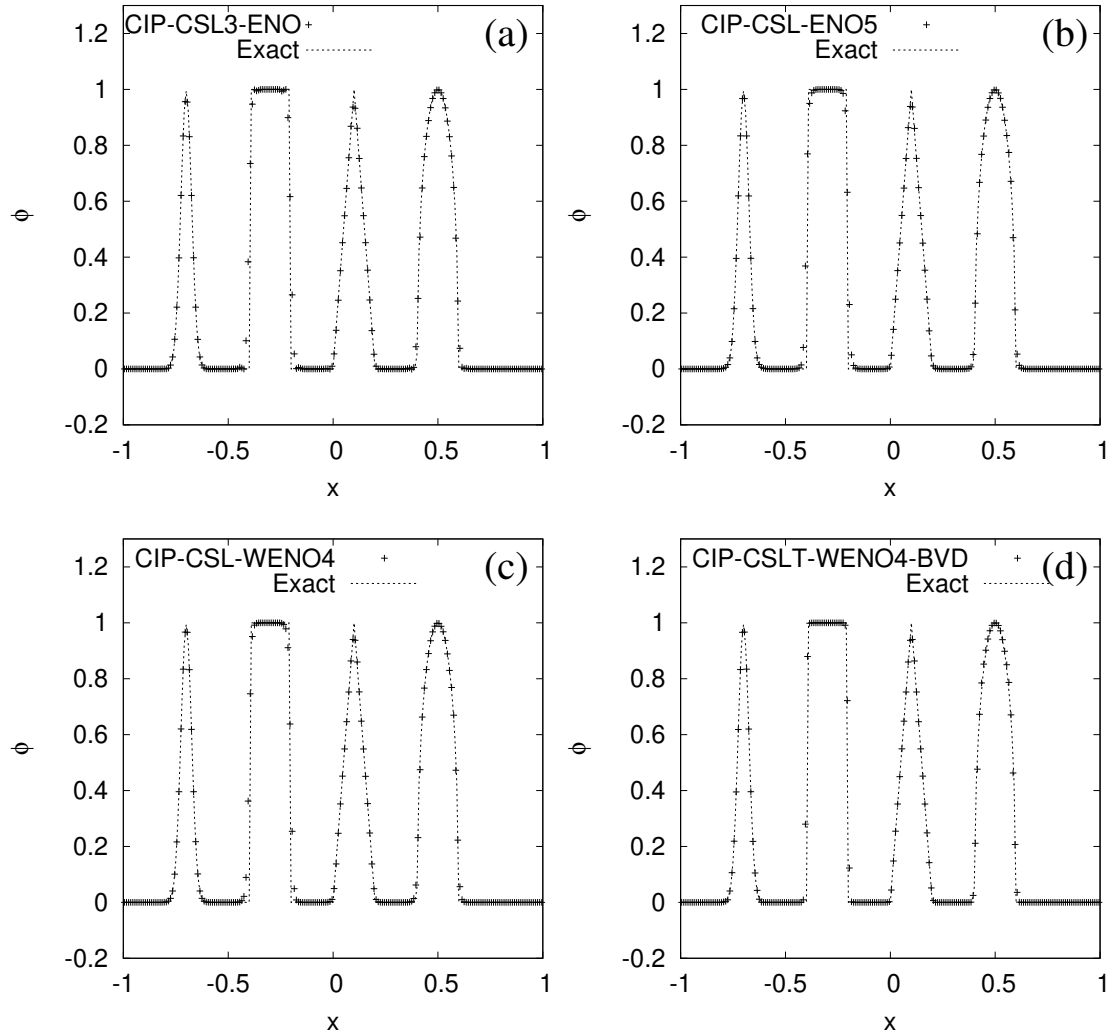


Figure 5.1: Numerical results of complex wave propagation test at time $t=2$ (1 period). $N=200$ and $CFL=0.4$ are used. (a) CIP-CSL3-ENO, (b) CIP-CSL-ENO5, (c) CIP-CSL-WENO4, (d) CIP-CSLT-WENO4-BVD.

It is observed that CIP-CSLT-WENO4-BVD has sharper solutions for discontinuities compared to other high-order CIP-CSL schemes (CIP-CSL3-ENO, CIP-CSL-ENO5, and CIP-CSL-WENO4). In addition, Table 5.3 shows that CIP-CSLT-WENO4-BVD has the least numerical errors.

Table 5.3: Numerical errors in complex wave propagation test at $t=2$ (1 period). $N=200$ and $CFL=0.4$ are used.

	Total error	Dissipation error	Dispersion error	L_1 error	L_∞ error
CIP-CSL3-ENO	1.40×10^{-3}	5.14×10^{-5}	1.35×10^{-3}	9.39×10^{-3}	2.65×10^{-1}
CIP-CSL-ENO5	1.10×10^{-3}	3.53×10^{-5}	1.06×10^{-3}	8.44×10^{-3}	2.31×10^{-1}
CIP-CSL-WENO4	1.21×10^{-3}	4.13×10^{-5}	1.17×10^{-3}	8.77×10^{-3}	2.54×10^{-1}
CIP-CSLT-WENO4-BVD	3.57×10^{-4}	2.68×10^{-6}	3.54×10^{-4}	5.26×10^{-3}	1.23×10^{-1}

5.3.3 Lax's problem

In this section, the numerical test of Lax's problem with strong shock and contact discontinuity is conducted. The initial condition is set as the same as that in Sec. 4.2.3. Fig. 5.2 illustrates the numerical results of the CIP-CSL3-ENO, CIP-CSL-ENO5, CIP-CSLWENO4, and CIP-CSLT-WENO4-BVD schemes at time $t=0.16$.

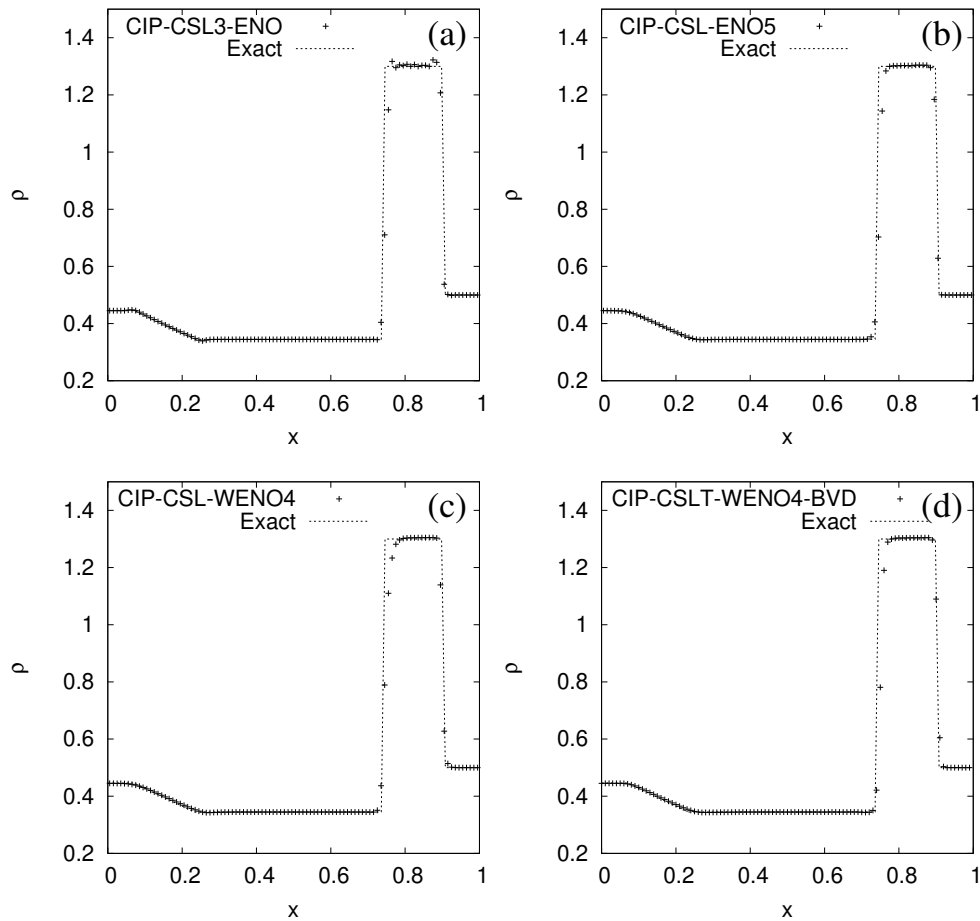


Figure 5.2: Numerical results of Lax's shock tube problem at $t=0.16$ and $N=100$. (a) CIP-CSL3-ENO, (b) CIP-CSL-ENO5, (c) CIP-CSL-WENO4, (d) CIP-CSLT-WENO4-BVD.

It is observed that CIP-CSL3-ENO has small numerical oscillations and CIP-CSL-WENO4 is diffusive in the discontinuous region. Both CIP-CSL-ENO5 and CIP-CSLT-WENO4-BVD capture discontinuities and shocks well without numerical oscillations.

5.3.4 Two blast waves interaction problem

In this section, the two interacting blast waves test is conducted. The initial condition is set as the same as that in Sec. 4.2.5. CIP-CSL3-ENO could not obtain the solution. The numerical solutions of density computed by CIP-CSLENO5, CIP-CSL-WENO4, and CIP-CSLT-WENO4-BVD are shown in Fig. 5.3. It is observed that both CIP-

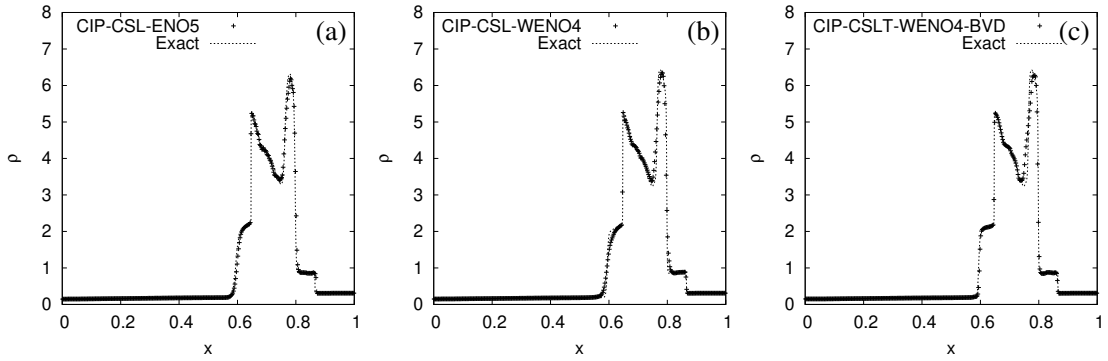


Figure 5.3: Numerical results of two interacting blast waves problem at $t=0.038$ and $N=400$. (a) CIP-CSL-ENO5, (b) CIP-CSL-WENO4, (c) CIP-CSLT-WENO4-BVD.

CSLENO5 and CIP-CSL-WENO4 are diffusive around $x = 0.6$ in the numerical solutions. However, CIP-CSLT-WENO4-BVD effectively reduce the numerical diffusion in the vicinity of discontinuities. The resolution of the left-most density discontinuity around $x = 0.6$ by CIP-CSLT-WENO4-BVD is superior to other CIP-CSL schemes.

5.3.5 2D circular explosion problem

In this section, the numerical simulation of a circular two-dimensional explosion of inviscid compressible flows is conducted to verify the proposed method as a solver for compressible flows that contains shock waves. An axis-symmetric explosion, which is reported in [139], is generated from the following initial condition

$$(\rho, u, v, p) = \begin{cases} (1, 0, 0, 1) & \text{if } r \leq 0.5 \\ (0.125, 0, 0, 0.1) & \text{otherwise,} \end{cases} \quad (5.15)$$

where the radius $r = \sqrt{x^2 + y^2}$ and the computation domain is $[-1, 1][[-1, 1]$. This axis-symmetric explosion configuration contains rarefaction wave, contact discontinuity and shock waves expanding inward.

Fig. 5.4 (top) shows the side view of the density profile at time $t = 0.25$ on a 200×200 Cartesian grid. Fig. 5.4 (bottom-left) and Fig. 5.4 (bottom-right) show the density along the cross-section of $x = y$ by using different mesh numbers (200×200 and 400×400), against the reference solution created by the VSIAM3 (Volume/Surface Integrated Average-based Multi-moment) scheme [103] with a high numerical resolution (10,000 cells). It is observed that shock, contact discontinuity, and rarefaction wave are well simulated by using the CIP-CSLT-WENO4-BVD scheme. In addition, the quality of the numerical solution improved by refining the mesh grid. The numerical solutions of the CIP-CSLT-WENO4-BVD scheme with 400×400 mesh grid agree well with the reference solutions. This indicates that the CIP-CSLT-WENO4-BVD scheme is capable of simulating compressible flows faithfully.

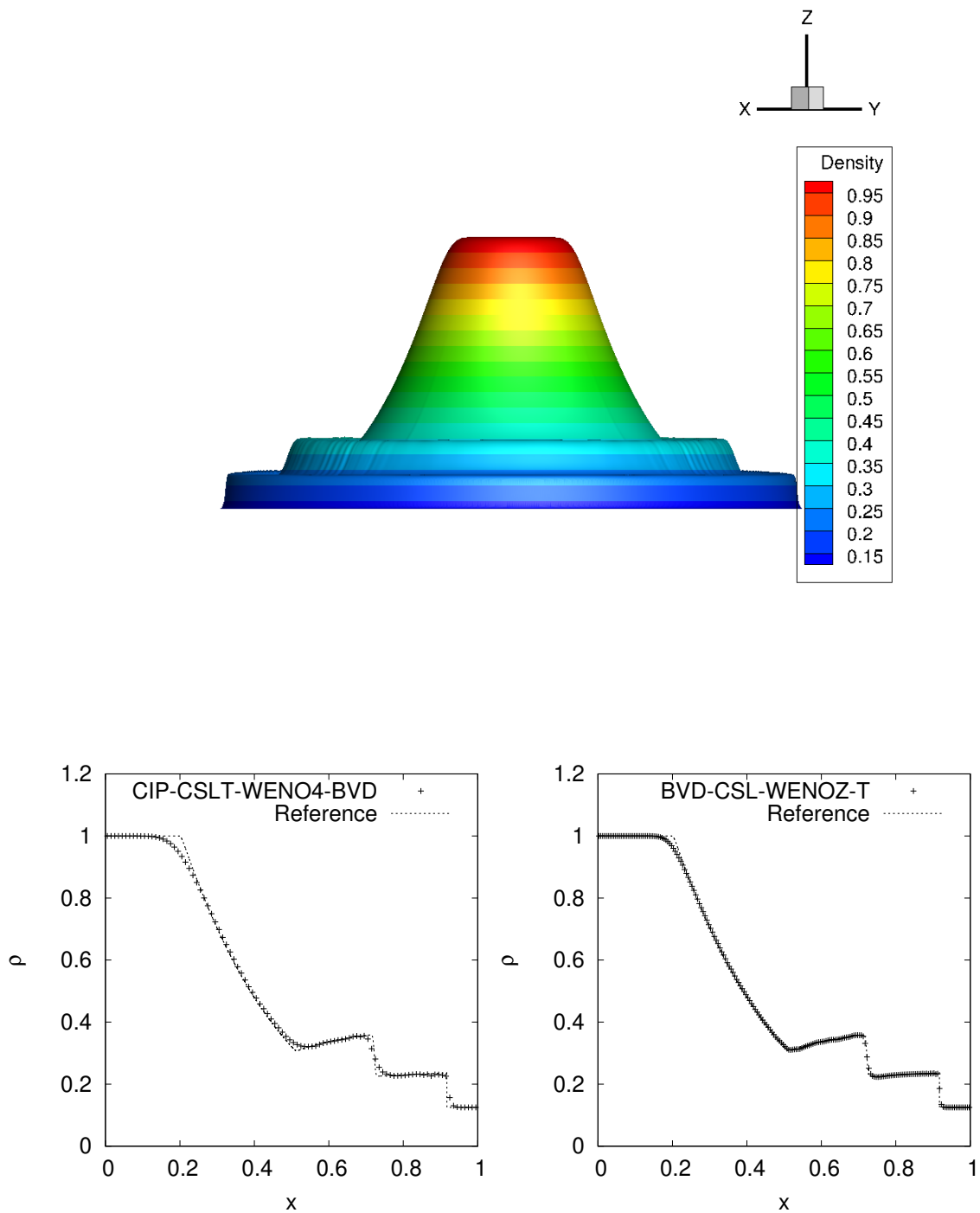


Figure 5.4: 2D circular explosion results of the CIP-CSLT-WENO4-BVD scheme at $t=0.25$. The density profile, side view (top) and the density profile along the cross-section of $x = y$ with 200×200 meshes (bottom left) and 400×400 meshes (bottom right).

5.4 Summary

In this chapter, the CIP-CSLT-WENO4-BVD scheme was proposed based on the CIP-CSL-WENO4 scheme and a newly proposed CIP-CSLT scheme. Firstly, we proposed the CIP-CSLT scheme based on the piecewise tangent hyperbolic function, which can represent the discontinuity with less numerical errors. Subsequently, we implemented a modified version of BVD algorithm in the CIP-CSL schemes. For the smooth region, the fourth-order CIP-CSL-WENO4 scheme is used to maintain high-order accuracy. For discontinuous regions, the reconstruction criterion of the CIP-CSLT-WENO4-BVD scheme was designed based on the proposed BVD algorithm, which can minimise the total boundary variations of the derivative.

The CIP-CSLT-WENO4-BVD scheme has been verified through various numerical benchmark tests. The numerical results reveal that the CIP-CSLT-WENO4-BVD scheme has the least numerical errors for advection tests compared to the CIP-CSL3-ENO, CIP-CSL-ENO5, and CIP-CSL-WENO4 schemes. The CIP-CSL-WENO4-BVD scheme uses the least mesh number and CPU time to achieve the given level of accuracy compare to WENO-JS, WENO-Z, and other CIP-CSL schemes for solving advection problems. It is also observed that the CIP-CSLT-WENO4-BVD scheme reduces the numerical diffusion in vicinity of discontinuities effectively. In addition, the numerical results of 2D explosion test have shown that the CIP-CSLT-WENO4-BVD scheme can be applied to compressible flows problem that contains shocks.

Implementation of Total Boundary Variation Diminishing (TBVD) algorithm with the TWENO and THINC schemes

It has been noticed that conventional weighted essentially non-oscillatory (WENO) schemes still suffer from excessive numerical diffusion. One of the reasons is that they tend to under-use adjacent smooth sub-stencils thus fail to obtain optimal interpolation. In this chapter, a novel reconstruction strategy is proposed for the fifth-order WENO scheme. Unlike the conventional fifth-order WENO scheme, we proposed a target WENO (TWENO) scheme to restore the highest possible order interpolation when three target sub-stencils or two adjacent target sub-stencils are smooth.

Based on the TWENO scheme and the THINC [40, 2] scheme, we propose the TBVD-TWENO-THINC scheme by implementing the Total Boundary Variation Diminishing (TBVD) [41] algorithm. The TBVD algorithm selects a reconstruction function between TWENO and THINC to minimise the total variations (jumps) of the reconstructed variables at cell boundaries. Consequently, the TBVD-TWENO-THINC scheme effectively reduces the numerical errors and the numerical diffusion near discontinuities.

6.1 Numerical method

6.1.1 Target WENO (TWENO) scheme

We consider the following hyperbolic conservation law

$$\frac{\partial \phi}{\partial t} + \frac{\partial f(\phi)}{\partial x} = 0, \quad (6.1)$$

where ϕ is the solution function and $f(\phi)$ is the flux function. In the finite volume method, the cell average value $\bar{\phi}_i$ defined in Eq. (2.14) is updated by

$$\frac{d\bar{\phi}_i}{dt} = -\frac{1}{\Delta x}(f_{i+1/2} - f_{i-1/2}). \quad (6.2)$$

The numerical flux $f_{i+1/2}$ and $f_{i-1/2}$ at cell boundaries are computed by a Riemann solver. To obtain the solution of the Riemann solver, the main task is to reconstruct the left- and right-side values $\phi_{i+1/2}^L$ and $\phi_{i+1/2}^R$ for cell boundaries $x_{i+1/2}$, $i = 1, 2, \dots, N$.

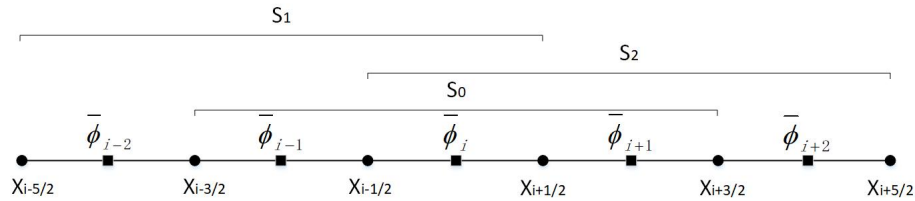


Figure 6.1: Sketch of the TWENO scheme with three sub-stencils S_0 , S_1 , and S_2

In the TWENO scheme, sub-stencils S_0 , S_1 and S_2 are used, as shown in Fig. 6.1. For those stencils, we can construct the interpolation functions $\phi_{i+1/2}^{S_0}$, $\phi_{i+1/2}^{S_1}$, and $\phi_{i+1/2}^{S_2}$ using the following formulas.

$$\begin{aligned} \phi_{i+1/2}^{S_0} &= -\frac{1}{6}\bar{\phi}_{i-1} + \frac{5}{6}\bar{\phi}_i + \frac{1}{3}\bar{\phi}_{i+1}, \\ \phi_{i+1/2}^{S_1} &= \frac{1}{3}\bar{\phi}_{i-2} - \frac{7}{6}\bar{\phi}_{i-1} + \frac{11}{6}\bar{\phi}_i, \\ \phi_{i+1/2}^{S_2} &= \frac{1}{3}\bar{\phi}_i + \frac{5}{6}\bar{\phi}_{i+1} - \frac{1}{6}\bar{\phi}_{i+2}. \end{aligned} \quad (6.3)$$

The reconstruction criteria of the TWENO scheme is designed by using the combination of $\beta_i^{\hat{j}}$ and $\tau_{\hat{j}}$ ($\hat{j} = 0, 1, 2$) in Eqs. (2.20), (2.22), and (4.11), which can indicate the

smoothness and the potential location of the discontinuity. Details of the relationship between $\hat{\beta}_i^j$ and τ_j have been explained in Sec. 4.1.2. Based on the indicators in Sec. 4.1.2, we design the reconstruction scheme by the following criteria.

Selection criteria:

- Case 1. If the entire reconstruction region between $x_{i-5/2}$ and $x_{i+5/2}$ is continuous, three smooth sub-stencils S_0 , S_1 , and S_2 in Fig. 6.1 are targeted and selected. In this case, the indicator is designed as $\tau_0 \leq \min(\beta_i^0, \beta_i^1, \beta_i^2)$. The reconstruction is based on $\phi_{i+1/2}^{S_0}$, $\phi_{i+1/2}^{S_1}$, and $\phi_{i+1/2}^{S_2}$, which are assigned with the optimal linear weights as

$$\phi_{i+1/2}^L = \frac{6}{10}\phi_{i+1/2}^{S_0} + \frac{1}{10}\phi_{i+1/2}^{S_1} + \frac{3}{10}\phi_{i+1/2}^{S_2}. \quad (6.4)$$

- Case 2. If the discontinuity exists in the region between $x_{i-5/2}$ and $x_{i-3/2}$, as

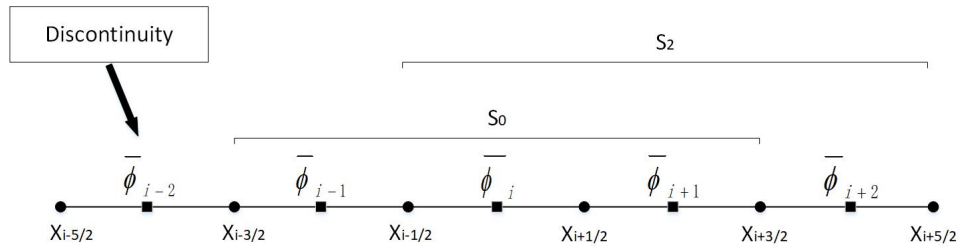


Figure 6.2: Discontinuity exists in sub-stencil S_1 , while adjacent sub-stencils S_0 and S_2 are smooth.

shown in Fig. 6.2, it suggests that the reconstruction solution is continuous in stencils S_0 and S_2 , but discontinuous in stencil S_1 . In this case, two smooth adjacent sub-stencils S_0 and S_2 are targeted and selected, and the indicator is designed as $\tau_1 > \min(\beta_i^0, \beta_i^1)$ and $\tau_2 \leq \min(\beta_i^0, \beta_i^2)$. The reconstruction is based on $\phi_{i+1/2}^{S_0}$ and $\phi_{i+1/2}^{S_2}$, which are assigned with the optimal linear weights as

$$\phi_{i+1/2}^L = \frac{1}{2}\phi_{i+1/2}^{S_0} + \frac{1}{2}\phi_{i+1/2}^{S_2}. \quad (6.5)$$

- Case 3. Analogously, if the discontinuity appears in the region between $x_{i+3/2}$ and $x_{i+5/2}$, as shown in Fig. 6.3, it suggests that the reconstruction solution is

continuous in stencils S_0 and S_1 , but discontinuous in stencil S_2 . In this case, two smooth adjacent sub-stencils S_0 and S_1 are targeted and selected, and the indicator is designed as $\tau_1 \leq \min(\beta_i^0, \beta_i^1)$ and $\tau_2 > \min(\beta_i^0, \beta_i^2)$. The reconstruction is based on $\phi_{i+1/2}^{S_0}$ and $\phi_{i+1/2}^{S_1}$, which are assigned with the optimal linear weights as

$$\phi_{i+1/2}^L = \frac{3}{4}\phi_{i+1/2}^{S_0} + \frac{1}{4}\phi_{i+1/2}^{S_1}. \quad (6.6)$$

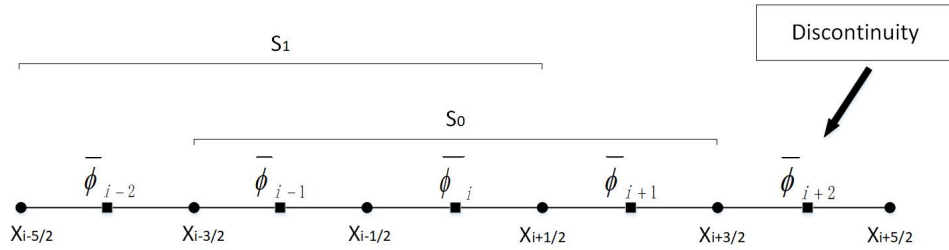


Figure 6.3: Discontinuity exists in sub-stencil S_2 , while adjacent sub-stencils S_0 and S_1 are smooth.

- Case 4. In addition to the above situations, all three sub-stencils S_0 , S_1 , and S_2 are targeted and selected. The reconstruction is based on $\phi_{i+1/2}^{S_0}$, $\phi_{i+1/2}^{S_1}$, and $\phi_{i+1/2}^{S_2}$, which are assigned with the non-linear weights as

$$\phi_{i+1/2}^L = \omega_i^0 \phi_i^{S_0}(x_{i+1/2}) + \omega_i^1 \phi_i^{S_1}(x_{i+1/2}) + \omega_i^2 \phi_i^{S_2}(x_{i+1/2}). \quad (6.7)$$

The non-linear weights ω_i^j are calculated by using Eqs. (2.19) and (2.23) of the WENO-Z scheme, as described in Sec. 2.3.3.

Summary of the reconstruction criteria of the TWENO scheme can be expressed as follows

$$\phi_{i+1/2}^L = \begin{cases} \frac{6}{10}\phi_{i+1/2}^{S_0} + \frac{1}{10}\phi_{i+1/2}^{S_1} + \frac{3}{10}\phi_{i+1/2}^{S_2} & \tau_0 \leq \min(\beta_i^0, \beta_i^1, \beta_i^2) \\ \frac{1}{2}\phi_{i+1/2}^{S_0} + \frac{1}{2}\phi_{i+1/2}^{S_2} & \tau_1 > \min(\beta_i^0, \beta_i^1) \text{ and } \tau_2 \leq \min(\beta_i^0, \beta_i^2), \\ \frac{3}{4}\phi_{i+1/2}^{S_0} + \frac{1}{4}\phi_{i+1/2}^{S_1} & \tau_1 \leq \min(\beta_i^0, \beta_i^1) \text{ and } \tau_2 > \min(\beta_i^0, \beta_i^2), \\ \omega_i^0 \phi_{i+1/2}^{S_0} + \omega_i^1 \phi_{i+1/2}^{S_1} + \omega_i^2 \phi_{i+1/2}^{S_2} & \text{otherwise.} \end{cases} \quad (6.8)$$

6.1.2 THINC with adaptive β^T

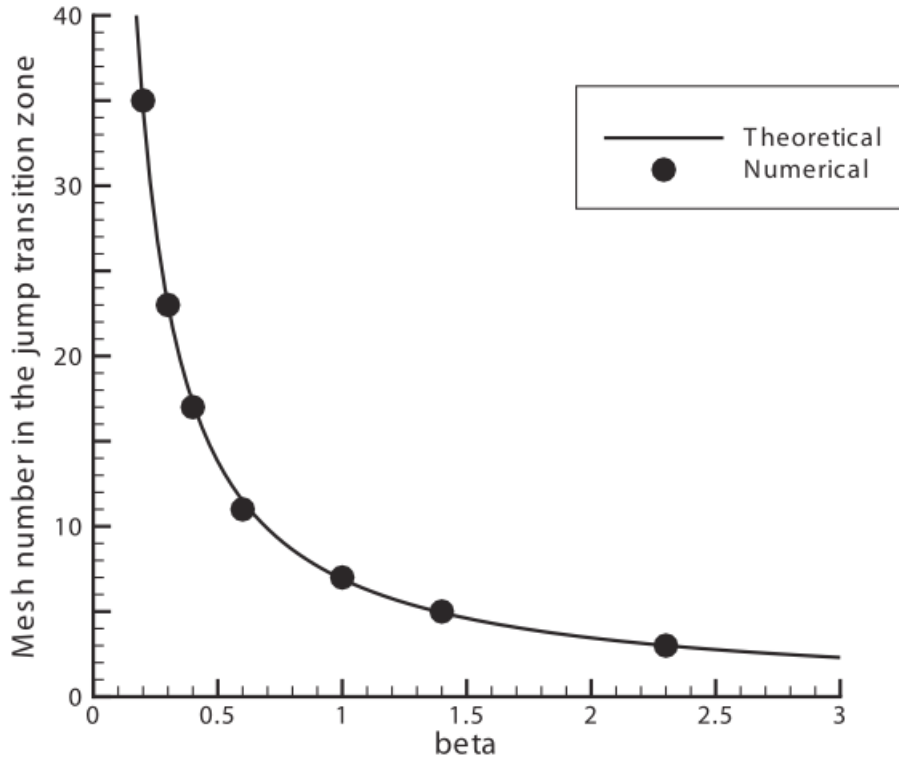


Figure 6.4: The relationship between the parameter β^T and the mesh number in the jump transition zone. [2].

THINC [40, 2] scheme is a jump-like reconstruction with a differentiable and monotone function, which is explained in Sec. 2.5.1. In the THINC scheme, β^T is a parameter to control the jump thickness of the tangential hyperbolic function and a constant $\beta^T = 1.6$ is used in BVD-WENOZ-THINC [90] scheme. To improve the numerical solutions of THINC, we propose the adaptive β^T based on a theoretical relation between the parameter β^T and the jump thickness as shown in Fig. 6.4 [2]. It is observed that the thickness of the jump transition in the THINC reconstruction can be modified by adjusting the value of parameter β^T .

The adaptive β^T in one dimension is designed as follows

$$\beta^T = \beta_{min}^T + (\beta_{max}^T - \beta_{min}^T) \frac{\min(|\bar{\phi}_i - \bar{\phi}_{i-1}|, |\bar{\phi}_{i+1} - \bar{\phi}_i|)}{\max(|\bar{\phi}_i - \bar{\phi}_{i-1}|, |\bar{\phi}_{i+1} - \bar{\phi}_i|)}. \quad (6.9)$$

Analogously, we can obtain the two-dimensional adaptive β^T for each direction as

$$\beta_x^T = \beta_{min}^T + (\beta_{max}^T - \beta_{min}^T) \frac{\min(|\bar{\phi}_{i,j} - \bar{\phi}_{i-1,j}|, |\bar{\phi}_{i+1,j} - \bar{\phi}_{i,j}|)}{\max(|\bar{\phi}_{i,j} - \bar{\phi}_{i-1,j}|, |\bar{\phi}_{i+1,j} - \bar{\phi}_{i,j}|)}, \quad (6.10)$$

$$\beta_y^T = \beta_{min}^T + (\beta_{max}^T - \beta_{min}^T) \frac{\min(|\bar{\phi}_{i,j} - \bar{\phi}_{i,j-1}|, |\bar{\phi}_{i,j+1} - \bar{\phi}_{i,j}|)}{\max(|\bar{\phi}_{i,j} - \bar{\phi}_{i,j-1}|, |\bar{\phi}_{i,j+1} - \bar{\phi}_{i,j}|)}. \quad (6.11)$$

With regards to the decision of the two ad hoc parameters β_{min}^T and β_{max}^T in Eq. (6.9), (6.10), and (6.11), from our numerical experiments, if β^T is from 1.6 to 2.0, the THINC scheme can accurately resolve the solutions for discontinuities. The numerical diffusion will decrease as β^T increase from 1.6 to 2.0. If β^T goes beyond 2.0, the numerical results become sharp but may cause numerical oscillation. If β^T goes below 1.6, the numerical results become more diffusive. Therefore, $\beta_{min}^T = 1.6$ and $\beta_{max}^T = 2.0$ are used to design the adaptive β^T and guarantee β^T is in a suitable range between 1.6 to 2.0.

6.1.3 TBVD-TWENO-THINC scheme

In this section, we propose a high-resolution numerical scheme by implementing the total boundary variation diminishing (TBVD) [41] algorithm with the TWENO and THINC schemes. Firstly, the minimum value of total boundary variations (TBV) for the TWENO and THINC reconstructions at the boundaries of each cell are defined as

$$\begin{aligned} TBV_i^{TWENO} = \min(& |\Phi_{i-1}^{TWENO,L}(x_{i-1/2}) - \Phi_i^{TWENO,R}(x_{i-1/2})| + |\Phi_{i+1}^{TWENO,R}(x_{i+1/2}) - \Phi_i^{TWENO,L}(x_{i+1/2})|, \\ & |\Phi_{i-1}^{THINC,L}(x_{i-1/2}) - \Phi_i^{TWENO,R}(x_{i-1/2})| + |\Phi_{i+1}^{THINC,R}(x_{i+1/2}) - \Phi_i^{TWENO,L}(x_{i+1/2})|, \\ & |\Phi_{i-1}^{TWENO,L}(x_{i-1/2}) - \Phi_i^{TWENO,R}(x_{i-1/2})| + |\Phi_{i+1}^{THINC,R}(x_{i+1/2}) - \Phi_i^{TWENO,L}(x_{i+1/2})|, \\ & |\Phi_{i-1}^{THINC,L}(x_{i-1/2}) - \Phi_i^{TWENO,R}(x_{i-1/2})| + |\Phi_{i+1}^{TWENO,R}(x_{i+1/2}) - \Phi_i^{TWENO,L}(x_{i+1/2})|), \end{aligned} \quad (6.12)$$

$$\begin{aligned} TBV_i^{THINC} = \min(& |\Phi_{i-1}^{THINC,L}(x_{i-1/2}) - \Phi_i^{THINC,R}(x_{i-1/2})| + |\Phi_{i+1}^{THINC,R}(x_{i+1/2}) - \Phi_i^{THINC,L}(x_{i+1/2})|, \\ & |\Phi_{i-1}^{TWENO,L}(x_{i-1/2}) - \Phi_i^{THINC,R}(x_{i-1/2})| + |\Phi_{i+1}^{TWENO,R}(x_{i+1/2}) - \Phi_i^{THINC,L}(x_{i+1/2})|, \\ & |\Phi_{i-1}^{THINC,L}(x_{i-1/2}) - \Phi_i^{THINC,R}(x_{i-1/2})| + |\Phi_{i+1}^{TWENO,R}(x_{i+1/2}) - \Phi_i^{THINC,L}(x_{i+1/2})|, \\ & |\Phi_{i-1}^{TWENO,L}(x_{i-1/2}) - \Phi_i^{THINC,R}(x_{i-1/2})| + |\Phi_{i+1}^{THINC,R}(x_{i+1/2}) - \Phi_i^{THINC,L}(x_{i+1/2})|), \end{aligned} \quad (6.13)$$

where $\Phi_{i-1}^{TWENO,L}(x_{i-1/2})$ and $\Phi_{i-1}^{THINC,L}(x_{i-1/2})$ represent the reconstructed left-side values at the cell boundary $x_{i-1/2}$ by the TWENO scheme and the THINC scheme, respectively. $\Phi_i^{TWENO,R}(x_{i-1/2})$ and $\Phi_i^{THINC,R}(x_{i-1/2})$ represent the reconstructed right-side values at the cell boundary $x_{i-1/2}$ by the TWENO scheme and the THINC scheme, respectively. Analogously, $\Phi_i^{TWENO,L}(x_{i+1/2})$ and $\Phi_i^{THINC,L}(x_{i+1/2})$ represent the reconstructed left-side values at the cell boundary $x_{i+1/2}$ by the TWENO scheme and the THINC scheme, respectively. $\Phi_{i+1}^{TWENO,R}(x_{i+1/2})$ and $\Phi_{i+1}^{THINC,R}(x_{i+1/2})$ represent the reconstructed right-side values at the cell boundary $x_{i+1/2}$ by the TWENO scheme and the THINC scheme, respectively. Fig. 6.5 illustrates one possible situation of calculating TBV_i^{THINC} .

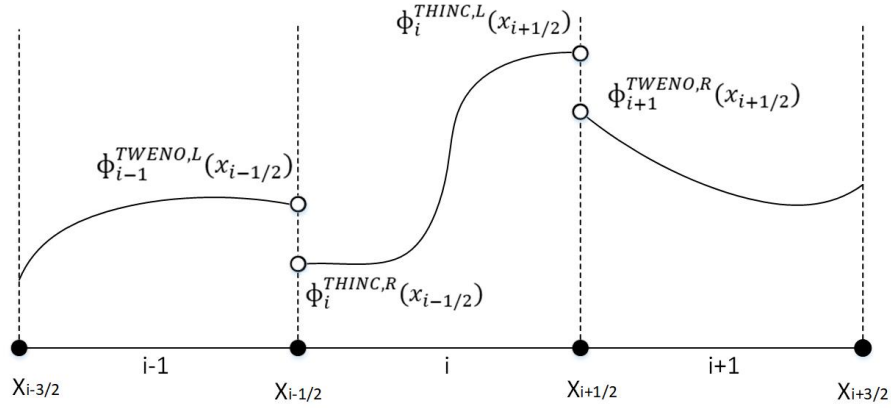


Figure 6.5: Illustration of one possible situation corresponding to $|\Phi_{i-1}^{TWENO,L}(x_{i-1/2}) - \Phi_i^{THINC,R}(x_{i-1/2})| + |\Phi_{i+1}^{TWENO,R}(x_{i+1/2}) - \Phi_i^{THINC,L}(x_{i+1/2})|$ when calculating TBV_i^{THINC} .

Using TBV_i^{TWENO} and TBV_i^{THINC} , we design the TBVD selection criterion for the left-side value $\phi_{i+1/2}^L$ as follows.

$$\phi_{i+1/2}^L = \begin{cases} \Phi_i^{THINC,L}(x_{i+1/2}) & \text{if } TBV_i^{THINC} < TBV_i^{TWENO}, \\ \Phi_i^{TWENO,L}(x_{i+1/2}) & \text{otherwise.} \end{cases} \quad (6.14)$$

Analogously, we can obtain the right-side value $\phi_{i+1/2}^R$.

6.1.4 Time evolution method

Given the spatial discretization, we employ three-stage third-order Strong Stability-Preserving Runge-Kutta (SSPRK) scheme

$$\begin{aligned}\phi_j^{(1)} &= \phi_j^n + \Delta t F(\phi_j^n), \\ \phi_j^{(2)} &= \frac{3}{4}\phi_j^n + \frac{1}{4}\phi_j^{(1)} + \frac{1}{4}\Delta t F(\phi_j^{(1)}), \\ \phi_j^{(n+1)} &= \frac{1}{3}\phi_j^n + \frac{2}{3}\phi_j^{(2)} + \frac{2}{3}\Delta t F(\phi_j^{(2)}),\end{aligned}\tag{6.15}$$

to solve the time evolution Ordinary Differential Equations (ODEs), where $\phi_j^{(1)}$ and $\phi_j^{(2)}$ denote the intermediate values at the sub-steps.

6.2 Analysis of the computational efficiency for TBVD-TWENO-THINC

In this section, we measure the computational efficiency of the proposed schemes by calculating the computational time of the advection of a square wave after one period. The results of the TWENO and TBVD-TWENO-THINC schemes are compared with that of the WENO-JS [1], WENOZ [32], BVD-WENOZ-THINC [90] schemes. The initial conditions are the same as those in Sec. 3.2.2. $t=2$ and $CFL=0.4$.

In this quantitative measurement, table 6.1 presents the mesh number and CPU time for different schemes to obtain a given level of accuracy (L_1 error = 1.0×10^{-3}). The results show that the TWENO scheme uses less mesh number and CPU time than WENO-JS and WENO-Z schemes. In addition, it is observed that the TBVD-TWENO-THINC scheme performs better than the BVD-WENOZ-THINC scheme and other WENO-type schemes. To achieve the given level of accuracy, the TBVD-TWENO-THINC scheme uses the least mesh number and costs the least CPU time compared to WENO-JS, WENO-Z, TWENO, and BVD-WENOZ-THINC schemes.

Table 6.1: Computational efficiency for solving square wave propagation problem by using WENO-JS, WENO-Z, TWENO, BVD-WENOZ-THINC, and TBVD-TWENO-THINC. $t=2$ and $CFL=0.4$.

Method	L_1 error	Mesh number	CPU time
WENO-JS	1.0×10^{-3}	8550	213.2s
WENO-Z	1.0×10^{-3}	5150	63.9s
TWENO	1.0×10^{-3}	4850	62.8s
BVD-WENOZ-THINC	1.0×10^{-3}	2120	27.5s
TBVD-TWENO-THINC	1.0×10^{-3}	1770	18.4s

6.3 Numerical results

We validate the proposed methods through various benchmark problems.

6.3.1 1D advection equation

In this section, we present the numerical results by solving the 1D scalar conservation law in Eq. (2.13) with periodic boundary conditions. The numerical results of the TWENO and TBVD-TWENO-THINC schemes are compared with the results of the WENO-Z[32] and BVD-WENOZ-THINC [90] schemes.

6.3.1.1 Sine wave propagation test

This test is used to check the convergence rate of the proposed TWENO and TBVD-TWENO-THINC schemes. The smooth initial condition is the same as that in Sec. 3.2.1. The computation domain is $[-1, 1]$, and velocity $u(x) = 1$ and periodic boundary conditions are used. Four different grid sizes ($N = 40, 80, 160$ and 320) are used

with $\Delta t = 0.4\Delta x$ and $\Delta x = 1/N$. The definitions of L_1 error and L_∞ error have been provided in Eq. (6.17) and Eq. (3.30), respectively.

Table 6.2: Errors and convergence rates for sine wave propagation test, at $t=2$.

Method	N	L_1 error	L_1 order	L_∞ error	L_∞ order
TWENO	40	9.50×10^{-6}	-	1.49×10^{-5}	-
	80	2.99×10^{-7}	4.99	4.70×10^{-7}	4.99
	160	9.40×10^{-9}	4.99	1.48×10^{-8}	4.99
	320	2.97×10^{-10}	4.98	4.68×10^{-10}	4.98
TBVD-TWENO-THINC	40	9.50×10^{-6}	-	1.49×10^{-5}	-
	80	2.99×10^{-7}	4.99	4.70×10^{-7}	4.99
	160	9.40×10^{-9}	4.99	1.48×10^{-8}	4.99
	320	2.97×10^{-10}	4.98	4.68×10^{-10}	4.98

Table 6.2 shows the numerical results of the TWENO and TBVD-TWENO-THINC schemes. It is observed that both TWENO and TBVD-TWENO-THINC have fifth-order accuracy for the smooth solution. It indicates that TBVD-TWENO-THINC automatically selects the highest possible polynomial interpolation for a smooth profile.

6.3.1.2 Square wave propagation test

In this section, the square wave propagation test is conducted to verify the proposed schemes of capturing discontinuity. In this test, $u(x) = 1$, the domain $[-1, 1]$, $N = 200$, $\Delta x = 2/N$, and periodic boundary conditions are used. The initial condition is given as

$$\phi(x, 0) = \begin{cases} 1 & \text{if } -0.4 \leq x < 0.4 \\ 0 & \text{otherwise.} \end{cases} \quad (6.16)$$

Fig. 6.6 shows the numerical results of the WENO-Z, TWENO, BVD-WENOZ-THINC, and TBVD-TWENO-THINC schemes at $t=2$ (1 period).

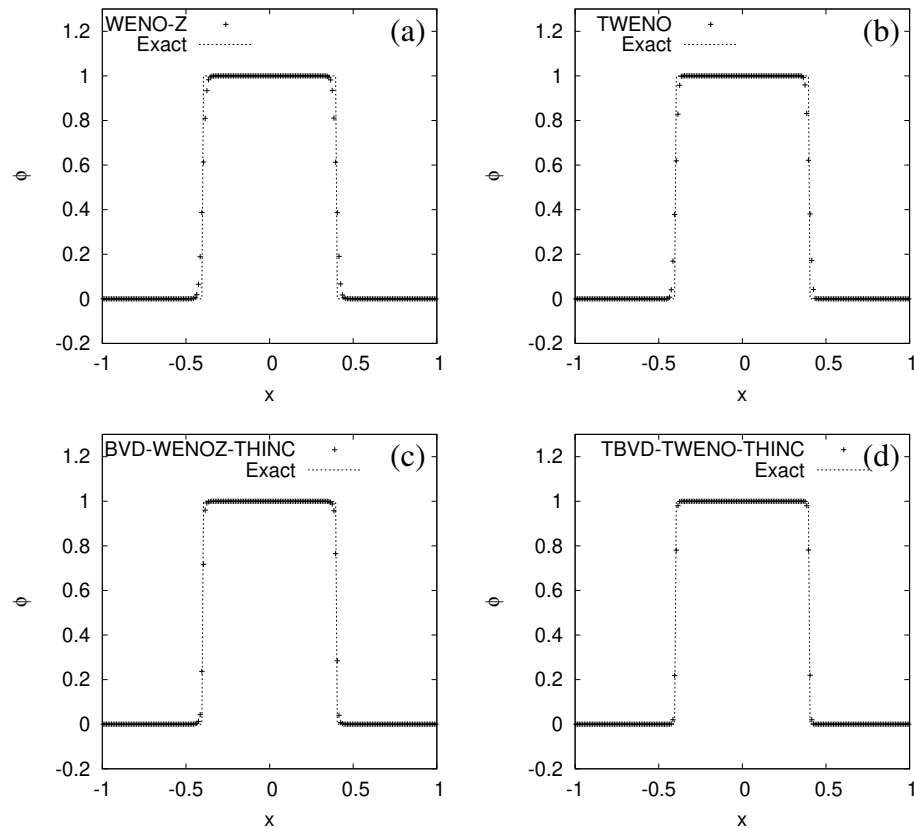


Figure 6.6: Numerical results of square wave propagation test at $t=2$. $N=200$ and $CFL=0.4$ are used. (a) WENO-Z, (b) TWENO, (c) BVD-WENOZ-THINC, (d) TBVD-TWENO-THINC.

It is observed that BVD-WENOZ-THINC and TBVD-TWENO-THINC perform better than WENO-Z and TWENO of capturing discontinuities. Table 6.3 presents the total errors, numerical dissipation errors, numerical dispersion errors, L_1 errors, and L_∞ errors of the WENO-Z, TWENO, BVD-WENOZ-THINC, and TBVD-TWENO-THINC schemes. The results reveal that TWENO has less numerical errors than WENO-Z. Both BVD-WENOZ-THINC and TBVD-TWENO-THINC reduce numerical errors effectively compared to WENOZ and TWENO. In addition, TBVD-TWENO-THINC has the least numerical errors.

Table 6.3: Errors in capturing square wave advection test at $t=2$. $N=200$ and $CFL=0.4$ are used.

	Total error	Dissipation error	Dispersion error	L_1 error	L_∞ error
WENO-Z	3.81×10^{-3}	9.72×10^{-5}	3.71×10^{-3}	1.34×10^{-2}	3.87×10^{-1}
TWENO	3.50×10^{-3}	7.54×10^{-5}	3.43×10^{-3}	1.20×10^{-2}	3.81×10^{-1}
BVD-WENOZ-THINC	1.40×10^{-3}	2.55×10^{-5}	1.37×10^{-3}	6.33×10^{-3}	2.85×10^{-1}
TBVD-TWENO-THINC	9.67×10^{-4}	1.55×10^{-5}	9.51×10^{-4}	4.81×10^{-3}	2.19×10^{-1}

6.3.1.3 Complex wave propagation test

In this section, the Jiang-Shu complex wave propagation test [1] is conducted with the same initial conditions in Sec. 3.2.3. Fig. 6.7 illustrates the numerical results of the WENO-Z, TWENO, BVD-WENOZ-THINC, and TBVD-TWENO-THINC schemes at $t=2$ (1 period). It is observed that both BVD-WENOZ-THINC and TBVD-TWENO-THINC perform better than WENO-Z and TWENO for discontinuities. In addition, TBVD-TWENO-THINC obtains sharper solutions for the cusps and the square profile than BVD-WENOZ-THINC. Table 6.4 presents the results of numerical errors of the WENO-Z, TWENO, BVD-WENOZ-THINC, and TBVD-TWENO-THINC schemes. The results reveal that TWENO has less numerical errors than WENO-Z. Both BVD-WENOZ-THINC and TBVD-TWENO-THINC have smaller numerical errors compared to WENOZ and TWENO, respectively. Moreover, TBVD-TWENO-THINC has the least numerical errors.

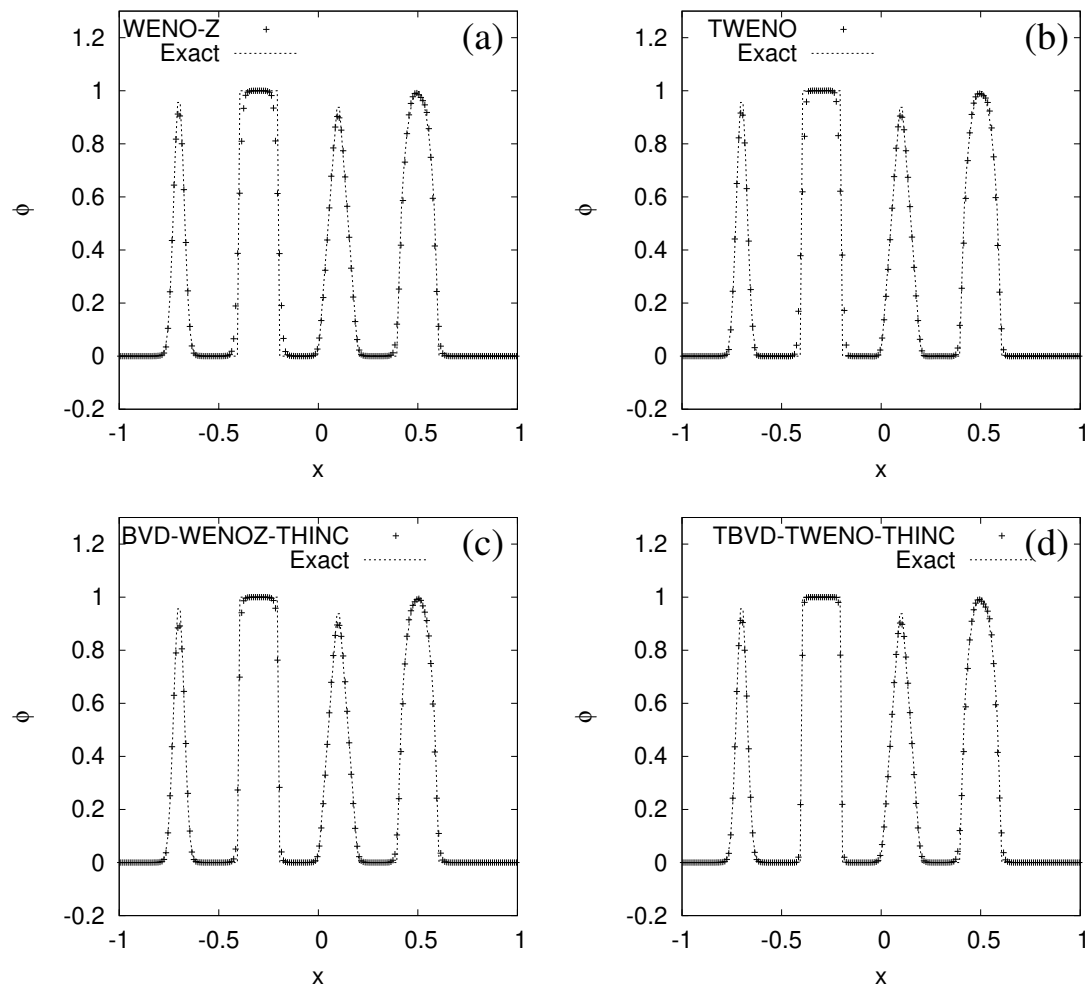


Figure 6.7: Numerical results of complex wave propagation test at $t=2$. $N=200$ and $CFL=0.4$ are used. (a) WENO-Z, (b) TWENO, (c) BVD-WENOZ-THINC, (d) TBVD-TWENO-THINC.

Table 6.4: Errors in capturing complex wave propagation test at $t=2$. $N=200$ and $CFL=0.4$ are used.

	Total error	Dissipation error	Dispersion error	L_1 error	L_∞ error
WENO-Z	4.28×10^{-3}	2.47×10^{-4}	4.03×10^{-3}	2.23×10^{-2}	3.87×10^{-1}
TWENO	3.92×10^{-3}	1.70×10^{-4}	3.75×10^{-3}	2.05×10^{-2}	3.80×10^{-1}
BVD-WENOZ-THINC	2.05×10^{-3}	1.01×10^{-4}	1.95×10^{-3}	1.59×10^{-2}	3.01×10^{-1}
TBVD-TWENO-THINC	1.44×10^{-3}	6.70×10^{-5}	1.37×10^{-3}	1.38×10^{-2}	2.19×10^{-1}

6.3.1.4 Extrema of the various smoothness problem

In this section, we verify the proposed scheme by performing the extrema of the various smoothness test. The initial conditions are the same as those in Sec. 3.2.4. The domain $[-1.0, 1.0]$, $u(x) = 1$, $N = 100$. Numerical results at $t = 2$ (1 period) are shown in Fig. 6.8. It is evident that BVD-WENOZ-THINC performs better than WENO-Z and TWENO for discontinuities. In addition, TBVD-TWENO-THINC obtains a sharper solution for discontinuities than BVD-WENOZ-THINC. Table 6.5 shows the results

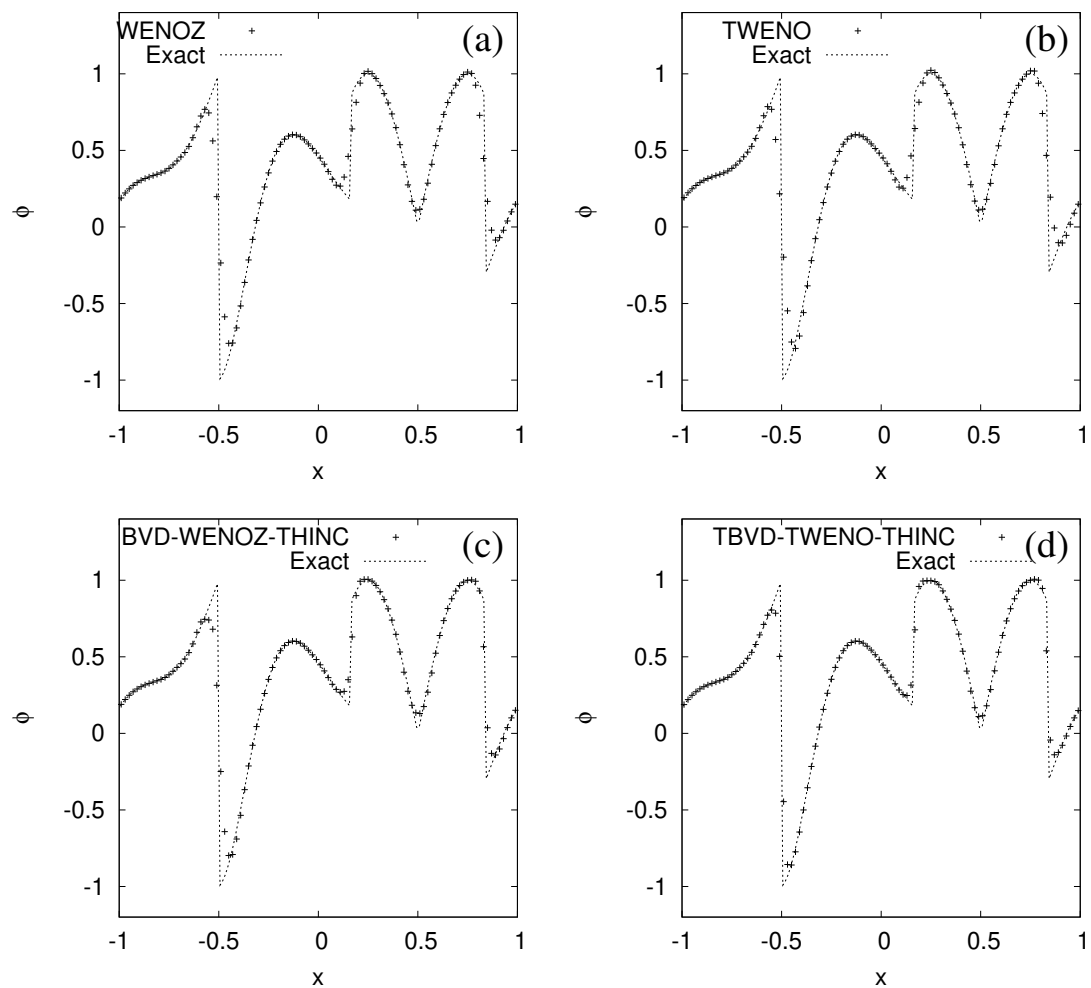


Figure 6.8: Numerical results of capturing the extrema of the various smoothness test at $t=2$. $N=100$ and $CFL=0.4$ are used. (a) WENO-Z, (b) TWENO, (c) BVD-WENOZ-THINC, (d) TBVD-TWENO-THINC.

Table 6.5: Numerical errors in capturing extrema of the various smoothness test at $t=2$. $N=100$ and $CFL=0.4$ are used.

	Total error	Dissipation error	Dispersion error	L_1 error	L_∞ error
WENO-Z	2.02×10^{-2}	2.70×10^{-3}	1.75×10^{-2}	5.08×10^{-2}	7.66×10^{-1}
TWENO	2.00×10^{-2}	2.55×10^{-3}	1.74×10^{-2}	5.07×10^{-2}	7.56×10^{-1}
BVD-WENOZ-THINC	1.42×10^{-2}	1.52×10^{-3}	1.27×10^{-2}	4.07×10^{-2}	7.36×10^{-1}
TBVD-TWENO-THINC	7.62×10^{-3}	7.16×10^{-4}	6.91×10^{-3}	2.78×10^{-2}	5.29×10^{-1}

of numerical errors of the WENO-Z, TWENO, BVD-WENOZ-THINC, and TBVD-TWENO-THINC schemes. Results show that TWENO has less numerical errors than WENO-Z. BVD-WENOZ-THINC and TBVD-TWENO-THINC have smaller numerical errors compared to WENOZ and TWENO. Overall, TBVD-TWENO-THINC has the least numerical errors. These results are consistent with the results of the complex wave propagation test.

6.3.2 1D Euler equations

In this section, we validate the proposed schemes by solving the Euler equations. Roe's approximate Riemann solver [61, 140, 70] (in Appendix B) is used. The numerical results of the proposed TBVD-TWENO-THINC scheme are compared to the results of the WENO-Z[32] and BVD-WENOZ-THINC [90] schemes.

6.3.2.1 Sod's problem

This test is used to solve the Sod's problem with shock and contact discontinuity. The initial condition is set as the same as that in Sec. 3.2.6. Fig. 6.9 shows the numerical results of density. It is observed that WENO-Z, BVD-WENOZ-THINC, and TBVD-TWENO-THINC capture contact discontinuity and shock well without numerical oscillation. For the discontinuity region, BVD-WENOZ-THINC and TBVD-TWENO-THINC resolve the discontinuity with less numerical diffusion compared to WENO-Z.

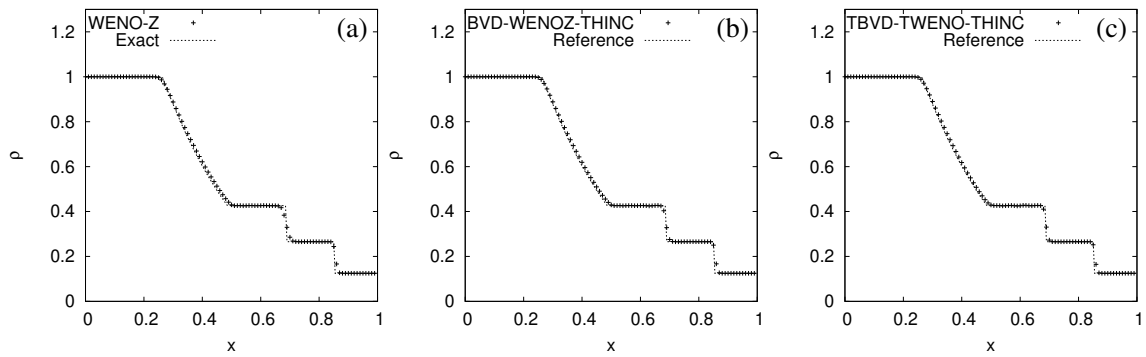


Figure 6.9: Numerical results for Sod's shock tube problem at $t = 0.2$ with density output (CFL=0.2 and $N=100$). (a) WENO-Z, (b) BVD-WENOZ-THINC, (c) TBVD-TWENO-THINC.

6.3.2.2 Lax's problem

This test is used to solve the Lax's problem with strong shock and contact discontinuity. The initial condition is set as the same as that in Sec. 4.2.3. Fig. 6.10 shows the numerical results at time $t=0.16$ with mesh size $N = 100$.

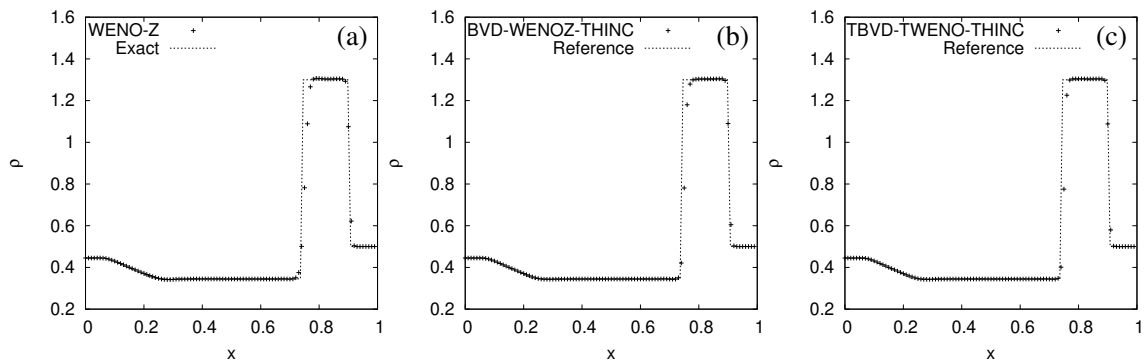


Figure 6.10: Numerical results of Lax's shock tube problem at $t=0.16$ (CFL=0.2 and $N=100$). (a) WENO-Z, (b) BVD-WENOZ-THINC, (c) TBVD-TWENO-THINC.

It is observed that WENO-Z, BVD-WENOZ-THINC, and TBVD-TWENO-THINC capture shocks well without numerical oscillation. BVD-WENOZ-THINC performs better than WENO-Z for capturing discontinuity. In addition, TBVD-TWENO-THINC

resolves the discontinuity with less numerical diffusion compared to BVD-WENOZ-THINC.

6.3.2.3 The shock turbulence problem

This test is used to solve the shock-turbulence problem [79] with discontinuity, low-frequency and high-frequency wave profiles. The initial condition is set as the same as that in Sec. 4.2.4. Fig. 6.11 shows the numerical results of WENO-Z, BVD-WENOZ-THINC and TBVD-TWENO-THINC at $t=0.18$. It is observed that there is

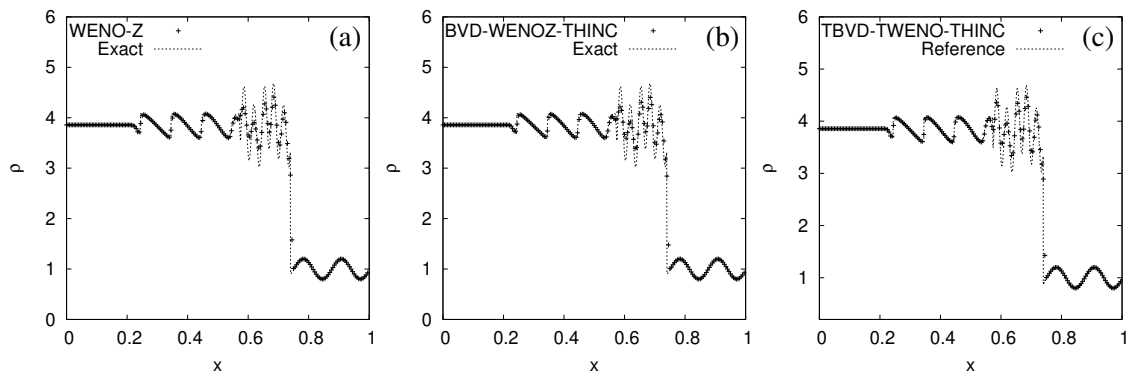


Figure 6.11: Numerical results of shock-turbulence interaction problem at time $t=0.18$ (CFL=0.2 and $N=200$). (a) WENO-Z, (b) BVD-WENOZ-THINC, (c) TBVD-TWENO-THINC.

no significant difference for capturing low-frequency wave profiles among all the compared schemes. However, for high-frequency wave profiles, TBVD-TWENO-THINC performs better than WENO-Z and BVD-WENOZ-THINC.

6.3.2.4 Two blast waves interaction problem

This test is used to solve the two interacting blast waves problem. The initial condition of this test is set as the same as that in Sec. 4.2.5. Due to the violent interaction, the existence of oscillation may cause the break up of the simulation. Another difficulty for

existing shock-capturing schemes is the overly smeared density discontinuities in the numerical solution [90]. The numerical results of WENO-Z, BVD-WENOZ-THINC, and TBVD-TWENO-THINC at time $t = 0.038$ are shown in Fig. 6.12.

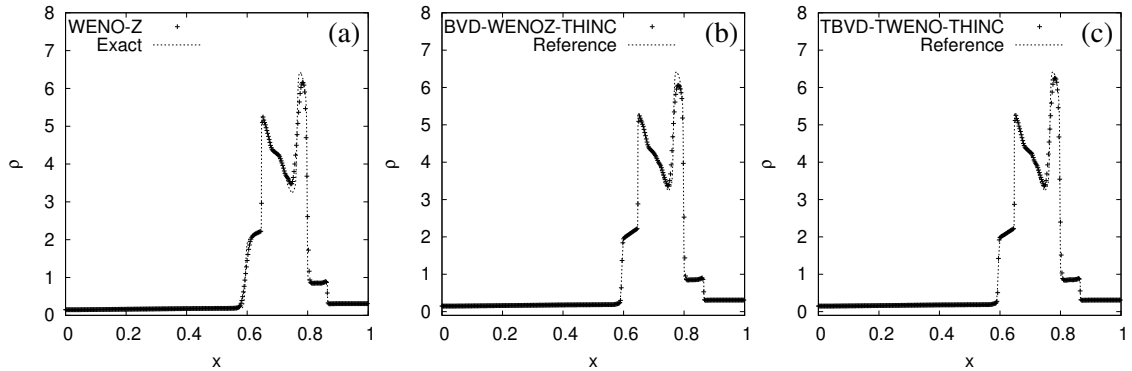


Figure 6.12: Numerical results of two interacting blast waves problem at $t=0.038$ and $N=400$. (a) WENO-Z, (b) BVD-WENOZ-THINC, (c) TBVD-TWENO-THINC.

It is observed that WENO-Z is diffusive near the left-most density discontinuity around $x = 0.6$. However, both BVD-WENOZ-THINC and TBVD-TWENO-THINC reduce the numerical diffusion in vicinity of the density discontinuity effectively. For the region around $x = 0.78$, TBVD-TWENO-THINC performs better than WENOZ and BVD-WENOZ-TINC. The resolution of the left-most density discontinuity around $x = 0.6$ by TBVD-TWENO-THINC is also superior to other compared schemes.

6.3.3 2D square profile propagation in diagonal direction test

In this section, we conduct the simulation of transporting a square profile with a constant diagonal velocity. The initial condition of the square profile is given in Fig. 6.13 (a). The numerical calculation domain is $[-1, 1]$ with the grid of 100×100 and the time is one revolution. Error is defined as

$$Error = \frac{1}{N^2} \sum_{\Omega} |\phi_{i,j} - \phi_{i,j}^{exact}|, \quad (6.17)$$

Here, Ω represents the domain, N is the mesh number in each direction. $\phi_{i,j}$ is the numerical solution and $\phi_{i,j}^{exact}$ is the exact solution.

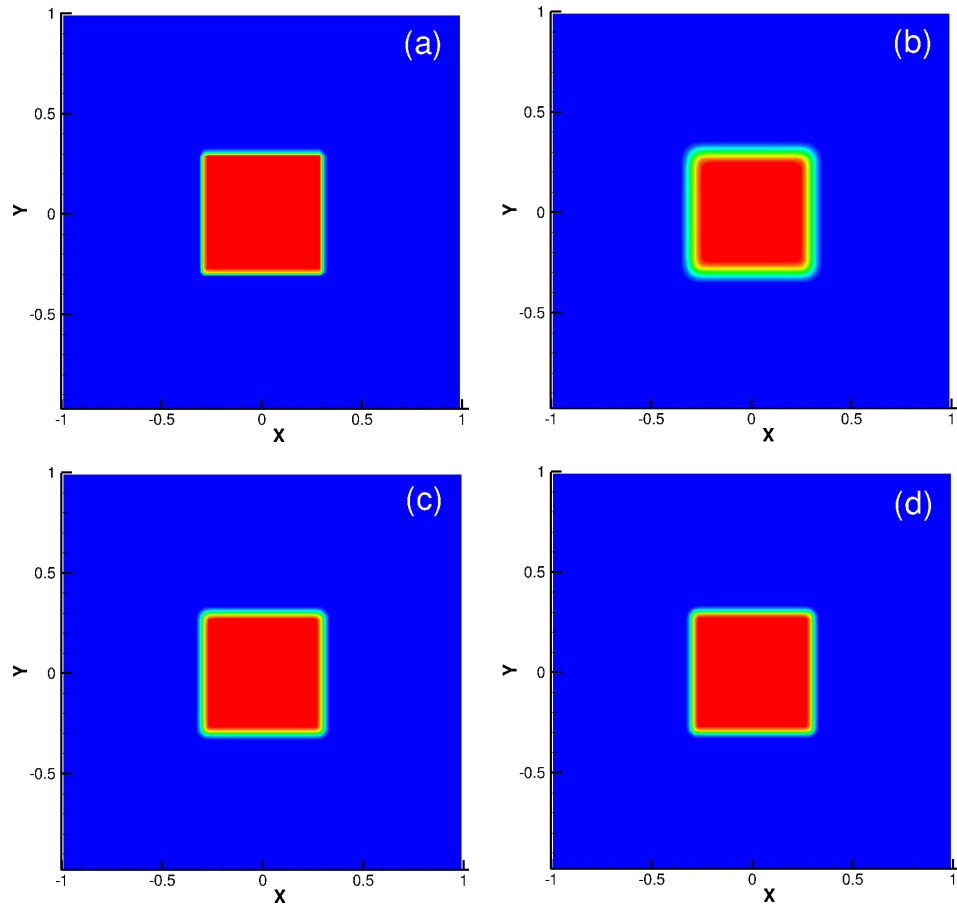


Figure 6.13: Numerical results of 2D square wave propagation test at $t=2$ from top views. (a) Initial profile, (b) WENO-Z, (c) BVD-WENOZ-THINC, (d) TBVD-TWENO-THINC.

From the results shown in Fig. 6.13, it can be observed that WENO-Z is more diffusive than BVD-WENOZ-THINC and TBVD-TWENO-THINC. Table 6.6 shows the numerical errors. BVD-WENOZ-THINC has a smaller numerical error than WENO-Z. In addition, TBVD-TWENO-THINC has the least numerical error.

Table 6.6: Errors in capturing 2D square wave propagation test, mesh: 100*100.

Method	Error
WENO-Z	1.27×10^{-2}
BVD-WENOZ-THINC	7.05×10^{-3}
TBVD-TWENO-THINC	5.73×10^{-3}

6.3.4 2D Zelasak's test

In this section, one revolution of Zelasak's test [141] is conducted on a Cartesian grid (200×200). In the Zelasak's test, a slotted disk is rotated with a constant angular velocity. The initial profile is given in Fig. 6.14 (a).

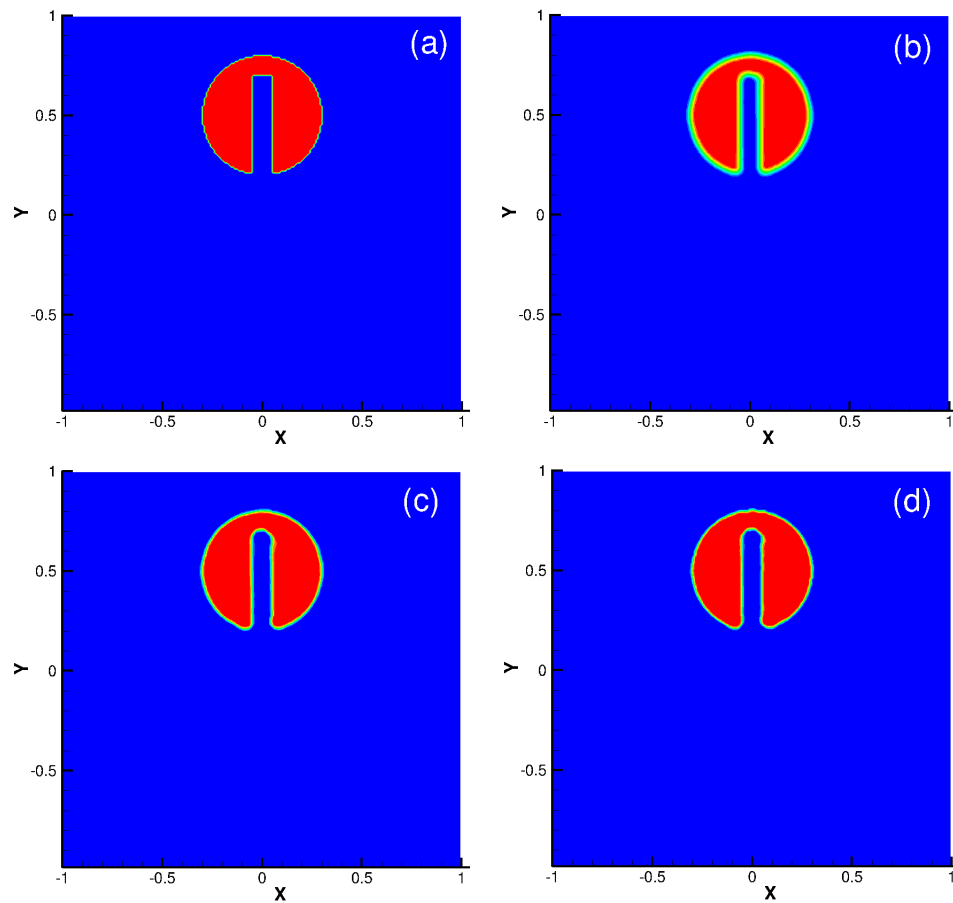


Figure 6.14: 2D Zelasak test. (a) Initial profile, (b) WENO-Z, (c) BVD-WENOZ-THINC, (d) TBVD-TWENO-THINC.

Table 6.7: Errors in capturing 2D Zelasak test, mesh: 200*200.

Method	Error
WENO-Z	9.04×10^{-3}
BVD-WENOZ-THINC	4.38×10^{-3}
TBVD-TWENO-THINC	3.69×10^{-3}

It can be observed in Fig. 6.14 that BVD-WENOZ-THINC and TBVD-TWENO-THINC resolve the shape of the rotation notched cylinder sharper than WENO-Z. Table 6.7 shows the numerical errors of the WENO-Z, TWENO, BVD-WENOZ-THINC, and TBVD-TWENO-THINC schemes. It can be found that TBVD-TWENO-THINC has the least numerical error. We also calculate the convergence study of the TBVD-TWENO-THINC scheme for this model problem in Table 6.8. The convergence is approximately linear.

Table 6.8: Errors and convergence rates for Zelasak test problem by TBVD-TWENO-THINC.

Grid spacing	1/50	Rate	1/100	Rate	1/200
TBVD-TWENO-THINC	1.88×10^{-2}	1.23	8.03×10^{-3}	1.12	3.69×10^{-3}

6.3.5 2D double-Mach reflection problem

To verify the proposed method in capturing strong shocks and vortices, the double-Mach reflection test [134] is conducted as a qualitative comparison in this section. This benchmark test involves a Mach 10 shock hitting a ramp which is inclined by 30 degrees. The coordinate system is aligned with the ramp for the numerical tests. Reflecting boundary condition is used on the bottom and an isolated moving oblique Mach 10 shock is imposed on the top. Inflow and outflow boundary conditions are used on the left and right sides. The domain is $[0, 4] \times [0, 1]$, $t = 0.2$. Fig. 6.15 shows the sketch of double-Mach reflection problem and Fig. 6.16 shows the experiment results

performed by Smith [4].

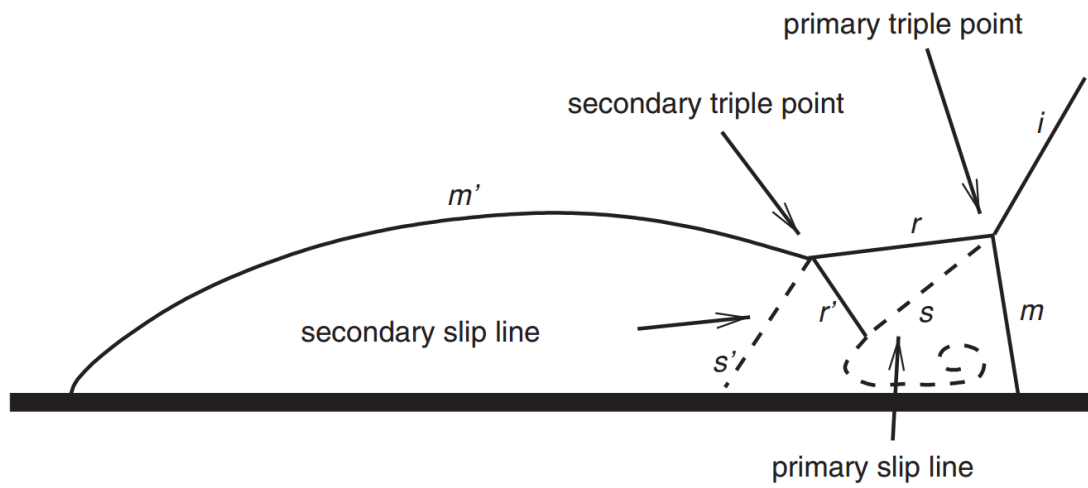


Figure 6.15: Sketch of double-Mach reflection problem [3].

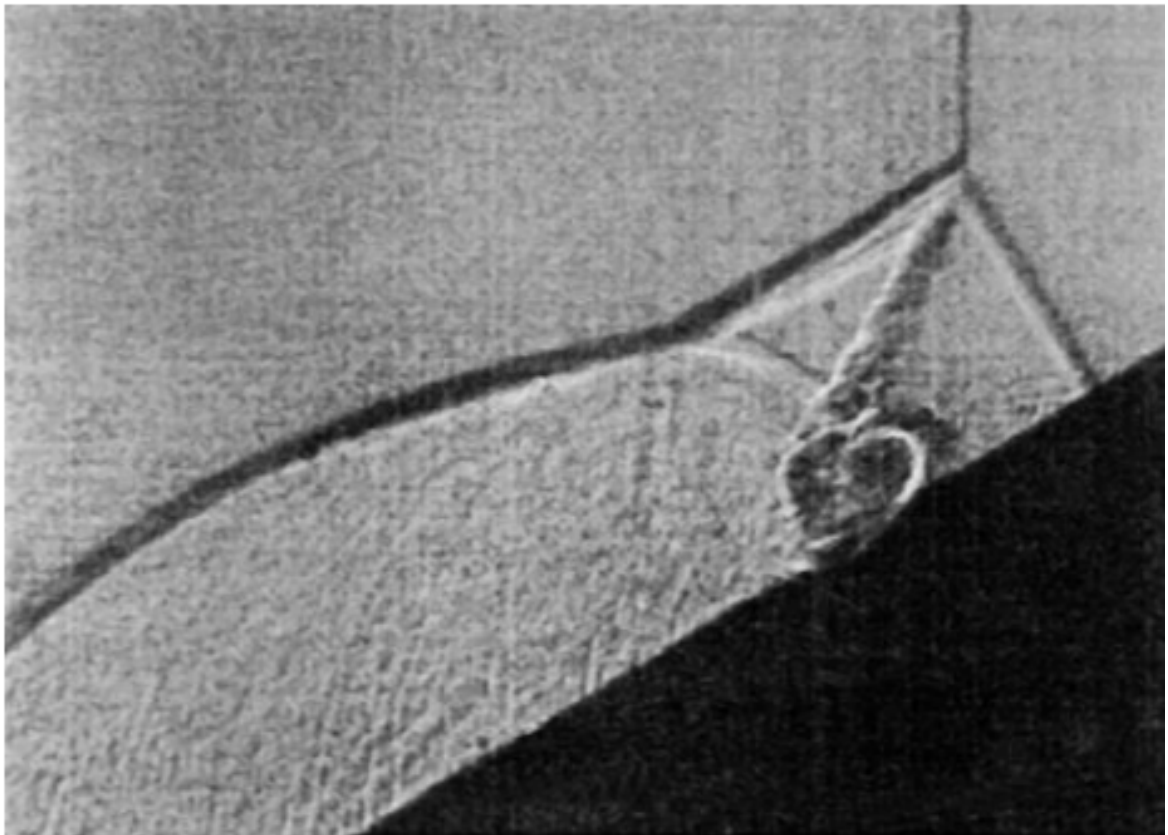


Figure 6.16: Experiment results of double-Mach reflection problem performed by L.G. Smith [4].

In the double-Mach reflection problem, when the shock runs up the ramp, a self-similar shock structure with two triple points evolves, as shown in Fig. 6.15. At the primary triple point, the Mach stem (m), the incident shock (i), and the reflected shock (r) are joined. The reflected wave emanates from the triple point and travels transversely behind the incident shock. When the reflected shock r breaks up, a secondary triple point is formed. At the secondary triple point, the secondary Mach stem (m'), the secondary reflected shock (r'), and the reflected shock r meet. From the primary triple point, a slip line (s) (sometimes called contact surface) emanates. The secondary reflected shock r' hits this slip line s and causes a curled flow structure, the resolution of which may serve as an indicator for the resolution of a numerical scheme [3].

Fig. 6.17 illustrates the numerical results of the WENO-Z, BVD-WENOZ-THINC, TBVD-TWENO-THINC, WENOCU-6 [33, 142], eighth-order TENO8 [89], and TENO8-opt [89] schemes in the region $[2, 3] \times [0, 1]$ with a 512×128 mesh. It is observed that the numerical results of WENO-Z, BVD-WENOZ-THINC, WENO-CU6, TENO8, and TENO8-opt are more diffusive compared to TBVD-TWENO-THINC. Specifically, TBVD-TWENO-THINC captures more small-scale structures along the slip line compared to that from other schemes. On the fine mesh 1024×256 (shown in Fig. 6.18), BVD-WENOZ-THINC, TBVD-TWENO-THINC, WENO-CU6, TENO8, and TENO8-opt are able to adequately resolve the small-scale vortex structures along the slip line. BVD-WENOZ-THINC is slightly more diffusive than TBVD-TWENO-THINC along the slip line.

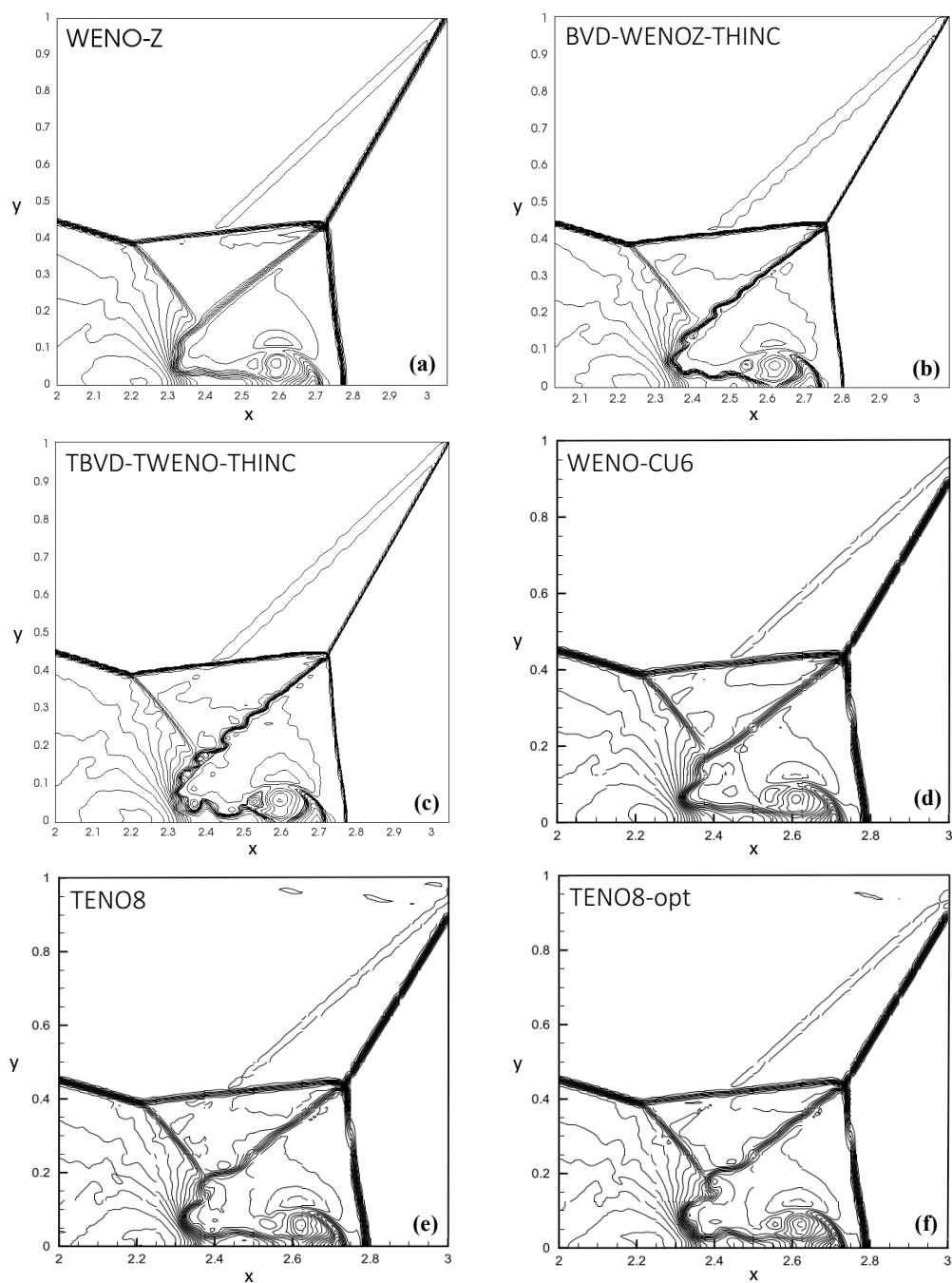


Figure 6.17: Zoomed-in view of double-Mach reflection test with a qualitative comparison: density contours by (a) WENO-Z, (b) BVD-WENOZ-THINC, (c) TBVD-TWENO-THINC, (d) WENO-CU6, (e) TENO8 and (f) TENO8-opt at $t = 0.2$, with a 512×128 mesh. This figure is drawn with density contours between 1.887 and 20.9.

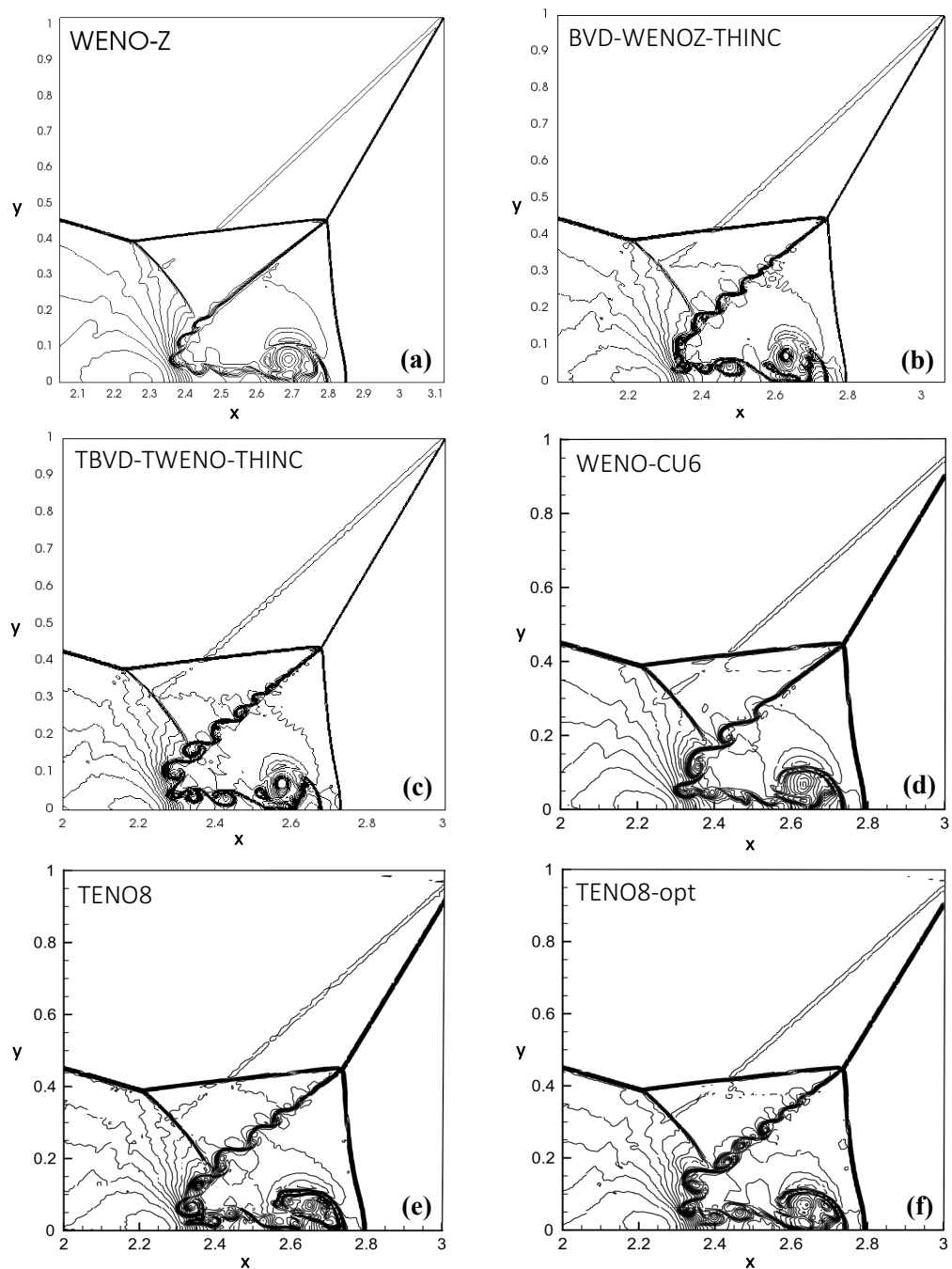


Figure 6.18: Zoomed-in view of double-Mach reflection test with a qualitative comparison: density contours by (a) WENO-Z, (b) BVD-WENOZ-THINC, (c) TBVD-TWENO-THINC, (d) WENO-CU6, (e) TENO8 and (f) TENO8-opt at $t = 0.2$, with a 1024×256 mesh. This figure is drawn with density contours between 1.887 and 20.9.

6.4 Summary

In this chapter, firstly, we proposed the TWENO scheme based on the fifth-order WENO scheme. Instead of using all adjacent smooth sub-stencils, the possible highest order interpolation was built on two target adjacent sub-stencils or three target sub-stencils. Secondly, an adaptive parameter was designed to control the jump thickness of the THINC scheme. Based on the TWENO and THINC schemes, a high-resolution TBVD-TWENO-THINC scheme was proposed by implementing the TBVD algorithm.

A variety of numerical tests were conducted to validate the TBVD-TWENO-THINC scheme. The results reveal that the TBVD-TWENO-THINC scheme has fifth-order accuracy for smooth solutions. For discontinuities, the TBVD-TWENO-THINC scheme has less numerical diffusion compared to the WENO-Z and BVD-WENOZ-THINC schemes. In addition, the numerical results of the double-Mach reflection tests have shown that the TBVD-TWENO-THINC scheme is able to better resolve the small-scale vortex structures along the slip line than the WENO-Z, BVD-WENOZ-THINC, WENO-CU6, TENO8 and TENO8-opt schemes with the same mesh of 512×128 . This suggests that the TBVD-TWENO-THINC scheme can be an effective high-resolution numerical scheme to simulate compressible flow problems.

Numerical simulation of compressible two-phase flows

Compressible two-phase flows contain a mixing region of two materials. The material interface of compressible two-phase flows makes the physics more complicate. When implementing the one-fluid model to compressible multiphase flow with moving interface, there are two substantial problems. Firstly, density and energy are calculated separately in addition to the indication function, hence special formulations are required to reach a balanced state among all variables for the interface cell. Secondly, the numerical dissipation in high-resolution schemes designed for solving single phase compressible flow involving shock waves tends to smear out discontinuities, including the material interfaces.

To resolve the first issue, in this chapter, the five-equation model [42] is used as the partial differential equation (PDE) that needs to be solved. This model combines Euler equations with interface indication function equations for each of fluid components, which is used as an efficient approximation to the state of the interface cell. To resolve the second issue, the proposed spatial reconstruction scheme in last chapter (TBVD-TWENO-THINC) is used to reduce numerical dissipation so as to maintain the sharpness of the jumps in volume fraction that identify the moving interfaces.

7.1 Computational model

For inviscid compressible two-phase flows, the five-equation model [42] is used as the computational model. By assuming that the material interface is in equilibrium of mixed pressure and velocity, the five-equation model comprises the following two continuity phasic mass equations, a momentum equation, an energy equation, and an advection equation of volume fraction:

$$\begin{aligned}
\frac{\partial}{\partial t}(\alpha_1 \rho_1) + \nabla \cdot (\alpha_1 \rho_1 \mathbf{u}) &= 0, \\
\frac{\partial}{\partial t}(\alpha_2 \rho_2) + \nabla \cdot (\alpha_2 \rho_2 \mathbf{u}) &= 0, \\
\frac{\partial}{\partial t}(\rho \mathbf{u}) + \nabla \cdot (\rho \mathbf{u} \otimes \mathbf{u}) + \nabla p &= 0, \\
\frac{\partial E}{\partial t} + \nabla \cdot (E \mathbf{u} + p \mathbf{u}) &= 0, \\
\frac{\partial \alpha_1}{\partial t} + \mathbf{u} \cdot \nabla \alpha_1 &= 0,
\end{aligned} \tag{7.1}$$

where ρ_k and $\alpha_k \in [0, 1]$ denote the k -th phasic density and volume fraction for $k = 1, 2$. Further, \mathbf{u} is the vector velocity, p is the pressure, and E is the total energy. The mixed volume fraction, density, and internal energy satisfy the following conditions.

$$\begin{aligned}
\alpha_1 + \alpha_2 &= 1, \\
\alpha_1 \rho_1 + \alpha_2 \rho_2 &= \rho, \\
\alpha_1 \rho_1 e_1 + \alpha_2 \rho_2 e_2 &= \rho e.
\end{aligned} \tag{7.2}$$

To close the system, the following Mie-Grüneisen equation of state is used for each phase as follows

$$p_k(\rho_k, e_k) = p_{\infty, k}(\rho_k) + \rho_k \Gamma_k(\rho_k)(e_k - e_{\infty, k}(\rho_k)), \tag{7.3}$$

where $\Gamma_k(\rho_k)$ is the Grüneisen coefficient and $p_{\infty, k}(\rho_k)$, $e_{\infty, k}(\rho_k)$ are the appropriately chosen states of the pressure and internal energy along some reference curves. This equation of state can be used for a wide variety of materials, including some gaseous or solid explosives and solid metals under high pressure. Based on the derivation in

[143], the mixture Grüneisen coefficient and $p_{\infty,k}(\rho_k)$, $e_{\infty,k}(\rho_k)$ can be expressed as

$$\begin{aligned}\frac{\alpha_1}{\Gamma_1(\rho_1)} + \frac{\alpha_2}{\Gamma_2(\rho_2)} &= \frac{1}{\Gamma}, \\ \alpha_1 \rho_1 e_{\infty,1}(\rho_1) + \alpha_2 \rho_2 e_{\infty,2}(\rho_2) &= \rho e_{\infty}, \\ \alpha_1 \frac{p_{\infty,1}(\rho_1)}{\Gamma_1(\rho_1)} + \alpha_2 \frac{p_{\infty,2}(\rho_2)}{\Gamma_2(\rho_2)} &= \frac{p_{\infty}(\rho)}{\Gamma(\rho)}.\end{aligned}\quad (7.4)$$

The mixture pressure can be expressed as

$$p = \left(\rho e - \sum_{k=1}^2 \alpha_k \rho_k e_{\infty,k}(\rho_k) + \sum_{k=1}^2 \alpha_k \frac{p_{\infty,k}(\rho_k)}{\Gamma_k(\rho_k)} \right) / \sum_{k=1}^2 \frac{\alpha_k}{\Gamma_k(\rho_k)}. \quad (7.5)$$

Eqs. (7.4) and (7.5) guarantee the mixed pressure to be free of spurious oscillations. This is important to prevent the spurious pressure oscillation across the material interfaces [143, 144, 145].

7.2 Numerical method

For the sake of simplicity, the numerical method is explained in one dimension. It can be directly extended to the multi-dimensions on structured grids in dimension-wise reconstruction fashion. One dimensional quasi-conservative five-equation model Eq. (7.1) can be written as

$$\frac{\partial \mathbf{q}}{\partial t} + \frac{\partial \mathbf{f}(\mathbf{q})}{\partial x} + \mathbf{B}(\partial \mathbf{q}) \frac{\partial \mathbf{q}}{\partial x} = 0, \quad (7.6)$$

where the vectors of physical variables \mathbf{q} is

$$\mathbf{q} = \begin{pmatrix} \alpha_1 \rho_1 \\ \alpha_2 \rho_2 \\ \rho u \\ E \\ \alpha_1 \end{pmatrix}, \quad (7.7)$$

and the vectors of flux functions $\mathbf{f}(\mathbf{q})$ is

$$\mathbf{f}(\mathbf{q}) = \begin{pmatrix} \alpha_1 \rho_1 u \\ \alpha_2 \rho_2 u \\ \rho u^2 + p \\ Eu + pu \\ 0 \end{pmatrix}, \quad (7.8)$$

The matrix \mathbf{B} is defined as

$$\mathbf{B} = \text{diag}(0, 0, 0, 0, u), \quad (7.9)$$

where u is the x component velocity. In finite volume method, the volume-integrated average value $\bar{\mathbf{q}}_i(t)$ is defined as

$$\bar{\mathbf{q}}_i(t) = \frac{1}{\Delta x} \int_{x_{i-1/2}}^{x_{i+1/2}} \mathbf{q}(x, t) dx. \quad (7.10)$$

The semi-discrete version of the finite volume formulation can be expressed as a system of ordinary differential equations (ODEs). Denoting the spatial discretization terms by $L(\bar{\mathbf{q}}_i(t))$, in the wave-propagation method, the spatial discretization is computed by

$$\frac{\partial \bar{\mathbf{q}}_i(t)}{\partial t} = L(\bar{\mathbf{q}}_i(t)) = -\frac{1}{\Delta x} (\mathcal{A}^R \Delta \mathbf{q}_{i-1/2} + \mathcal{A}^L \Delta \mathbf{q}_{i+1/2} + \mathcal{A} \Delta \mathbf{q}_i), \quad (7.11)$$

where $\mathcal{A}^R \Delta \mathbf{q}_{i-1/2}$ and $\mathcal{A}^L \Delta \mathbf{q}_{i+1/2}$ are the right-moving and left-moving fluctuations, which can be calculated by

$$\mathcal{A}^R \Delta \mathbf{q}_{i-1/2} = \sum_{k=1}^3 [s^k(\mathbf{q}_{i-1/2}^L, \mathbf{q}_{i-1/2}^R)]^R \mathcal{W}^k(\mathbf{q}_{i-1/2}^L, \mathbf{q}_{i-1/2}^R), \quad (7.12)$$

$$\mathcal{A}^L \Delta \mathbf{q}_{i+1/2} = \sum_{k=1}^3 [s^k(\mathbf{q}_{i+1/2}^L, \mathbf{q}_{i+1/2}^R)]^L \mathcal{W}^k(\mathbf{q}_{i+1/2}^L, \mathbf{q}_{i+1/2}^R), \quad (7.13)$$

and $\mathcal{A} \Delta \mathbf{q}_i$ is the total fluctuation, which can be calculated by

$$\mathcal{A} \Delta \mathbf{q}_i = \sum_{k=1}^3 [s^k(\mathbf{q}_{i-1/2}^R, \mathbf{q}_{i+1/2}^L)] \mathcal{W}^k(\mathbf{q}_{i-1/2}^R, \mathbf{q}_{i+1/2}^L), \quad (7.14)$$

where $\mathbf{q}_{i\pm 1/2}^L$ and $\mathbf{q}_{i\pm 1/2}^R$ are the key point values to obtain the Riemann numerical flux. In this work, $\mathbf{q}_{i\pm 1/2}^L$ and $\mathbf{q}_{i\pm 1/2}^R$ are reconstructed by the TBVD-TWENO-THINC scheme proposed in Chapter 6. Given the reconstructed values $\mathbf{q}_{i-1/2}^L$ and $\mathbf{q}_{i-1/2}^R$, the moving speed s^k and the jumps \mathcal{W}^k of three propagating discontinuities can be solved by the HLLC Riemann solver [54] as described below.

Firstly, the minimum and maximum moving speeds $s^1(\mathbf{q}_{i-1/2}^L, \mathbf{q}_{i-1/2}^R)$ and $s^3(\mathbf{q}_{i-1/2}^L, \mathbf{q}_{i-1/2}^R)$ can be estimated as

$$s^1 = \min(u_{i-1/2}^L - c_{i-1/2}^L, u_{i-1/2}^R - c_{i-1/2}^R), \quad (7.15)$$

$$s^2 = \min(u_{i-1/2}^L + c_{i-1/2}^L, u_{i-1/2}^R + c_{i-1/2}^R), \quad (7.16)$$

where $c_{i-1/2}^L$ and $c_{i-1/2}^R$ are sound speeds calculated by reconstructed values $\mathbf{q}_{i-1/2}^L$ and $\mathbf{q}_{i-1/2}^R$, respectively. Using s^1 and s^2 , the speed of the middle wave can be estimated by

$$s^3 = \frac{p_{i-1/2}^R - p_{i-1/2}^L + \rho_{i-1/2}^L u_{i-1/2}^L (s^1 - u_{i-1/2}^L) - \rho_{i-1/2}^R u_{i-1/2}^R (s^3 - u_{i-1/2}^R)}{\rho_{i-1/2}^L (s^1 - u_{i-1/2}^L) - \rho_{i-1/2}^R (s^3 - u_{i-1/2}^R)}. \quad (7.17)$$

The intermediate state variables $\mathbf{q}_{i-1/2}^{*R}$ and $\mathbf{q}_{i-1/2}^{*L}$ are computed as

$$\mathbf{q}_{i-1/2}^{*R} = \frac{(u_{i-1/2}^R - s^3)\mathbf{q}_{i-1/2}^R + (p_{i-1/2}^R \mathbf{n}_{i-1/2}^R - p_{i-1/2}^* \mathbf{n}_{i-1/2}^*)}{s^2 - s^3}, \quad (7.18)$$

$$\mathbf{q}_{i-1/2}^{*L} = \frac{(u_{i-1/2}^L - s^1)\mathbf{q}_{i-1/2}^L + (p_{i-1/2}^L \mathbf{n}_{i-1/2}^L - p_{i-1/2}^* \mathbf{n}_{i-1/2}^*)}{s^2 - s^1}, \quad (7.19)$$

where the vector $\mathbf{n}_{i-1/2}^L = (0, 0, 1, u_{i-1/2}^L, 0)$ and $\mathbf{n}_{i-1/2}^* = (0, 0, 1, s^2, 0)$. The intermediate pressure can be estimated as

$$\begin{aligned} p_{i-1/2}^* &= \rho_{i-1/2}^L (u_{i-1/2}^L - s^1)(u_{i-1/2}^L - s^2) + p_{i-1/2}^L \\ &= \rho_{i-1/2}^R (u_{i-1/2}^R - s^1)(u_{i-1/2}^R - s^2) + p_{i-1/2}^R. \end{aligned} \quad (7.20)$$

Then, the jumps \mathcal{W}^k can be computed as

$$\begin{aligned}\mathcal{W}^1 &= \mathbf{q}_{i-1/2}^{*L} - \mathbf{q}_{i-1/2}^L, \\ \mathcal{W}^2 &= \mathbf{q}_{i-1/2}^{*R} - \mathbf{q}_{i-1/2}^{*L}, \\ \mathcal{W}^3 &= \mathbf{q}_{i-1/2}^R - \mathbf{q}_{i-1/2}^{*R}.\end{aligned}\tag{7.21}$$

Given the spatial discretization, the following three-stage third-order Strong Stability-Preserving (SSP) Runge-Kutta scheme [146] is employed to solve the time evolution of ODEs.

$$\begin{aligned}\bar{\mathbf{q}}_i^* &= \bar{\mathbf{q}}_i^n + \Delta t L(\bar{\mathbf{q}}_i^n), \\ \bar{\mathbf{q}}_i^{**} &= \frac{3}{4}\bar{\mathbf{q}}_i^n + \frac{1}{4}\bar{\mathbf{q}}_i^* + \frac{1}{4}\Delta t L(\bar{\mathbf{q}}_i^*), \\ \bar{\mathbf{q}}_i^{n+1} &= \frac{1}{3}\bar{\mathbf{q}}_i^n + \frac{2}{3}\bar{\mathbf{q}}_i^* + \frac{2}{3}\Delta t L(\bar{\mathbf{q}}_i^{**}),\end{aligned}\tag{7.22}$$

where $\bar{\mathbf{q}}_i^*$ and $\bar{\mathbf{q}}_i^{**}$ denote the intermediate values at the sub-steps.

7.3 Numerical results

7.3.1 Passive advection of a square liquid column

To validate the ability of the proposed scheme for simulating compressible two-phase problems, we first consider an interface-only problem in one dimension. The problem consists of a square liquid column in gas transported with a uniform velocity $u = 10^2 m/s$ under equilibrium pressure $p = 10^5$ Pa in a shock tube of one meter. The stiffened gas equation of state is used to model the thermodynamic behaviour of liquid and gas. The material-dependent functions are

$$\Gamma_k = \gamma_k - 1, \quad p_{\infty,k}(\rho_k) = \gamma_k \mathfrak{B}_k, \quad e_{\infty,k}(\rho_k) = 0.\tag{7.23}$$

A typical set of the initial physical material-dependent quantities are presented in the Table 7.1. The numerical results in Fig. 7.1 show that the TBVD-TWENO-THINC scheme can solve the sharp interface without numerical oscillations across the interfaces. The reconstruction is implemented in all state variables, which preserves the thermo-dynamical consistency among the physical fields.

Table 7.1: Material quantities for liquid (k=1) and gas (k=2) in the stiffened gas equation of state.

k	$\rho_k (kg/m^3)$	γ_k	\mathfrak{B}_k (Pa)
1	10^3	4.4	6×10^8
2	1	1.4	0

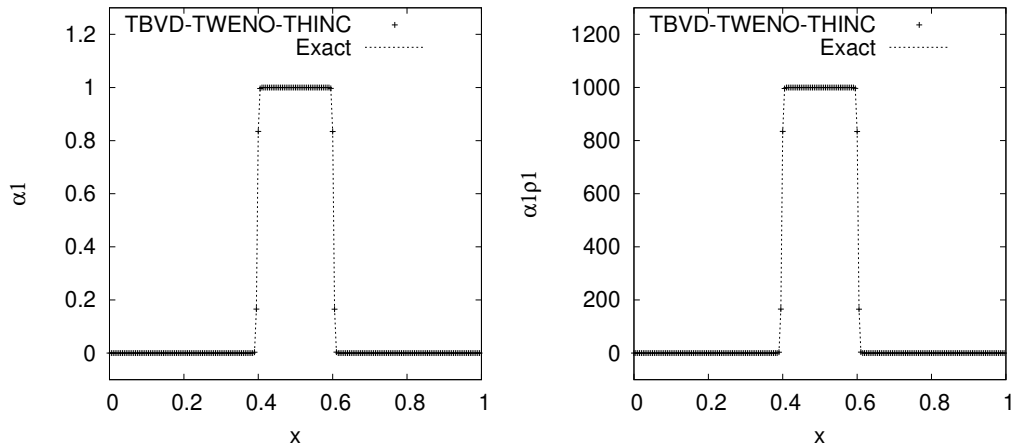


Figure 7.1: Numerical results of a passive advection of a square liquid column. $N=200$, $t = 10$ ms. Left: volume fraction (α_1), right: mass fraction ($\alpha_1 \rho_1$).

7.3.2 Two-material impact problem

In this section, we consider the two-phase impact problem [143, 147]. In this test, a right-moving copper (phase 1) plate interacts with a solid explosive (phase 2) with the speed $u = 1500$ km/s, the uniform atmospheric condition has pressure $p_0 = 10^5$ and temperature $T_0 = 300$ K throughout the domain. The Cochran-Chan equation of state is used to model material properties. The material-dependent functions are

$$\begin{aligned}
 \Gamma_k &= \gamma_k - 1, \\
 p_{\infty,k}(\rho_k) &= \mathfrak{B}_{1k} \left(\frac{\rho_{0k}}{\rho_k} \right)^{-\epsilon_{1k}} - \mathfrak{B}_{2k} \left(\frac{\rho_{0k}}{\rho_k} \right)^{-\epsilon_{2k}}, \\
 e_{\infty,k}(\rho_k) &= \frac{-\mathfrak{B}_{1k}}{\rho_{0k}(1-\epsilon_{1k})} \left[\left(\frac{\rho_{0k}}{\rho_k} \right)^{1-\epsilon_{1k}} - 1 \right] + \frac{\mathfrak{B}_{2k}}{\rho_{0k}(1-\epsilon_{2k})} \left[\left(\frac{\rho_{0k}}{\rho_k} \right)^{1-\epsilon_{2k}} - 1 \right] - C_{vk} T_0.
 \end{aligned} \tag{7.24}$$

A typical set of the initial physical material-dependent quantities for this test are shown in the Table 7.2.

Table 7.2: Material quantities for copper (k=1) and explosive (k=2) in Cochran-Chan equation of state.

k	$\rho_k(kg/m^3)$	γ_k	\mathfrak{B}_{1k} (GPa)	\mathfrak{B}_{2k} (GPa)	ϵ_{1k}	ϵ_{2k}	Cvk (J/kg·K)
1	8900	3	145.67	147.75	2.99	1.99	393
2	1840	1.93	12.87	13.42	4.1	3.1	1087

The numerical results in Fig. 7.2 show the copper volume fraction and mass fraction. It is observed that there is a good agreement of solution behaviours in the proposed TBVD-TWENO-THINC scheme.

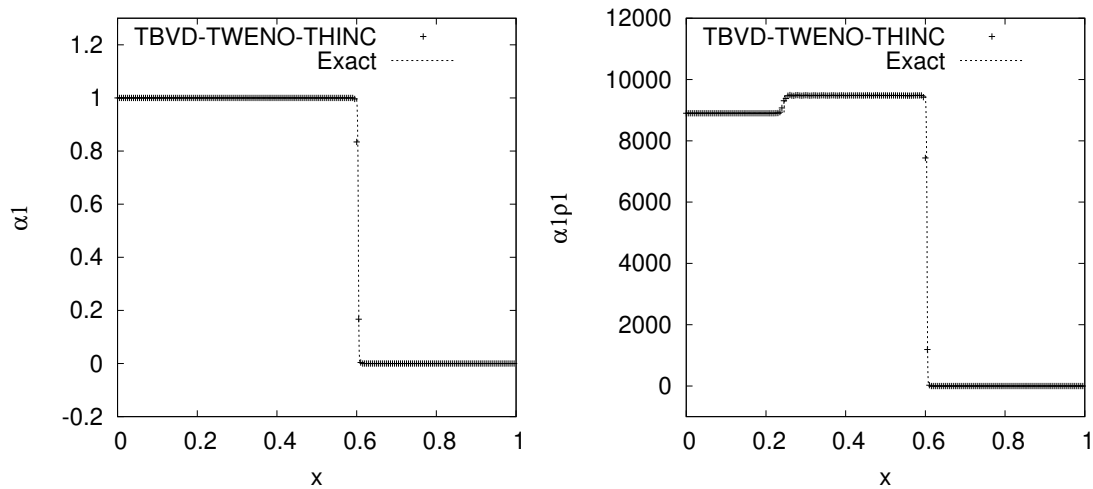


Figure 7.2: Numerical results of the two-material impact test. $N=200$, $t = 85\mu s$. left: volume fraction (α_1), right: mass fraction ($\alpha_1\rho_1$).

7.3.3 2D shock-bubble interaction problem

In this section, we conduct the shock-bubble interaction test, which is a compressible two-phase flow with moving interfaces problem. In this test, we investigate the inter-

actions between a shock and a bubble, which involves the collision of a shock wave of Mach 1.22 in the air impacting a circular bubble gas. In the experiments performed by Haas et al. [148] and James et al. [149], a stationary cylindrical gas bubble is impacted by a leftward-moving Mach 1.22 planar shock wave in air. The bubbles were produced by inflating a cylindrical former whose walls were made from a very thin membrane of nitrocellulose. Good control was exercised over the shape of the bubble and the resultant flows were almost two-dimensional, thus the two-dimensional computational set-up can be expected to mimic the experiments fairly [149].

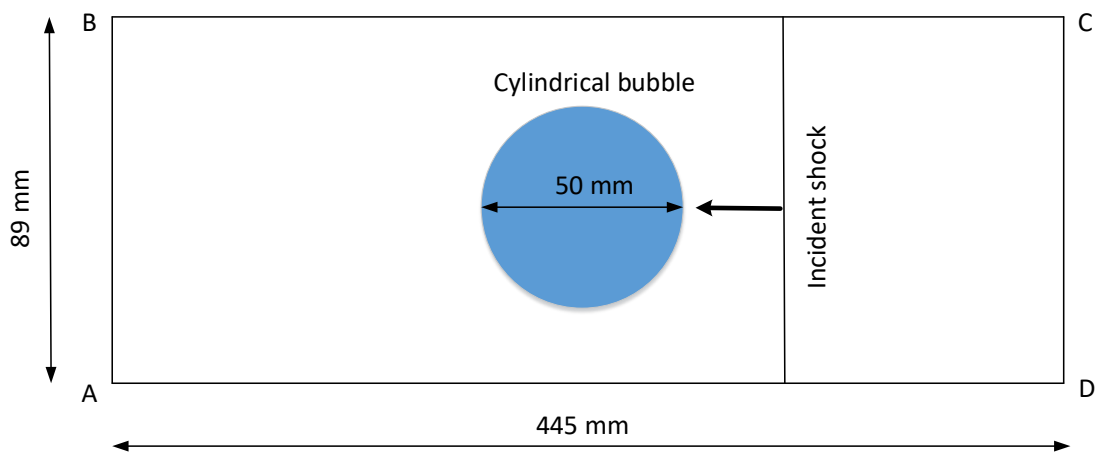


Figure 7.3: A schematic of the computational domain

The schematic of the computational set-up is shown in Fig. 7.3. The computation domain is $[0, 445] \times [0, 89]mm^2$. The radius of the bubble is $r_0 = 25$ mm, and the location of the shock is $x = 275$ mm. The domain is discretized by Cartesian grids with the mesh size $\Delta x = \Delta y = \frac{1}{4}$ mm, which represents a grid resolution of 400 cells across the bubble diameter. The symmetric-plane boundary conditions are used on the top and bottom, and the zero-gradient boundary conditions are used on the left and right. In the numerical test, both air and bubble are modelled as perfect gases. The initial state variables of 2D shock-bubble interaction test are shown in Table 7.3.

Table 7.3: The initial state quantities of 2D shock-bubble interaction problem. Inside the gas bubble ($k=1$), pre-shock regions outside the bubble ($k=2$), and post-shock regions outside the bubble ($k=3$).

k	$\rho_1(\text{kg/m}^3)$	$\rho_2(\text{kg/m}^3)$	u (m/s)	v (m/s)	p (Pa)	α_1
1	3.863	1.225	0	0	1.01325×10^5	$1 - 10^{-8}$
2	3.863	1.225	0	0	1.01325×10^5	10^{-8}
3	3.863	1.686	113.5	0	1.59×10^5	$1 - 10^{-8}$

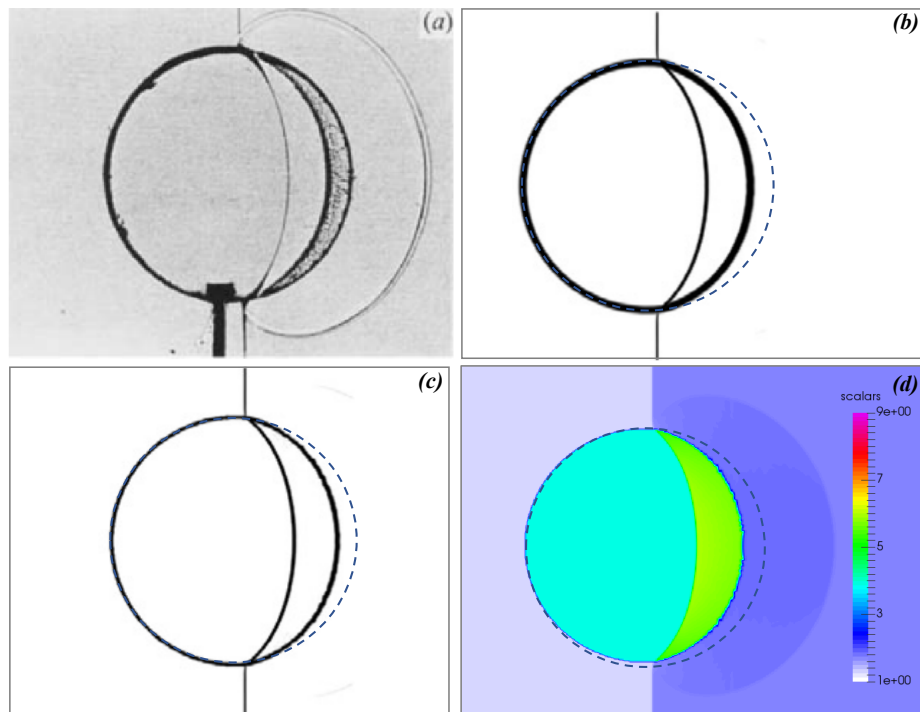


Figure 7.4: Results for a planar Mach 1.22 shock wave in air interacting with a circular R22 gas bubble at $t = 55 \mu\text{s}$. (a) experiment, (b) VOF, (c) VOF with interface-sharpening, and (d) TBVD-TWENO-THINC.

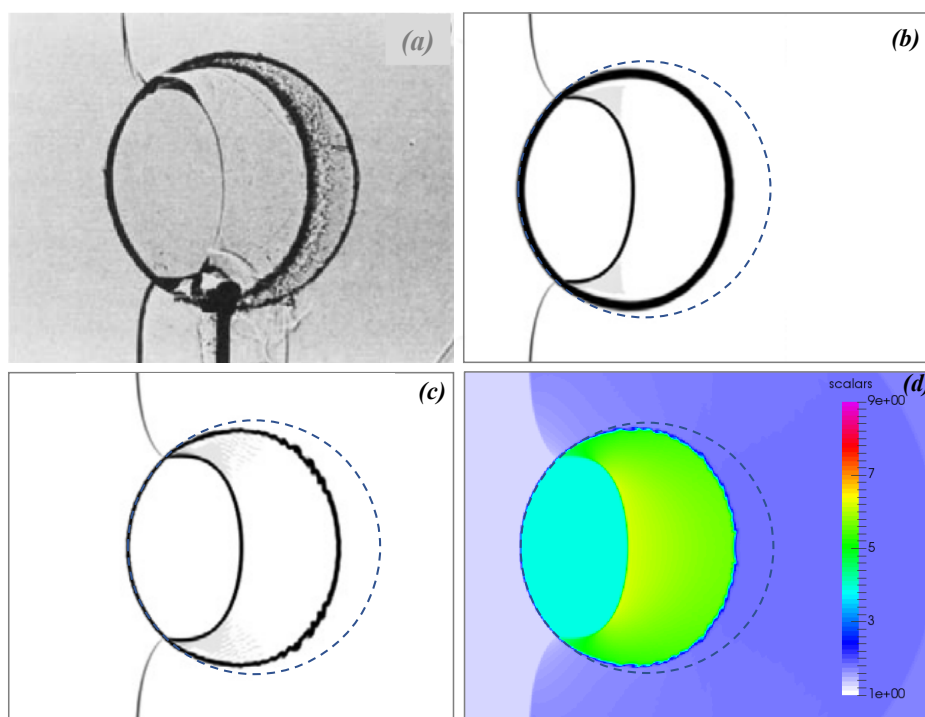


Figure 7.5: Same as Fig. 7.4, but at $t = 115 \mu\text{s}$

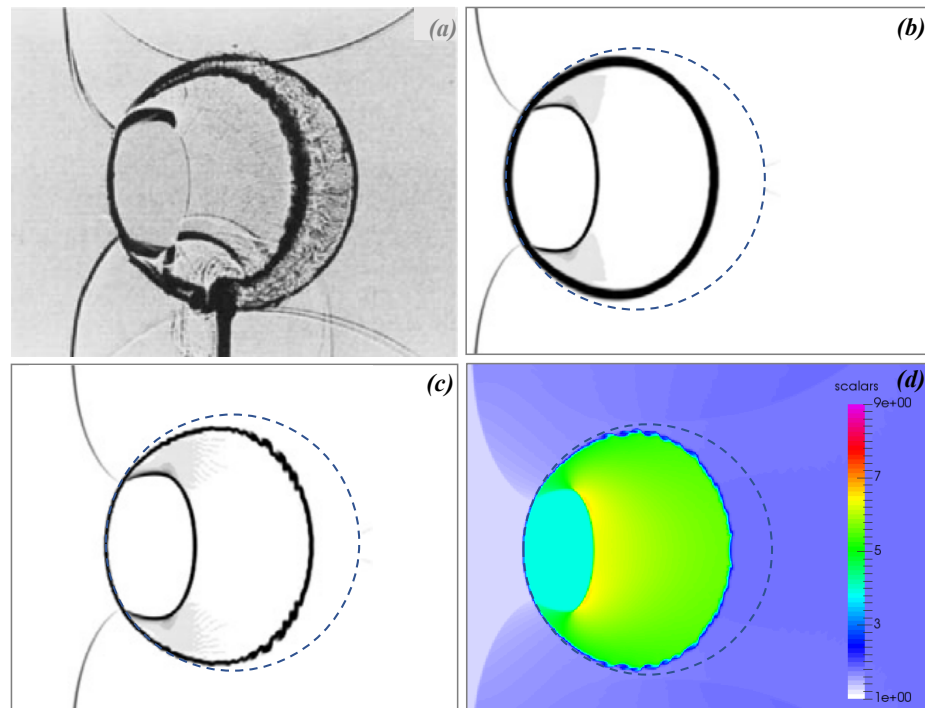


Figure 7.6: Same as Fig. 7.4, but at $t = 135 \mu\text{s}$

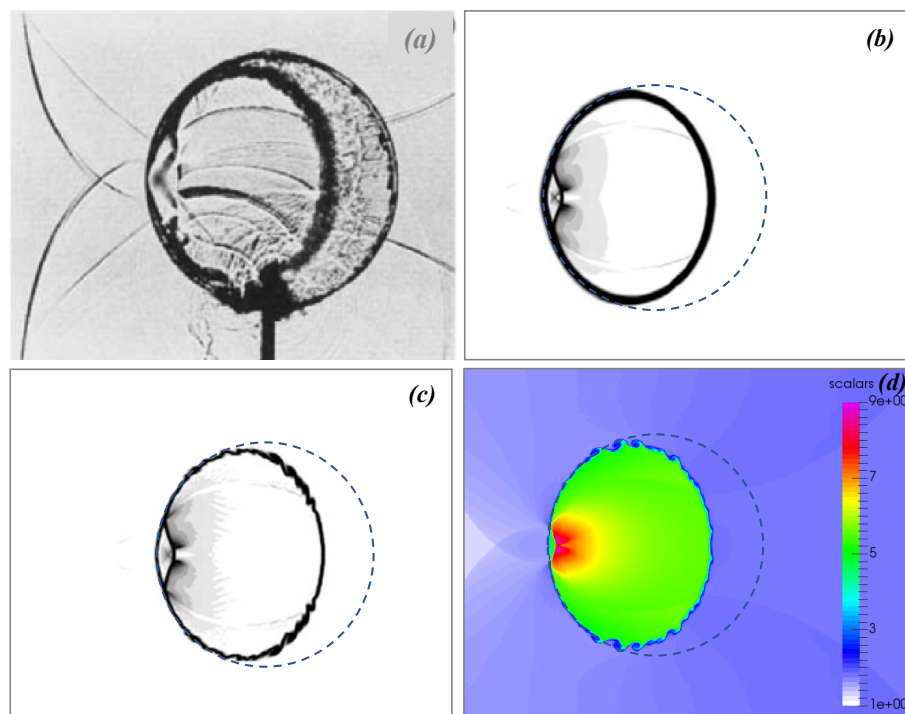


Figure 7.7: Same as Fig. 7.4, but at $t = 187 \mu\text{s}$

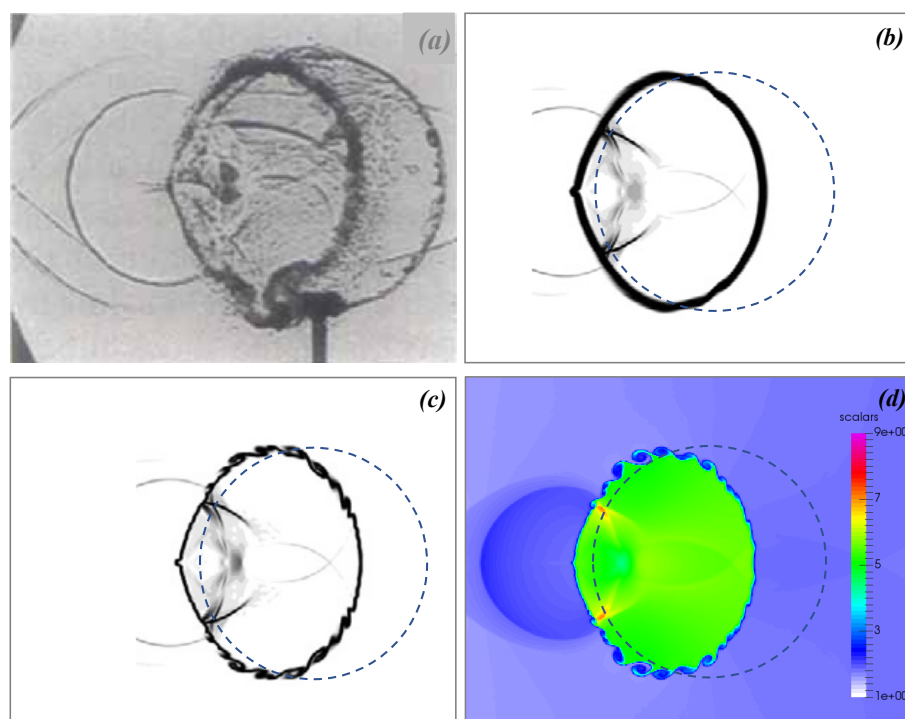


Figure 7.8: Same as Fig. 7.4, but at $t = 247 \mu\text{s}$

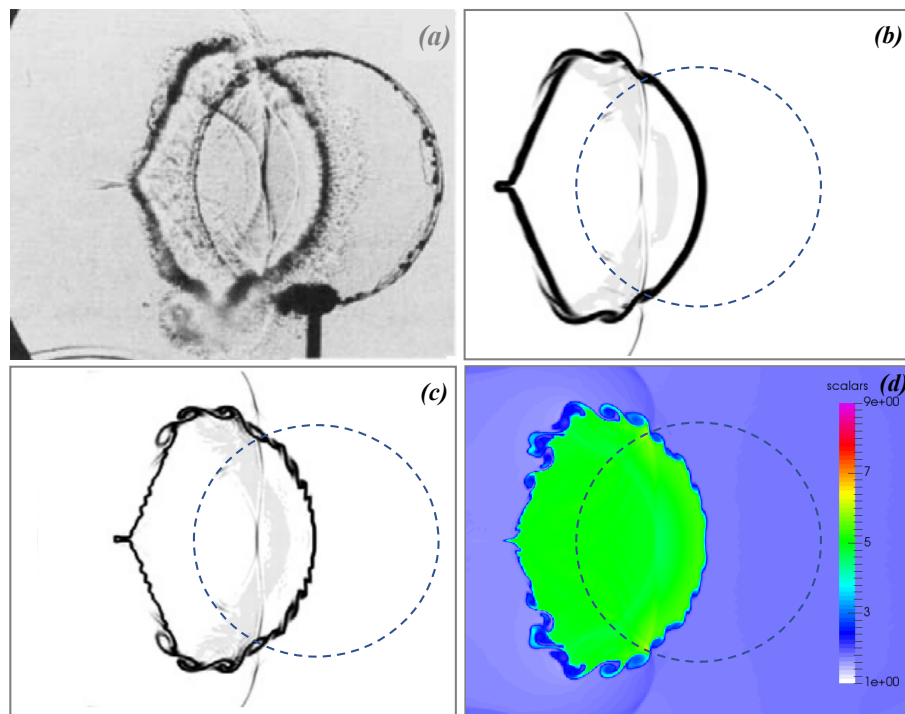


Figure 7.9: Same as Fig. 7.4, but at $t = 342 \mu\text{s}$

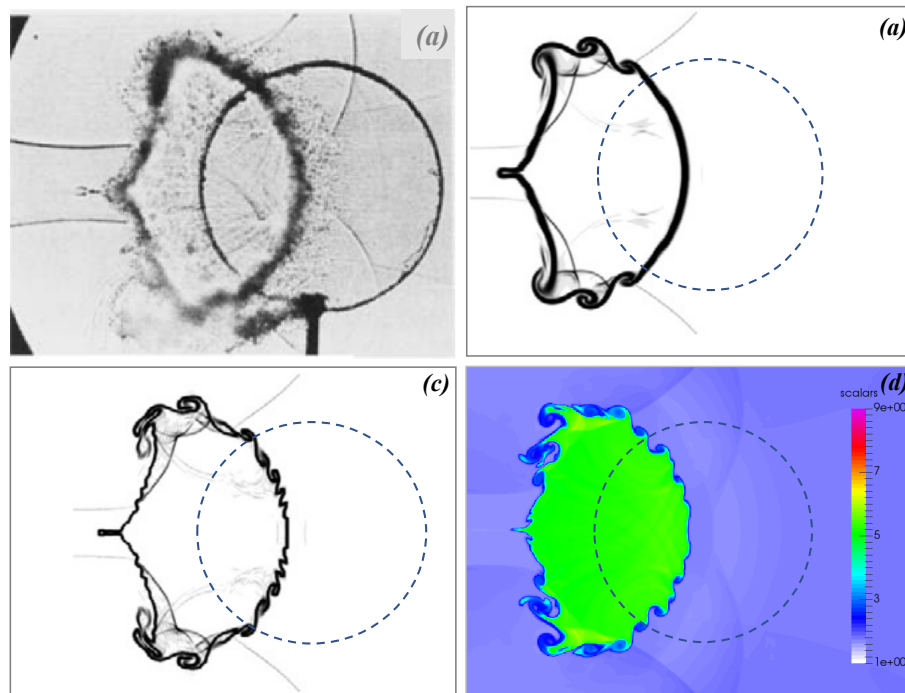


Figure 7.10: Same as Fig. 7.4, but at $t = 417 \mu\text{s}$

Figs. 7.4, 7.5, 7.6, 7.7, 7.8, 7.9, and 7.10 illustrate the results of the density at different times $t = 55 \mu s, 115 \mu s, 135 \mu s, 187 \mu s, 247 \mu s, 342 \mu s, 417 \mu s$ by the TBVD-TWENO-THINC scheme compared to the experimental results and previous numerical simulations by volume-of-fluid (VOF) methods (including the results with and without the application of anti-diffusion interface-sharpening) [150] on same grids. The circle in the experimental results represent the initial bubble frame, and the dash line circle in the numerical results represent the initial bubble profile.

In the early stage at $t = 55 \mu s$, the bubble experiences only large-scale deformations, so that no non-resolved scales are generated. The interface profile captured by numerical methods at this time agrees well with the experimental results. As time moves on, due to the vorticity induced by incident shock impact, the instability develops along with the interface, which begins to roll up and produces small filaments, as shown in Figs. 7.5, 7.6, 7.7, 7.8, 7.9, and 7.10. These fine structures tend to be smeared out by numerical schemes with large numerical dissipation unless high-resolution computational meshes are used [150]. It is observed that the TBVD-TWENO-THINC scheme maintains the compact thickness of the material interfaces and gives large-scale flow structures similar with the results computed from the VOF method with the application of anti-diffusion interface-sharpening technique on the same grid resolution.

It should be noted that numerical simulation captures more small-scale vortical structures compared to experimental results. It is probably due to the absence of physical viscosity in the flow model. In the numerical simulation, which is inviscid, the vortices will be continuously enforced when refined grid resolution is used [151]. The significance of the TBVD-TWENO-THINC scheme with reduced numerical dissipation lies in the real-case applications. For instance, in molecular or turbulent mixing problems, physical dissipation plays an important role. The flow structures can be more faithfully reproduced by using high-resolution numerical scheme with reduced numerical dissipation.

7.4 Summary

In this chapter, the TBVD-TWENO-THINC scheme was applied to solve the five-equation model for compressible two-phase flow problems. The proposed scheme was validated through the numerical benchmark tests in comparison to the analytical solutions and experiment results. The numerical results of the sharp-interface test reveal that the TBVD-TWENO-THINC scheme accurately captures the sharp interface. In addition, the numerical results of 2D Shock-bubble interaction problem have shown that the TBVD-TWENO-THINC scheme reproduces the complex flow features with less numerical dissipation. This suggests that the TBVD-TWENO-THINC scheme can be an effective and practical approach to be applied in the simulation of compressible two-phase flow problems where the physical dissipation plays an important role.

Summary and future work

8.1 Summary

In this study, several high-resolution numerical schemes on the basis of the CIP-CSL, ENO, WENO, THINC, and BVD methods were proposed for compressible flows and compressible two-phase flows. The main achievements can be summarised as below:

1. Two ENO-type of indicators were designed for the CIP-CSL framework. The first ENO indicator was designed for the CIP-CSL3-ENO scheme, which is reconstructed based on the CIP-CSL3D scheme and a newly proposed CIP-CSL3U scheme. This ENO indicator was devised on the basis of a type of ratios of successive gradients, which intentionally selects non-smooth stencils but can efficiently minimise numerical oscillations. The CIP-CSL3-ENO scheme approximately has fourth-order accuracy for the sine wave propagation test and captures discontinuities and smooth solutions well in various test problems. The CIP-CSL3-ENO scheme minimises numerical oscillation and diffusion more efficiently than the CIP-CSL3D scheme and the CIP-CSL3U scheme individually. The second ENO indicator was designed for the CIP-CSL-ENO5 scheme, which is reconstructed based on the CIP-CSL3D, CIP-CSL3U, and CIP-CSLR schemes and the newly proposed CIP-CSL4Q scheme. This ENO indicator was devised on the basis of the total variation of the derivatives. The CIP-CSL-ENO5

scheme accurately capture both smooth and discontinuous solutions simultaneously by selecting an appropriate reconstruction function. The CIP-CSL-ENO5 scheme has fifth-order accuracy for smooth solutions. Meanwhile, the CIP-CSL-ENO5 scheme has smaller numerical errors than the CIP-CSLR and CIP-CSL3-ENO schemes in various test problems. In addition, it was observed that the CIP-CSL3-ENO scheme cannot resolve the numerical solution for the two blast waves interaction test. The CIP-CSL-ENO5 scheme addressed this issue based on a combination of high-order polynomials and a monotone reconstruction with rational function.

2. To reduce the numerical diffusion in vicinity of discontinuities for the CIP-CSL scheme, we firstly proposed the CIP-CSLT (CIP-CSL with a piecewise tangent hyperbolic function) scheme. The CIP-CSLT scheme is able to represent the jump-like discontinuity with less numerical diffusion. Subsequently, a high-resolution scheme CIP-CSLT-WENO4 was proposed on the basis of the CIP-CSLT scheme and the CIP-CSL-WENO4 (CIP-CSL with a WENO limiter) scheme. The reconstruction criteria of the CIP-CSLT-WENO4 scheme was designed based on a modified version of the boundary variation diminishing (BVD) algorithm, which can minimise the total boundary variations of the derivative.

The superiority of the CIP-CSLT-WENO4 scheme has been verified through various numerical benchmark tests in comparison to other high-order CIP-CSL schemes. Numerical results have shown that the CIP-CSLT-WENO4 scheme has the least numerical errors and minimises numerical diffusion with minimum numerical oscillations. The numerical results of 2D explosion have shown that the CIP-CSLT-WENO4-BVD scheme can be applied to compressible flows problem that contains shocks.

3. To reduce the numerical errors for the conventional fifth-order WENO scheme, we proposed the target WENO (TWENO) scheme. Unlike the conventional fifth-order WENO scheme, which assigns non-linear weights to all three sub-stencils,

the TWENO scheme was designed to restore the highest possible order interpolation when three target sub-stencils or two target adjacent sub-stencils are smooth. Numerical results of the advection tests have shown that the TWENO scheme has smaller numerical errors than the WENO-Z scheme.

To further improve the accuracy of the TWENO scheme, we proposed a high-resolution scheme TBVD-TWENO-THINC based on the TWENO scheme and the THINC scheme. The reconstruction criterion of the TBVD-TWENO-THINC scheme was designed based on the total boundary variation diminishing (TBVD) algorithm, which can minimise the total boundary variations to effectively reduce numerical diffusion in the vicinity of discontinuities.

A variety of numerical benchmark tests were conducted to validate the capability of the TBVD-TWENO-THINC scheme. Numerical results have shown that, for smooth solutions, the TBVD-TWENO-THINC scheme has fifth-order accuracy by automatically selecting the high-order polynomial interpolation. For discontinuities, the TBVD-TWENO-THINC scheme effectively reduce the numerical diffusion by minimising the total boundary variations at the cell boundaries. In addition, the TBVD-TWENO-THINC scheme uses the least mesh number to achieve the given level of accuracy compare to WENO-JS, WENO-Z, BVD-WENOZ-THINC, and other CIP-CSL schemes for solving advection problems. Moreover, the numerical results of the 2D double-Mach reflection tests have shown that the TBVD-TWENO-THINC scheme is able to better resolve the small-scale vortex structures along the slip line compared to the WENO-Z, BVD-WENOZ-THINC, WENO-CU6, TENO8 and TENO8-opt schemes using the same coarse mesh. This suggests that the TBVD-TWENO-THINC scheme can be an effective high-resolution numerical scheme to simulate compressible flow problems.

4. Finally, the TBVD-TWENO-THINC scheme was successfully implemented in the five-equation model for compressible two-phase flow problems. Numerical

results show that TBVD-TWENO-THINC scheme is able to accurately capture the sharp interface and reproduces the complex flow features of compressible two-phase flows problems with less numerical dissipation. This suggests that the TBVD-TWENO-THINC scheme can be an effective and practical method to simulate compressible two-phase flow problems.

8.2 Future work

1. Whereas tremendous efforts have been made in the study of compressible flows, turbulence is still regarded as one of the unresolved problems of classical physics. Moreover, the interaction between shocks and turbulence can make the compressible fluid system even more complicated. The coexistence of shocks, discontinuities, and turbulent features brings challenges to the high-resolution scheme. Thus, the proposed high-resolution schemes in this thesis are expected to be applied to simulate turbulence problems.
2. High-resolution schemes on unstructured grids should be further explored. An extension of the proposed scheme on unstructured grids is preferable for practical simulations. For compressible multi-phase flow, the limiter-free schemes to unstructured grids are expected to be an efficient means to control numerical oscillations.
3. The numerical model should be further explored to simulate more complex phenomena of compressible flow problems. Advanced numerical models with extra terms in governing equations can be constructed to describe more phenomenon in high-speed compressible flow problems in practical engineering applications e.g. cavitation. Therefore, the proposed high-resolution schemes are expected to solve these advanced numerical models for more phase-change phenomenon.

Appendix A

Fourier analysis of the CIP-CSL3U and CIP-CSL3D schemes

A.1 Mathematical formulations of Fourier analysis of the CIP-CSL3U and CIP-CSL3D schemes

The following equations are mathematical formulations of Fourier analysis which are given in Chapter 3. Φ_x , Φ_{xx} and Φ_{xxx} represent the first derivative of Φ , second derivative and third derivative, respectively.

The spatial derivatives of CSL3U at $x_{i-1/2}$ in Fourier space:

$$\begin{aligned} \Phi_x(w) = & \left(-\frac{31}{6} - \frac{14}{3} \cos(w) + \frac{8}{w} \sin(w) + \frac{1}{w} \sin(2w) - \frac{1}{6} \cos(2w) \right) \\ & + \left(-\frac{14}{3} \sin(w) - \frac{8}{w} \cos(w) + \frac{9}{w} - \frac{1}{w} \cos(2w) - \frac{1}{6} \sin(2w) \right) j, \end{aligned} \quad (\text{A.1})$$

$$\begin{aligned} \Phi_{xx}(w) = & \left(13 + 22 \cos(w) - \frac{24}{w} \sin(w) - \frac{6}{w} \sin(2w) + \cos(2w) \right) \\ & + \left(22 \sin(w) - \frac{30}{w} + \frac{24}{w} \cos(w) + \frac{6}{w} \cos(2w) + \sin(2w) \right) j, \end{aligned} \quad (\text{A.2})$$

$$\begin{aligned} \Phi_{xxx}(w) = & \left(-14 - 32 \cos(w) + \frac{24}{w} \sin(w) + \frac{12}{w} \sin(2w) - 2 \cos(2w) \right) \\ & + \left(-32 \sin(w) + \frac{36}{w} - \frac{24}{w} \cos(w) - \frac{12}{w} \cos(2w) - 2 \sin(2w) \right) j. \end{aligned} \quad (\text{A.3})$$

The spatial derivatives of CSL3D at $x_{i-1/2}$ in Fourier space:

$$\begin{aligned} \Phi_x(w) = & \left(-\frac{2}{3} \cos(w) + \frac{2}{w} \sin(w) - \frac{4}{3} \right) \\ & + \left(-\sin(w) + \frac{4}{w} - \frac{4}{w} \cos(w) \right) j, \end{aligned} \quad (\text{A.4})$$

$$\Phi_{xx}(w) = -2 \cos(w) + \frac{12}{w} \sin(w) - 10, \quad (\text{A.5})$$

$$\begin{aligned} \Phi_{xxx}(w) = & \left(16 \cos(w) - \frac{48}{w} \sin(w) + 32 \right) \\ & + \left(12 \sin(w) + \frac{24}{w} \cos(w) - \frac{24}{w} \right) j. \end{aligned} \quad (\text{A.6})$$

The spatial derivatives of CSL3U at $x_{x+1/2}$ in Fourier space:

$$\begin{aligned} \Phi_x(w) = & - \left(-\frac{2}{3} \cos(w) + \frac{2}{w} \sin(w) - \frac{4}{3} \right) \\ & + \left(-\sin(w) + \frac{4}{w} - \frac{4}{w} \cos(w) \right) j, \end{aligned} \quad (\text{A.7})$$

$$\Phi_{xx}(w) = -2 \cos(w) + \frac{12}{w} \sin(w) - 10, \quad (\text{A.8})$$

$$\begin{aligned} \Phi_{xxx}(w) = & - \left(16 \cos(w) - \frac{48}{w} \sin(w) + 32 \right) \\ & + \left(12 \sin(w) + \frac{24}{w} \cos(w) - \frac{24}{w} \right) j. \end{aligned} \quad (\text{A.9})$$

The spatial derivatives of CSL3D at $x_{x+1/2}$ in Fourier space:

$$\begin{aligned} \Phi_x(w) = & - \left(-\frac{31}{6} - \frac{14}{3} \cos(w) + \frac{8}{w} \sin(w) + \frac{1}{w} \sin(2w) - \frac{1}{6} \cos(2w) \right) \\ & + \left(-\frac{14}{3} \sin(w) - \frac{8}{w} \cos(w) + \frac{9}{w} - \frac{1}{w} \cos(2w) - \frac{1}{6} \sin(2w) \right) j, \end{aligned} \quad (\text{A.10})$$

$$\begin{aligned} \Phi_{xx}(w) = & \left(13 + 22 \cos(w) - \frac{24}{w} \sin(w) - \frac{6}{w} \sin(2w) + \cos(2w) \right) \quad (\text{A.11}) \\ & - \left(22 \sin(w) - \frac{30}{w} + \frac{24}{w} \cos(w) + \frac{6}{w} \cos(2w) + \sin(2w) \right) j, \end{aligned}$$

$$\begin{aligned} \Phi_{xxx}(w) = & - \left(-14 - 32 \cos(w) + \frac{24}{w} \sin(w) + \frac{12}{w} \sin(2w) - 2 \cos(2w) \right) \quad (\text{A.12}) \\ & + \left(-32 \sin(w) + \frac{36}{w} - \frac{24}{w} \cos(w) - \frac{12}{w} \cos(2w) - 2 \sin(2w) \right) j. \end{aligned}$$

The spatial derivatives of CSL3U at x_i in Fourier space:

$$\begin{aligned} \Phi_x(w) = & \frac{1}{12} \left(\cos\left(\frac{3w}{2}\right) + 23 \cos\left(\frac{w}{2}\right) - \frac{30}{w} \sin\left(\frac{w}{2}\right) - \frac{6}{w} \sin\left(\frac{3w}{2}\right) \right) \quad (\text{A.13}) \\ & + \left(\sin\left(\frac{3w}{2}\right) + 33 \sin\left(\frac{w}{2}\right) + \frac{6}{w} \cos\left(\frac{3w}{2}\right) - \frac{6}{w} \cos\left(\frac{w}{2}\right) \right) j, \end{aligned}$$

$$\Phi_{xx}(w) = \left(12 \cos\left(\frac{w}{2}\right) - \frac{24}{w} \sin\left(\frac{w}{2}\right) \right), \quad (\text{A.14})$$

$$\begin{aligned} \Phi_{xxx}(w) = & \left(-\cos\left(\frac{3w}{2}\right) - 23 \cos\left(\frac{w}{2}\right) + \frac{30}{w} \sin\left(\frac{w}{2}\right) + \frac{6}{w} \sin\left(\frac{3w}{2}\right) \right) \quad (\text{A.15}) \\ & - \left(\sin\left(\frac{3w}{2}\right) + 9 \sin\left(\frac{w}{2}\right) + \frac{6}{w} \cos\left(\frac{3w}{2}\right) - \frac{6}{w} \cos\left(\frac{w}{2}\right) \right) j. \end{aligned}$$

The spatial derivatives of CSL3D at x_i in Fourier space:

$$\begin{aligned} \Phi_x(w) = & \frac{1}{12} \left(-\cos\left(\frac{3w}{2}\right) - 23 \cos\left(\frac{w}{2}\right) + \frac{30}{w} \sin\left(\frac{w}{2}\right) + \frac{6}{w} \sin\left(\frac{3w}{2}\right) \right) \quad (\text{A.16}) \\ & + \left(\sin\left(\frac{3w}{2}\right) + 33 \sin\left(\frac{w}{2}\right) + \frac{6}{w} \cos\left(\frac{3w}{2}\right) - \frac{6}{w} \cos\left(\frac{w}{2}\right) \right) j, \end{aligned}$$

$$\Phi_{xx}(w) = \left(12 \cos\left(\frac{w}{2}\right) - \frac{24}{w} \sin\left(\frac{w}{2}\right) \right), \quad (\text{A.17})$$

$$\begin{aligned} \Phi_{xxx}(w) = & \left(\cos\left(\frac{3w}{2}\right) + 23 \cos\left(\frac{w}{2}\right) - \frac{30}{w} \sin\left(\frac{w}{2}\right) - \frac{6}{w} \sin\left(\frac{3w}{2}\right) \right) \quad (\text{A.18}) \\ & - \left(\sin\left(\frac{3w}{2}\right) + 9 \sin\left(\frac{w}{2}\right) + \frac{6}{w} \cos\left(\frac{3w}{2}\right) - \frac{6}{w} \cos\left(\frac{w}{2}\right) \right) j. \end{aligned}$$

Appendix B

Roe's Riemann solver for Euler equations

For 1D Euler equations

$$\mathbf{U}_t + \mathbf{F}(\mathbf{U})_x = 0, \quad (\text{B.1})$$

where

$$\mathbf{U} = \begin{pmatrix} \rho \\ \rho v \\ E \end{pmatrix}, \quad \mathbf{F}(\mathbf{U}) = \begin{pmatrix} \rho v \\ \rho v^2 + p \\ v(E + p) \end{pmatrix}. \quad (\text{B.2})$$

Here, ρ is the density, v is the velocity, p is the pressure, and E is the total energy. For the ideal gas, the total energy is given by

$$E = \frac{p}{\gamma - 1} + \frac{1}{2}\rho v^2, \quad (\text{B.3})$$

where γ is heat capacity ratio. Equations B.1 can also be written in quasi-linear form

$$\mathbf{U}_t + \mathbf{A}(\mathbf{U})\mathbf{U}_x = 0, \quad (\text{B.4})$$

where $\mathbf{A}(\mathbf{U})$ is the Jacobian Matrix defined by

$$\mathbf{A}(\mathbf{U}) = \begin{bmatrix} 0 & 1 & 0 \\ \frac{1}{2}(\gamma - 3)v^2 & (3 - \gamma)v & \gamma - 1 \\ \frac{1}{2}(\gamma - 1)v^3 - vH & H - (\gamma - 1)v^2 & \gamma v \end{bmatrix}, \quad (\text{B.5})$$

Here, H is the total specific enthalpy defined by

$$H = \frac{(E + p)}{\rho}. \quad (\text{B.6})$$

The eigenvalues of Jacobian matrix $\mathbf{A}(\mathbf{U})$ are given by,

$$\lambda_1 = v - a, \quad \lambda_2 = v, \quad \lambda_3 = v + a, \quad (\text{B.7})$$

where a is the sound speed, $a = \sqrt{\left(\frac{\partial p}{\partial \rho}\right)_s}$. By using the the EOS of ideal gases, the sound speed a can be given by

$$a = \sqrt{\frac{\gamma p}{\rho}}. \quad (\text{B.8})$$

The corresponding right eigenvectors of Jacobian matrix $\mathbf{A}(\mathbf{U})$ are

$$\mathbf{R} = \begin{bmatrix} 1 & 1 & 1 \\ v - a & v & v + a \\ H - va & V & H + va \end{bmatrix}, \quad (\text{B.9})$$

where each eigenvector is the column of the matrix \mathbf{R} . The left eigenvectors of Jacobian matrix $\mathbf{A}(\mathbf{U})$ are

$$\mathbf{L} = \begin{bmatrix} \frac{1}{2} \left(\frac{V(\gamma - 1)}{a^2} + \frac{v}{a} \right) & -\frac{1}{2} \left(\frac{v(\gamma - 1)}{a^2} + \frac{1}{a} \right) & \frac{(\gamma - 1)}{2a^2} \\ 1 - \frac{V(\gamma - 1)}{a^2} & \frac{v(\gamma - 1)}{a^2} & -\frac{\gamma - 1}{a^2} \\ \frac{1}{2} \left(\frac{V(\gamma - 1)}{a^2} - \frac{v}{a} \right) & -\frac{1}{2} \left(\frac{v(\gamma - 1)}{a^2} - \frac{1}{a} \right) & \frac{(\gamma - 1)}{2a^2} \end{bmatrix}, \quad (\text{B.10})$$

where each row of matrix \mathbf{L} corresponds to each left eigenvector. Here, $V = \frac{1}{2}v^2$.

For Roe's Riemann solver, initially we have a jump in the conservative variable

$$\Delta \mathbf{U} = \mathbf{U}^R - \mathbf{U}^L. \quad (\text{B.11})$$

The Roe average[70] for velocity v , total enthalpy $H = \frac{(E + p)}{\rho}$, and sound speed a

is given by

$$\begin{aligned}\tilde{v} &= \frac{\sqrt{\rho_L}v_L + \sqrt{\rho_R}v_R}{\sqrt{\rho_L} + \sqrt{\rho_R}} \\ \tilde{H} &= \frac{\sqrt{\rho_L}H_L + \sqrt{\rho_R}H_R}{\sqrt{\rho_L} + \sqrt{\rho_R}} \\ \tilde{a} &= \left((\gamma - 1) \left(\tilde{H} - \frac{1}{2}\tilde{v}^2 \right) \right)^{\frac{1}{2}},\end{aligned}\tag{B.12}$$

where the \tilde{v} , \tilde{H} , and \tilde{a} is the Roe-averaged value of v , H and a . v_L , H_L , and ρ_L is given from the left-side conservative variables \mathbf{U}^L and v_R , H_R and ρ_R are given from right side conservative variables \mathbf{U}^R . The Roe-averaged Jacobian matrix $\mathbf{A}(\mathbf{U})$ of (B.5) is given by

$$\bar{\mathbf{A}}(\mathbf{U}) = \begin{bmatrix} 0 & 1 & 0 \\ \frac{1}{2}(\gamma - 3)\tilde{v}^2 & (3 - \gamma)\tilde{v} & \gamma - 1 \\ \frac{1}{2}(\gamma - 1)\tilde{v}^3 - \tilde{v}\tilde{H} & \tilde{H} - (\gamma - 1)\tilde{v}^2 & \gamma\tilde{v} \end{bmatrix},\tag{B.13}$$

with the eigenvalues are defined by

$$\lambda_1 = \tilde{v} - \tilde{a}, \quad \lambda_2 = \tilde{v}, \quad \lambda_3 = \tilde{v} + \tilde{a},\tag{B.14}$$

The Roe-averaged right eigenvectors are defined by

$$\bar{\mathbf{R}} = \begin{bmatrix} 1 & 1 & 1 \\ \tilde{v} - \tilde{a} & \tilde{v} & \tilde{v} + \tilde{a} \\ \tilde{H} - \tilde{v}\tilde{a} & \frac{1}{2}\tilde{v}^2 & \tilde{H} + \tilde{v}\tilde{a} \end{bmatrix},\tag{B.15}$$

and the left eigenvectors are given by

$$\bar{\mathbf{L}} = \begin{bmatrix} \frac{1}{2} \left(\frac{\tilde{V}(\gamma - 1)}{\tilde{a}^2} + \frac{\tilde{v}}{\tilde{a}} \right) & -\frac{1}{2} \left(\frac{\tilde{v}(\gamma - 1)}{\tilde{a}^2} + \frac{1}{\tilde{a}} \right) & \frac{(\gamma - 1)}{2\tilde{a}^2} \\ 1 - \frac{\tilde{V}(\gamma - 1)}{\tilde{a}^2} & \frac{\tilde{v}(\gamma - 1)}{\tilde{a}^2} & -\frac{\gamma - 1}{\tilde{a}^2} \\ \frac{1}{2} \left(\frac{\tilde{V}(\gamma - 1)}{\tilde{a}^2} - \frac{\tilde{v}}{\tilde{a}} \right) & -\frac{1}{2} \left(\frac{\tilde{v}(\gamma - 1)}{\tilde{a}^2} - \frac{1}{\tilde{a}} \right) & \frac{(\gamma - 1)}{2\tilde{a}^2} \end{bmatrix},\tag{B.16}$$

where $\tilde{V} = \frac{1}{2}\tilde{v}^2$. We can see that with only the Roe-averaged variable v , H and a , the whole Roe-averaged eigenstructures of 1D Euler equations can be recovered.

For the 2D Euler equations

$$\mathbf{U}_t + \mathbf{F}(\mathbf{U})_x + \mathbf{G}(\mathbf{U})_y = 0, \quad (\text{B.17})$$

where,

$$\mathbf{U} = \begin{pmatrix} \rho \\ \rho u \\ \rho v \\ E \end{pmatrix}, \quad \mathbf{F}(\mathbf{U}) = \begin{pmatrix} \rho u \\ \rho u^2 + p \\ \rho uv \\ u(E + p) \end{pmatrix}, \quad \mathbf{G}(\mathbf{U}) = \begin{pmatrix} \rho v \\ \rho uv \\ \rho v^2 + p \\ v(E + p) \end{pmatrix}, \quad (\text{B.18})$$

where ρ is the density, p the pressure, (u, v) the velocity component in x and y direction, and E is the total energy. Equations (B.17) can also be written in a quasi-linear form as

$$\mathbf{U}_t + \mathbf{A}(\mathbf{U})\mathbf{U}_x + \mathbf{B}(\mathbf{U})\mathbf{U}_y = 0. \quad (\text{B.19})$$

The Jacobian matrix $\mathbf{A}(\mathbf{U})$ corresponding to flux $\mathbf{F}(\mathbf{U})$ is defined by

$$\mathbf{A}(\mathbf{U}) = \begin{bmatrix} 0 & 1 & 0 & 0 \\ -u^2 + (\gamma - 1)\mathbf{V} & -(\gamma - 3)u & -(\gamma - 1)v & (\gamma - 1) \\ -uv & v & u & 0 \\ u(\mathbf{V}(\gamma - 1) - H) & H - u^2(\gamma - 1) & -(\gamma - 1)uv & \gamma u \end{bmatrix}, \quad (\text{B.20})$$

where

$$\begin{aligned} \mathbf{V} &= \frac{1}{2}(u^2 + v^2), \\ H &= \frac{P + E}{\rho}. \end{aligned} \quad (\text{B.21})$$

The eigenvalues of Jacobian matrix $\mathbf{A}(\mathbf{U})$ are

$$\lambda_1 = u - a, \quad \lambda_2 = u, \quad \lambda_3 = u, \quad \lambda_4 = u + a, \quad (\text{B.22})$$

where a is the sound speed. For ideal gases EOS, the sound speed a and total enthalpy H can be calculated by

$$\begin{aligned} a &= \sqrt{\frac{\gamma P}{\rho}}, \\ H &= \frac{a^2}{\gamma - 1} + \mathbf{V}. \end{aligned} \quad (\text{B.23})$$

The corresponding right eigenvectors are given by

$$\mathbf{R}^x = \begin{bmatrix} 1 & 0 & 1 & 1 \\ u - a & 0 & u & u + a \\ v & 1 & v & v \\ H - ua & v & \mathbf{V} & H + ua \end{bmatrix}, \quad (\text{B.24})$$

where each column of the matrix \mathbf{R}^x is corresponding to each right eigenvector. And the left eigenvectors are given by

$$\mathbf{L}^x = \begin{bmatrix} \frac{1}{2}(\gamma - 1)\frac{\mathbf{V}}{a^2} + \frac{u}{2a} & -\frac{1}{2}\left(\frac{u(\gamma - 1)}{a^2} + \frac{1}{a}\right) & -\frac{v(\gamma - 1)}{2a^2} & \frac{(\gamma - 1)}{2a^2} \\ -v & 0 & 1 & 0 \\ 1 - (\gamma - 1)\frac{\mathbf{V}}{a^2} & (\gamma - 1)\frac{u}{a^2} & (\gamma - 1)\frac{v}{a^2} & -\frac{(\gamma - 1)}{a^2} \\ \frac{1}{2}(\gamma - 1)\frac{\mathbf{V}}{a^2} - \frac{u}{2a} & -\frac{1}{2}\left(\frac{u(\gamma - 1)}{a^2} - \frac{1}{a}\right) & -\frac{v(\gamma - 1)}{2a^2} & \frac{(\gamma - 1)}{2a^2} \end{bmatrix}, \quad (\text{B.25})$$

where each row of the matrix \mathbf{L}^x is corresponding to each left eigenvector.

The Jacobian matrix of $\mathbf{B}(\mathbf{U})$ corresponding to flux $\mathbf{G}(\mathbf{U})$ is defined by

$$\mathbf{B}(\mathbf{U}) = \begin{bmatrix} 0 & 0 & 1 & 0 \\ -uv & v & u & 0 \\ -v^2 + (\gamma - 1)\mathbf{V} & -(\gamma - 1)u & -(\gamma - 3)v & (\gamma - 1) \\ v(\mathbf{V}(\gamma - 1) - H) & -(\gamma - 1)uv & H - v^2(\gamma - 1) & \gamma v \end{bmatrix}. \quad (\text{B.26})$$

The eigenvalues of Jacobian matrix $\mathbf{B}(\mathbf{U})$ are

$$\lambda_1 = v - a, \quad \lambda_2 = v, \quad \lambda_3 = v, \quad \lambda_4 = v + a, \quad (\text{B.27})$$

The corresponding right eigenvectors are given by

$$\mathbf{R}^y = \begin{bmatrix} 1 & 0 & 1 & 1 \\ u & 1 & u & u \\ v - a & 0 & v & v + a \\ H - va & u & \mathbf{V} & H + va \end{bmatrix}. \quad (\text{B.28})$$

Here, the column of the matrix \mathbf{R}^y corresponds to each eigenvector of $\mathbf{B}(\mathbf{U})$. The left eigenvectors of $\mathbf{B}(\mathbf{U})$ are given by

$$\mathbf{L}^y = \begin{bmatrix} \frac{1}{2}(\gamma - 1)\frac{\mathbf{V}}{a^2} + \frac{v}{2a} & -\frac{u(\gamma - 1)}{2a^2} & -\frac{1}{2}\left(\frac{v(\gamma - 1)}{a^2} + \frac{1}{a}\right) & \frac{(\gamma - 1)}{2a^2} \\ -u & 1 & 0 & 0 \\ 1 - (\gamma - 1)\frac{\mathbf{V}}{a^2} & (\gamma - 1)\frac{u}{a^2} & (\gamma - 1)\frac{v}{a^2} & -\frac{(\gamma - 1)}{a^2} \\ \frac{1}{2}(\gamma - 1)\frac{\mathbf{V}}{a^2} - \frac{v}{2a} & -\frac{u(\gamma - 1)}{2a^2} & -\frac{1}{2}\left(\frac{v(\gamma - 1)}{a^2} - \frac{1}{a}\right) & \frac{(\gamma - 1)}{2a^2} \end{bmatrix}, \quad (\text{B.29})$$

where each row of the matrix \mathbf{L}^y corresponds to each left eigenvector.

The Roe averaged velocity (u, v) , total enthalpy H , and sound speed a is given by,

$$\begin{aligned} \tilde{u} &= \frac{\sqrt{\rho_L}u_L + \sqrt{\rho_R}u_R}{\sqrt{\rho_L} + \sqrt{\rho_R}} \\ \tilde{v} &= \frac{\sqrt{\rho_L}v_L + \sqrt{\rho_R}v_R}{\sqrt{\rho_L} + \sqrt{\rho_R}} \\ \tilde{H} &= \frac{\sqrt{\rho_L}H_L + \sqrt{\rho_R}H_R}{\sqrt{\rho_L} + \sqrt{\rho_R}} \\ \tilde{a} &= \left((\gamma - 1)\left(\tilde{H} - \frac{1}{2}\tilde{\mathbf{V}}^2\right) \right)^{\frac{1}{2}}, \end{aligned} \quad (\text{B.30})$$

for the initial jump

$$\Delta\mathbf{U} = \mathbf{U}^R - \mathbf{U}^L, \quad (\text{B.31})$$

where $\tilde{\mathbf{V}} = \frac{1}{2}(\tilde{v}^2 + \tilde{u}^2)$. Then, we can obtain the Roe averaged Jacobian matrix and its eigenvalues and eigenvectors by replacing the variable u, v, H , and a by the Roe averaged value $\tilde{u}, \tilde{v}, \tilde{H}$, and \tilde{a} . For example, the Roe average of Jacobian matrix $\mathbf{A}(\mathbf{U})$

in (B.20) can be deduced by

$$\bar{\mathbf{A}}(\mathbf{U}) = \begin{bmatrix} 0 & 1 & 0 & 0 \\ -\tilde{u}^2 + (\gamma - 1)\mathbf{V} & -(\gamma - 3)\tilde{u} & -(\gamma - 1)\tilde{v} & (\gamma - 1) \\ -\tilde{u}\tilde{v} & \tilde{v} & \tilde{u} & 0 \\ \tilde{u}(\tilde{\mathbf{V}}(\gamma - 1) - \tilde{H}) & \tilde{H} - \tilde{u}^2(\gamma - 1) & -(\gamma - 1)\tilde{u}\tilde{v} & \gamma\tilde{u} \end{bmatrix}. \quad (\text{B.32})$$

The eigenvalues of $\bar{\mathbf{A}}(\mathbf{U})$ are given by

$$\lambda_1 = \tilde{u} - \tilde{a}, \quad \lambda_2 = \tilde{u}, \quad \lambda_3 = \tilde{u}, \quad \lambda_4 = \tilde{u} + \tilde{a}, \quad (\text{B.33})$$

and the right eigenvectors are given by

$$\bar{\mathbf{R}}^x = \begin{bmatrix} 1 & 0 & 1 & 1 \\ \tilde{u} - \tilde{a} & 0 & \tilde{u} & \tilde{u} + \tilde{a} \\ \tilde{v} & 1 & \tilde{v} & \tilde{v} \\ H - \tilde{u}\tilde{a} & \tilde{v} & \tilde{\mathbf{V}} & H + \tilde{a}\tilde{u} \end{bmatrix}, \quad (\text{B.34})$$

while the left eigenvectors are defined by

$$\bar{\mathbf{L}}^x = \begin{bmatrix} \frac{1}{2}(\gamma - 1)\frac{\tilde{\mathbf{V}}}{\tilde{a}^2} + 1\frac{\tilde{u}}{2\tilde{a}} & -\frac{1}{2}\left(\frac{\tilde{u}(\gamma - 1)}{\tilde{a}^2} + \frac{1}{\tilde{a}}\right) & -\frac{\tilde{v}(\gamma - 1)}{2\tilde{a}^2} & \frac{(\gamma - 1)}{2\tilde{a}^2} \\ -\tilde{v} & 0 & 1 & 0 \\ 1 - (\gamma - 1)\frac{\tilde{\mathbf{V}}}{\tilde{a}^2} & (\gamma - 1)\frac{\tilde{u}}{\tilde{a}^2} & (\gamma - 1)\frac{\tilde{v}}{\tilde{a}^2} & -\frac{(\gamma - 1)}{\tilde{a}^2} \\ \frac{1}{2}(\gamma - 1)\frac{\tilde{\mathbf{V}}}{\tilde{a}^2} - \frac{\tilde{u}}{2\tilde{a}} & -\frac{1}{2}\left(\frac{\tilde{u}(\gamma - 1)}{\tilde{a}^2} - \frac{1}{\tilde{a}}\right) & -\frac{\tilde{v}(\gamma - 1)}{2\tilde{a}^2} & \frac{(\gamma - 1)}{2\tilde{a}^2} \end{bmatrix}. \quad (\text{B.35})$$

Similarly, we can obtain the Roe averaged Jacobian matrix $\mathbf{B}(\mathbf{U})$ in (B.26) and its eigenvectors and eigenvalues in a similar manner.

Bibliography

- [1] G. Jiang, C. Shu, Efficient implementation of weighted eno schemes, *Journal of Computational Physics* 126 (1) (1996) 202 – 228.
- [2] F. Xiao, S. Ii, C. Chen, Revisit to the THINC scheme: a simple algebraic VOF algorithm, *Journal of Computational Physics* 230 (19) (2011) 7086–7092.
- [3] F. Kemm, On the proper setup of the double mach reflection as a test case for the resolution of gas dynamics codes, *Computers Fluids* 132 (2016) 72 – 75.
- [4] L. G. Smith, *Photographic investigations of the reflection of plane shocks in air*, 1945.
- [5] T. B. Gatski, J. P. Bonnet, *Compressibility, turbulence and high speed flow*, Academic Press, 2013.
- [6] H. I. Saravanamuttoo, G. F. C. Rogers, H. Cohen, *Gas turbine theory*, Pearson Education, 2001.
- [7] W. Kim, S. Menon, H. C. Mongia, Large-eddy simulation of a gas turbine combustor flow, *Combustion Science and Technology* 143 (1-6) (1999) 25–62.
- [8] P. Moin, S. V. Apte, Large-eddy simulation of realistic gas turbine combustors, *AIAA journal* 44 (4) (2006) 698–708.
- [9] M. D. Turrell, P. J. Stopford, K. J. Syed, E. Buchanan, Cfd simulation of the flow within and downstream of a high-swirl lean premixed gas turbine combustor, in:

- ASME Turbo Expo 2004: Power for Land, Sea, and Air, American Society of Mechanical Engineers, 2004, pp. 31–38.
- [10] L. Y. Gicquel, G. Staffelbach, T. Poinso, Large eddy simulations of gaseous flames in gas turbine combustion chambers, *Progress in Energy and Combustion Science* 38 (6) (2012) 782–817.
- [11] B. Ahmadi Befrui, A. Gosman, R. Issa, A. Watkins, An implicit non-iterative solution procedure for the calculation of flows in reciprocating engine chambers, *Computer methods in applied mechanics and engineering* 79 (3) (1990) 249–279.
- [12] D. C. Haworth, S. H. El Tahry, Probability density function approach for multidimensional turbulentflow calculations with application to in-cylinder flows in reciprocating engines, *AIAA journal* 29 (2) (1991) 208–218.
- [13] L. Selle, G. Lartigue, T. Poinso, R. Koch, K. U. Schildmacher, W. Krebs, B. Prade, P. Kaufmann, D. Veynante, Compressible large eddy simulation of turbulent combustion in complex geometry on unstructured meshes, *Combustion and Flame* 137 (4) (2004) 489–505.
- [14] D. Bogdanoff, Compressibility effects in turbulent shear layers, *AIAA journal* 21 (6) (1983) 926–927.
- [15] M. S. Plesset, A. Prosperetti, Bubble dynamics and cavitation, *Annual review of fluid mechanics* 9 (1) (1977) 145–185.
- [16] F. R. Young, *Cavitation*, World Scientific, 1999.
- [17] C. E. Brennen, *Cavitation and bubble dynamics*, Cambridge University Press, 2014.
- [18] J. R. Blake, D. Gibson, Cavitation bubbles near boundaries, *Annual review of fluid mechanics* 19 (1) (1987) 99–123.

-
- [19] J. D. Anderson, J. Wendt, *Computational fluid dynamics*, Vol. 206, Springer, 1995.
- [20] G. Tryggvason, R. Scardovelli, S. Zaleski, *Direct numerical simulations of gas–liquid multiphase flows*, Cambridge University Press, 2011.
- [21] C. B. Laney, *Computational gasdynamics*, Cambridge university press, 1998.
- [22] S. Patankar, *Numerical heat transfer and fluid flow*, CRC press, 1980.
- [23] C. Hirsch, *Numerical computation of internal and external flows: The fundamentals of computational fluid dynamics*, Elsevier, 2007.
- [24] P. Wesseling, *Principles of computational fluid dynamics*, Vol. 29, Springer Science & Business Media, 2009.
- [25] D. Anderson, J. C. Tannehill, R. H. Pletcher, *Computational fluid mechanics and heat transfer*, CRC Press, 2016.
- [26] C. Canuto, M. Y. Hussaini, A. Quarteroni, A. Thomas Jr, et al., *Spectral methods in fluid dynamics*, Springer Science & Business Media, 2012.
- [27] C. Shu, High order weighted essentially nonoscillatory schemes for convection dominated problems, *SIAM review* 51 (1) (2009) 82–126.
- [28] A. Harten, B. Engquist, S. Osher, S. R. Chakravarthy, Uniformly high order accurate essentially non-oscillatory schemes, III, *Journal of Computational Physics* 71 (2) (1987) 231 – 303.
- [29] X. Liu, S. Osher, T. Chan, Weighted essentially non-oscillatory schemes, *Journal of Computational Physics* 115 (1) (1994) 200 – 212.
- [30] C. Shu, Essentially non-oscillatory and weighted essentially non-oscillatory schemes for hyperbolic conservation laws, in: *Advanced numerical approximation of nonlinear hyperbolic equations*, Springer, 1998, pp. 325–432.

-
- [31] A. K. Henrick, T. D. Aslam, J. M. Powers, Mapped weighted essentially non-oscillatory schemes: Achieving optimal order near critical points, *Journal of Computational Physics* 207 (2) (2005) 542 – 567.
- [32] R. Borges, M. Carmona, B. Costa, W. S. Don, An improved weighted essentially non-oscillatory scheme for hyperbolic conservation laws, *Journal of Computational Physics* 227 (6) (2008) 3191 – 3211.
- [33] X. Hu, Q. Wang, N. Adams, An adaptive central-upwind weighted essentially non-oscillatory scheme, *Journal of Computational Physics* 229 (23) (2010) 8952 – 8965.
- [34] R. Tanaka, T. Nakamura, T. Yabe, Constructing exactly conservative scheme in a non-conservative form, *Computer Physics Communications* 126 (3) (2000) 232 – 243.
- [35] N. Onodera, T. Aoki, K. Yokoi, A fully conservative high-order upwind multi-moment method using moments in both upwind and downwind cells, *International Journal for Numerical Methods in Fluids* 42:28.
- [36] Q. Li, S. Omar, X. Deng, K. Yokoi, Constrained interpolation profile conservative semi-lagrangian scheme based on third-order polynomial functions and essentially non-oscillatory (cip-csl3eno) scheme, *Communications in Computational Physics* 22 (3) (2017) 765–788.
- [37] Z. Sun, F. Xiao, A semi lagrangian multi moment finite volume method with fourth order weno projection, *International Journal for Numerical Methods in Fluids* 83 (4) (2016) 351–375.
- [38] S. Godunov, A difference method for numerical calculation of discontinuous solutions of the equations of hydrodynamics, *Matematicheskii Sbornik* 47 (1959) 271–306.

- [39] Z. Wang, High-order methods for the Euler and Navier–Stokes equations on unstructured grids, *Progress in Aerospace Sciences* 43 (1) (2007) 1–41.
- [40] F. Xiao, Y. Honma, T. Kono, A simple algebraic interface capturing scheme using hyperbolic tangent function, *International Journal for Numerical Methods in Fluids* 48 (9) (2005) 1023–1040.
- [41] X. Deng, S. Inaba, B. Xie, K. M. Shyue, F. Xiao, High fidelity discontinuity-resolving reconstruction for compressible multiphase flows with moving interfaces, *Journal of Computational Physics*.
- [42] G. Allaire, S. Clerc, S. Kokh, A five-equation model for the simulation of interfaces between compressible fluids, *Journal of Computational Physics* 181 (2) (2002) 577–616.
- [43] L. C. Evans, *Partial differential equations*.
- [44] A. D. Polyanin, W. E. Schiesser, A. I. Zhurov, *Partial differential equation*, *Scholarpedia* 3 (10) (2008) 4605.
- [45] D. M. Young, D. R. Kincaid, *Partial differential equations*, John Wiley and Sons Ltd., 2003.
- [46] A. Harten, High resolution schemes for hyperbolic conservation laws, *Journal of Computational Physics* 49 (3) (1983) 357 – 393.
- [47] J. Crank, et al., *The mathematics of diffusion*, Oxford university press, 1979.
- [48] G. D. Smith, *Numerical solution of partial differential equations: finite difference methods*, Oxford university press, 1985.
- [49] C. Grossmann, H.-G. Roos, M. Stynes, *Numerical treatment of partial differential equations*, Vol. 154, Springer, 2007.
- [50] J. H. Ferziger, M. Peric, *Computational methods for fluid dynamics*, Springer Science & Business Media, 2012.

- [51] C. A. Fletcher, *Computational techniques for fluid dynamics 2: Specific techniques for different flow categories*, Springer Science & Business Media, 2012.
- [52] B. A. Finlayson, *The method of weighted residuals and variational principles*, Vol. 73, SIAM, 2013.
- [53] H. K. Versteeg, W. Malalasekera, *An introduction to computational fluid dynamics: the finite volume method*, Pearson education, 2007.
- [54] E. F. Toro, *Riemann solvers and numerical methods for fluid dynamics: a practical introduction*, Springer Science & Business Media, 2013.
- [55] R. Eymard, T. Gallouët, R. Herbin, *Finite volume methods*, *Handbook of numerical analysis* 7 (2000) 713–1018.
- [56] R. J. LeVeque, *Finite volume methods for hyperbolic problems*, Vol. 31, Cambridge university press, 2002.
- [57] F. Moukalled, L. Mangani, M. Darwish, et al., *The finite volume method in computational fluid dynamics, An Advanced Introduction with OpenFOAM and Matlab* (2016) 3–8.
- [58] Y. Wu, K. F. Cheung, *Explicit solution to the exact riemann problem and application in nonlinear shallow-water equations*, *International Journal for Numerical Methods in Fluids* 57 (11) (2008) 1649–1668.
- [59] V. Deledicque, M. V. Papalexandris, *An exact riemann solver for compressible two-phase flow models containing non-conservative products*, *Journal of Computational Physics* 222 (1) (2007) 217–245.
- [60] L. Rezzolla, O. Zanotti, *An improved exact riemann solver for relativistic hydrodynamics*, *Journal of Fluid Mechanics* 449 (2001) 395–411.
- [61] P. Roe, *Approximate riemann solvers, parameter vectors, and difference schemes*, *Journal of computational physics* 43 (2) (1981) 357–372.

- [62] J. J. Quirk, A contribution to the great riemann solver debate, in: *Upwind and High-Resolution Schemes*, Springer, 1997, pp. 550–569.
- [63] L. Sainsaulieu, Finite volume approximation of two phase-fluid flows based on an approximate roe-type riemann solver, *Journal of Computational Physics* 121 (1) (1995) 1–28.
- [64] T. Flåtten, S. T. Munkejord, The approximate riemann solver of roe applied to a drift-flux two-phase flow model, *ESAIM: Mathematical Modelling and Numerical Analysis* 40 (4) (2006) 735–764.
- [65] B. Einfeldt, On godunov-type methods for gas dynamics, *SIAM Journal on Numerical Analysis* 25 (2) (1988) 294–318.
- [66] E. F. Toro, M. Spruce, W. Speares, Restoration of the contact surface in the hll-riemann solver, *Shock waves* 4 (1) (1994) 25–34.
- [67] E. F. Toro, The hll and hllc riemann solvers, in: *Riemann Solvers and Numerical Methods for Fluid Dynamics*, Springer, 1999, pp. 315–339.
- [68] T. Linde, A practical, general-purpose, two-state hll riemann solver for hyperbolic conservation laws, *International Journal for Numerical Methods in Fluids* 40 (3-4) (2002) 391–402.
- [69] X. Ying, S. S. Wang, Improved implementation of the hll approximate riemann solver for one-dimensional open channel flows, *Journal of Hydraulic Research* 46 (1) (2008) 21–34.
- [70] E. Toro, *Riemann solvers and numerical methods for fluid dynamics*, Third Edition, Springer-Verlag, Berlin, 2009.
- [71] P. Batten, N. Clarke, C. Lambert, D. M. Causon, On the choice of wavespeeds for the hllc riemann solver, *SIAM Journal on Scientific Computing* 18 (6) (1997) 1553–1570.

- [72] D. S. Balsara, A two-dimensional hllc riemann solver for conservation laws: Application to euler and magnetohydrodynamic flows, *Journal of Computational Physics* 231 (22) (2012) 7476–7503.
- [73] A. Mignone, G. Bodo, An hllc riemann solver for relativistic flows. hydrodynamics, *Monthly Notices of the Royal Astronomical Society* 364 (1) (2005) 126–136.
- [74] X. Hu, N. A. Adams, G. Iaccarino, On the hllc riemann solver for interface interaction in compressible multi-fluid flow, *Journal of Computational Physics* 228 (17) (2009) 6572–6589.
- [75] D. S. Balsara, M. Dumbser, R. Abgrall, Multidimensional hllc riemann solver for unstructured meshes—with application to euler and mhd flows, *Journal of Computational Physics* 261 (2014) 172–208.
- [76] S. Osher, F. Solomon, Upwind difference schemes for hyperbolic systems of conservation laws, *Mathematics of computation* 38 (158) (1982) 339–374.
- [77] S. Osher, Riemann solvers, the entropy condition, and difference, *SIAM Journal on Numerical Analysis* 21 (2) (1984) 217–235.
- [78] B. Van Leer, Towards the ultimate conservative difference scheme, *Journal of Computational Physics* 135 (2) (1997) 229–248.
- [79] C. Shu, S. Osher, Efficient implementation of essentially non-oscillatory shock-capturing schemes, *Journal of Computational Physics* 77 (2) (1988) 439 – 471.
- [80] C. Shu, S. Osher, Efficient implementation of essentially non-oscillatory shock-capturing schemes, ii, in: *Upwind and High-Resolution Schemes*, Springer, 1989, pp. 328–374.
- [81] Z. Cheng, Y. Liu, M. Zhang, J. Wang, Ib-weno method for incompressible flow with elastic boundaries, *Journal of Computational and Applied Mathematics*.

- [82] C. Y. Jung, T. B. Nguyen, A new adaptive weighted essentially non-oscillatory weno scheme for hyperbolic conservation laws, *Journal of Computational and Applied Mathematics* 328 (2018) 314 – 339.
- [83] Y. Xing, High order finite volume weno schemes for the shallow water flows through channels with irregular geometry, *Journal of Computational and Applied Mathematics* 299 (2016) 229 – 244.
- [84] J. Qiu, Weno schemes with lax-wendroff type time discretizations for hamilton-jacobi equations, *Journal of Computational and Applied Mathematics* 200 (2) (2007) 591 – 605.
- [85] B. Costa, W. S. Don, High order hybrid central-weno finite difference scheme for conservation laws, *Journal of Computational and Applied Mathematics* 204 (2) (2007) 209 – 218.
- [86] F. Hu, R. Wang, X. Chen, A modified fifth-order weno method for hyperbolic conservation laws, *Journal of Computational and Applied Mathematics* 303 (2016) 56 – 68.
- [87] C. Huang, R. Wang, Mapped cweno scheme for hyperbolic conservation laws, *Journal of Computational and Applied Mathematics* 344 (2018) 229 – 244.
- [88] L. Fu, X. Y. Hu, N. A. Adams, A family of high-order targeted eno schemes for compressible-fluid simulations, *Journal of Computational Physics* 305 (2016) 333 – 359.
- [89] L. Fu, X. Y. Hu, N. A. Adams, Targeted eno schemes with tailored resolution property for hyperbolic conservation laws, *Journal of Computational Physics* 349 (2017) 97–121.
- [90] Z. Sun, S. Inaba, F. Xiao, Boundary variation diminishing (bvd) reconstruction: A new approach to improve godunov schemes, *Journal of Computational Physics* 322 (2016) 309 – 325.

- [91] K. Shyue, F. Xiao, An Eulerian interface sharpening algorithm for compressible two-phase flow: The algebraic THINC approach, *Journal of Computational Physics* 268 (2014) 326–354.
- [92] D. Cassidy, J. Edwards, M. Tian, An investigation of interface-sharpening schemes for multi-phase mixture flows, *Journal of Computational Physics* 228 (16) (2009) 5628–5649.
- [93] T. Yabe, R. Tanaka, T. Nakamura, F. Xiao, An exactly conservative semi-lagrangian scheme (CIP-CSL) in one dimension, *Monthly Weather Review* 129 (2) (2001) 332–344.
- [94] F. Xiao, T. Yabe, Completely conservative and oscillationless semi-lagrangian schemes for advection transportation, *Journal of Computational Physics* 170 (2) (2001) 498 – 522.
- [95] F. Xiao, T. Yabe, X. Peng, H. Kobayashi, Conservative and oscillation-less atmospheric transport schemes based on rational functions, *Journal of Geophysical Research: Atmospheres* 107 (D22).
- [96] K. Yokoi, A numerical method for free-surface flows and its application to droplet impact on a thin liquid layer, *Journal of Scientific Computing* 35 (2) (2008) 372–396.
- [97] T. Yabe, F. Xiao, T. Utsumi, The constrained interpolation profile method for multiphase analysis, *Journal of Computational Physics* 169 (2) (2001) 556 – 593.
- [98] T. Nakamura, R. Tanaka, T. Yabe, K. Takizawa, Exactly conservative semi-lagrangian scheme for multi-dimensional hyperbolic equations with directional splitting technique, *Journal of computational physics* 174 (1) (2001) 171–207.

- [99] F. Xiao, Profile-modifiable conservative transport schemes and a simple multi-integrated moment formulation for hydrodynamics, in: *Computational Fluid Dynamics 2002*, Springer, 2003, pp. 106–111.
- [100] F. Xiao, A. Ikebata, An efficient method for capturing free boundaries in multi-fluid simulations, *International journal for numerical methods in fluids* 42 (2) (2003) 187–210.
- [101] F. Xiao, Unified formulation for compressible and incompressible flows by using multi-integrated moments I: one-dimensional inviscid compressible flow, *Journal of Computational Physics* 195 (2) (2004) 629 – 654.
- [102] F. Xiao, A. Ikebata, T. Hasegawa, Numerical simulations of free-interface fluids by a multi-integrated moment method, *Computers and Structures* 83 (6â7) (2005) 409 – 423, *frontier of Multi-Phase Flow Analysis and Fluid-Structure* *Frontier of Multi-Phase Flow Analysis and Fluid-Structure*.
- [103] F. Xiao, R. Akoh, S. Ii, Unified formulation for compressible and incompressible flows by using multi-integrated moments II: Multi-dimensional version for compressible and incompressible flows, *Journal of Computational Physics* 213 (1) (2006) 31 – 56.
- [104] X. Li, D. Chen, X. Peng, K. Takahashi, F. Xiao, A multimoment finite-volume shallow-water model on the Yin-Yang overset spherical grid, *Monthly Weather Review* 136 (8) (2008) 3066–3086.
- [105] K. Yokoi, A practical numerical framework for free surface flows based on CLS-VOF method, multi-moment methods and density-scaled CSF model: Numerical simulations of droplet splashing, *Journal of Computational Physics* 232 (1) (2013) 252 – 271.
- [106] K. Yokoi, A density-scaled continuum surface force model within a balanced force formulation, *Journal of Computational Physics* 278 (2014) 221 – 228.

- [107] C. Shu, Total-variation-diminishing time discretizations, *SIAM Journal on Scientific and Statistical Computing* 9 (6) (1988) 1073–1084.
- [108] S. Ii, F. Xiao, CIP/multi-moment finite volume method for euler equations: A semi-lagrangian characteristic formulation, *Journal of Computational Physics* 222 (2) (2007) 849 – 871.
- [109] J. M. Hyman, Accurate monotonicity preserving cubic interpolation, *SIAM Journal on Scientific and Statistical Computing* 4 (4) (1983) 645–654.
- [110] P. Colella, P. R. Woodward, The piecewise parabolic method (PPM) for gas-dynamical simulations, *Journal of Computational Physics* 54 (1) (1984) 174 – 201.
- [111] J. Hesthaven, T. Warburton, *Nodal discontinuous Galerkin methods: algorithms, analysis, and applications*, Springer-Verlag, New York, 2007.
- [112] H. Terashima, G. Tryggvason, A front-tracking/ghost-fluid method for fluid interfaces in compressible flows, *Journal of Computational Physics* 228 (11) (2009) 4012–4037.
- [113] X. Y. Hu, B. C. Khoo, An interface interaction method for compressible multi-fluids, *Journal of Computational Physics* 198 (1) (2004) 35–64.
- [114] X. Y. Hu, B. Khoo, N. A. Adams, F. Huang, A conservative interface method for compressible flows, *Journal of Computational Physics* 219 (2) (2006) 553–578.
- [115] T. Liu, B. Khoo, C. Wang, The ghost fluid method for compressible gas–water simulation, *Journal of Computational Physics* 204 (1) (2005) 193–221.
- [116] R. R. Nourgaliev, T. G. Theofanous, High-fidelity interface tracking in compressible flows: unlimited anchored adaptive level set, *Journal of Computational Physics* 224 (2) (2007) 836–866.

- [117] J. Blake, B. Taib, G. Doherty, Transient cavities near boundaries. part 1. rigid boundary, *Journal of Fluid Mechanics* 170 (1986) 479–497.
- [118] J. Blake, B. Taib, G. Doherty, Transient cavities near boundaries part 2. free surface, *Journal of Fluid Mechanics* 181 (1987) 197–212.
- [119] C. W. Hirt, B. D. Nichols, Volume of fluid (vof) method for the dynamics of free boundaries, *Journal of computational physics* 39 (1) (1981) 201–225.
- [120] S. O. Unverdi, G. Tryggvason, A front-tracking method for viscous, incompressible, multi-fluid flows, *Journal of computational physics* 100 (1) (1992) 25–37.
- [121] S. Osher, J. A. Sethian, Fronts propagating with curvature-dependent speed: algorithms based on hamilton-jacobi formulations, *Journal of computational physics* 79 (1) (1988) 12–49.
- [122] F. H. Harlow, J. E. Welch, Numerical calculation of time-dependent viscous incompressible flow of fluid with free surface, *The physics of fluids* 8 (12) (1965) 2182–2189.
- [123] T. Vignesh, S. Bakshi, Noniterative interface reconstruction algorithms for volume of fluid method, *International Journal for Numerical Methods in Fluids* 73 (1) (2013) 1–18.
- [124] M. Sussman, A second order coupled level set and volume-of-fluid method for computing growth and collapse of vapor bubbles, *Journal of Computational Physics* 187 (1) (2003) 110–136.
- [125] S. Popinet, S. Zaleski, Bubble collapse near a solid boundary: a numerical study of the influence of viscosity, *Journal of Fluid Mechanics* 464 (2002) 137–163.
- [126] S. J. Lind, T. N. Phillips, Bubble collapse in compressible fluids using a spectral element marker particle method. part 1. newtonian fluids, *International Journal for Numerical Methods in Fluids* 70 (9) (2012) 1167–1187.

- [127] S. J. Lind, T. N. Phillips, Bubble collapse in compressible fluids using a spectral element marker particle method. part 2. viscoelastic fluids, *International Journal for Numerical Methods in Fluids* 71 (9) (2013) 1103–1130.
- [128] G. Tryggvason, A. Esmaeeli, J. Lu, S. Biswas, Direct numerical simulations of gas/liquid multiphase flows, *Fluid dynamics research* 38 (9) (2006) 660–681.
- [129] Y. Imai, T. Aoki, Accuracy study of the IDO scheme by fourier analysis, *Journal of Computational Physics* 217 (2) (2006) 453 – 472.
- [130] G. A. Sod, A survey of several finite difference methods for systems of nonlinear hyperbolic conservation laws, *Journal of Computational Physics* 27 (1) (1978) 1 – 31.
- [131] Y. Shen, G. Zha, Improvement of weighted essentially non-oscillatory schemes near discontinuities, *Computers & Fluids* 96 (2014) 1–9.
- [132] C. Huang, F. Xiao, T. Arbogast, Fifth order multi-moment weno schemes for hyperbolic conservation laws, *Journal of Scientific Computing* 64 (2) (2015) 477–507.
- [133] Z. Sun, H. Teng, F. Xiao, A slope constrained 4th order multi-moment finite volume method with weno limiter, *Communications in Computational Physics* 18 (2015) 901–930.
- [134] P. Woodward, P. Colella, The numerical simulation of two-dimensional fluid flow with strong shocks, *Journal of computational physics* 54 (1) (1984) 115–173.
- [135] G. Strang, On the construction and comparison of difference schemes, *SIAM Journal on Numerical Analysis* 5 (3) (1968) 506–517.
- [136] S. Ziyao, X. Feng, A semi-lagrangian multi-moment finite volume method with fourth-order weno projection, *International Journal for Numerical Methods in Fluids* 83 (4) 351–375.

- [137] L. L. Takacs, A two-step scheme for the advection equation with minimized dissipation and dispersion errors, *Monthly Weather Review* 113 (6) (1985) 1050–1065.
- [138] U. Ghia, K. Ghia, C. Shin, High-re solutions for incompressible flow using the navier-stokes equations and a multigrid method, *Journal of Computational Physics* 48 (3) (1982) 387 – 411.
- [139] E. F. Toro, *Riemann solvers and numerical methods for fluid dynamics: a practical introduction*, Springer Science & Business Media, 2013.
- [140] D. Zhao, H. Shen, J. Lai, G. T. III, Approximate riemann solvers in fvm for 2d hydraulic shock wave modeling, *Journal of Hydraulic Engineering* 122 (12) (1996) 692–702.
- [141] S. T. Zalesak, Fully multidimensional flux-corrected transport algorithms for fluids, *Journal of computational physics* 31 (3) (1979) 335–362.
- [142] X. Hu, N. Adams, Scale separation for implicit large eddy simulation, *Journal of Computational Physics* 230 (19) (2011) 7240 – 7249.
- [143] K. Shyue, A fluid-mixture type algorithm for compressible multicomponent flow with mie–grüneisen equation of state, *Journal of Computational Physics* 171 (2) (2001) 678–707.
- [144] K. Shyue, A fluid-mixture type algorithm for compressible multicomponent flow with van der waals equation of state, *Journal of Computational Physics* 156 (1) (1999) 43–88.
- [145] R. Abgrall, S. Karni, Computations of compressible multifluids, *Journal of computational physics* 169 (2) (2001) 594–623.
- [146] S. Gottlieb, C. W. Shu, E. Tadmor, Strong stability-preserving high-order time discretization methods, *SIAM review* 43 (1) (2001) 89–112.

-
- [147] R. Saurel, R. Abgrall, A multiphase godunov method for compressible multi-fluid and multiphase flows, *Journal of Computational Physics* 150 (2) (1999) 425–467.
- [148] J. F. Haas, B. Sturtevant, Interaction of weak shock waves with cylindrical and spherical gas inhomogeneities, *Journal of Fluid Mechanics* 181 (1987) 41–76.
- [149] J. J. Quirk, S. Karni, On the dynamics of a shock–bubble interaction, *Journal of Fluid Mechanics* 318 (1996) 129–163.
- [150] K. So, X. Hu, N. A. Adams, Anti-diffusion interface sharpening technique for two-phase compressible flow simulations, *Journal of Computational Physics* 231 (11) (2012) 4304–4323.
- [151] J. Luo, X. Hu, N. A. Adams, Efficient formulation of scale separation for multi-scale modeling of interfacial flows, *Journal of Computational Physics* 308 (2016) 411–420.